

## ABSTRACT

Title of Document: NANOMECHANICAL PROPERTIES AND  
BUCKLING INSTABILITY OF PLASMA  
INDUCED DAMAGED LAYER ON  
POLYSTYRENE

Tsung-Cheng Lin, Doctor of Philosophy, 2012

Directed By: Professor, Raymond J. Phaneuf,  
Department of Materials Science and  
Engineering

In this thesis we report on an investigation of an elastic buckling instability as a driving force for the roughening of polystyrene, a model resist, during Ar<sup>+</sup> plasma etching. Polystyrene films etched by pure Ar<sup>+</sup> plasma with different ion energies were characterized using both atomic force microscopy topography and force curve measurements. By using height-height correlation function in analyzing the AFM measured topography images, we find that surface corrugation of etched polystyrene film surfaces all display a dominant wrinkle wavelength ( $\lambda$ ), which is a function of ion energy. Next, we characterized the mechanical properties of these samples using AFM force curve measurements in a controlled ambient environment. We analyzed the measured force curves using a systematic algorithm based on statistical fitting procedures, and taking into account the adhesive interaction, in order to determine the effective elastic modulus of the films. We find that the effective elastic modulus ( $E_{BL}$ )

of the etched samples increases monotonically with increasing ion energy, but the changes are rather subtle as compared to the elastic modulus ( $E_{PS}$ ) of the unetched one.

In order to test the validity of a buckling instability as the mechanism for surface roughening in our polystyrene-Ar plasma system, the elastic modulus of individual layer (i.e. ion-damaged layer plus unmodified foundation) needs to be determined. We present a determination of the damaged layer elastic modulus ( $E_{DL}$ ) from the effective elastic modulus of the damaged layer/polystyrene bilayer structure ( $E_{BL}$ ), based upon a finite element method simulation taking into account the thickness and elastic modulus of the damaged layers. We extract the damaged layer elastic modulus versus etching ion energy initially within the approximation of a spherical tip in contact with a flat sample surface. We next extend our model, by considering a periodic corrugated film surface, with its amplitude and wavelength determined by AFM, to take into account the effect of roughness induced by plasma exposure. The damaged layer elastic modulus extracted from these two approximations gives of quantitative agreement, and thus evidence for the correlation between buckling instability and plasma-induced roughening.

NANOMECHANICAL PROPERTIES AND BUCKLING INSTABILITY OF  
PLASMA INDUCED DAMAGED LAYERS ON POLYSTYRENE

By

Tsung-Cheng Lin

Dissertation submitted to the Faculty of the Graduate School of the  
University of Maryland, College Park, in partial fulfillment  
of the requirements for the degree of  
Doctor of Philosophy  
2012

Advisory Committee:  
Professor Raymond J. Phaneuf, Chair  
Professor Gottlieb S. Oehrlein  
Professor John Melngailis  
Professor Mohamad Al-Sheikhly  
Professor Robert M. Briber

© Copyright by  
Tsung-Cheng Lin  
2012

## Dedication

To my parents, my brother, Han-Mei,

and

my grandmother.

## Acknowledgements

Above all, I would like to thank my advisor, Professor Raymond J. Phaneuf, for his fully support and guidance during the past six years in helping me to complete this thesis research. He gave me the opportunities to take solid trainings and do good science. His enthusiasm and persistence in both teaching and research are very encouraging to me not only in doing research but also in dealing with every challenge. It's a very valuable experience in my life to have worked with him.

I would also like to thank Dr. Hung-Chih Kan who always gave me valuable suggestions and support at crucial moments during the period of my thesis research. It's always enlightening through every time talking with him no matter on scientific subjects or life philosophy.

A number of works described in this thesis are a result of collaboration, therefore I acknowledge my colleagues for their contributions here. Firstly, Professor Gottlieb S. Oehrlein provided plasma etching/characterization facilities, and generously shared his valuable knowledge and experiences in plasma etching. Dr. Robert L. Bruce carried out the plasma etching for the samples. At the University of Texas, Austin, Professor C. Grant Willson provided the facilities and reagents for synthesis of the polymer samples, and Dr. Brian Long performed the synthesis of the polymer samples. At the University of California, Berkeley, Professor David B. Graves directed the ion-beam experiment and MD simulations, while Dr. Dustin Nest and Dr. Joseph J. Végé performed the works respectively. Dr. Hung-Chih Kan provided help in developing FORTRAN code for force curve analysis and simulation of surface evolution (Appendix: Nanolithography). Dr. Sherman Guo provided help

in facilitating several cumbersome data analysis and developing C<sup>++</sup> code for AFM nanolithography.

Special acknowledgement to each member of my thesis research committees: Professor Gottlieb S. Oehrlein, Professor John Melngailis, Professor Robert M. Briber, and Professor Mohamad Al-Sheikhly. They are all inspiring scientists and teachers, and it's been my great privilege to talk with them about my research.

Also, I would like to express maximum gratitude to my colleagues and friends who have been liberally sharing thoughts and giving assistance during the past few years. They are: Chuan-Fu Lin, Dr. Sherman Guo, Dr. Tim Corrigan, Dr. Taesoon Kwon, Dr. Shu-Ju Tsai, Dr. Ping-Yen Hsieh and his lovely family, Dale Huang, Dominic Britti, Amy Marquardt, Miriam Cezza, Dr. Daniel Hines, Dr. Michael Dreyer, Dr. Clifford Hull, Greg Latini, Laurence C. Olver, Steve Brown, and Dr. Karen Gaskel.

Finally, I would like to thank my father, Shih-Hsiung Lin, my mother, Yu-Lan Wu, and my brother, Tsung-Po Lin, for their endless support and love. A special thank to Han-Mei Tso for her consideration and care during these years.

# Table of Contents

<b>Dedication .....</b>	<b>ii</b>
<b>Acknowledgement .....</b>	<b>iii</b>
<b>Table of Contents .....</b>	<b>v</b>
<b>List of Tables .....</b>	<b>vii</b>
<b>List of Figures .....</b>	<b>viii</b>
<b>Chapter: 1 Introduction .....</b>	<b>1</b>
<b>1.1 Motivation .....</b>	<b>1</b>
<b>1.2 Reactive ion etching of polymer thin film .....</b>	<b>4</b>
<b>1.2.1 Plasma-polymer surface interaction .....</b>	<b>4</b>
<b>1.2.2 Formation of damaged layer .....</b>	<b>5</b>
<b>1.2.3 Mechanisms for roughness formation .....</b>	<b>7</b>
<b>1.2.4 Early results for simple model polymers .....</b>	<b>9</b>
<b>1.3 Buckling instability .....</b>	<b>15</b>
<b>1.4 Nanomechanics for surface characterization .....</b>	<b>18</b>
<b>1.5 Contact mechanics .....</b>	<b>19</b>
<b>1.6 Outlines of thesis .....</b>	<b>25</b>
<b>Chapter: 2 Experiment and measurement .....</b>	<b>27</b>
<b>2.1 Sample preparation .....</b>	<b>28</b>
<b>2.2 Topography characterization of etched films .....</b>	<b>31</b>
<b>2.3 AFM force curve analysis .....</b>	<b>39</b>
<b>2.3.1 General look of a force curve .....</b>	<b>39</b>
<b>2.3.2 Force curve measurement setup .....</b>	<b>43</b>
<b>2.3.3 Analysis of measured force curve .....</b>	<b>45</b>
<b>2.3.3.1 Calibration of cantilever response .....</b>	<b>45</b>
<b>2.3.3.2 Extraction of elastic modulus from measured force curve .....</b>	<b>48</b>
<b>2.3.4 Analysis result of pristine and etched polystyrene sample .....</b>	<b>57</b>
<b>2.4 Summary .....</b>	<b>62</b>
<b>Chapter 3: Extraction of damaged layer elastic modulus .....</b>	<b>63</b>
<b>3.1 Linear elasticity .....</b>	<b>64</b>
<b>3.2 Hertzian Theory .....</b>	<b>66</b>
<b>3.3 Simulation of penetration on pristine polystyrene .....</b>	<b>68</b>
<b>3.4 Simulation of penetration on etched polystyrene .....</b>	<b>76</b>
<b>3.4.1 Flat surface approximation .....</b>	<b>76</b>
<b>3.4.2 Corrugated surface approximation .....</b>	<b>90</b>
<b>3.5 Summary .....</b>	<b>114</b>

<b>Chapter 4: Summary and Conclusions .....</b>	<b>116</b>
<b>Chapter 5: Future works .....</b>	<b>120</b>
<b>Appendix A: Nanolithography by AFM .....</b>	<b>123</b>
<b>A.1 Introduction .....</b>	<b>123</b>
<b>A.2 Experiment .....</b>	<b>123</b>
<b>A.2.1 Nano-scratching .....</b>	<b>124</b>
<b>A.2.2 Annealing of nano grooves .....</b>	<b>124</b>
<b>A.3 Results .....</b>	<b>127</b>
<b>A.4 Theoretical model and simulation .....</b>	<b>133</b>
<b>A.5 Discussion .....</b>	<b>139</b>
<b>Appendix B: X-ray photoelectron spectroscopy (XPS) .....</b>	<b>144</b>
<b>Appendix C: Ambient controlled AFM .....</b>	<b>147</b>
<b>Appendix D: FORTRAN program code for analyzing measured force curve ..</b>	<b>153</b>
<b>Appendix E: Finite element method with COMSOL .....</b>	<b>166</b>
<b>E.1 Theory background of stress-strain relationship in COMSOL .....</b>	<b>170</b>
<b>E.2 Step by step procedure for COMSOL simulation .....</b>	<b>174</b>
<b>Appendix F: Model geometry design and boundary conditions .....</b>	<b>185</b>
<b>Bibliography .....</b>	<b>188</b>

## List of Tables

<b>Table 1.1</b> Relation between the contact radius, $a$ , the sample deformation, $\delta$ , and the adhesion force, $F_{ad}$ for a spherical tip on a flat surface according to the Hertz, DMT, and JKR models. ....	21
<b>Table 2.1</b> The thickness of damaged layer ( $t$ ) as determined by XPS; the average surface corrugation amplitude ( $A$ ) as determined by AFM; and the dominant wavelength ( $\lambda$ ) as determined from height-height correlation analysis, as functions of ion energy for plasma-etched polystyrene. ....	38
<b>Table 2.2</b> The $\alpha$ parameters resulting in the best P-T fit for different conditioned polystyrene films. The errors come from the standard deviations by averaging of multiple force curves. ....	61
<b>Table 3.1</b> Values of materials properties of the silica probe and polystyrene slab used in the simulations: elastic modulus ( $E$ ), Poisson's ratio ( $\nu$ ), and density ( $\rho$ ). ....	71

## List of Figures

### Chapter 1

**Figure 1.1** Schematic of buckling of a damaged layer formed on a polymer film exposed to ion bombardment. ....3

**Figure 1.2** Schematics of chemical structures of model polymers used in plasma etching experiment and vacuum beam experiments done by Bruce *et al.* and Nest *et al.* respectively. ....13

**Figure 1.3** Side views of the polystyrene cell for a single MD simulation, indicating a transition from the initial surface to a highly modified surface at steady state. Corresponding changes in sputter yield and the ratio of number of atoms (H:C) at the damaged region from the initial to the final state are from  $\sim 5.7$  to  $\sim 0.017$  Eq.  $C/Ar^+$  and from 1.0 to 0.11 respectively. The value for the H:C ratio and the damaged layer thickness for the steady-state surface are averaged over 5 separate surface compositions during the last 2500  $Ar^+$  impacts of the simulation (at a interval of 500 impacts), after steady state has been established. ....14

**Figure 1.4** Schematics of buckling instability-driven film wrinkling and delamination under a compressive stress. ....17

**Figure 1.5** Interaction force (per unit area) as a function of distance for the Hertz, DMT, and JKR models, compared to a realistic interaction. ....21

**Figure 1.6** Interaction force (per unit area) as a function of distance for the MD model. A constant adhesive stress  $\sigma_0$  acts between the surfaces over a distance  $d_t$ , resulting in the work of adhesion  $W = \sigma_0 \times d_t$ . No interaction force acts at distance beyond  $Z_0 + d_t$ .  $Z_0$  is the equilibrium separation of the surfaces. ....24

### Chapter 2

**Figure 2.1** Cross-sectional view of schematic of the inductively coupled plasma (ICP) reactor used in this work. ....30

**Figure 2.2** AFM topographic images of (a) pristine (unetched) polystyrene and (b)-(d) polystyrene films after 60 seconds exposure of Ar plasma with varying maximum ion energies of (b) 50 eV, (c) 75 eV, and (d) 100 eV. Field of view in each case is 500 nm. ....33

**Figure 2.3** Correlation maps corresponding to the AFM images of Fig 2.2, i.e.: (a) pristine PS, (b) 50 eV, (c) 75 eV, and (d) 100 eV. For the pristine polystyrene sample, there is only one maximum peak locating at the center of the map, (a), reflecting no

dominant spatial wavelength on the surface. On the Ar-plasma treated samples, a second ring appears about the map centers. ....34

**Figure 2.4** Illustration of the determination of the dominant wrinkle wavelength ( $\lambda$ ).  $\lambda$  is picked out from the first local maximum peak shows on the azimuthally averaged line profile (black solid line). ....35

**Figure 2.5** (a) Family of curves of azimuthally-averaged line profiles across the center of correlation maps calculated from AFM images for polystyrene samples etched at a series of ion energies. (b) Same curves as in (a), replotted with reduced vertical scale. ....37

**Figure 2.6** Schematic of the relative position of the cantilever and the sample surface during a cycle of force curve measurement. Note that each specific spot on the force curve corresponds to different degree of cantilever bending, e.g. the “jump-to-contact” (c), “zero-deflection point” (e), and the “jump off” (h). ....42

**Figure 2.7** SEM images of a spherical silica probe used in the force curve measurement. The nominal diameter of the sphere is 3.5  $\mu\text{m}$ . ....44

**Figure 2.8** Schematic illustration of the relation between the effective bilayer stiffness ( $E_{BL}$ ) and the individual components ( $E_{DL}$  &  $E_{PS}$ ). ....44

**Figure 2.9** (a) Raw, photodetector voltage versus  $Z_{\text{piezo}}$  curve of a Si<100> substrate. (b) The corresponding cantilever deflection versus  $Z_{\text{piezo}}$  curve of (a) when the sensitivity is determined. ....47

**Figure 2.10** Schematic illustration of a spherical probe (radius of R) penetrating into a film with a penetration depth  $\delta$  (relative to undeformed surface,  $Z=0$ ). The radius of the circular contact area at zero load is  $a_0$ . ....49

**Figure 2.11** The measured force curve of an pristine polystyrene sample, where  $D_{\text{pd}}$  denotes the deflection of the cantilever detected by the photodiode sensor. The range in which the indentation process takes place is 70nm, with a scan rate of 1 Hz. ....54

**Figure 2.12** Illustration of procedures for extraction of sample elastic modulus from a measured force curve following the method of Lin et al.: **(a)** Determination of zero force point ( $D_l, \delta_l$ ); **(b)** Determination of contact point ( $D_0, Z_0$ ). Note that this example is a retraction force curve measured on a ~400 nm thick pristine polystyrene film. ....55

**Figure 2.13** Plot of tip-sample force vs. penetration for the retraction curve illustrated in figure 2.11. In the inset, the repulsive part of the force–penetration curve is fitted to the JKR form, corresponding to  $\alpha = 1$ . ....56

**Figure 2.14** AFM-measured force curves showing the cantilever deflection ( $D_{\text{pd}}$ ) as a function of the displacement of the cantilever’s supported end ( $Z_{\text{piezo}}$ ), at right, and as

a function of  $\delta = Z_{piezo} - D_{pd}$ , at left, for polystyrene samples treated by different  $Ar^+$  ion energies: (a) pristine, (b) 50 eV, (c) 75 eV, (d) 100 eV, and (e) 150 eV. The solid and dashed curves in each plot on the left are the minimum least-square-error fits to L-J forms, and power law+linear function, respectively; the solid curves on the right are minimum least-square-error fits to the P-T algorithm. ....59, 60

**Figure 2.15** Extracted elastic modulus of pristine polystyrene film and effective bilayer elastic moduli ( $E_{BL}$ ) for polystyrene films exposed to Ar plasma with different ion energies, versus  $Ar^+$  ion energy, as determined from measured AFM-force curves. ....61

### Chapter 3

**Figure 3.1** Schematic illustration of a spherical probe in point-contact with two conformations of film under a zero applied load: (a) a single layer film, (b) a bilayer film. ....69

**Figure 3.2** Simulated local vertical displacement maps for a silica sphere loaded against an unetched polystyrene film whose thickness is 400 nm. (a)The vertical (z-directional) displacement maps when the applied load is 19 nN and 38 nN respectively. (b) Simulated load-penetration relation (open circle) and the fit to a 3/2-power law dependence (solid curve). ....71

**Figure 3.3** Simulated vertical displacement maps of penetration on a unetched polystyrene film with different film thickness: (a) 100 nm; (b) 200 nm; (c) 400 nm; (d) 800 nm; (e)1600 nm; (f) 3200 nm. The applied load is 38 nN for all cases. ....73

**Figure 3.4** (a) Simulated load-penetration relations (open circle) and the 3/2-power law fits (solid line) for different thickness polystyrene films; (b) residual curves for corresponding fits in (a). ....74

**Figure 3.5** Apparent elastic modulus ( $E_{PS}$ ) of a polystyrene thin film as a function of film thickness based upon Hertz formula for a sphere loaded against a semi-infinite slab (equation 3.10). The dashed line marks the value input in this series of simulation, which is 2.24GPa. ....75

**Figure 3.6** Simulated vertical displacement maps of penetration on a damaged layer (DL)/polystyrene film with different DL thickness: (a) 0.25 nm; (b) 0.5 nm; (c) 1 nm; (d) 1.29 nm; (e)1.98 nm; (f) 2.5 nm; (g) 5 nm; (h) 10 nm; (i) 20 nm. For all cases, the underlying polystyrene layer is 400 nm, and the applied load is 38 nN. ....78

<b>Figure 3.7</b> The simulated load-penetration relations (open circle) and the 3/2-power law fits (solid line) for different thick damaged layers on top of a fixed thickness (400 nm) polystyrene film. ....	79
<b>Figure 3.8</b> (a) Residual curves for 3/2-power law fits of the simulated load-penetration data in figure 3.7; (b) zoomed-in residuals of the highlight in (a). ....	80
<b>Figure 3.9</b> Apparent effective elastic modulus ( $E_{BL}$ ) for a damaged layer/polystyrene bilayer structure as a function of damaged layer thickness. The values within the area highlighted by red dashed rectangle are replotted with a different vertical scale in the inset, with the green solid line indicating the simulated elastic modulus for a 400 nm thick unetched polystyrene film. ....	81
<b>Figure 3.10</b> Simulated vertical displacement maps for a load of 38 nN between a spherical silica probe and a bilayer film structure with damaged layer thicknesses of: (a) 1.08 nm, (b) 1.29 nm, (c) 1.61 nm, and (d) 1.98 nm. $E_{DL}$ is 400 GPa and the underlying polystyrene thickness is 400 nm for all cases. ....	83
<b>Figure 3.11</b> Simulated Force-versus-Penetration curves for a bilayer film structure with damaged layer thicknesses of: (a) 1.08 nm, (b) 1.29 nm, (c) 1.61 nm, and (d) 1.98 nm. The open circles represent the simulated values, and the fits to a 3/2-power law are shown as the solid lines. $E_{DL}$ is 400 GPa and the underlying polystyrene thickness is 400 nm for all cases. ....	84
<b>Figure 3.12</b> Simulated effective bilayer elastic modulus ( $E_{BL}$ ) vs. damaged layer elastic modulus ( $E_{DL}$ ) for a 400 nm thick polystyrene layer, covered with thin model damaged layers. Each solid curve corresponds to a measured damaged layer thickness, as indicated. The open circles are interpolated from the AFM-measured effective bilayer moduli. All values of $E_{BL}$ are normalized to the elastic modulus of unetched polystyrene film. The normalization factor was obtained by force curve measurement (2.24 GPa) and finite element simulation (2.43 GPa), for the measured, and calculated cases, respectively. ....	86
<b>Figure 3.13</b> Value of the elastic modulus of the damaged layer ( $E_{DL}$ ) determined by interpolation in figure 3.12 as a function of Ar-ion energy. The uncertainty for each value corresponds to the uncertainties of the measured effective bilayer elastic moduli ( $E_{BL}$ ) on each curve in figure 3.12. ....	87
<b>Figure 3.14</b> The ratio of the dominant wrinkle wavelength ( $\lambda$ ) to the damaged layer's thickness ( $t$ ), plotted as a function of damaged layer's elastic modulus ( $E_{DL}$ ) determined by two methods. The results from calculation based on the buckling instability theory, with $E_{DL}$ determined from force curve analysis are shown as open circles; the ratios of the measured dominant wavelength to the thickness determined from XPS are shown by open circles (see table 2.1). ....	89
<b>Figure 3.15</b> Schematic geometry and the boundary conditions for simulation of local vertical strain for a spherical probe loaded against a corrugated surface. The corrugation is assumed axially symmetric (axis shown in red) and radially sinusoidal,	

with the wavelength and amplitude determined experimentally by AFM and height-height correlation analysis. ....91

**Figure 3.16** Meshed geometries for FEM simulations of the contact systems for two extreme cases, with the apex of the probe centered above: (a) a crest, and (b) a trough. The red dashed arrows denote the 2D symmetry axis. ....92

**Figure 3.17** FEM-simulated vertical displacement for the probe apex centered above a crest (left) or a trough (right) of a corrugated bilayer film, for corrugation amplitudes of: (a) 6 nm; (b) 4.5 nm; (c) 3 nm; (d) 1.5 nm; (e) 0.75 nm; (f) 0.35 nm; (g) 0 nm. The thickness of the damaged layer and the underlying polystyrene layer are 1.29 nm and 400 nm respectively, and the applied load is 38 nN. ....95

**Figure 3.18** Summary of simulated load-penetration relations for a spherical probe loaded against cylindrically corrugated surfaces. In each case the variation for the sphere apex centered above a crest is shown by open squares, apex above a trough is shown by closed diamonds, and the average by close circles. The solid curves show best fits of the average to a 3/2-power law. The individual panels are for different corrugation amplitudes: (a) 0.35 nm; (b) 0.75 nm; (c) 1.5 nm; (d) 3 nm; (e) 4.5 nm; (f) 6 nm. ....96

**Figure 3.19** (a) FEM-simulated average load-penetration curves and 3/2-power law fits for the example shown in figure 3.18; (b) residual curves for corresponding fits in (a). ....97

**Figure 3.20** Simulated average effective bilayer elastic modulus ( $E_{BL}$ ) for a corrugated bilayer film structure as a function of corrugation amplitude. The elastic modulus and thickness of the damaged layer used in the series of simulation are 400 GPa and 1.29 nm respectively, while the underlying polystyrene layer was fixed at 400nm thick. The wavelength is fixed at 40 nm for all cases. ....98

**Figure 3.21** Simulated vertical displacement maps for a spherical probe centered above a crest (left) or a trough (right) on corrugated bilayer films with different wavelengths: (a) 40 nm; (b) 60 nm; (c) 80 nm; (d) 100 nm; (e) 120 nm; (f) 140 nm; (g) 160 nm. The thickness of the damaged layer and the underlying polystyrene film are 1.29 nm and 400 nm respectively, and the applied load is 38 nN. ....100, 101

**Figure 3.22** Summary of simulated load-penetration relations for a spherical probe loaded against a model cylindrically corrugated surface. The dependence for the apex above the crest is shown by open squares, above the trough by solid diamonds, the average by solid circles. The solid curves show a fit of the average to a 3/2-power law. The corrugation wavelengths varying as follows: (a) 40 nm; (b) 60 nm; (c) 100 nm; (d) 120 nm; (e) 140 nm; (f) 160 nm. ....102

**Figure 3.23** (a) Summary of simulated average load-penetration curves and fits to a 3/2-power law for the example for the wavelength dependence shown in figure 3.22; (b) the corresponding residual curves for the fits shown in (a). ....103

**Figure 3.24** Simulated average effective bilayer elastic modulus ( $E_{BL}$ ) of a corrugated bilayer film as a function of corrugation wavelength. The elastic modulus and thickness of the damaged layer used in the series of simulation are 400 GPa and 1.29 nm respectively, while the thickness of the underlying polystyrene film is fixed at 400 nm thick. The amplitude is fixed at 1.5 nm for all cases. ....104

**Figure 3.25** Simulated vertical displacement maps for a spherical silica probe loaded against a cylindrically corrugated surface for the apex centered above a crest (left) and above a trough (right) for damaged layers of thickness: (a) 1.08 nm (b) 1.29 nm (c) 1.61 nm (d) 1.98 nm.  $E_{DL}$  is 400 GPa, and the load is 38 nN for all cases in the example. ....106, 107

**Figure 3.26** Simulated load-vs.-Penetration curves for a spherical silica probe-bilayer film system. The case for the apex of the probe centered above the crest is plotted as open squares; the case for the apex centered above the trough is plotted as close diamonds. The average of these two cases is plotted as closed circles; the solid curves best fits to a 3/2-power law. The damaged layer thicknesses are (a) 1.08 nm, (b) 1.29 nm, (c) 1.61 nm, and (d) 1.98 nm.  $E_{DL}$  is 400 GPa for all cases. ....108

**Figure 3.27** Simulated effective bilayer elastic modulus ( $E_{BL}$ ) as a function of damaged layer elastic modulus ( $E_{DL}$ ) for a 400 nm thick polystyrene layer, covered with thin corrugated damaged layers, with thicknesses as indicated (solid lines). The open squares are the interpolated values using the effective bilayer moduli determined by force curve analysis. The interpolated and the simulated values are normalized to the elastic modulus of the unetched polystyrene film, obtained by force curve measurement (2.24 GPa), and finite element simulation (2.43 GPa) respectively. ....110

**Figure 3.28** The interpolated elastic modulus of the damaged layer ( $E_{DL}$ ) as a function of  $Ar^+$  ion energy. The uncertainty for each value comes from the uncertainties of the measured effective bilayer elastic moduli ( $E_{BL}$ ). ....111

**Figure 3.29** The ratio of the dominant wrinkle wavelength ( $\lambda$ ) to the damaged layer thickness ( $t$ ), plotted as a function of damaged layer elastic modulus ( $E_{DL}$ ), based on buckling theory (open circles), and experimentally measured closed circles). Comparison based on the flat surface approximation is shown on the left; that based on the approximation with consideration of surface roughness is shown on the right. ....113

## Appendix A

**Figure A.1** Schematic of the experimental setup for the annealing of the patterned PaMS sample. ....126

<b>Figure A.2</b> Schematic of a zigzag path scribing by an AFM probe. Individual segments are along the direction perpendicular to the long side of the groove. ....	128
<b>Figure A.3</b> Topographic AFM image and the averaged cross-sectional profile of a section (marked red) for a groove scribed by 100 passes, as illustrated in figure A.2. ....	128
<b>Figure A.4</b> Schematics of a 2-step zigzag scribing of an AFM probe to make symmetric shoulders for a single groove. ....	129
<b>Figure A.5</b> Topographic AFM image and the averaged cross-sectional profile of a section (marked in red) for a groove scribed by 100 passes as illustrated in figure A.4. ....	129
<b>Figure A.6</b> Topographic AFM image and the averaged cross-sectional profile of a section (marked in red) for a 5×1 array of 2μm long grooves scribed by 2-step zigzag scratching with 50 passes for each single groove. ....	130
<b>Figure A.7</b> Topographic AFM images of the as-patterned and thermally-annealed (at ~170°C) nanogroove patterned PaMS. Grooves are 2μm long. Panels left to right show effect of increasing amount of annealing time. Rows are for various average-groove widths/periodicities: row (a) 35.2 nm / 86.3 nm, row (b) 41.0 nm / 307.6 nm, row (c) 57.4 nm / 448.8 nm, row (d) 62.5 nm / 617.2 nm. Note that the image field of view for each case shown is 6 μm × 6 μm. ....	132
<b>Figure A.8</b> Average cross-sectional line profiles (solid lines) within a section around the middle of the array of grooves; results for groove width/periodicity: (a) 35.2 nm / 86.3 nm, (b) 41.0 nm / 307.6 nm, (c) 57.4 nm / 448.8 nm, (d) 62.5 nm / 617.2 nm, are presented for different total annealing time as indicated. The dashed curves are calculated line profiles based on equation A.1 with $\mu=4\times 10^{12}$ Pa-s for each total annealing time. ....	135
<b>Figure A.9</b> The difference in the height between the highest ( $h_{\max}$ ) and the lowest ( $h_{\min}$ ) points on the measured and calculated line profile for different $\mu$ as a function of total annealing time, for two cases with groove width/periodicity: (a) 35.2 nm / 86.3 nm, (b) 62.5 nm / 617.2 nm. ....	136
<b>Figure A.10</b> Graphical illustration for the calculation of mass loss from AFM measured topographic image. The mass loss is the variation in the product of the area of the scanned image and the value of the difference between the average height over the whole image and that over the unpatterned area (  ) in the same image with respect to total annealing time. ....	137
<b>Figure A.11</b> The difference between the average height over the whole AFM image ( $h_{\text{all}}$ ) and that of the unpatterned area ( $h_{\text{unpat}}$ ) plotted as functions of total annealing time for groove arrays with groove width/periodicity: (a) 35.2 nm / 86.3 nm, (b) 41.0 nm / 307.6 nm, (c) 57.4 nm / 448.8 nm, (d) 62.5 nm / 617.2 nm. Note that all cases were calculated from 6 μm × 6 μm AFM images. ....	138

**Figure A.12** The functions of the Fourier series composed by the coefficients and wavelengths of the first few Fourier components obtained from the FFT of the corresponding AFM measured average cross-sectional line profiles for different arrays of grooves with groove width/periodicity of: (a) 35.2 nm / 86.3 nm, (b) 41.0 nm / 307.6 nm, (c) 57.4 nm / 448.8 nm, (d) 62.5 nm / 617.2 nm, presented for different total annealing time respectively. ....141

**Figure A.13** Relaxation of the amplitudes for corresponding Fourier components obtained by FFT from the average cross-sectional AFM line profiles, as functions of total annealing time, for different arrays of grooves with groove width/periodicity of: (a) 35.2 nm / 86.3 nm, (b) 41.0 nm / 307.6 nm, (c) 57.4 nm / 448.8 nm, (d) 62.5 nm / 617.2 nm. ....142

**Figure A.14** Plot of logarithm of the relaxation time ( $\tau$ ) obtained from the simple exponential fit of some of the relaxation curves shown in figure A.13 plotted versus logarithm of the wavelength ( $\lambda$ ) for corresponding Fourier components obtained by FFT from the AFM measured average cross-sectional line profiles. The overall data points shown in this plot were well fitted by a straight line with a slope of  $1.31 \pm 0.166$ . ....143

## ***Appendix B***

**Figure B.1** Schematic of the principle of X-ray photoelectron spectroscopy (XPS). A core level electron is ejected with kinetic energy ( $E_K$ ) by an incident photon with energy ( $h\nu$ ) higher than the sum of binding energy ( $E_B$ ) and instrumental work function ( $\phi$ ). ....146

## ***Appendix C***

**Figure C.1** Schematic drawing and corresponding pictures of the modified AFM with the function of ambient controlling. ....148

**Figure C.2** Extracted elastic modulus ( $E$ ) of PMMA from approach and retraction force curves as a function of Z-directional scan rate, under various amount of dry nitrogen purging time: (a) in air; (b) 4 hours; (c) 26 hours; (d) 49 hours. ....151

**Figure C.3** Extracted elastic modulus ( $E$ ) of PMMA from approach and retraction force curves as a function of Z-directional scan offset, under various amount of dry nitrogen purging time: (a) 4 hours; (b) 26 hours; (c) 49 hours. ....152

## ***Appendix D***

**Figure D.1** Schematic illustration of the execution and resulting files generated by the FORTRAN program code for the algorithm of the analysis of the raw data of the AFM measured force curve. ....155

**Figure D.2** FORTRAN program code for the algorithm of analysis of the AFM measured force curve. ....156-165

## ***Appendix E***

**Figure E.1** Examples of the operating environment of COMSOL Multiphysics FEM package in a 2D axial-symmetric coordinate system: (a) CAD drawing mode, (b) Mesh mode (zoomed-in), and (c) Post-processing mode (zoomed-in Z-direction displacement map). ....169

## ***Appendix F***

**Figure F.1** Schematic geometry and the boundary conditions for finite element analysis simulation of the penetration for two cases, (a) penetration on a single-layer film (PS only); (b) penetration on a bilayer film structure (polystyrene film plus damaged layer). ....187

# ***Chapter 1:***

## ***Introduction***

### **1.1 Motivation**

The drive toward ever-smaller dimensions has made controlled patterning of materials at the nanometer scale crucial in the fabrication of ultra large scale integrated electronics. During the past decades due to breakthroughs in lithographic techniques, e.g. e-beam<sup>1.1</sup>, extreme-UV (EUV)<sup>1.2, 1.3</sup>, and nanoimprint<sup>1.4, 1.5</sup> lithography, etc., one is now able to define a mask pattern with the minimum feature size down to sub-10 nanometers<sup>1.6-1.8</sup>. However, the subsequent pattern transferring process, e.g. plasma etching, is ever more challenging, i.e. achieving the same shape and dimensions in the underlying material as what was defined by the patterned resist. The roughness generated on the surface and sidewall of the resist during the plasma etching process is one of the main factors that limit the minimum feature size of the transferred pattern, since it is also transferred. Therefore, controlling the roughening of resist materials during exposure to a plasma is critical, and only possible if we have good understanding of the underlying physical mechanisms. Unfortunately, such an understanding has not been established as yet.

In very recent work<sup>1.9, 1.10</sup>, we found evidence that a previously unexpected effect might be responsible for most of the roughening of certain polymeric films:

that a large mismatch in the stiffness of a thin damaged layer produced by ion etching, and that of the underlying film might drive the film to buckle<sup>1.11-1.13</sup>. This is illustrated schematically in figure 1.1. In particular, an analysis of the roughness produced by Ar<sup>+</sup> ion etching of polystyrene films over a range of energies showed that the dominant wavelength of the corrugation scaled with the thickness of the damaged layer, in agreement with what would be expected for a buckling instability<sup>1.9</sup>, which predicts

$$\lambda = 2\pi t \left[ \frac{E_f (1 - \nu_s^2)}{3E_s (1 - \nu_f^2)} \right]^{1/3},$$

where  $\lambda$  is the wavelength of the corrugation,  $t$  is the film thickness,  $E_f$ ,  $\nu_f$ , and  $E_s$ ,  $\nu_s$  are the elastic modulus and Poisson's ratio of the film and substrate, respectively. A striking aspect of the application of this model to our system is that based upon the observed dominant wavelengths of approximately 30-80 nm, the damaged layer moduli, corresponding to  $E_f$  in above equation, are apparently very high indeed: more than two orders of magnitude larger than that for underlying polystyrene, corresponding to  $E_s$  in above equation.

Establishing whether a buckling instability is indeed responsible for the roughening of polystyrene and other resist films during plasma etching would be of great technological importance, and would be possible if the modulus of the damaged layer could be determined directly. This is challenging, as the effective modulus should be dominated by that of the softer underlying film. In this thesis we report on

just such a determination, based upon careful atomic force microscopy (AFM) force curve measurements, combined with numerical simulations by the finite element method to extract the damaged later elastic modulus from the nanomechanical response of the combined bilayer system.

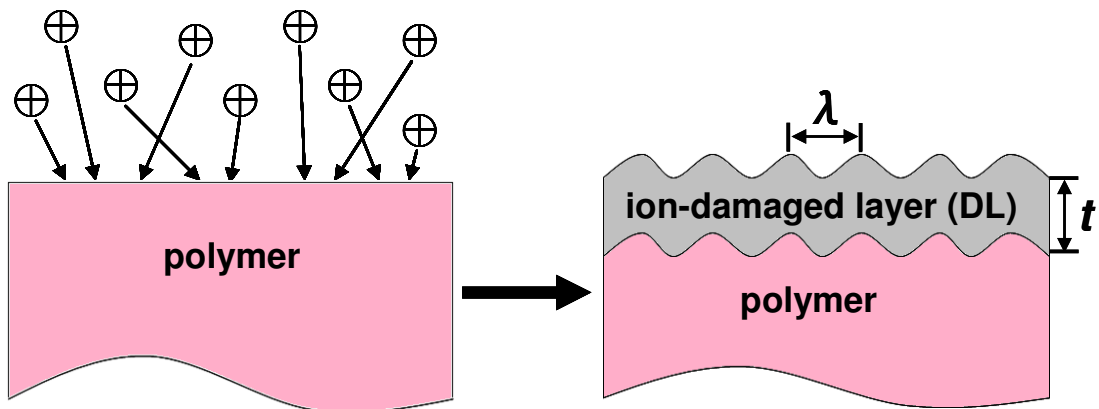


**Figure 1.1** Schematic of buckling of a damaged layer formed on a polymer film exposed to ion bombardment.

## **1.2 Reactive ion etching of polymer thin film**

Plasma is a partially ionized gas, consisting of equal amount of positive and negative ions, along with neutrals, electrons, and photons (UV/Vacuum UV). It has been widely used in the application of etching for pattern transfer during the manufacturing of electronics due to its anisotropy, relatively high transfer fidelity, and cleanliness.<sup>1.14</sup> Reactive ion etching (RIE) is one of the most important and widely-used dry etching techniques. In RIE the etching process takes place with both the chemical removal by reactive ions/radicals and the physical removal by energetic ions. During this process, reactive species can interact with the polymeric mask material lying on top of the substrate, altering the properties, chemical structures/compositions, and surface morphology of the polymer film, and lead to undesired consequences for the electronic devices, e.g. degradation of electrical performance<sup>1.15</sup>.

### **1.2.1 Plasma-polymer surface interaction**

During the exposure of a polymer material to a plasma, the constituents of the plasma can interact with the polymer molecules and cause effects in different ways.

Ion bombardment can affect the polymer film at near-surface, both physically and chemically. Accelerated ions can alter the polymer surface by physical sputtering of the material from the surface and chemical modifications of the material structures or compositions. Both effects will become more significant at increasing the ion energies. Depending on the types of chemical bonds within the polymer material, the ions can preferentially break certain types of bonds and selectively remove one

constituent over another, causing the local depletion and changing the chemical composition at near-surface.<sup>1.16-1.18</sup>

Electrons cause much less significant effect on the polymer surface than the ions do since the energy of the electrons bombarding the surface is only on the order of a few eV, which is unlikely sufficient for bond breakage.<sup>1.19</sup>

Neutrals affect the polymer surface depending on their reactivity with the polymer molecules. In a pure Argon plasma, thermal neutrals are chemically inert and exhibiting temperature slightly above room temperature<sup>1.20</sup> causing little effect on the polymer surface. Fast moving neutrals cause similar effects to those of ions, and the excited neutrals may assist material removal by potential sputtering.

Energetic photons generated in a plasma can also modify the polymer material in the near-surface, with different levels usually depending on the feed gas used in the discharge, polymer structure, and photon energy.<sup>1.10, 1.21-1.23</sup> The most important are the UV and vacuum UV (VUV) photons, which modify the polymer by chain cross-linking, main-chain scission, or side-chain removal.<sup>1.24-1.26</sup> The Argon plasma emits radiations in the VUV range.<sup>1.10, 1.27</sup> For hydrocarbon polymers, the absorption coefficient for the VUV radiation can be several orders of magnitudes larger than that for UV.<sup>1.10</sup>

### **1.2.2 Formation of damaged layer**

As mentioned above, the constituents of a plasma can interact with the molecules or the atomic constituents in the molecules of the polymer material at near-surface region, and cause drastic change in the structure or chemical composition

within the impacted region. During bombardment with energetic ions, the depth at which the polymer near-surface will be affected depends on how deep the incident ions can penetrate into the material. This is mainly a function of the ion energy and incident angle.<sup>1.10, 1.16</sup> Within the penetrated region, the scattered energetic ions can selectively induce bond breaking and remove certain atomic constituents from the molecules depending on the bond type or strength. This will cause a depletion of certain constituents of the molecules, and further change the composition within the penetration depth of the ions. For Ar<sup>+</sup> ions with a kinetic energy of about 100eV incident upon a polymer surface at a normal incident angle, a densified amorphous carbon-rich layer as a result of removal of hydrogen or oxygen atoms is formed to a depth of about 2 nm.<sup>1.10</sup> This thin ion-induced damaged layer may be a matter of concern since the physical properties (e.g. thermal, mechanical, etc.) of the new generated layer is quite different from the unmodified underlying polymer.

UV and VUV photons can also be absorbed by most polymer materials, which can cause different level modification at the near-surface of the polymer material. Depending on the photon energy and polymer type (which reflects on the absorption coefficient of the material at certain wavelength range), the depth influenced by these energetic photons can vary from tens to hundreds of nanometers, which is significantly much larger than that caused by the ions. The absorption of the photons follows the Beer-Lambert law, i.e. the absorption depth falls off exponentially with the absorption coefficient of the material.<sup>1.10, 1.28, 1.29</sup> This type of absorption, occurring during the exposure to a plasma, generally causes the excitation of electrons. This is highly molecular-dependent, resulting either in subsequent chain-

scission or cross-linking reactions of the molecules.<sup>1.10, 1.24-1.26</sup> In an Ar plasma, the radiation is in the VUV range (i.e. 100-200 nm in wavelength), and can be absorbed at the near-surface of polystyrene at a penetration depth of about 40 nm.<sup>1.10</sup> As mentioned above, the effects of this kind of absorption varies from material to material. For example, the absorption under the same etching condition (e.g. pure Ar plasma) could result in cross-linking in a P4VP, enhanced chain-scission in P $\alpha$ MS, while insignificant changes happen in a polystyrene,<sup>1.10, 1.30</sup> which distinguish the subsequent behaviors for those systems.

These damaged layers are of potential importance since they may exhibit much different mechanical nature than that of the underlying unmodified film.

### **1.2.3 Mechanisms for roughness formation**

Corrugations transferred from a roughened resist polymer to the underlying material during a dry etching process have long been a big concern in development of nanotechnology. To enhance control of this issue, there have been a number of studies attempting to explore the mechanisms for plasma-induced roughening. In general, the directions of these studies can be divided into two categories: intrinsic and extrinsic.<sup>1.10</sup>

”Intrinsic roughening” is considered to result from instability of the plasma/polymer interface during its propagation which involves mass transport (e.g. arrival of the reactive species at the exiting interface, departure of the reaction products from the interface) usually driven by the variation in the local chemical potential across the interface.<sup>1.10</sup> This interface propagation is not in equilibrium both

vertically and laterally. In the vertical direction, driven by the chemical and electrical potential gradient the reactive neutrals and ions move toward the interface where there is probability for a reaction to take place. The reaction products may be released locally from the interface with some probability, driving the interface moving downward locally to form instantaneous atomic or molecular scale roughness. In the lateral direction, smoothing of the interface occurs driven by the lateral diffusion of the reactants and the relaxation of the polymer molecules. Hence in the steady-state the roughness of the surface is a result of the kinetic competition between the vertical moving of the interface and the lateral diffusion/relaxation.<sup>1.10</sup> A number of models (e.g. continuum height evolution, flux-remission, scaling theory, etc.)<sup>1.17, 1.31-141</sup> have been proposed based on this assumption; however, most are based on the studies on hard materials, just few are against polymer materials<sup>1.17, 1.38, 1.41</sup>.

In “extrinsic roughening” of polymers in a plasma environment, is impurity, polymer-molecular structure dependent. There are some studies on the role of cross-linking induced by ion-bombardment or UV/VUV radiation plays in the surface roughening of polymers. Sumiya et al. explained the roughening on the polymer film by correlating the induced cross-linking to polymer aggregation (usually is considered as a state when polymer chains are massed into dense tangled clusters) leading to nano-scale inhomogeneities in mass and density at the near-surface.<sup>1.42-1.44</sup> Some studies have shown that surface roughening could be reduced by enhanced cross-linking, or enhanced by higher degrees of chain-scission and mobility of the polymer chains.<sup>1.45, 1.46</sup>

A potential breakthrough in our understanding comes from very recent work in which Bruce et al. proposed a buckling instability model for the explanation of initial roughening of polymer surface during plasma exposure.<sup>1.9, 1.30</sup> In this model, ion bombardment during the plasma exposure of polymer films results in the formation of a thin, stiff, compressive-stressed damaged layer bound to the much softer underlying unmodified film; the large difference in the modulus of the damaged layer and that of the underlying film results in a buckling instability, with the formation of wrinkles producing surface roughness. We discuss this model in the next section, and its investigation forms the major part of this thesis.

#### **1.2.4 Early results for simple model polymers**

Several studies about the plasma-polymer interactions had been done earlier by our collaborative works using a number of simple model polymers whose degradation mechanisms in the plasma environment are well-known. Examples of these model polymers used in these works are shown in figure 1.2.

To understand the effects of polymer structures on the etching behaviors under plasma exposure, Bruce *et al.* used polystyrene and its derivatives whose chemical structures are similar to each other except for the position of a side methyl group or a different element composition on the side group, e.g. poly- $\alpha$ -methylstyrene (P $\alpha$ MS), poly-4-methylstyrene (P4MS), and poly-4-vinylpyridine (P4VP), in different types of plasma exposure, e.g. Ar, VUV-only, and 10% C<sub>4</sub>F<sub>8</sub>/Ar.<sup>1.30, 1.47</sup> Ellipsometry analysis and a bi-layer optical model based on the obtained refractive index and extinction coefficient show evidence that an amorphous carbon-rich damaged layer of

an ion-energy-dependent thickness, as was confirmed by XPS analysis and molecular dynamics (MD) simulations<sup>1.16, 1.48</sup>, was created by ion bombardment on top of an unmodified polymer layer with a thickness decreasing during the plasma exposure. What makes the differences is the response of these different structured polymers to the UV/VUV radiations. PαMS is known to be prone to chain-scission reactions while polystyrene, P4MS, and P4VP are known to undergo cross-linking reactions under the UV/VUV irradiations. In addition, PαMS has a relatively low ceiling temperature (66°C) compared to the other type of polymers, making it a significant character that the etch rate increases much faster than the others with elevating substrate temperatures.

To answer a critical question that “What drives the roughening of polymers during plasma exposure?”, Bruce *et al.* proposed that the top ion-damaged layer plays a critical role in the evolution of the polymer surface morphology in the plasma environment. By assuming that the thin damaged layer is amorphous carbon, using the literature values of the mechanical properties in conjunction with the observed surface properties, e.g. thickness, dominant wavelength of surface corrugation, a “buckling instability” was qualitatively proven as a key mechanism that initiates surface roughening during plasma processing. A preliminary result was published for a polystyrene-Ar plasma system, which states that the compressive stress, built up within the ion-damaged layer as a result of densification and a large difference in the elastic modulus between itself and the underlying unmodified layer, drives the surface to wrinkle in the small deformation limit when exceeding a critical value.<sup>1.9</sup> This result was also used to explain the difference in the roughening behaviors of other

type of polymer-plasma systems.<sup>1.30</sup> Particularly, the negligible roughening behavior of P4VP during either Ar or 10% C<sub>4</sub>F<sub>8</sub>/Ar plasmas was attributed to its strong response to UV/VUV irradiations, that a significant induced cross-linking region under the top ion-damaged layer reduces the difference in the elastic modulus between them, resulting in suppression of surface roughening; while an enhanced surface roughening was seen on PαMS due to the radiation-induced chain-scission region under the ion-damaged layer, increasing the difference in the elastic modulus by softening the irradiation-affected region. Polystyrene shows non-extreme roughening behavior due to its insensitivity to the UV/VUV radiation.

The results described above were also confirmed by vacuum beam experiments and MD simulations. In the vacuum beam experiment, Nest et al. studied the effects of the Ar ion beam and the UV/VUV irradiation on the roughening behaviors of 193 nm and 248 nm photoresist polymers respectively<sup>1.49</sup>, shown in figure 1.2. The 193 nm resist was found to be roughened more severely than 248nm as a result of that the oxygen-containing bonds (C=O and C-O-C) in the 193 nm resist are prone to be broke under the exposure to UV/VUV irradiations, while such bond breaking is not seen in the hydrocarbon based 248 nm resist. And again, this radiation-induced bond breakage results in significant temperature-dependent roughening in the case of 193 nm resist, which is similar to the result from the plasma etching of PαMS. A further vacuum beam study of PαMS and P4MS as well as the role of ceiling temperature show consistent results with that obtained from the plasma etching experiment.<sup>1.46</sup>

In the molecular dynamics (MD) simulations, Végh et al. examined the effects of Ar<sup>+</sup> ion bombardment on a polystyrene surface.<sup>1.16, 1.48</sup> The simulation results show that a heavily cross-linked dehydrogenated damaged layer in the near-surface region forms after some initial ion flux (shown in figure 1.3), which is consistent with the results obtained by plasma and vacuum beam experiments. The formation of the damaged layer is a result of competition among sputtering, ion-induced dehydrogenation, and cross-linking. Hydrogen is preferentially removed from this region, and once a significant cross-linking has occurred, the hydrogen-depletion zone rapidly transfers to the final amorphous structure as steady-state etch is approached. And this result explains well on the experimentally observed significant drop in sputter yield (SY) of polystyrene at flux of Ar<sup>+</sup> ion bombardment.

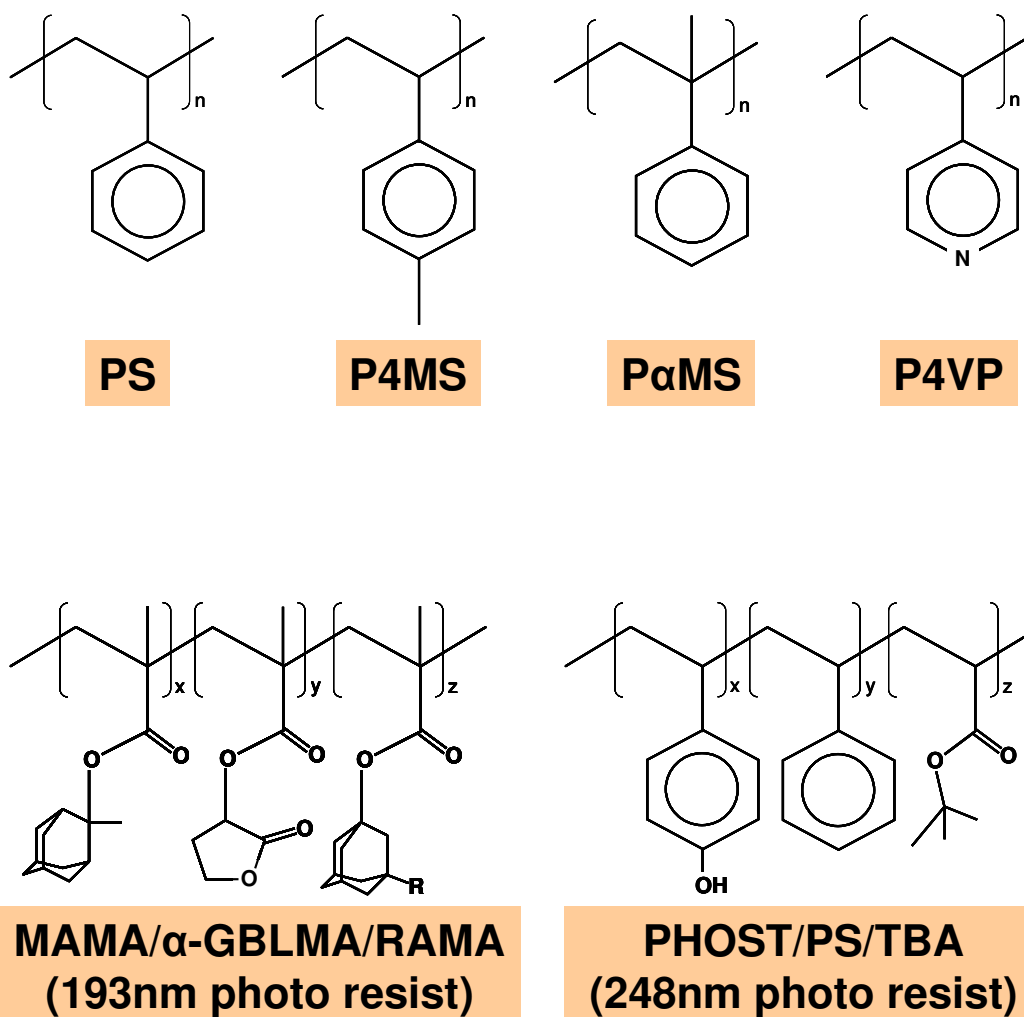


**Figure 1.2** Schematics of chemical structures of model polymers used in plasma etching experiment and vacuum beam experiments done by Bruce *et al.* and Nest *et al.* respectively.

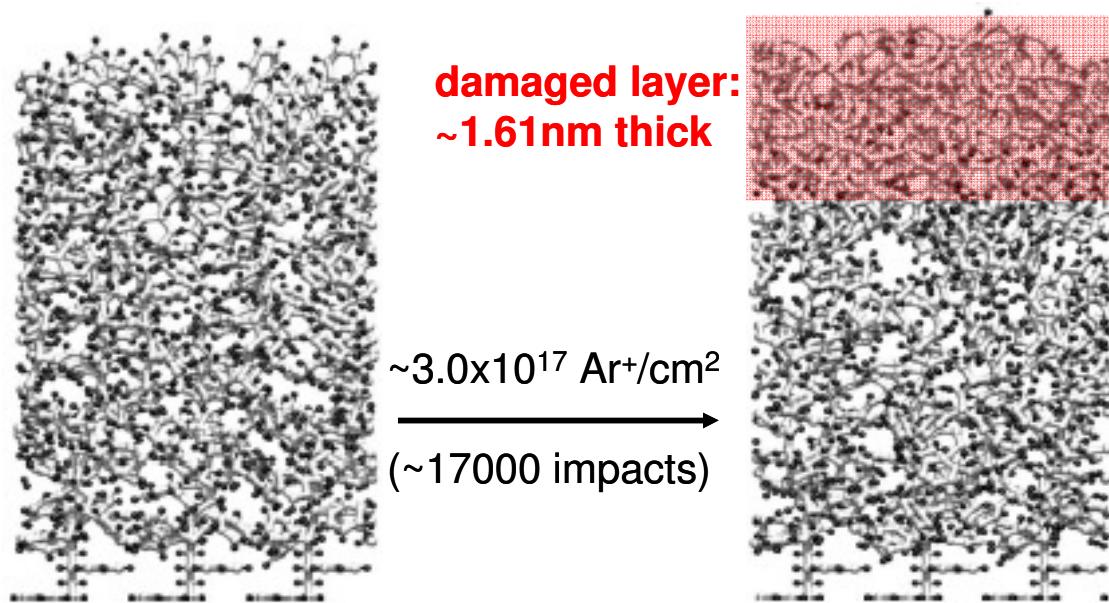


**Figure 1.3** Side views of the polystyrene cell for a single MD simulation, indicating a transition from the initial surface to a highly modified surface at steady state.<sup>1.48</sup> Corresponding changes in sputter yield and the ratio of number of atoms (H:C) at the damaged region from the initial to the final state are from  $\sim 5.7$  to  $\sim 0.017$  Eq.  $C/\text{Ar}^+$  and from 1.0 to 0.11 respectively. The value for the H:C ratio and the damaged layer thickness for the steady-state surface are averaged over 5 separate surface compositions during the last 2500  $\text{Ar}^+$  impacts of the simulation (at a interval of 500 impacts), after steady state has been established.

### 1.3 Buckling instability

Mechanical instabilities driven by mechanical stress, externally applied or internal strain can take place over an extremely wide range of length scales. They are an important issue in the structure and properties of natural and artificial material systems. The buckling instability in particular has drawn a great deal of attention both in scientific research, and in engineering applications.<sup>1.50-1.58</sup> From the early understanding of the failure of the sandwich structure employed by the aircraft wings, there has been continuous efforts in research of this ubiquitous phenomenon at multiple length scales and in complex material/structural systems.<sup>1.53, 1.58</sup> Of the diverse systems being studied, perhaps the simplest and most typical is a thin stiff layer bonded to a thick compliant base (e.g., a thin metal film deposited on a thick polymer substrate). Such a structure generally stores strain energy at the interface between the two layers due to external or internal factors (e.g. thermal expansion, mechanical stretching), and imposes a stress within the thin stiff layer. In the case of a compressive stress, beyond a critical value, then the film starts to buckle, resulting in either wrinkling<sup>1.50-1.58</sup> or delamination<sup>1.59, 1.60</sup>. This is indicated schematically shown in figure 1.4.

Wrinkling driven by a buckling instability is an intriguing phenomenon since the resulting surface patterns generally show wavelength selection. For a thin stiff film with thickness  $t$  and elastic modulus  $E_f$  on a thick strained compliant substrate with elastic modulus  $E_s$ , the characteristic wavelength  $\lambda$ <sup>1.9, 1.57</sup> in the small deformation, linear elasticity limit is given by:

$$\lambda = 2\pi t \left[ \frac{E_f (1 - \nu_s^2)}{3E_s (1 - \nu_f^2)} \right]^{1/3}, \quad (1.1)$$

where  $\nu_f$  and  $\nu_s$  are the Poisson's ratios of the film and substrate, respectively. The wrinkle amplitude  $A$ <sup>1.9, 1.57</sup> in this same limit is given by:

$$A = t \left( \frac{\sigma}{\sigma_c} - 1 \right)^{1/2}, \quad (1.2)$$

where  $\sigma$  and  $\sigma_c$  are the compressive stress and the critical compressive stress of the film, respectively. Equation 1.1 predicts that  $\lambda$  depends only on the thickness ( $t$ ) and the elastic properties ( $E$  and  $\nu$ ) of the film and substrate but not on the stress ( $\sigma$ ) applied on the film, while equation 1.2 predicts that the amplitude is stress dependent.

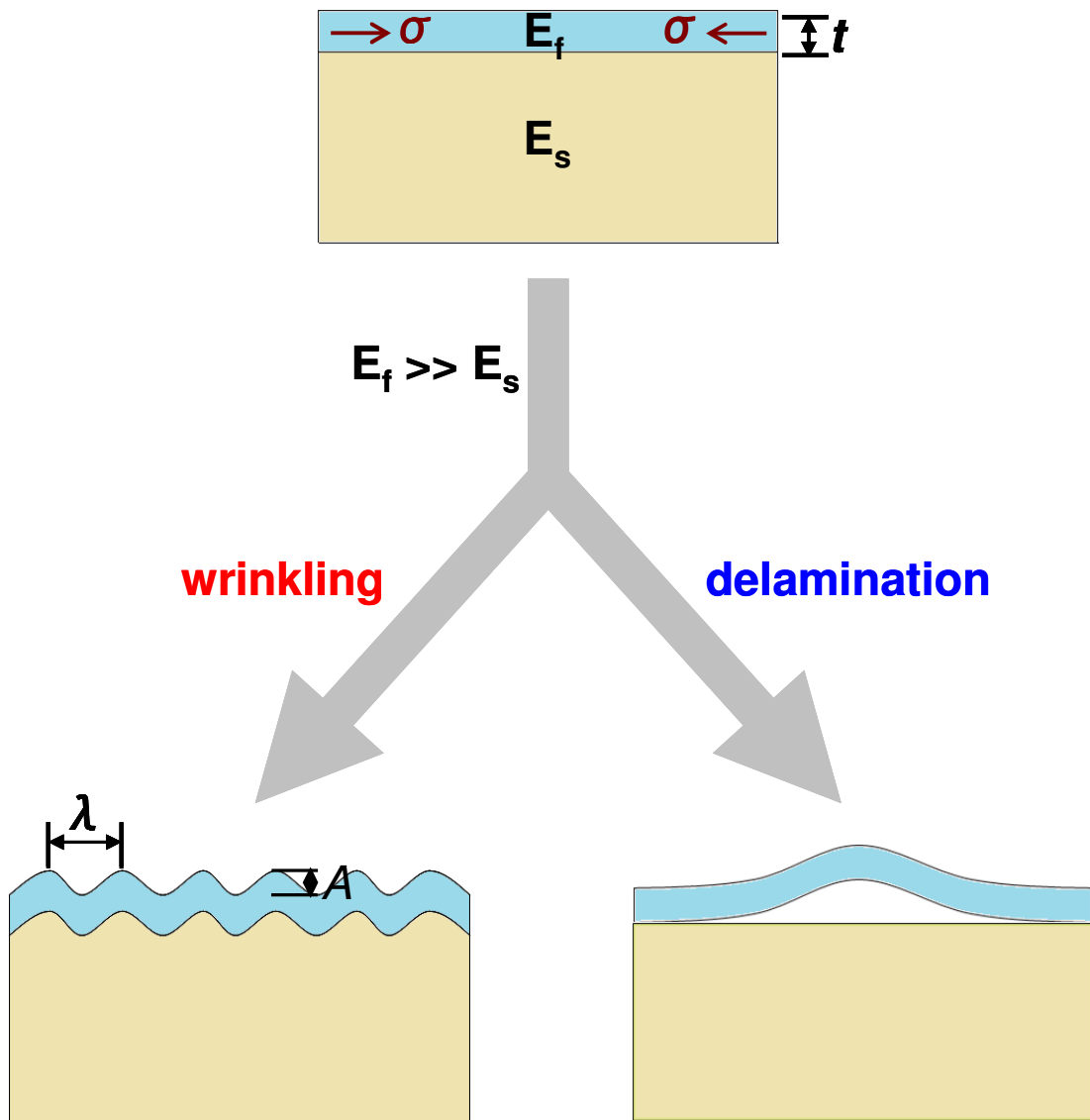


**Figure 1.4** Schematics of buckling instability-driven film wrinkling and delamination under a compressive stress.

## 1.4 Nanomechanics for surface characterization

Nanomechanics is the broad field which deals with the mechanical properties of material systems at the nanometer scale. The characterization of nanomechanical properties at the surface or near-surface is of significant technological interest as many modes of failure (e.g. buckling, fracture, wear, etc.) at surfaces/interfaces at the nanometer length scales. The properties of interest include elasticity, hardness, adhesion, residual stress, fracture toughness, elastic-plastic deformation, and viscoelasticity. A number of techniques are used in investigation of these properties, of which the most widely-used are nanoindentation, and AFM-force curve measurement. Nanoindentation measures the relation between the load and displacement during the indenting process. It provides information of the mechanical properties of the material within the small volume being probed. The load resolution is typically limited to  $\mu\text{N}$ <sup>1.61</sup>. AFM on the other hand provides much higher resolution both in load and displacement down to pN and nanoscale,<sup>1.62-1.64</sup> respectively. This makes it ideal for the study of surface force, adhesion, and deformation behavior in the regime where elastic behavior is dominant. Several additional techniques have been developed for probing nanomechanical properties of materials, e.g. surface force apparatus (SFA)<sup>1.63, 1.65</sup>, some less direct techniques like osmotic stress method<sup>1.65</sup> and total internal reflection microscopy (TIRM)<sup>1.65</sup>, etc.. Compared to those techniques, AFM has the advantages of being easy to use, less material restrictions, and rather simple instrumentation.

## 1.5 Contact mechanics

The expansion of the field surface nanomechanics during past few decades has relied not only on the fast growth in measurement techniques (e.g. nanoindentation, AFM force measurement, etc.) but also on the development of theoretical models for describing the contact between solid objects. From bulk to nanometer scales, researchers have applied theories of continuum contact mechanics in analyzing tribological data to determine the fundamental properties (e.g. elastic modulus, hardness, adhesion force, etc.) of materials with increasing accuracy. A number of theories describing contact between two solid bodies have been developed. A major difference among them is the role played by surface adhesion forces in the system. The pioneering model of contact mechanics was first proposed by Hertz<sup>1.66</sup>. He considered the contact between two elastic spheres, having infinitely steep repulsion when in contact, without taking into account long range interactions and adhesion. Under these assumptions along with the further assumption of a frictionless contact, he was able to derive analytical expressions for the area of contact and deformation versus applied compressive load. Since two objects in a Hertzian contact do not adhere to each other, they will separate freely at zero or negative load.

Decades after Hertz, Johnson, Kendall, and Roberts (known as “JKR”)<sup>1.67</sup> extended the understanding of contact mechanics by taking into account the surface energies of the contacting objects, resulting a finite contact area even at zero applied load. Their model also leads to a greater contact area under a given applied load than Hertz’s prediction. In addition, it predicts that there is a finite tensile load required to separate the two objects, due to an adhesion force ( $F_{ad}$ ). This is a function of the

surface energy but not of the elastic modulus of the object. Subsequent to JKR, Derjaguin, Muller, and Toporov (known as “DMT”)<sup>1.68</sup> proposed that any attractive interaction force between the solid objects has a finite range, which would cause influence in the region just outside the contact zone, i.e. where the surfaces are closely spaced. The DMT theory assumes that the deformed shape of the object is Hertzian and independent of the adhesion force after contact, i.e. still a finite contact area at a zero load due to adhesion force. The influence of adhesion force in the DMT theory is to increase the total load the surfaces experience, beyond that externally applied. Comparisons of these three theories are summarized in figure 1.5 and table 1.1. Figure 1.5 shows the interaction force (per unit area) between two objects with respect to the distance between them for the Hertz, DMT, JKR models respectively, compared to a real case. For Hertzian contact, there is no attractive interaction force, only hard wall repulsion at contact. The DMT curve shows a long-range attractive interaction force (i.e. the Van der Waal’s force) which acts like an additional load, and the profile at contact remains hard wall repulsion as Hertzian. The JKR model includes a short-range adhesion force which is basically a delta function of strength  $W$ , and this force acts only within the contact area. In the realistic force-versus-distance, the integral of the area enclosed within the attractive region well corresponds to the work of adhesion  $W$ . Table 1.1 summarizes the relation between the contact radius ( $a$ ), the sample deformation ( $\delta$ ), and the adhesion force ( $F_{ad}$ ) for the contact between a spherical object and a flat surface (radius infinite) according to the Hertz, DMT, and JKR models.

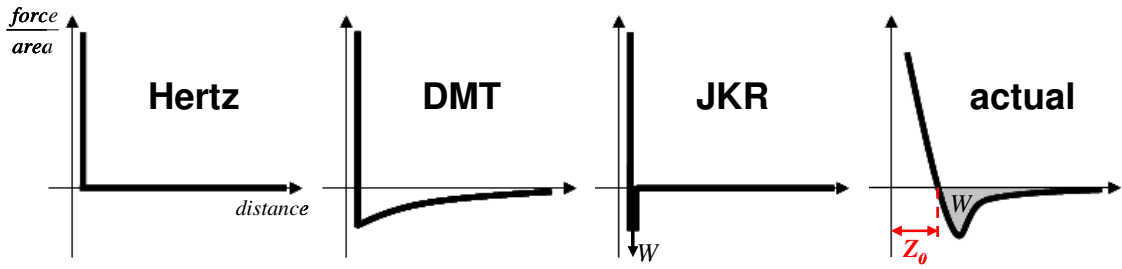


**Figure 1.5** Interaction force (per unit area) as a function of distance for the Hertz, DMT, and JKR models, compared to a realistic interaction.<sup>1.69</sup>

	Hertz	DMT	JKR
$a$	$\left(\frac{RF}{E_{tot}}\right)^{\frac{1}{3}}$	$\left[\frac{R}{E_{tot}}(F + 2\pi RW)\right]^{\frac{1}{3}}$	$\left\{\frac{R}{E_{tot}}\left[F + 3\pi RW + (6\pi RWF + (3\pi RW)^2)^{\frac{1}{2}}\right]\right\}^{\frac{1}{3}}$
$\delta$	$\frac{a^2}{R} = \left(\frac{F^2}{RE_{tot}^2}\right)^{\frac{1}{3}}$	$\frac{a^2}{R} = \frac{(F + 2\pi RW)^{\frac{2}{3}}}{(RE_{tot}^2)^{\frac{1}{3}}}$	$\frac{a^2}{R} = \frac{2}{3} \left(\frac{6\pi Wa}{E_{tot}}\right)^{\frac{1}{2}}$
$F_{ad}$	0	$2\pi RW$	$\frac{3\pi RW}{2}$

**Table 1.1** Relation between the contact radius,  $a$ , the sample deformation,  $\delta$ , and the adhesion force,  $F_{ad}$  for a spherical tip on a flat surface according to the Hertz, DMT, and JKR models.<sup>1.64</sup>

Note that in table 1.1,  $R$  is the radius of the sphere,  $W$  is the work of adhesion per unit area,  $F$  is the load applied between the sphere and the flat surface, and  $E_{tot}$  is the reduced elastic modulus of the contact system which is defined as following:

$$\frac{1}{E_{tot}} = \frac{3}{4} \left( \frac{1-\nu_s^2}{E_s} + \frac{1-\nu_t^2}{E_t} \right), \quad (1.3)$$

where  $E_t$  and  $E_s$  are the elastic moduli of the spherical and the flat objects, and  $\nu_t$  and  $\nu_s$  are the Poisson ratios for these two objects, respectively.

An intermediate form between the two limiting cases of JKR and DMT models was proposed by Maugis and Dugdale (known as “MD”)<sup>1.70</sup>. To approximate the actual interaction force-distance relation shown in the bottom right panel in figure 1.5, he considered a “Dugdale” (square well) potential to describe the attractive interaction force between two contacting spheres, see figure 1.6. He describes the deformation of a sample by making use of a transition parameter ( $\lambda$ ),

$$\lambda = 2\sigma_0 \left( \frac{R}{\pi W E_{tot}^2} \right)^{1/3}, \quad (1.4)$$

where  $\sigma_0$  is the minimum attractive interaction force of a Lennard-Jones potential. In the intermediate regime  $0.1(\text{DMT}) \leq \lambda \leq 5(\text{JKR})$ , the MD equations are,

$$\frac{\lambda \bar{a}^{-2}}{2} \left[ (m^2 - 2) \tan^{-1} \sqrt{m^2 - 1} + \sqrt{m^2 - 1} \right] + \frac{4\lambda^2 \bar{a}}{3} \left[ \sqrt{m^2 - 1} \tan^{-1} \sqrt{m^2 - 1} - m + 1 \right] = 1, \quad (1.5a)$$

$$\bar{F} = \bar{a}^{-3} - \lambda \bar{a}^{-2} \left( \sqrt{m^2 - 1} + m^2 \tan^{-1} \sqrt{m^2 - 1} \right), \quad (1.5b)$$

$$\bar{\delta} = \bar{a}^{-2} - \frac{4\lambda \bar{a}}{3} \sqrt{m^2 - 1}, \quad (1.5c)$$

where  $m$  is the ratio between contact radius ( $a$ ) and the radius of an annular region at which adhesion force starts to be taken into account. In above equations, contact radius ( $a$ ), applied load ( $F$ ), and sample deformation ( $\delta$ ) are represented in non-dimension forms,

$$\bar{a} = a \left( \frac{E_{tot}}{\pi W R^2} \right)^{1/3} ; \quad \bar{F} = \frac{F}{\pi W R} ; \quad \bar{\delta} = \delta \left( \frac{E_{tot}^2}{\pi^2 W^2 R} \right)^{1/3}. \quad (1.6)$$

However, it is difficult to utilize the MD equations in analyzing the experimentally measured load-distance data since it requires simultaneously solving two equations (equation 1.5a and 1.5b) by varying certain parameters between limits which depend on  $\lambda$ . Practically, it is rather cumbersome to carry out data analysis by common software that using automated statistical fitting procedure. Later on, several user-friendly approximate general equations based on MD model were presented by Carpick, Ogletree, Salmeron (known as ‘‘COS’’) <sup>1.71</sup>, Piétrement and Troyon (known

as “PT”)<sup>1.72</sup>, respectively, which facilitating the study of contact problems toward more general form. Note that all of the models described above were developed based on the contact between two spheres. Sneddon<sup>1.73</sup> extends the application to shape-dependent contact in which the object shape can be described by smooth functions, e.g. cones, flat cylinders, and spheres), which is useful in the application of indentation measurement with non-spherical probe.

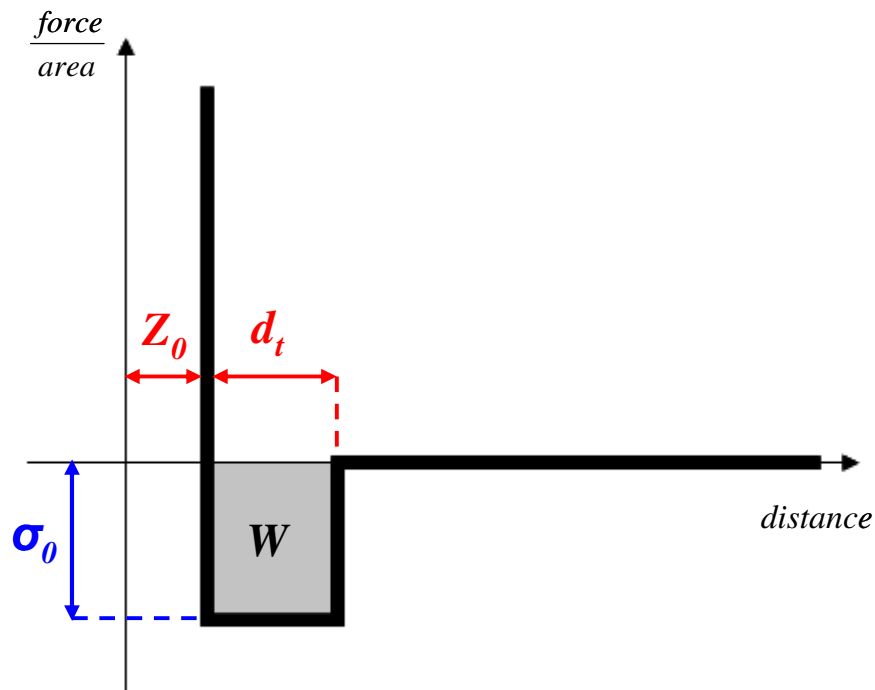


**Figure 1.6** Interaction force (per unit area) as a function of distance for the MD model. A constant adhesive stress  $\sigma_0$  acts between the surfaces over a distance  $d_t$ , resulting in the work of adhesion  $W = \sigma_0 \times d_t$ . No interaction force acts at distance beyond  $Z_0 + d_t$ .  $Z_0$  is the equilibrium separation of the surfaces.<sup>1.69</sup>

## 1.6 Outline of thesis

In this thesis, we present an investigation of the influences of ion energy during the exposure to an Ar plasma on the nanomechanical properties of a prototypical resist material, polystyrene. AFM force curve measurements were used to measure the effective elastic modulus of the bilayer film structure consisting of a top ultrathin ion-induced damaged layer and a thick unmodified polystyrene underlayer. Using numerical simulations in which we simulated the effective bilayer elastic modulus by varying the thickness and stiffness of individual layer, we extract the damaged layer's elastic modulus from the AFM measurements. The so-determined damaged layers' elastic moduli, as well as the dominant surface wrinkle wavelength characterized by AFM enabled us to test quantitatively the model of a buckling instability as a mechanism for roughening of polystyrene during plasma exposure. The remainder of thesis is organized as following:

In chapter 2, we present the results of AFM measurement of force curves measured from the polystyrene samples which were either pristine or treated by pure Ar plasma with varying ion energies. The surfaces of both types of polystyrene samples were characterized by AFM in tapping mode and analyzed by height-height correlation function to determine the dominant surface wrinkle wavelength. Next, we characterized the mechanical properties of these samples by using the AFM force curve measurement technique in an ambient controlled environment. The measured force curves were analyzed with an systematic algorithm which using statistical fitting procedures in order to determine the effective elastic modulus of the films, taking into account the adhesive interaction.

In chapter 3, we present a determination of the damaged layer elastic modulus from the effective elastic modulus of the damaged layer/polystyrene bilayer structure. This is based upon a finite element method simulation which takes into account thickness and elastic modulus of the damaged layers. By interpolation within the simulated relationship between the effective bilayer elastic modulus and the damaged layer elastic modulus, we extract the damaged layer elastic modulus versus etching ion energy. We initially approximate the real situation using a model in which a spherical tip is in contact with a flat sample surface. We next extend our model, by considering a periodic corrugated film surface to take into account the effect of roughness induced by plasma exposure. The damaged layer elastic modulus extracted from these two approximations gives different results of quantitative evidence for the correlation between buckling instability and plasma-induced roughening. We find excellent agreement from the corrugated film approximation.

Chapter 4 summarizes the main conclusions made in chapter 2 and 3. Finally, in chapter 5 we will give a brief prospect of what we might do to extend this study in the future, based on our approach and the results presented in this thesis.

## ***Chapter 2:***

### ***Experiment and Measurement***

We were motivated by the results of our previous collaborative works to test the validity of a buckling instability as the major mechanism for the formation of surface roughness of a model photoresist material – polystyrene during exposure to an Argon plasma. In this chapter, I will demonstrate how we used Atomic Force Microscopy and force curve analysis to determine two critical parameters in interpreting the buckling instability theory (equation 1.1) for both pristine and plasma-exposed polystyrene samples: the dominant wavelength ( $\lambda$ ) of the surface corrugation and the elastic modulus ( $E$ ). I will describe a delicate and systematic procedure which accounts for adhesive contact, in analyzing measured force curves. I will show that this allows direct determination of the effective elastic modulus ( $E_{BL}$ ) of pristine as well as the Ar-plasma etched polystyrene films with good precision and accuracy, and that this allows extraction of the ultrathin damaged layer's elastic modulus ( $E_{DL}$ ). Finally I will show that this allows a quantitative test of the buckling theory as a model for the observed plasma-induced surface roughening.

## 2.1 Sample preparation

The polystyrene we used in this experiment was synthesized by one of our collaborators, Brian Long, from Professor C. G. Willson's group at University of Texas. The degree of polymerization was 201 which results in the polymer of ~21000 g/mole in the number-average molar mass ( $M_n$ ) and ~1.5 in polydispersity. Polystyrene was spin-coated onto Si wafers and baked at 90°C for 1 minute. The average starting thickness of the polystyrene films was ~400 nm. The coated wafer was diced into similar sized (~ 2.5 cm × 2.5 cm) small pieces for different plasma etching conditions.

The plasma etching was carried out by Robert Bruce, from Professor Gottlieb Oehrlein's group at the University of Maryland. The plasma etcher used in this experiment is a special home-built and well-characterized inductively coupled plasma (ICP) reactor which is schematically shown in figure 2.1. The plasma is generated inductively through the coils situating on top of a quartz window, and is powered through a L-type matching network at a frequency of 13.56 MHz with a power supply (0-2000 W). The ion bombardment on a substrate of 125 mm in diameter can be independently controlled by an additional bias power supply with a frequency of 3.7 MHz, generating 0-250 W power. The distance between the quartz window and the substrate is 14.5 cm. The bottom electrode where the substrate is placed is cooled at a temperature of 10°C by a chiller. The achievable base pressure is below  $1 \times 10^{-6}$  Torr, and the standard operating conditions are 10mTorr of operating pressure and 40 sccm of gas flow rate.

The bias power was set at a series of values from 0-150W for establishing constant substrate biases and comparable Ar<sup>+</sup> ion energies bombardment on the polystyrene film. The maximum ion energies in each cases were measured by adding the plasma potential (-25 V) to the substrate bias voltage (-25 V to -150 V). During the plasma exposure, the substrate temperature was kept at ~40°C by thermal contact with an underlying substrate which in turn was bonded to a chiller. The temperature was monitored by use of in-situ ellipsometry, and the fact that the complex index of refraction (n-ik) of polystyrene changes with temperature. Our observations of no change in the experimentally determined values of n-ik subsequent to extinguishing the plasma, indicated that the temperature of the etched polystyrene did not change.

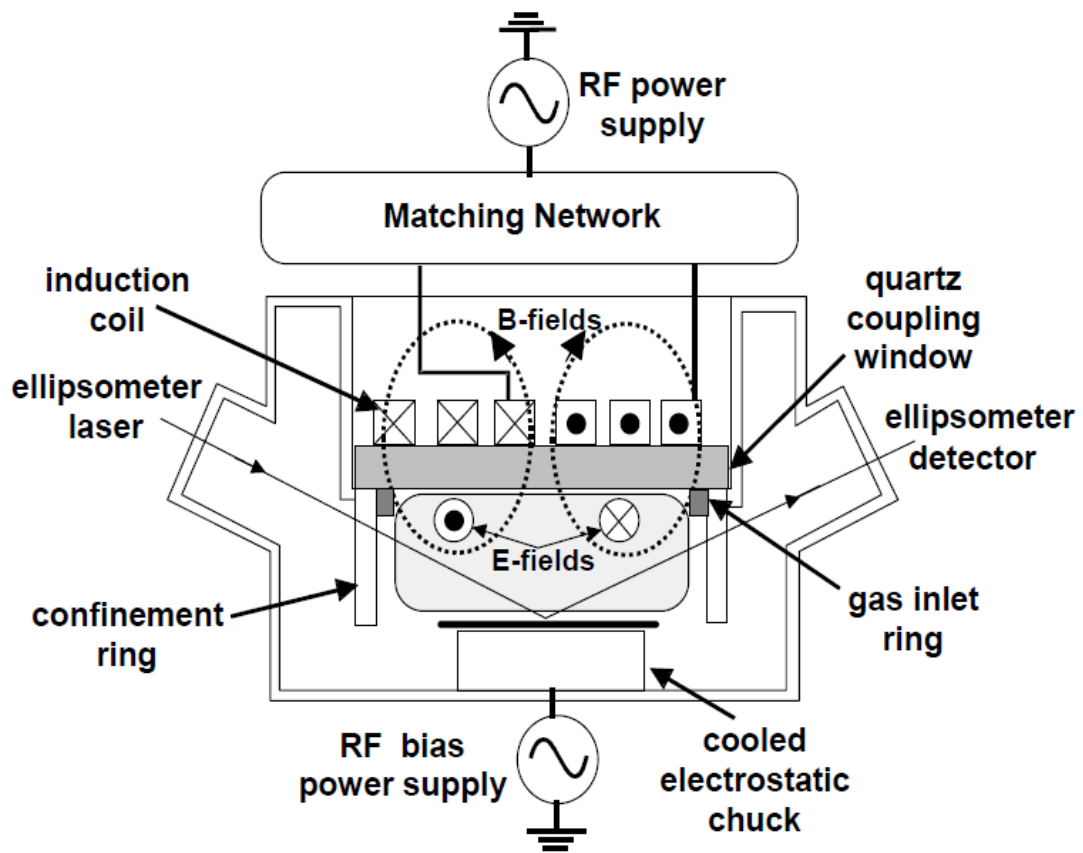


**Figure 2.1** Cross-sectional view of schematic of the inductively coupled plasma (ICP) reactor used in this work<sup>2.1</sup>.

## 2.2 Topography characterization of etched films

We used a commercial (Digital Instruments, Dimension 5000) atomic force microscopy (AFM) with a regular pyramidal-shaped probe in tapping mode to characterize the topography of our polystyrene samples. Example topographic images of the pristine and the etched polystyrene surfaces, for a series of different ion energies are shown in figure 2.2. From these AFM images, we clearly see that exposure of polystyrene film to an Ar plasma indeed causes significant measured roughness at the film surface beyond that of the pristine one. As can be seen from these images, the amplitude and the characteristic lateral length scale both increase with increasing etching ion energy. We summarize the measured RMS roughness in table 2.1. The error bars corresponds to the standard deviation in the RMS amplitudes based on a number of measurements for at least 5 in each case.

For each topographic image subsequent to plasma etching, we observe a seemingly nearly randomly distributed pattern of protrusions, however in each case there seems to be a dominant wavelength. For analyzing the roughness of our surfaces statistically we use height-height correlation function in stead of conventional fast Fourier transform (FFT) method. This is because we find that the results of FFT tend to be noisy for our images, while the correlation function is less so. The functional form of the height-height correlation chosen for our statistical analysis is:

$$g(\mathbf{R}) = \langle h(\vec{r} + \vec{R}) \cdot h(\vec{r}) \rangle - \langle h \rangle^2, \quad (2.1)$$

where  $h$  is the local height of the surface,  $\vec{r}$  and  $\vec{R}$  are two-dimensional translation vectors lying within the average surface plane, and  $\langle \rangle$  represents the ensemble

average over  $\bar{r}$ . This function measures how the correlation in height between two different locations of the surface falls off with distance due to roughness. A perfectly flat surface would show a uniform value of zero outside a central spike in the correlation map, while a surface with a perfectly periodic array of patterns would show a set of peaks spaced with the same unit mesh as the array. A randomly rough surface will show a central peak in the correlation map whose height is the square of the RMS amplitude and whose width is related to the “correlation length”,  $\xi$ , while non- randomly rough surface will show a significant peak at the center of the correlation map, surrounded by a ring of local maxima whose intensity varies depending on the degree of correlation at the corresponding characteristic lateral length scale - we will call it “the dominant wavelength” in the remainder of this thesis.

We calculated maps of the correlation function from AFM topographic images of unetched polystyrene films and for films etched at a number of Ar ion energies. The correlation maps corresponding to the AFM images shown in figure 2.2 are presented in figure 2.3. In the correlation map of the pristine polystyrene film, there is only one maximum peak located at the center of the correlation map. For the maps from etched polystyrene samples (figure 2.3 (b)-(d)) in addition to the central spike we see a set of broader local maxima as arranged in a ring around the center of the map. The radius of the ring formed by these local maxima increases noticeably and monotonically with the Ar ion energy, signifying an increase in the characteristic lateral length scale of the corrugation with ion energy.

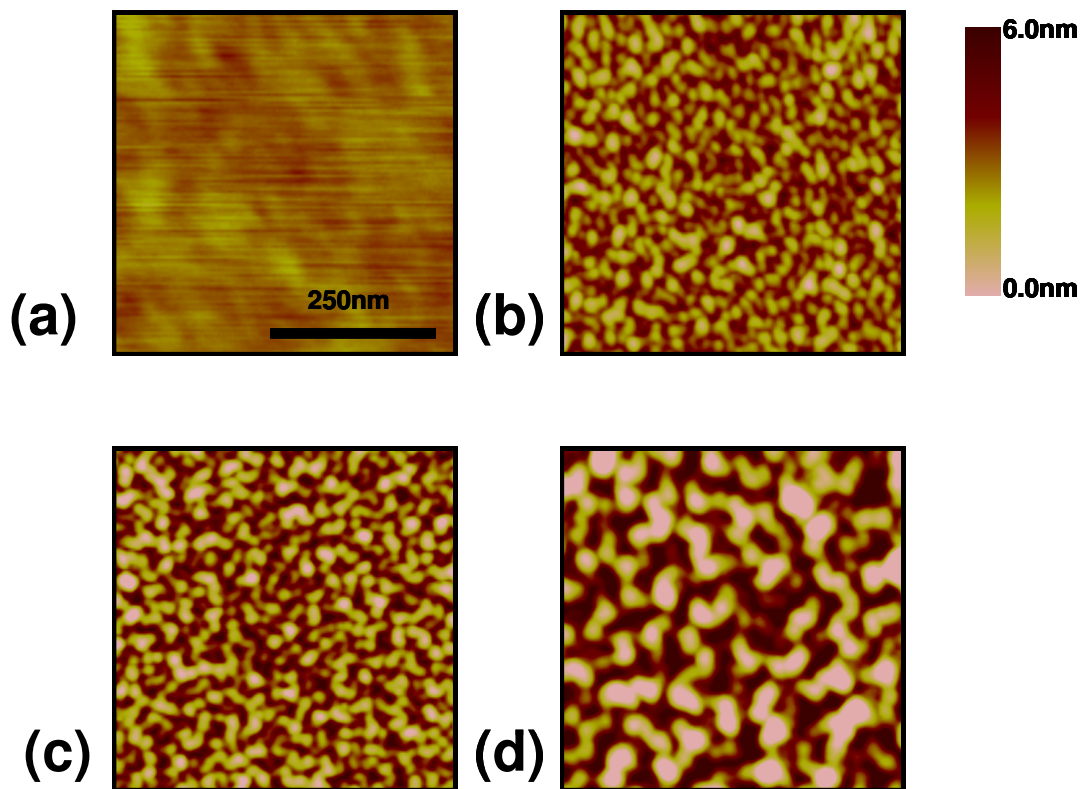


**Figure 2.2** AFM topographic images of (a) pristine (unetched) polystyrene and (b)-(d) polystyrene films after 60 seconds exposure of Ar plasma with varying maximum ion energies of (b) 50 eV, (c) 75 eV, and (d) 100 eV. Field of view in each case is 500 nm.

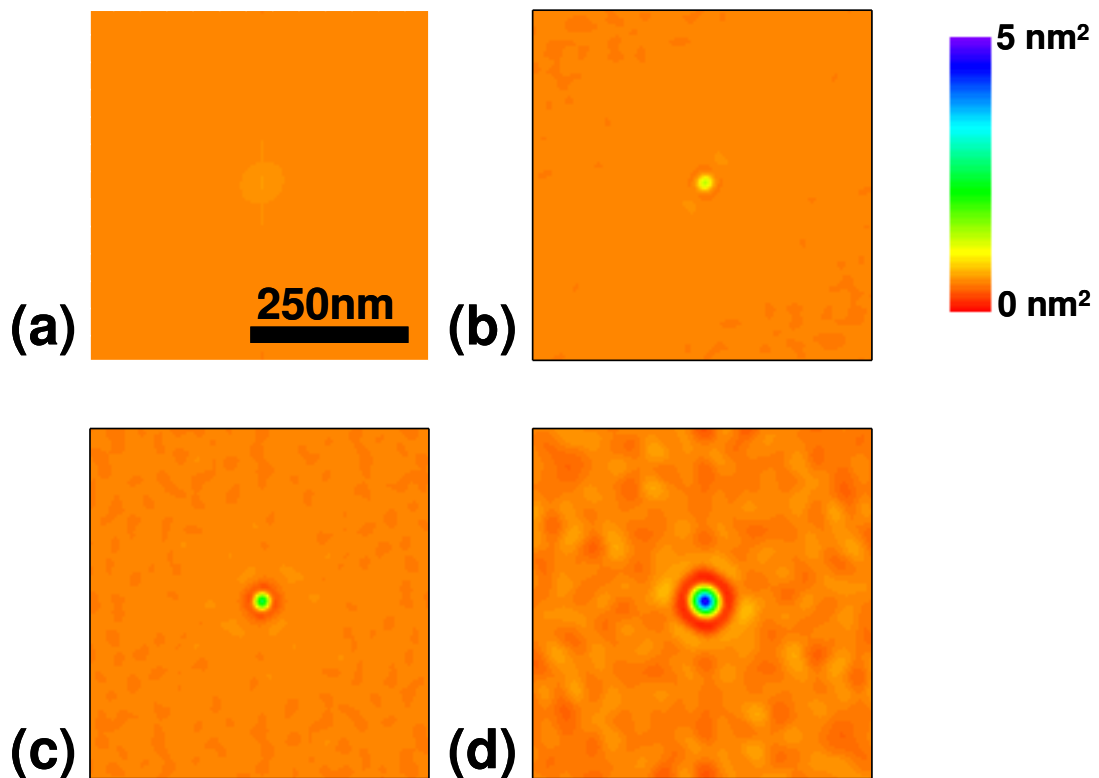


**Figure 2.3** Correlation maps corresponding to the AFM images of Fig 2.2, i.e.: (a) pristine PS, (b) 50 eV, (c) 75 eV, and (d) 100 eV. For the pristine polystyrene sample, there is only one maximum peak locating at the center of the map, (a), reflecting no dominant spatial wavelength on the surface. On the Ar-plasma treated samples, a second ring appears about the map centers.

We use the radius of the secondary ring in our correlation maps, indicated schematically in figure 2.4, as a measure of the dominant wavelength ( $\lambda$ ) of the corrugation of the surface topography.

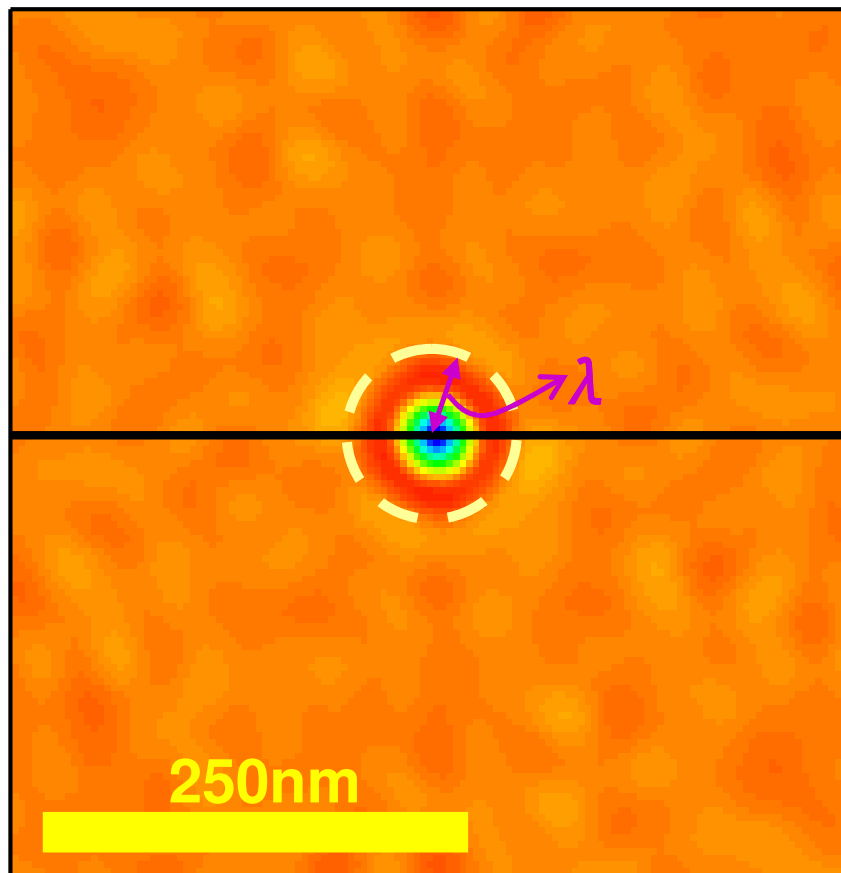


**Figure 2.4** Illustration of the determination of the dominant wrinkle wavelength ( $\lambda$ ).  $\lambda$  is picked out from the first local maximum peak shows on the azimuthally averaged line profile (black solid line).

To improve the statistics associated with determining  $\lambda$ , we take line profiles across the maps, and average these azimuthally. We determine the position of the first local maximum peak based on where the first derivative of the average line profile passes through zero. A surface with a well defined near-periodicity typically shows a first local maximum at a lateral length scale twice that at which the first local minimum occurs. A family of curves of azimuthally-averaged line profiles for polystyrene samples etched at different ion energies is shown in figure 2.5. We find that for the four cases shown, the first local minima all occur at values approximately half that for the first local maxima. In addition we find that the peak (marked with colored arrows) moves monotonically to larger length scales with increasing ion energy. This latter observation is consistent with the visual impression from inspection of AFM topographic images (see figure 2.2). The dominant wrinkle wavelength ( $\lambda$ ) vs. ion energy is summarized in table 2.1. As the first minimum is more pronounced than first maximum, we adopt twice the value of the lateral length scale where the first local minimum occurs as our  $\lambda$ . The uncertainties reported correspond to the half width at half minimum of the dip corresponding to the first local minimum.

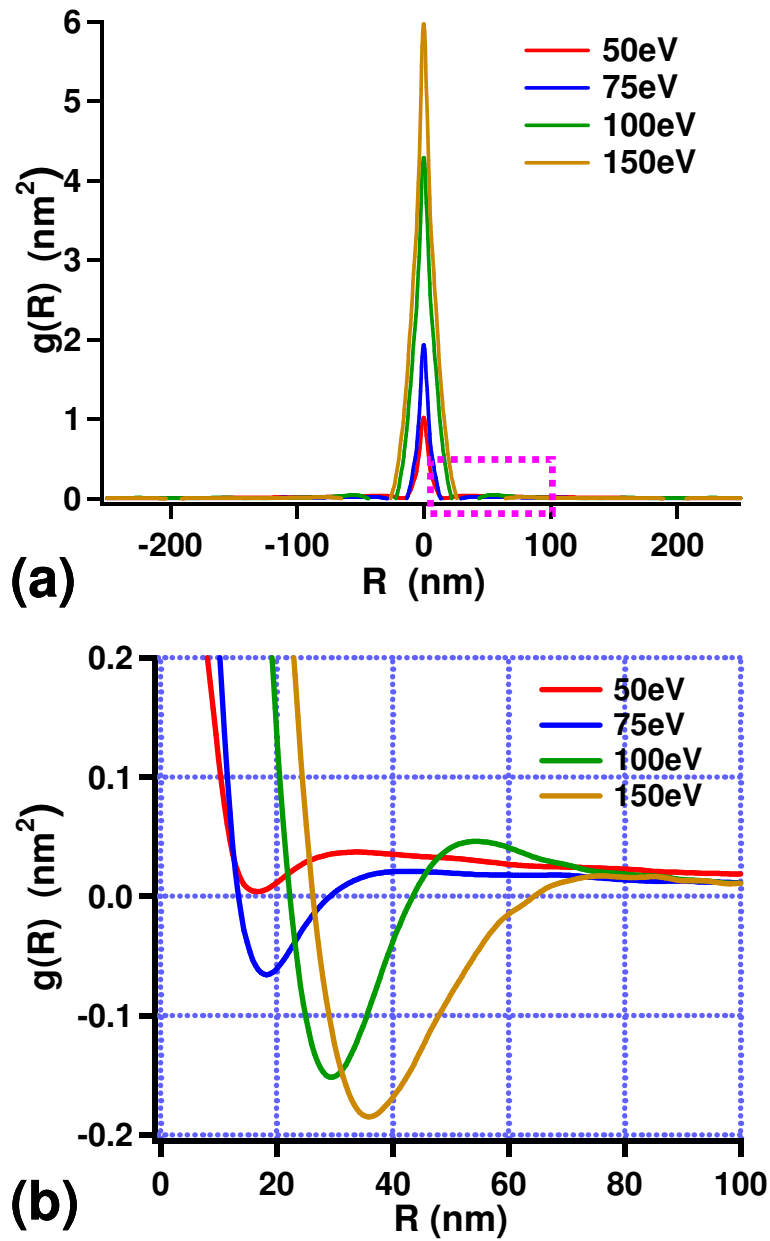


**Figure 2.5** (a) Family of curves of azimuthally-averaged line profiles across the center of correlation maps calculated from AFM images for polystyrene samples etched at a series of ion energies. (b) Same curves as in (a), replotted with reduced vertical scale.

	<b>Max. Ion Energy (eV)</b>			
	<b>50</b>	<b>75</b>	<b>100</b>	<b>150</b>
<b><math>t \pm \Delta t</math> (nm)</b>	$1.08 \pm 0.03$	$1.29 \pm 0.03$	$1.61 \pm 0.05$	$1.98 \pm 0.03$
<b><math>A \pm \Delta A</math> (nm)</b>	$0.95 \pm 0.05$	$1.50 \pm 0.04$	$2.11 \pm 0.05$	$3.32 \pm 0.05$
<b><math>\lambda \pm \Delta \lambda</math> (nm)</b>	$32 \pm 6.8$	$40 \pm 8.3$	$56 \pm 11.6$	$73 \pm 14.6$

**Table 2.1** The thickness of damaged layer ( $t$ ) as determined by XPS<sup>2.2, 2.3</sup>; the average surface corrugation amplitude ( $A$ ) as determined by AFM; and the dominant wavelength ( $\lambda$ ) as determined from height-height correlation analysis, as functions of ion energy for plasma-etched polystyrene.

## 2.3 AFM force curve analysis

AFM is capable of acquiring local mechanical and surface chemical properties (e.g. elasticity, hardness, adhesion, etc.) by measuring vertical deflection of the free end of the cantilever as the vertical displacement of the supported end is varied. This allows the determination of a “force curve”. The resulting mechanical property determination is superior to that from other conventional nanoindenters, as AFM produces force curve measurements with very high spatial resolution (down to several tens nanometers), and with very fine control of applied force (in a range of nanonewtons to piconewtons). For this reason, AFM force curve measurement has been widely and successfully used in studies of polymers<sup>2.4-2.6</sup>, biological systems<sup>2.7</sup>, interfacial phenomena<sup>2.8, 2.9</sup>, even single molecules<sup>2.10-2.12</sup>. To relate a measured force curve to that material’s mechanical properties, it is important to apply contact theory properly. In the following subsection, I will briefly introduce the determination of force curves and review several contact theories commonly used to extract mechanical information from them.

### 2.3.1 General look of a force curve

A force curve measured using AFM consists of a plot of the deflection of the unsupported end of the cantilever with respect to the displacement of the piezoelectric scanner controlling the vertical displacement of the supported end of the cantilever. A schematic example of such a force curve, with the relative position of the cantilever and the sample surface, as well as the response of the cantilever during a cycle of one measurement is shown in figure 2.6. At the beginning of the cycle, the separation

between the probe and the sample surface is large so that the probe senses nearly zero interaction force with the surface, and no deflection is observed (stage **(a)**). As the cantilever continues approaching the sample at a constant velocity, various attractive forces (e.g., short- and long-range force) between the tip and surface, result in a deflection of the cantilever toward the sample surface (stage **(b)**). Once the total force gradient acting on the probe exceeds the stiffness of the cantilever, the probe jumps into contact with the sample surface (jump-to-contact) at stage **(c)**, causing an abrupt change in the cantilever deflection. At stage **(d)** during approach, the probe and the sample are in contact, and the deflection of the cantilever is dominated by the mutual electronic repulsion between the overlapping atomic (or molecular) orbital of the probe and the sample respectively, bending the cantilever away from the surface. After completing a predefined maximum moving distance of the cantilever, the piezo-scanner begins to move the supported end of the cantilever in the opposite direction. During the retraction process, the cantilever bends “backward” due to a decreasing applied load. Generally, as the change of bending passes through the zero-deflection point (point **(e)**), the probe does not detach from the sample surface due to an adhesion force, resulting, e.g. from bonds formed during contact; this results in the cantilever bending downward more (stage **(f)**). This continues up to some displacement beyond the initial contact point (minimum of stage **(c)**), i.e. that occurring during the approaching process. When the spring force of the cantilever stored during the retraction process overcomes the adhesion force, the probe jumps free from the sample surface abruptly (point **(g)** to **(h)**), and the cantilever is back in its starting undeflected state.

Note that the shape of the curve in the contact region (d) provides information on whether the sample is deforming in response to the force applied to the cantilever. The slope of the curve at region (d) is a function of the elastic modulus and the geometry of the probe and sample surface, and will approach to one for very stiff tip-sample systems.<sup>2.13, 2.14</sup> There is no additional information content if the segments of the approaching and retraction curves at the contact region are parallel to each other. If these two segments are not parallel, the hysteresis indicates that some plastic deformation occurs within the tip-sample system.<sup>2.15, 2.16</sup>

A useful force curve should be represented as a plot of “force vs. probe-sample surface distance”. The force applied on the cantilever can be simply calculated by Hooke’s law,

$$F = -k_c \delta_c, \quad (2.2)$$

where  $k_c$  is the spring constant of the cantilever, and  $\delta_c$  is the deflection of the cantilever.<sup>2.17</sup>

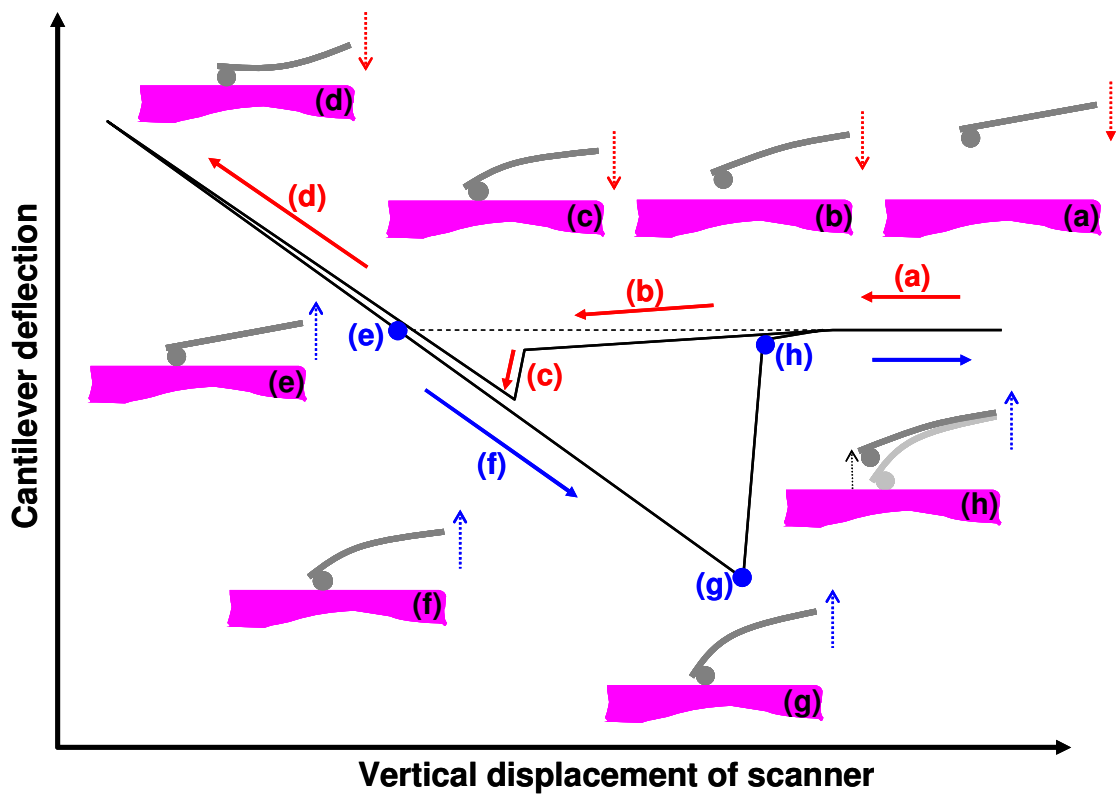


**Figure 2.6** Schematic of the relative position of the cantilever and the sample surface during a cycle of force curve measurement. Note that each specific spot on the force curve corresponds to different degree of cantilever bending, e.g. the “jump-to-contact” (c), “zero-deflection point” (e), and the “jump off” (h).

### 2.3.2 Force curve measurement setup

We carried out force curve measurements using a commercial AFM (DI series 5000), which we modified for operation in a dry nitrogen atmosphere to eliminate meniscus effects due to humidity. To facilitate quantitative analysis of the force curves, we employed special probes consisting of a silica sphere of known radius (1.75  $\mu\text{m}$ ), rigidly bonded to a silicon cantilever, as shown in figure 2.7. We investigated the effect of the approach/retraction velocity, the nitrogen purge time, and the effect of the overall penetration on the measured force curves, and carried out measurements for unetched and plasma-treated polystyrene samples under conditions for which the shape of the force curves was not sensitive to small changes in these experimental parameters (see details of the ambient control AFM in Appendix C).

One should note that what can be obtained directly from measured force curves of plasma-etched polystyrene samples is the effective stiffness of a bilayer structure ( $E_{BL}$ ), due to the elastic response of the top damaged layer ( $E_{DL}$ ) and that of the underlying unmodified polystyrene layer ( $E_{PS}$ ); see the schematic illustration in figure 2.8. To extract the elastic modulus of the damaged layer ( $E_{DL}$ ), it is essential to know the relationship between  $E_{BL}$  and  $E_{DL}$ . To acquire this dependence, we carried out a series of numerical simulations using the finite element method. We will describe this in detail in chapter 3.

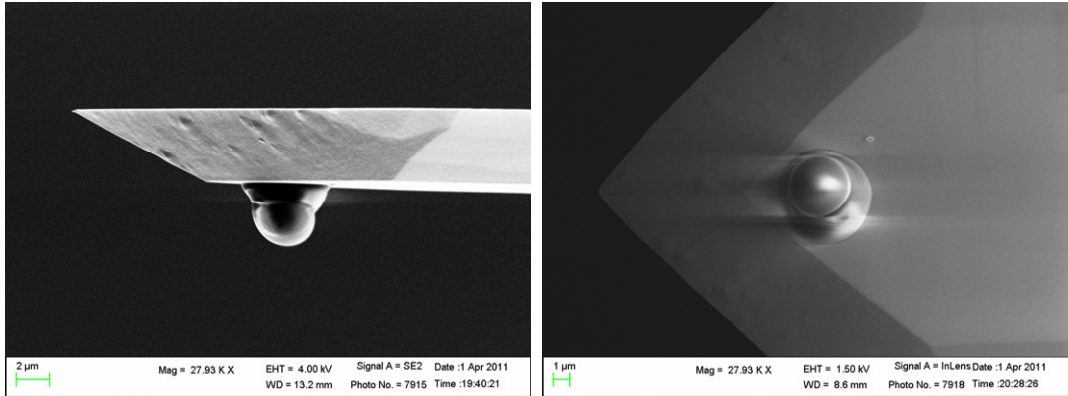


**Figure 2.7** SEM images of a spherical silica probe used in the force curve measurement. The nominal diameter of the sphere is  $3.5 \mu\text{m}$ .

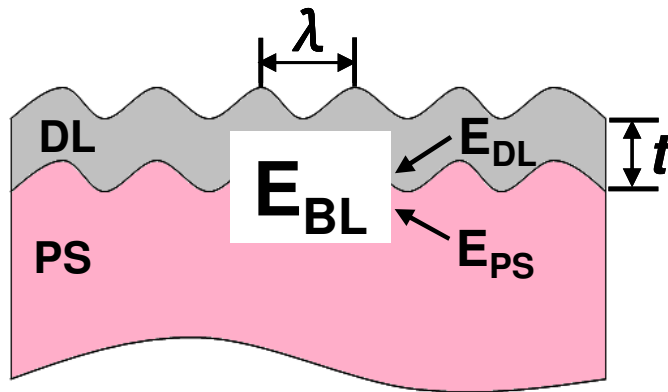


**Figure 2.8** Schematic illustration of the relation between the effective bilayer stiffness ( $E_{BL}$ ) and the individual components ( $E_{DL}$  &  $E_{PS}$ ).

### 2.3.3 Analysis of measured force curve

#### 2.3.3.1 Calibration of cantilever response

The quantities measured directly in a force curve are the photodiode voltage ( $D_{pd}$ ) versus the displacement of the piezoelectric scanner ( $Z_{piezo}$ ). To interpret this, the deflection of cantilever needs to be converted from a voltage into a distance (measured, e.g., in nm); one can then calculate the force applied on the cantilever knowing its spring constant. In other words, the response of the cantilever to the movement of the Z-directional piezoelectric scanner, known as “sensitivity”, needs to be determined. In AFM force curve measurements, this parameter must be extracted from the force curve itself and not through an independent method.

As mentioned above, the “sensitivity” describes the ratio of the cantilever response to the Z-directional actuation of the piezoelectric scanner. In an ideal case the slope of the linear part of the contact region in the  $D_{pd}$ -versus- $Z_{piezo}$  curve is the sensitivity of the cantilever-sample system: this is the case for a very stiff probe-sample system.<sup>2.18</sup> Performing a force curve slope determination on a much softer sample than the probe material will cause a false interpretation, because not only the cantilever deflection but the deformation of the sample must be taken into account to reflect the total Z-directional actuation. Therefore, we use a clean silicon substrate to calibrate the sensitivity of our cantilever before measuring force curves from our polystyrene samples. As the sensitivity is also a function of cantilever geometry (e.g. shorter cantilever gives a higher sensitivity as well as the position of the laser spot shot on the cantilever<sup>2.18</sup>), we perform a new such calibration for each probe.

An example raw force curve for a silicon<100> substrate is shown in figure 2.9 (a). In the preliminary deflection-versus-displacement plot, no hysteresis is observed within the linear part of the contact region, which means that no plastic deformation occurred during the measurement. Note that the unit of the vertical axis in figure 2.9 (a) is Volt as this corresponds to the signal generated by the split photodetector. Once the sensitivity is determined by the slope of the linear part of the contact region, between the two red arrows, this voltage is converted to cantilever deflection measured in nanometers, see figure 2.9 (b). The force  $F$  is determined by multiplying the spring constant of the cantilever with its deflection in nanometer, as described by equation 2.2. In practice, we take the average of the slopes from approach and retraction curve, repeated at multiple positions on the silicon substrate. The overall average value is used as the sensitivity for that probe.

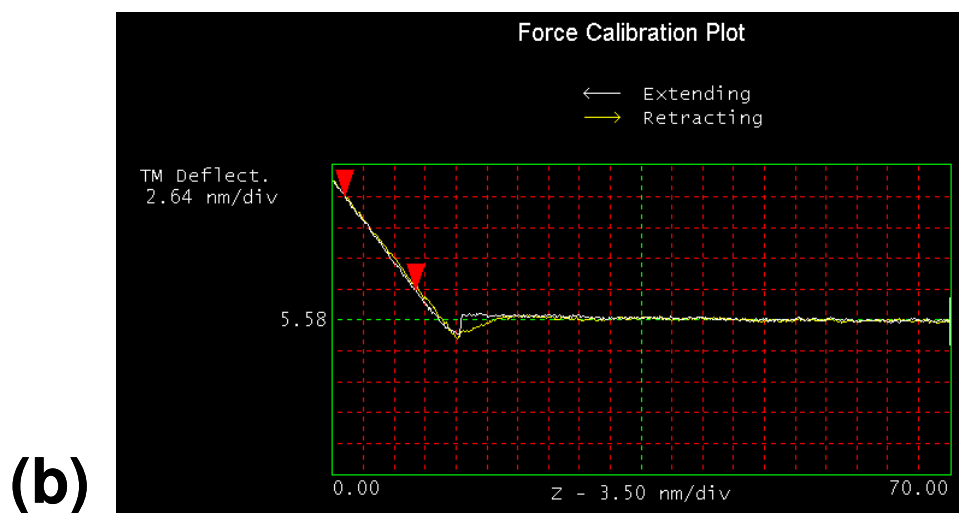
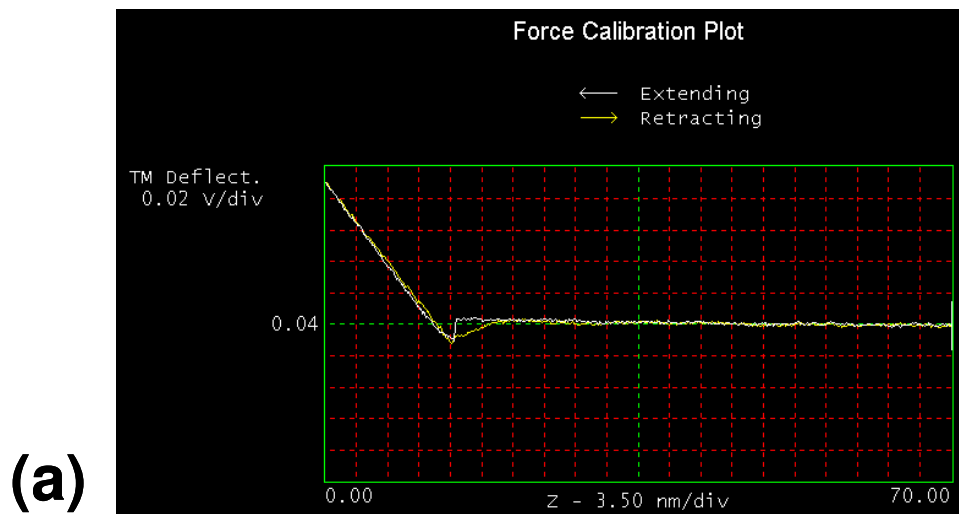


**Figure 2.9** (a) Raw, photodetector voltage versus  $Z_{piezo}$  curve of a Si<100> substrate. (b) The corresponding cantilever deflection versus  $Z_{piezo}$  curve of (a) when the sensitivity is determined.

### 2.3.3.2 Extraction of elastic modulus from measured force curve

As mentioned above, information about the elasticity of the material being probed is contained in the contact region of the force curve. However, a simple fitting of the force-versus-penetration data in this region generally does not result in reliable and reproducible results, as it ignores the attractive interaction force between the probe and sample, which plays a significant role in determination of the contact point, beyond which the force curve can be fitted with an appropriate model of contact mechanics.

Generally not known what the appropriate form of contact mechanics should be applied. The two extreme cases are due to Johnson, Kendall and Roberts (JKR)<sup>2.19</sup> and due to Derjaguin, Muller and Torporov (DMT)<sup>2.20</sup>, corresponding to adhesion within an area of contact, and outside an area of contact, respectively. A more general model was suggested by Maugis and Dugdale (MD)<sup>2.21</sup> which allows one to interpolate between these two extremes represented by JKR and DMT. Following the MD model, several other models were proposed using empirical approach to approximate the MD model, transforming it to a more practical form for interpretation of measured force curves, among which the Carpick-Ogletree-Salmeron (known as “COS” model)<sup>2.22</sup> and the Pietrement-Troyon (known as “P-T” model)<sup>2.23</sup> are the most widely used.

In the work reported in this thesis we followed the algorithm suggested by Lin et al.<sup>2.24, 2.25</sup>, in which they used in analyzing their force curve measured on soft materials based on Pietrement-Troyon force-penetration relation,

$$\delta = \frac{a_0^2}{R} \left[ \left( \frac{\alpha + \sqrt{1 + F / F_{ad}}}{1 + \alpha} \right)^{\frac{4}{3}} - S \left( \frac{\alpha + \sqrt{1 + F / F_{ad}}}{1 + \alpha} \right)^{\frac{2\beta}{3}} \right], \quad (2.3)$$

where  $a_0$  is the contact radius at zero load,  $R$  is radius of the AFM tip, and  $F$  is the load, schematically shown in figure 2.10. In equation (2.3), the attractive interaction force (or adhesive force)  $F_{ad}$ , pre-factor  $S$ , and exponent  $\beta$  are all functions of the parameter  $\alpha$ , which varies between 0 and 1, corresponding to the JKR and DMT limits, respectively. We discuss its significant in terms of physical quantities below. We note in passing that, a simpler approach, suggested by Sun, et al.<sup>2.26</sup> was found to produce values of the film elastic modulus which were highly sensitive to slight variations in the experimental force curves and thus judged unreliable.

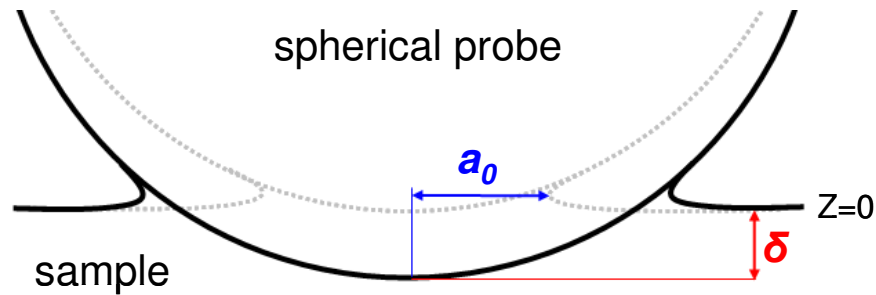


**Figure 2.10** Schematic illustration of a spherical probe (radius of  $R$ ) penetrating into a film with a penetration depth  $\delta$  (relative to undeformed surface,  $Z=0$ ). The radius of the circular contact area at zero load is  $a_0$ .

We next use a measured force curve, for a pristine polystyrene sample to illustrate the implementation of the P-T algorithm; see figure 2.11. In practice we carry out the algorithm for the retraction part of the force plot, which is shown in figure 2.12. Note that the vertical axis in figure 2.12 has been converted to displacement (nm), using the measured sensitivity for the probe, as described above. As a first step, the data are replotted with the deflection of the cantilever ( $D_{pd}$ ) along the vertical axis, and the difference between the displacement of the cantilever's supported end and the deflection of the cantilever,  $\delta = Z_{piezo} - D_{pd}$ , along the horizontal axis (figure 2.12(a)). We fit the portion of the curve well before contact to a linear dependence and the portion well within the apparent contact regime to a  $D_{pd} = D^* + b \times (\delta - \delta^*)^{3/2}$  power law; the latter form is predicted by Hertzian mechanics for a spherical probe, and a semi-infinite slab sample. The "optimum" point ( $D^*$ ,  $\delta^*$ ) is taken to be that which produces the least total mean-square-error (MSE) in the fit. Next the range of the  $D_{pd}$ -versus- $\delta$  plot between the initial point of the linear, non-contact region fit and  $\delta^*$  is fit to a Lennard-Jones (L-J) form.<sup>2.25</sup> Where the  $D_{pd}$ -versus- $\delta$  curve, in the small separation regime, crosses through the asymptotic (large separation) value of the L-J fit is taken to be the point of zero tip-sample force ( $D_I$ ,  $\delta_I$ ).

We obtain the adhesive force ( $F_{ad}$ ) by the product of the cantilever's force constant (as supplied by the manufacturer) and the difference between the minimum  $D_{pd}$  and  $D_I$ . For the example shown in figure 2.12(a) ( $D_I$ ,  $\delta_I$ ) = (15.04975 nm, 49.20005 nm), and  $F_{ad} = 332.96$  nN.

Next we plot the deflection of the cantilever ( $D_{pd}$ ) versus the displacement of the cantilever's supporting end ( $Z_{piezo}$ ), and use this to determine the contact point ( $D_0, Z_0$ ). To do this we fit the contact region to the Pietrement-Troyon (P-T) relation, expressed in the AMF-specific form which presents a relation between the displacement of the cantilever's supported end and the deflection of the cantilever, as shown in the following equation,

$$Z = Z_0 + D - D_0 + \frac{a_0^2}{R} \left\{ \left[ \frac{\alpha + \sqrt{1 + k_c (D - D_1) / F_{ad}}}{1 + \alpha} \right]^{4/3} - S \left[ \frac{\alpha + \sqrt{1 + k_c (D - D_1) / F_{ad}}}{1 + \alpha} \right]^{2/3\beta} \right\}, \quad (2.4)$$

where  $Z$  is the displacement of the cantilever's supporting end,  $D$  is the deflection of the cantilever,  $a_0$  is the contact radius at zero applied force,  $R$  is the radius of the probe,  $k_c$  is the spring constant of the cantilever, and  $\alpha$  is an adjustable fitting parameter. In this rearranged form of the P-T equation,  $Z_0, D_0, F_{ad}, a_0, S$ , and  $\beta$  are all functions of  $\alpha$ .

According to the MD model,  $\alpha = 0$  corresponds to the DMT limit, while  $\alpha = 1$  corresponds to the JKR limit. We treat  $\alpha$  as a fitting parameter, with the best value corresponding to the least mean-square difference between the data and the fit; physically it can be regarded as an interpolation between the DMT and JKR limits. In the example shown, for pristine polystyrene, we find  $\alpha = 0.999999977648$ , which is

essentially the JKR limit. Therefore in the example shown in figure 2.11(b), we determined that  $(D_0, Z_0) = (6.183 \text{ nm}, 53.147 \text{ nm})$ .

Figure 2.13 shows the force-versus-penetration curve derived from the retraction curve of figure 2.12; the inset shows a fit of the curve in the apparent contact regime to the JKR equation. We find that the fit to this model is excellent.

Next we consider the significance of the parameter  $\alpha$ . It is related to a second nondimensional parameter  $\lambda$  in the MD theory,

$$\lambda = 2\sigma_0 \left( \frac{R}{\pi K^2 \gamma} \right)^{1/3}, \quad (2.5)$$

by the approximate relation,

$$\lambda(\alpha) \approx -0.924 \times \ln(1 - 1.02\alpha), \quad (2.6)$$

where  $\sigma_0$  is the maximum value of the attractive force in the Lennard-Jones potential and the Dugdale approximation,  $R$  is the radius of the tip,  $\gamma$  is the tip-sample interface energy, which is determined from the adhesive force ( $F_{ad}$ ) via equations 2.7 and 2.8<sup>2.25</sup>,

$$\overline{F_{ad}} = \frac{F_{ad}}{\pi\gamma R} \quad (2.7)$$

$$\overline{F_{ad}}(\alpha) = 0.267\alpha^2 - 0.767\alpha + 2.000, \quad (2.8)$$

where  $\overline{F_{ad}}$  is the non-dimensionalized form defined in MD model, and  $K$  is the elastic constant of the sample.

With the P-T algorithm applied in the example shown in figure 2.12, we obtained a value of adhesive force ( $F_{ad}$ ) of 332.9627 nN, allowing us to further calculate  $\gamma = 0.01996145$  N/m. Using the calculated  $\gamma$  and taking 1750 nm as the radius of the probe, we obtain an effective sample stiffness of  $K = 3.5528$  GPa, based on equations 2.5 and 2.6.

Finally we calculate the elastic modulus of the film,  $E_f$  from:

$$K = \frac{4E_f}{3(1-\nu^2)} \quad (2.9)$$

where  $E_f$  and  $\nu$  are the Young's modulus and the Poisson ratio of the sample respectively. Taking 0.33 as the Poisson's ratio<sup>2.2, 2.27</sup>, we obtain the elastic modulus of the pristine polystyrene film of this example, equal to 2.37 GPa.

To streamline the implementation of this sophisticated procedure, we developed a FORTRAN code which applies the algorithm described above to measured force curves in collaboration with Dr. Hung-Chih Kan, National Chung Cheng University, Taiwan. The details of the FORTRAN program are provided in Appendix D.

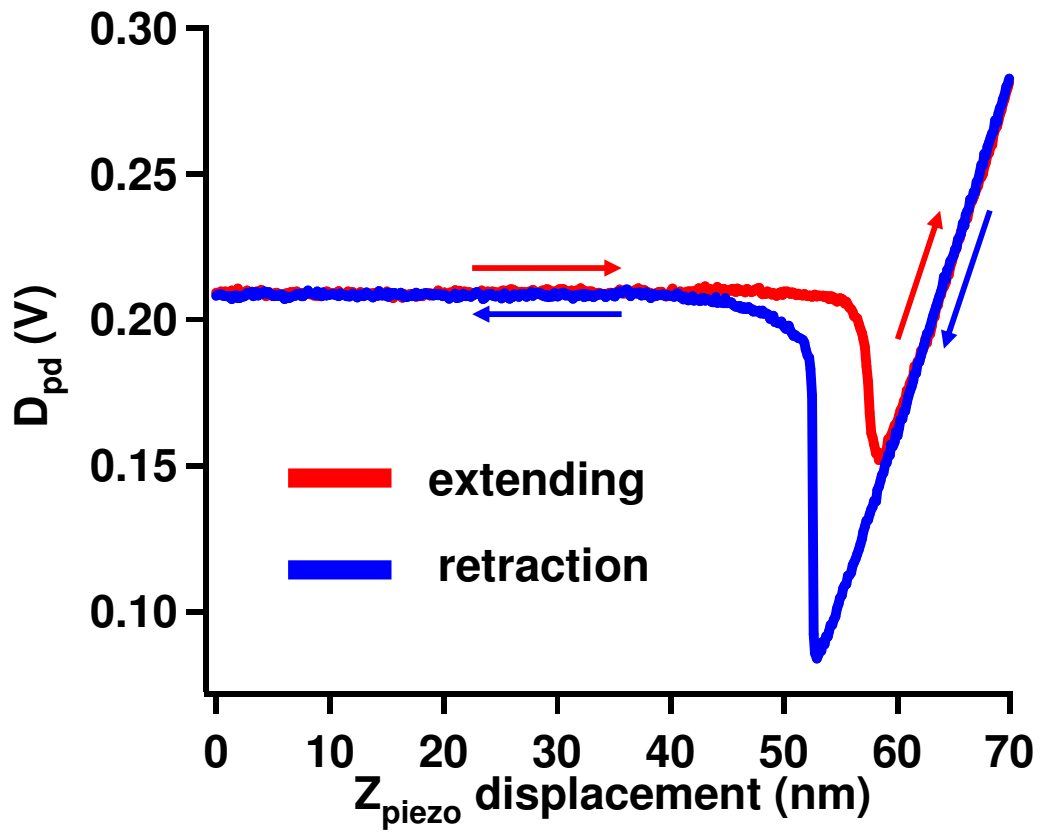


**Figure 2.11** The measured force curve of an pristine polystyrene sample, where  $D_{pd}$  denotes the deflection of the cantilever detected by the photodiode sensor. The range in which the indentation process takes place is 70 nm, with a scan rate of 1 Hz.

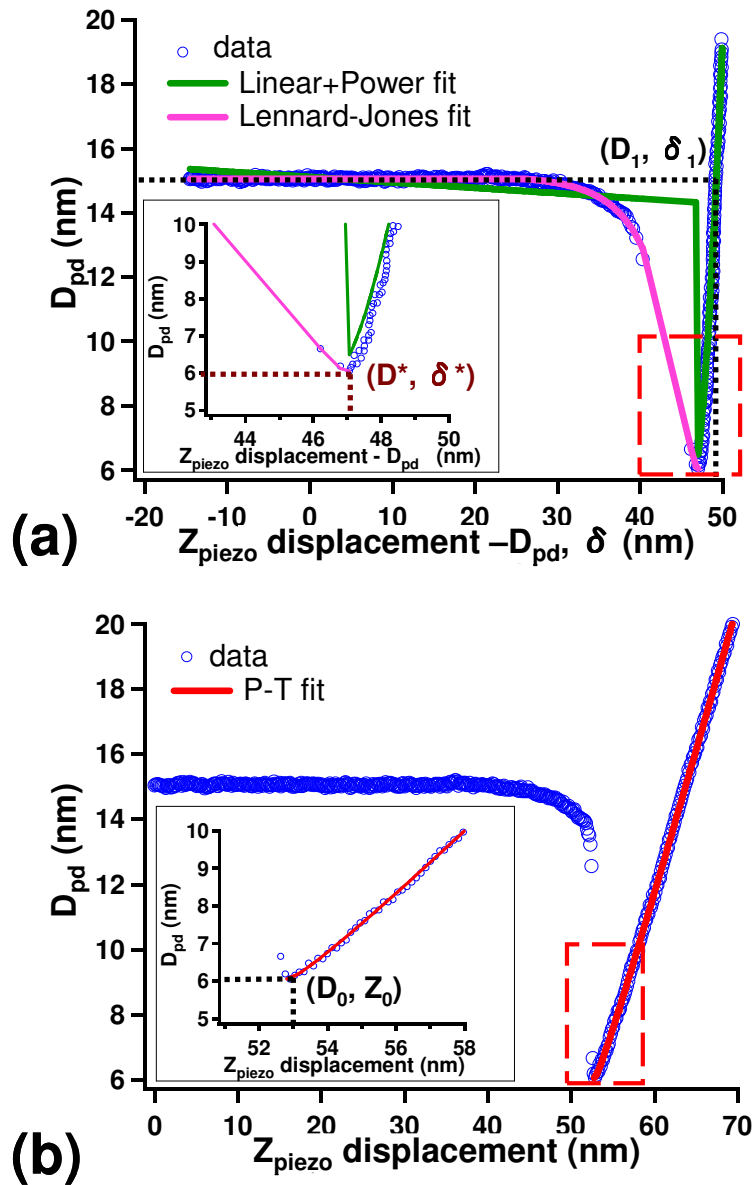


**Figure 2.12** Illustration of procedures for extraction of sample elastic modulus from a measured force curve following the method of Lin et al. <sup>2.24, 2.25</sup>: **(a)** Determination of zero force point  $(D_1, \delta_1)$ ; **(b)** Determination of contact point  $(D_0, Z_0)$ . Note that this example is a retraction force curve measured on a  $\sim 400$  nm thick pristine polystyrene film.

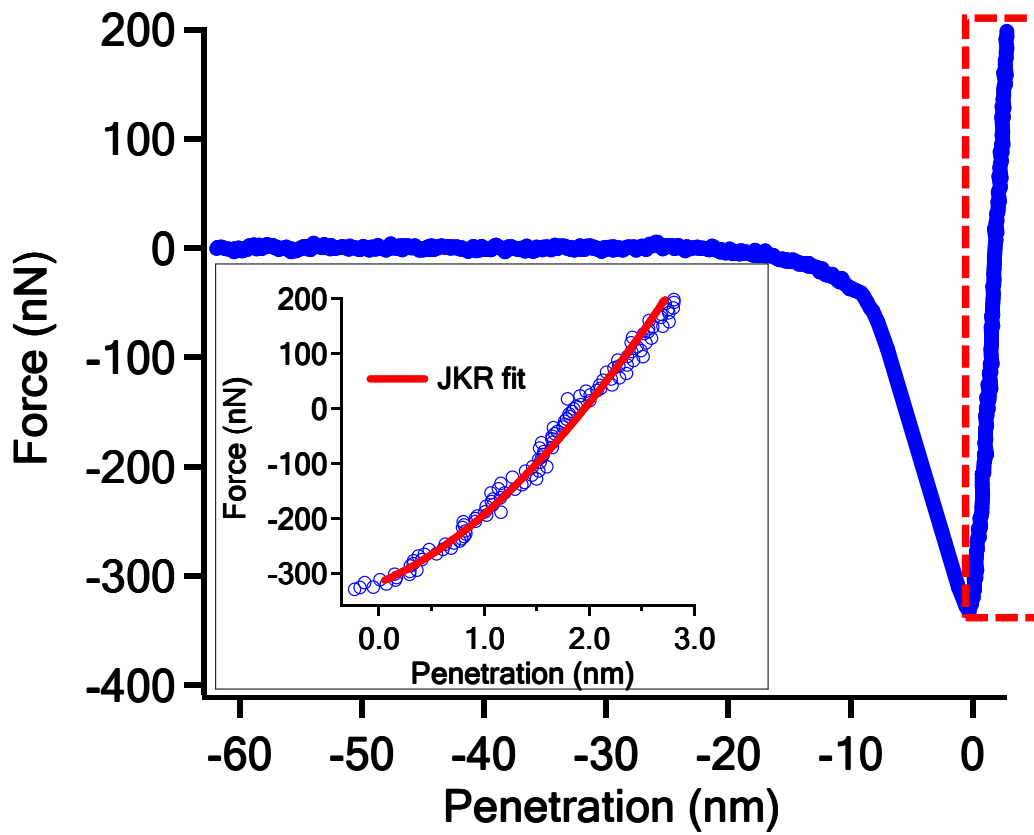
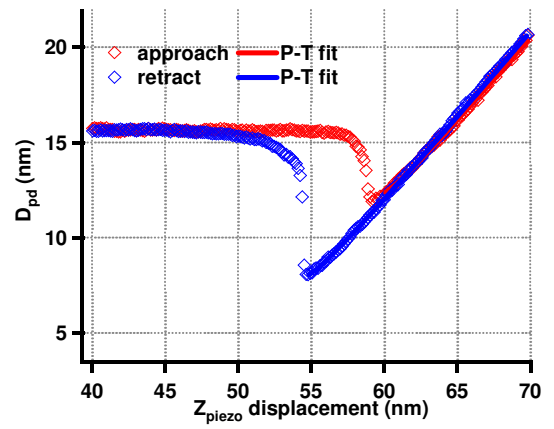
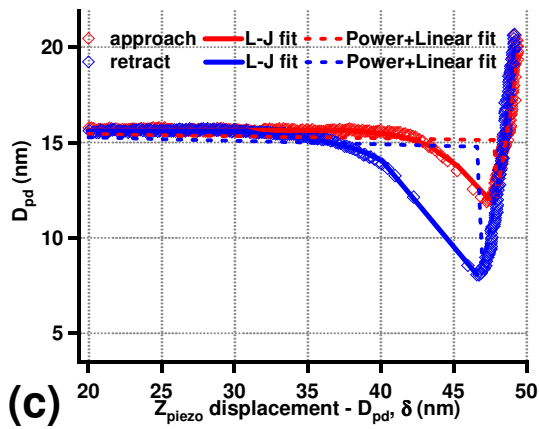
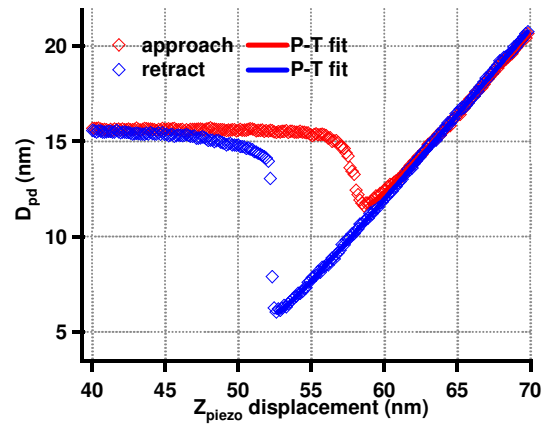
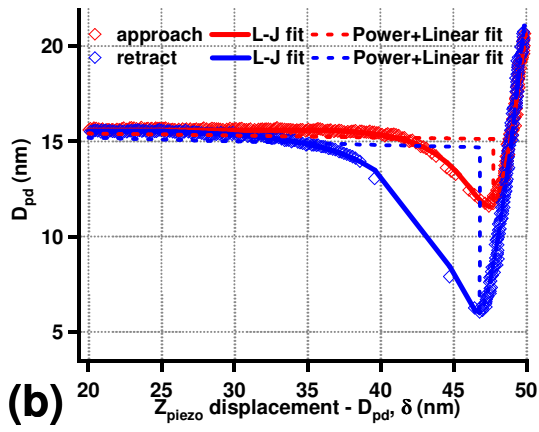
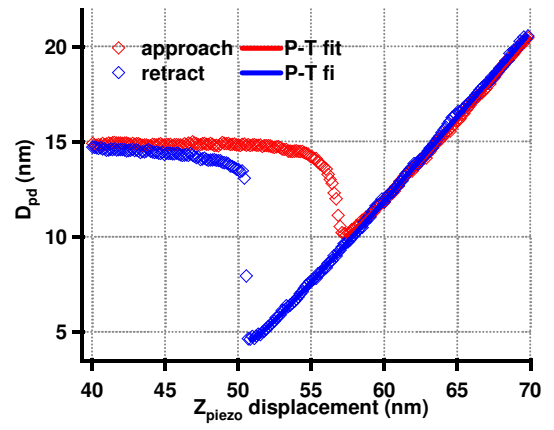
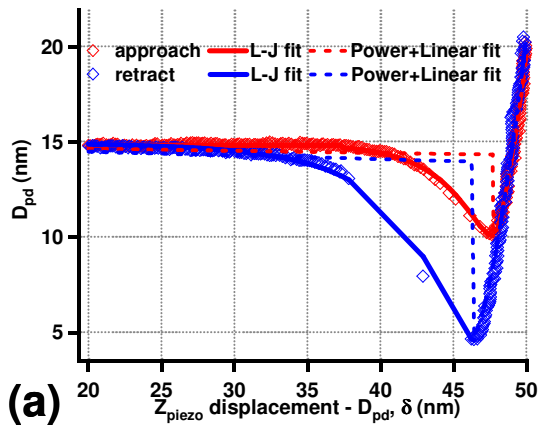


**Figure 2.13** Plot of tip-sample force vs. penetration for the retraction curve illustrated in figure 2.11. In the inset, the repulsive part of the force–penetration curve is fitted to the JKR form, corresponding to  $\alpha = 1$ .

### 2.3.4 Analysis result of pristine and etched polystyrene sample

In this section we discuss the results of the application of the procedures described above in section 2.3.3.2 in analyzing our force curves measured at multiple positions across the surfaces of unetched and Ar-plasma etched polystyrene samples. Figure 2.14 shows example measured force curves with the vertical scale set to allow visibility of variations in the contact region. Figure 2.14 (a)-(e) are for (a) unetched polystyrene, (b) etched at 50 eV, (c) etched at 75 eV, (d) etched at 100 eV, and (e) etched at 150 eV. The deflection of the cantilever ( $D_{pd}$ ) is plotted as a function of the displacement of the cantilever's supporting end ( $Z_{piezo}$ ), and in the panel on the left it is plotted versus the difference between the displacement of the cantilever's supported end and the deflection of the cantilever ( $\delta = Z_{piezo} - D_{pd}$ ). In each panel no significant hysteresis occurs within the contact region. Based on this observation we can assume the response of the cantilever to the sample surface within this region is dominated by elastic response, i.e. no significant plastic deformation takes place during our force curve measurements. For the plots of  $D_{pd}$ -versus- $\delta$  (left panels), the dashed curves show the fits to the power plus linear functions as described above, while solid curves show the fits to the Lennard-Jones (L-J) form. We find that it is possible to fit the data to the latter form for both approaching and retraction curves. After determination of the zero-tip-sample-force point, we employed the Pietrement-Troyon (P-T) algorithm for each  $D_{pd}$ -versus- $Z_{piezo}$  plot to determine the contact point and parameter  $\alpha$ , as shown in the right panel of each plot. The contact region of each force curve is well fit by this form.

The  $\alpha$  parameters resulting in the best P-T fit for different conditions samples respectively are summarized in table 2.2. These were used in calculation of the effective elastic modulus of the pristine and Ar-plasma exposed polystyrene films. We summarize these calculated effective elastic moduli in figure 2.15. The quoted uncertainties come from variations in the values determined from approaching and retraction curves, and from multiple measurements at different positions on the sample surfaces. Figure 2.15 shows a monotonic increase in the effective bilayer elastic modulus ( $E_{BL}$ ) with respect to the maximum Ar<sup>+</sup>-ion energies. However, it is apparent that the values for the etched samples are close to that for the pristine one. As we will show below, this shows that the effect of the effective modulus of the damaged layer is small, even though they are much stiffer than their underlying films. A major conclusion of what follows is that to pick out the slight difference in the effective elastic modulus for a bilayer film structure with a much thinner and stiffer top layer than the underlying, one needs to carry out both measurement and analysis using an extremely careful and systematic approach.



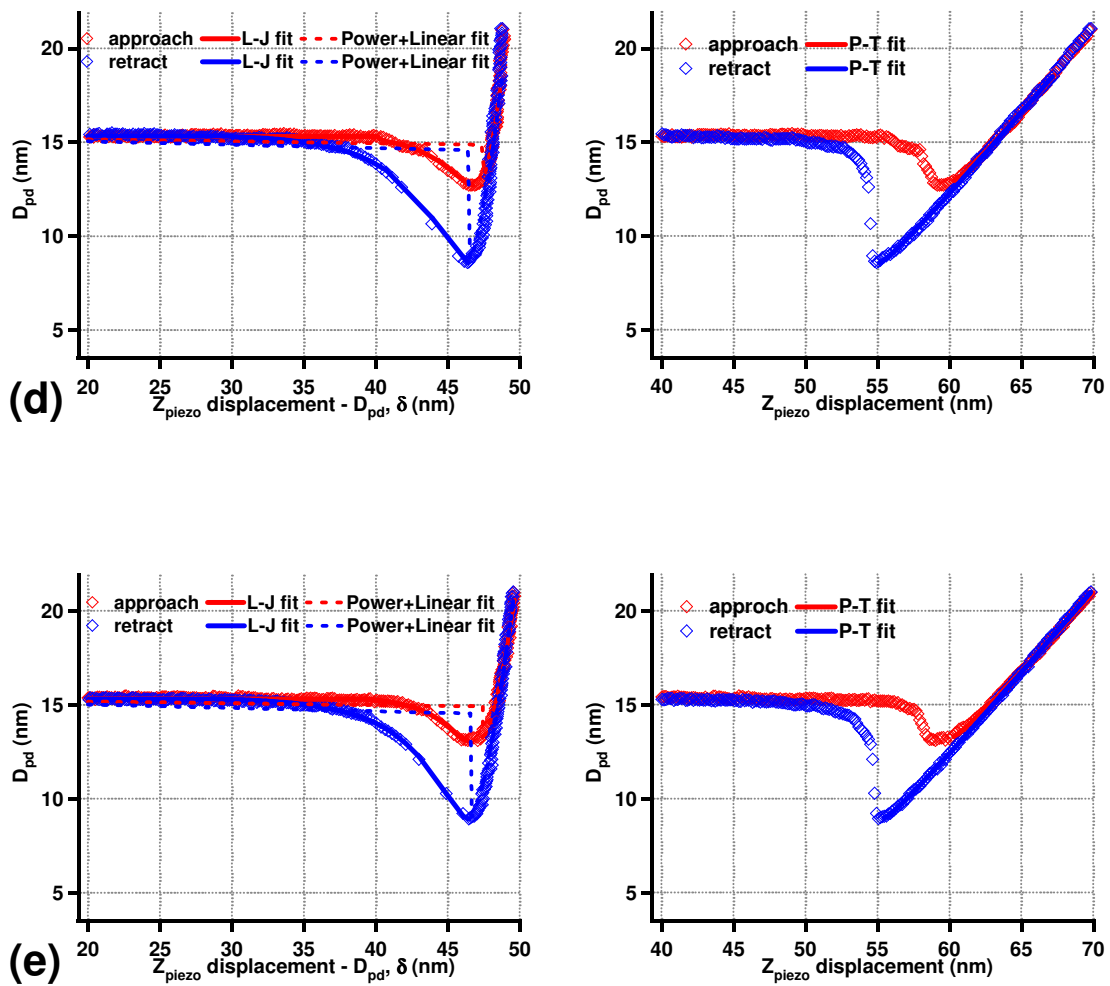


**Figure 2.14** AFM-measured force curves showing the cantilever deflection ( $D_{pd}$ ) as a function of the displacement of the cantilever's supported end ( $Z_{piezo}$ ), at right, and as a function of  $\delta = Z_{piezo} - D_{pd}$ , at left, for polystyrene samples treated by different  $\text{Ar}^+$  ion energies: (a) pristine, (b) 50 eV, (c) 75 eV, (d) 100 eV, and (e) 150 eV. The solid and dashed curves in each plot on the left are the minimum least-square-error fits to L-J forms, and power law+linear function, respectively; the solid curves on the right are minimum least-square-error fits to the P-T algorithm.

	unetched	Max. Ion Energy (eV)			
		50	75	100	150
<b>approach</b>	$0.9250 \pm 0.08$	$0.8300 \pm 0.03$	$0.8271 \pm 0.03$	$0.8129 \pm 0.05$	$0.7960 \pm 0.02$
<b>retraction</b>	$0.9310 \pm 0.05$	$0.8720 \pm 0.04$	$0.8700 \pm 0.02$	$0.8543 \pm 0.03$	$0.8340 \pm 0.06$

**Table 2.2** The  $\alpha$  parameters resulting in the best P-T fit for different conditioned polystyrene films. The errors come from the standard deviations by averaging of multiple force curves.

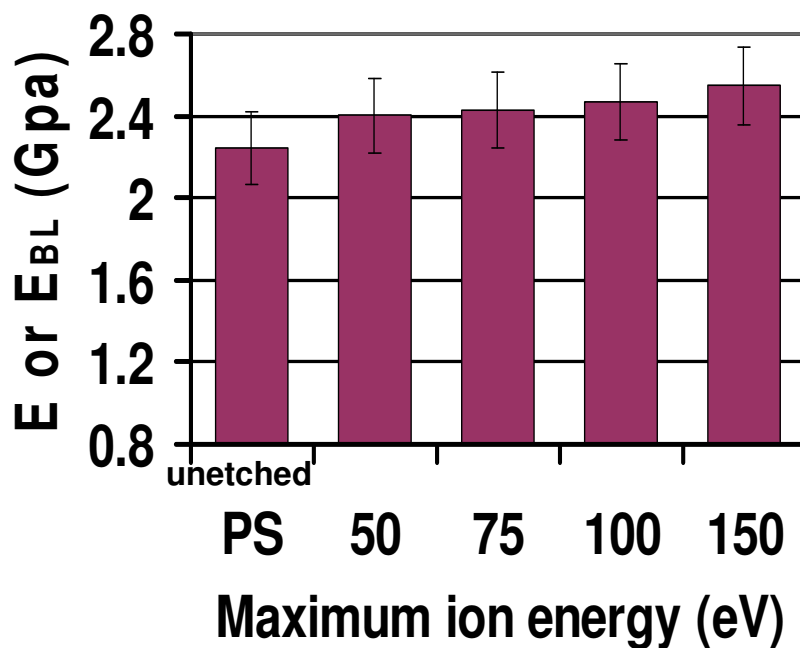


**Figure 2.15** Extracted elastic modulus of pristine polystyrene film and effective bilayer elastic moduli ( $E_{BL}$ ) for polystyrene films exposed to Ar plasma with different ion energies, versus  $\text{Ar}^+$  ion energy, as determined from measured AFM-force curves.

## 2.4 Summary

We summarize our results in this chapter as following.

First, by using height-height correlation function analysis, we found that for the Ar-plasma etched polystyrene samples, there is a pronounced dominant surface wavelength ( $\lambda$ ) on each sample etched with different Ar<sup>+</sup>-ion energies. The  $\lambda$  and the measured RMS roughness were both found to increase with increasing Ar<sup>+</sup>-ion energy, which qualitatively agrees with what could be visually observed from the AMF topography images.

Second, we described a reliable and reproducible quantitative analysis of the effective modulus of unetched and plasma-etched polystyrene thin films using AFM force curves measured in a controlled atmosphere using spherical AFM probes with well-known tip radii. We described a systematic procedure of stepwise algorithm based on an intermediate adhesive contact model (i.e. MD model) in treating our AFM measured force curves, giving us the elastic modulus of the pristine polystyrene ( $E_{PS}$ ) within the reasonable range compared to literature values.

Third, we presented force curve measurements and data analysis results for Ar-plasma etched polystyrene thin films. We found that the effective bilayer elastic modulus ( $E_{BL}$ ) increases monotonically with increasing Ar<sup>+</sup>-ion energy imposed on the sample during plasma exposure. Comparison between the measured effective elastic modulus of the pristine polystyrene sample and those of the etched samples shows that the impact on the overall film stiffness with the introduction of the top ultrathin damaged layer is subtle.

## ***Chapter 3:***

### ***Extraction of Damaged Layer Elastic Modulus***

In the last chapter, we showed that the effective elastic modulus ( $E_{BL}$ ) of etched polystyrene films can be extracted based upon a model of the contact mechanics which includes adhesive forces. In this chapter, we consider how the elastic modulus of the ultrathin damaged layer can be extracted from the effective elastic modulus for the damaged layer plus underlying unmodified film, using a linear elasticity approach to describe the response of a model bilayer plus spherical probe system to an applied force in the absence of adhesion. I will discuss how the bilayer film's response to a loaded spherical probe in our simulation based on two simplifying assumptions for the film surface morphology: (1) the “flat surface approximation” and (2) the “corrugated surface approximation”. In the last, I will describe how we use our simulations along with the experimental results presented in the last chapter to test the validity of a buckling instability as the mechanism for roughening of polystyrene during exposure to an Ar plasma. We begin with a brief review of the underlying concepts.

### 3.1 Linear elasticity

The subject of linear elasticity<sup>3.1</sup> is concerned with the determination of the stress and displacements in an object as a result of an external applied load (e.g. mechanical or thermal), for those cases in which the object recovers its original state upon the removal of the load. The fundamental equations of linear elasticity consist of:

- (1) A generalization of Newton's second law, which is the equation of motion:

$$\vec{\nabla} \cdot \vec{\sigma} + \vec{F} = \rho \vec{\ddot{u}}, \quad (3.1)$$

- (2) The strain vs. displacement relation:

$$\vec{\epsilon} = \frac{1}{2} \left[ \vec{\nabla} \vec{u} + (\vec{\nabla} \vec{u})^T \right], \text{ and} \quad (3.2)$$

- (3) Hook's law which can be expressed as:

$$\vec{\sigma} = \vec{C} : \vec{\epsilon}, \quad (3.3)$$

where  $\vec{\sigma}$  is the stress tensor,  $\vec{\epsilon}$  is the infinitesimal strain tensor,  $\vec{u}$  is the displacement,  $\vec{C}$  is the stiffness tensor, and  $\vec{F}$  is the body force per volume.

Generally, the experiments which we are attempting to analyze are carried out in a quasistatic ("elastostatic") manner, so that the time derivatives of the

displacement ( $\vec{u}$ ) are close to zero, and the first of these equations can be written approximately as:

$$\vec{\nabla} \cdot \vec{\sigma} + \vec{F} \approx 0. \quad (3.4)$$

In addition, for isotropic materials, Hook's law can be written as:

$$\varepsilon_{ij} = \frac{1}{E} [\sigma_{ij} (1 + \nu) - \nu \delta_{ij} \sigma_{kk}], \quad (3.5)$$

where  $E$  is the bulk modulus,  $\nu$  is Poisson's ratio,  $\sigma_{kk} = \sigma_{11} + \sigma_{22} + \sigma_{33}$ , and  $\delta_{ij}$  is the Kronecker delta function, in Cartesian coordinates this gives:

$$\varepsilon_i = \frac{1}{E} [\sigma_i (1 + \nu) - \nu (\sigma_X + \sigma_Y + \sigma_Z)]. \quad (3.6)$$

### 3.2 Hertzian Theory

We next review the results of the theory developed by Hertz<sup>3.2</sup> for the case of a sphere loaded against an isotropic elastic infinite half slab in the absence of adhesion. Further assumptions in this theory are:

- (1) The strains are small so that all deformations are within elastic limit.
- (2) The area of contact is much smaller than the characteristic radius of each body in contact, i.e. each body can be considered as an elastic half-space.
- (3) The surfaces in contact are frictionless.
- (4) The surfaces are continuous and non-conforming.

Violation of any of the assumptions above will raise the complexity of the contact problem, hence classified as “non-Hertzian”.

In this case, the sphere and slab make contact over an area whose radius ( $a$ ), projected into the plane of the undeformed slab of

$$a = \left( \frac{RF}{E} \right)^{1/3}, \quad (3.7)$$

where  $R$  is the radius of the undeformed sphere,  $F$  is the loading force,  $E$  is the system moduli related to the elastic modulus and Poisson's ratios of the sphere and slab as following:

$$\frac{1}{E} = \frac{3}{4} \left( \frac{1 - \nu_{slb}^2}{E_{slb}} + \frac{1 - \nu_{sph}^2}{E_{sph}} \right), \quad (3.8)$$

where  $E_{sph}$  and  $E_{slb}$  are the modulus of the sphere and slab, and  $\nu_{slb}$  and  $\nu_{sph}$  are the Poisson ratios for the slab and sphere, respectively. The penetration ( $\delta$ ) of the apex of the sphere below the plane of the surface of the undeformed slab in the Hertzian model is:

$$\delta = \frac{a^2}{R} = \frac{F}{Ea}. \quad (3.9)$$

Combining equations 3.7 and 3.9 yields the Hertzian relation between the loading force ( $F$ ) and the penetration ( $\delta$ ),

$$F = \left( ER^{1/2} \right) \delta^{3/2}. \quad (3.10)$$

To go beyond this simple model, it is generally required to use a numerical approach. In the next section, we present the results of such an approach, based upon a Finite Element Method (FEM) solution of the equations of elastostatics (i.e. equations 3.1-3.3) for the case of interest in this thesis: that of a spherical probe loaded against an ultrathin stiff damaged layer on a film of finite thickness.

### **3.3 Simulation of penetration on unetched polystyrene**

In this section we describe the results of numerical simulations for the response of an unetched polystyrene film to a loaded spherical silica probe during the penetration as a function of applied load. We assume the Hertzian case, as described in section 3.2, in the elastostatic limit. We approximate the film surface is flat in this simplest model. A more advanced treatment, taking into account the fact that surface roughness on the spherical probe and the film affects the result of penetration when compared to that from two perfectly smooth surfaces will be described later. The geometry for this simulation is shown schematically in figure 3.1(a), for a spherical probe in point-contact with a film under zero applied load. Examples of the results are presented in figure 3.2(a) for loads of 19 nN and 38 nN. The colors represent the calculated local vertical displacements of volume elements within the tip and the polystyrene film. The film thickness of 400 nm was determined by ellipsometry<sup>3.3</sup>. The elastic modulus is determined for an AFM force curve measurement to be 2.24 GPa. (The detailed parameters and boundary conditions are presented in Appendix F). As expected, under the larger loading force, there is larger area of greater vertical displacement around the apex of the tip than the smaller one.

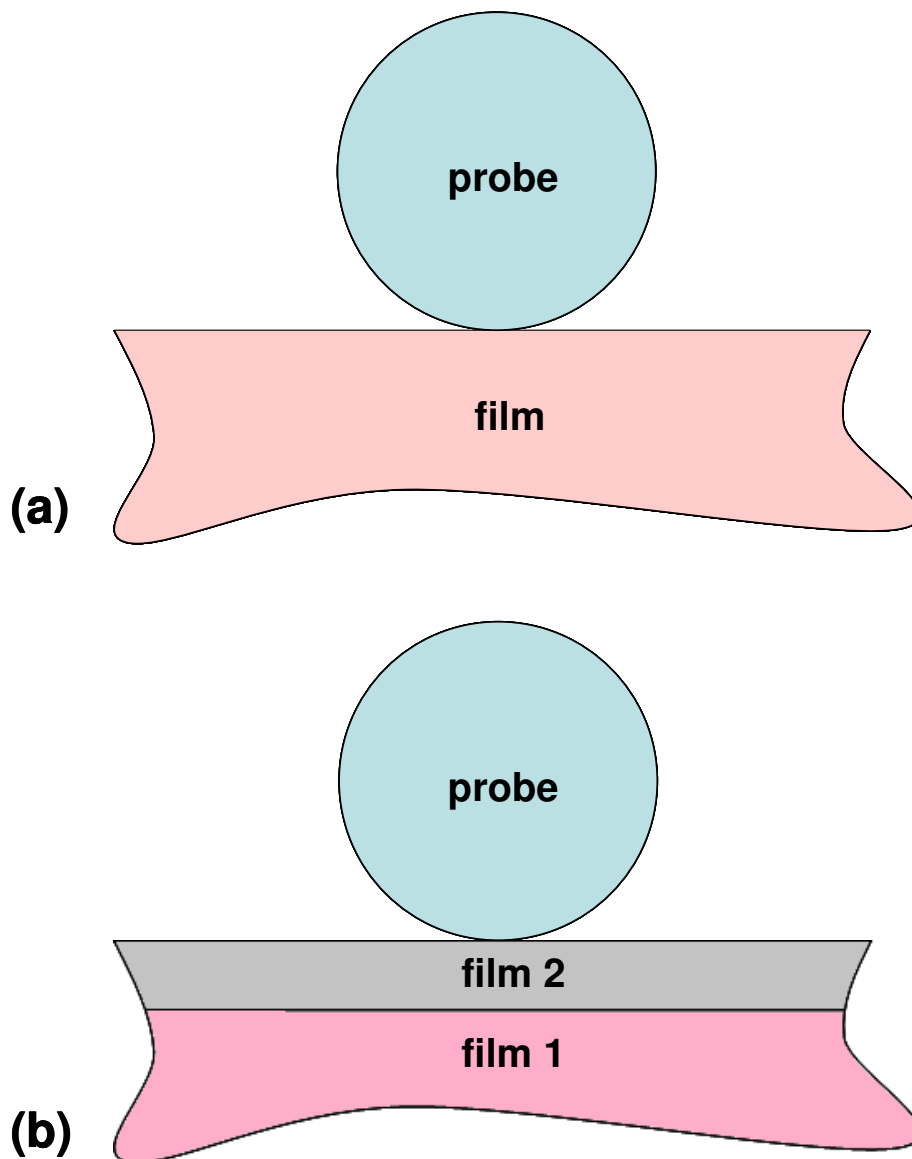


**Figure 3.1** Schematic illustration of a spherical probe in point-contact with two conformations of film under a zero applied load: (a) a single layer film, (b) a bilayer film.

The penetration ( $\delta$ ) is taken to be the vertical displacement at the position of the apex of the hemispherical tip. Figure 3.2(b) summarizes the value of penetration ( $\delta$ ) versus applied load ( $F$ ) for this case as open circles. The solid curve shows a fit of the force-vs.-penetration data to a  $3/2$ -power law dependence, as predicted by the Hertz model. From this we estimate the effective elastic modulus of the sphere plus slab,  $E_{tot}$ . The least mean-square-error fit for the set of data points on the plot in figure 3.2(b) is presented as the solid line in the same plot, and we find that the fit is quite good.

However, we find that the elastic modulus determined by this method for the unetched polystyrene ( $E_{PS}$ ) is approximately 8% larger than accepted value: 2.43 GPa, compared to 2.24 GPa. We note that the Hertzian model is for a semi-infinite slab, while our film has a finite thickness. To determine whether the finite film thickness causes the apparent increase in the simulated elastic modulus for the unetched film, we carried out a series of simulations for the penetration on different thick unetched films. We followed the geometry and boundary conditions shown in figure F.1(a) (presented in Appendix F) for these series of simulations. Values of the material properties (i.e. elastic modulus ( $E$ ), Poisson's ratio ( $\nu$ ), and density ( $\rho$ )) of the silica spherical probe and the polystyrene film used in the simulations are summarized in table 3.1.

	$E$ (GPa)	$\nu$	$\rho$ (g/cm <sup>3</sup> )
<b>Silica probe</b>	75 <sup>3.4</sup>	0.17 <sup>3.5</sup>	2.2 <sup>3.7</sup>
<b>Polystyrene</b>	2.24	0.33 <sup>3.3</sup>	1.05 <sup>3.6</sup>

**Table 3.1** Values of materials properties of the silica probe and polystyrene slab used in the simulations: elastic modulus ( $E$ ), Poisson's ratio ( $\nu$ ), and density ( $\rho$ ).

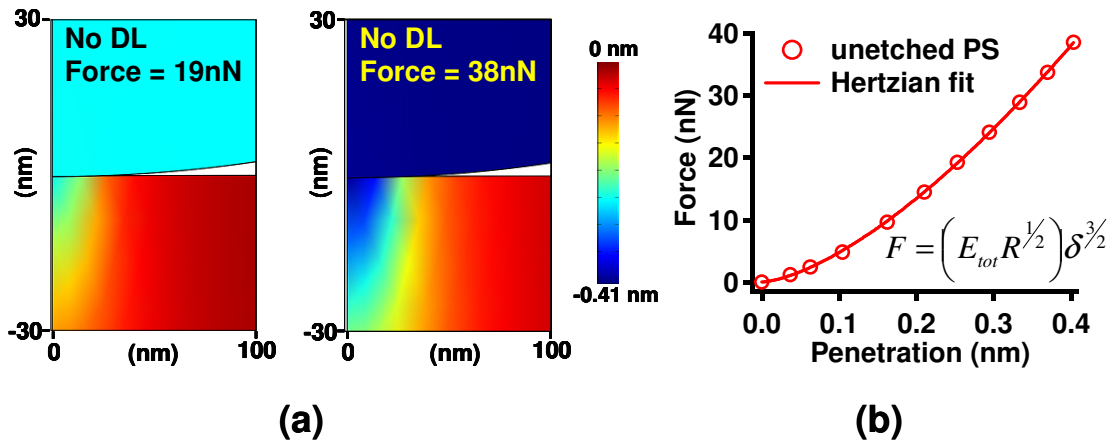


**Figure 3.2** Simulated local vertical displacement maps for a silica sphere loaded against an unetched polystyrene film whose thickness is 400 nm. (a) The vertical ( $z$ -directional) displacement maps when the applied load is 19 nN and 38 nN respectively. (b) Simulated load-penetration relation (open circle) and the fit to a 3/2-power law dependence (solid curve).

Figure 3.3 shows the simulated local vertical displacement of volume elements within the tip and the polystyrene film. From this figure we can visually determine an increase in penetration depth at the vicinity of the apex of the probe with increasing film thickness for the same applied load. Figure 3.4(a) summarizes the simulated penetration depth at the probe's apex position as a function of applied load, along with the corresponding least mean-square-error fits to a  $3/2$ -power law fit, for a range of different thickness of the polystyrene film. Figure 3.4(b) shows residual curves for each case. We see there is a systematic error in the fit to the form for the semi-infinite slab model, but that the thicker the film is, the better the fit. Finally we calculated the apparent elastic modulus of the film for each case from the best-fit pre-factor of the penetration term to the form of equation 3.10, followed by equation 3.8. The results are summarized in figure 3.5. We find that the apparent elastic modulus of the film approaches the actual value as the film thickness increases well beyond the radius of the sphere. This result is in agreement with recent calculations of the effect of a finite thickness of a compliant film on a rigid substrate by Sburlati<sup>3,4</sup>. This explains the  $\sim 8\%$  difference in the apparent, finite thickness film modulus and the actual value which observed previously. With this result, we can anticipate that the simulated elastic modulus of the single layer film is the same as the input which is supposed to be the bulk value when the film being simulated is infinitely thick.

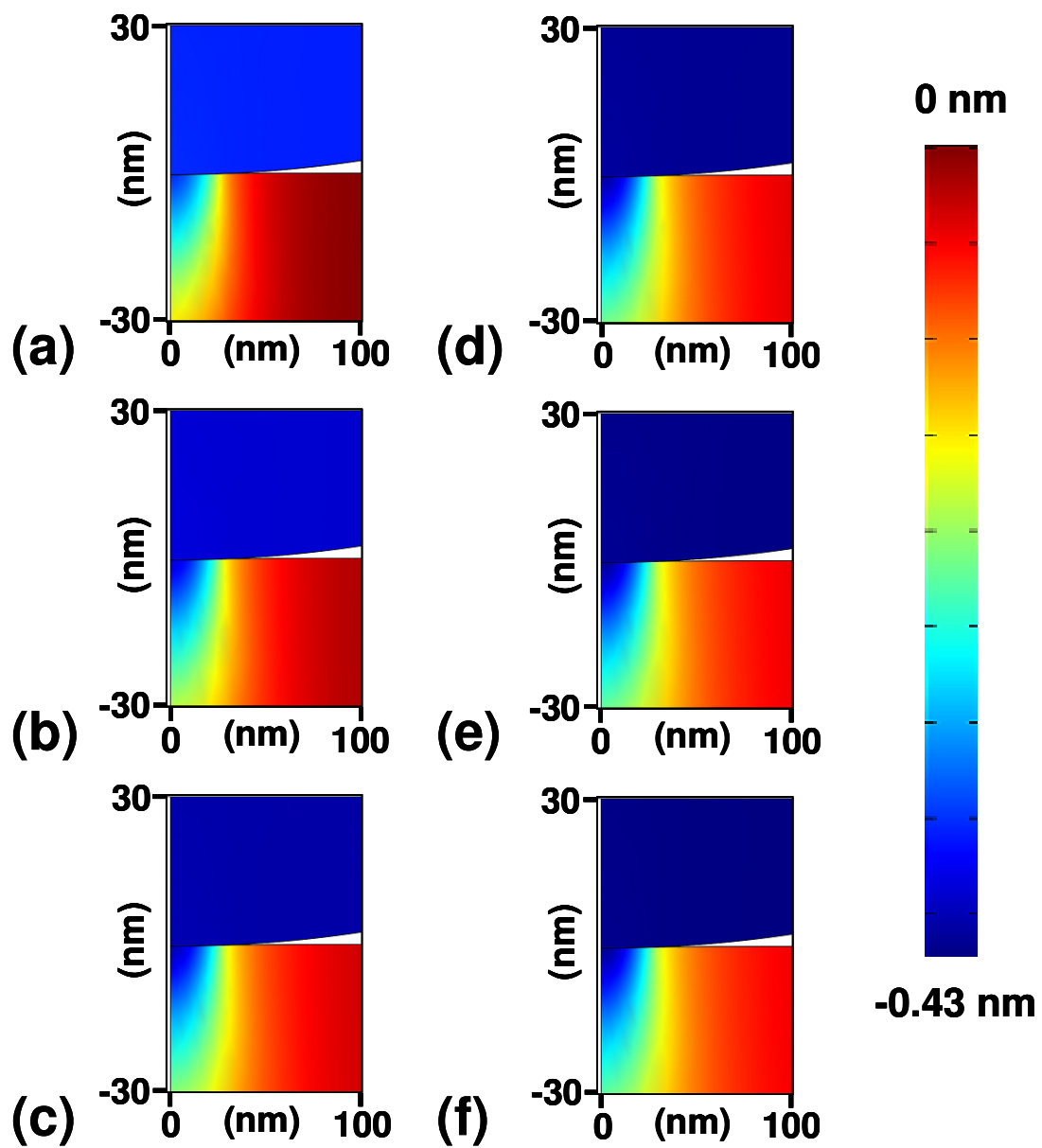


**Figure 3.3** Simulated vertical displacement maps of penetration on a unetched polystyrene film with different film thickness: (a) 100 nm; (b) 200 nm; (c) 400 nm; (d) 800 nm; (e) 1600 nm; (f) 3200 nm. The applied load is 38 nN for all cases.

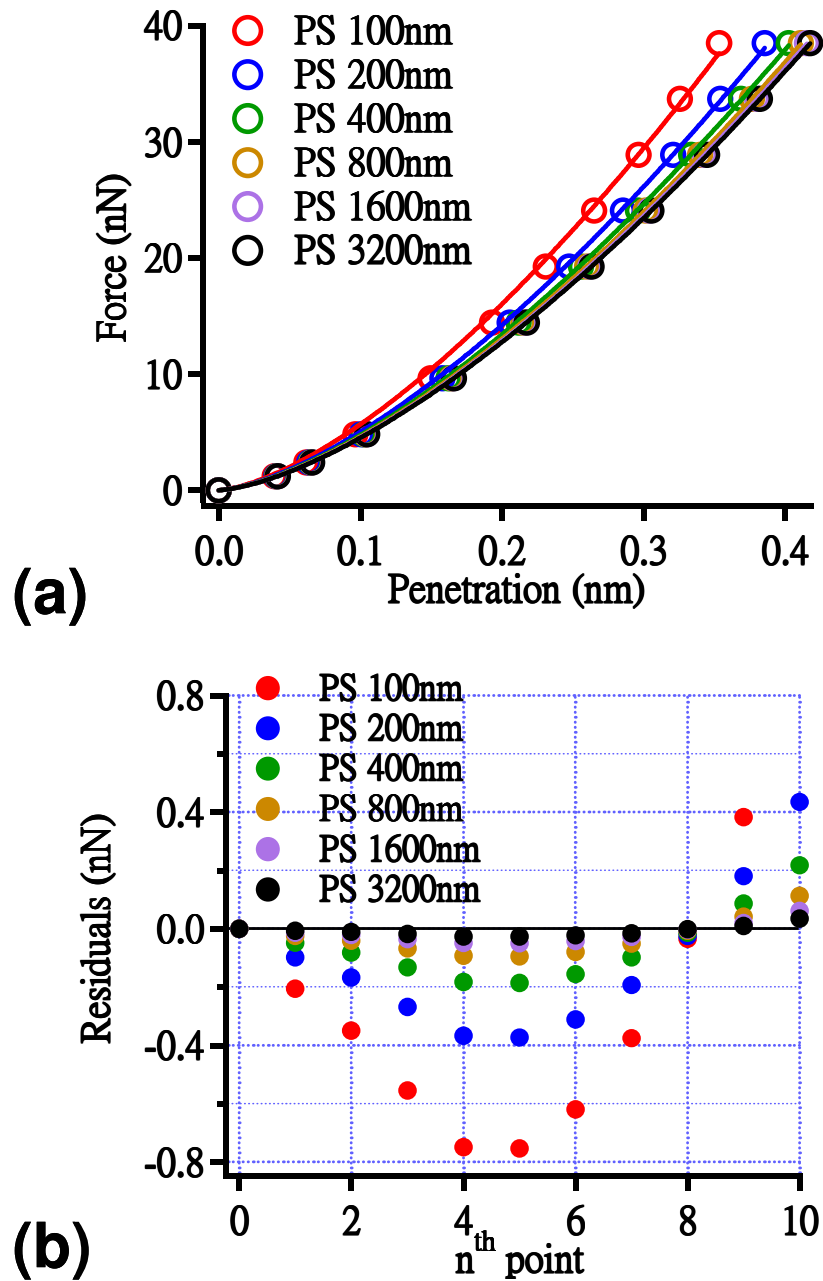


**Figure 3.4** (a) Simulated load-penetration relations (open circle) and the 3/2-power law fits (solid line) for different thickness polystyrene films; (b) residual curves for corresponding fits in (a).

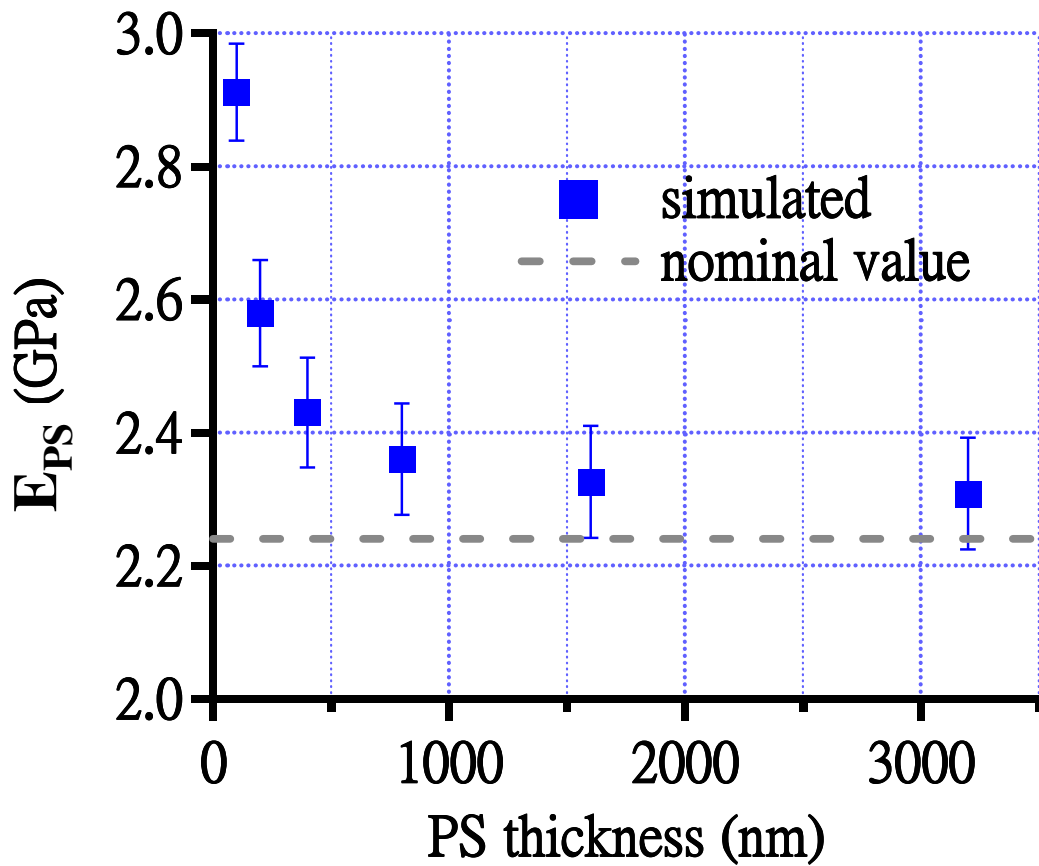


**Figure 3.5** Apparent elastic modulus ( $E_{PS}$ ) of a polystyrene thin film as a function of film thickness based upon Hertz formula for a sphere loaded against a semi-infinite slab (equation 3.10). The dashed line marks the value input in this series of simulation, which is 2.24GPa.

### **3.4 Simulation of penetration on etched polystyrene**

Now we turn our focus to how a model bilayer, made up of a thin damaged layer and underlying unmodified polystyrene film responds to contact with a spherical silica probe within a Hertzian model. The geometry is illustrated in figure 3.1(b). Below we consider the apparent modulus for initially flat layers. In section 3.4.2, I will present results of simulations for an initially corrugated film surface with a simple structure.

#### **3.4.1 Flat surface approximation**

Using finite element method, we carried out a series of simulations of the elastostatic response of bilayer structures consisting of model damaged layers of varying thickness on an underlying polystyrene film whose initial thickness is fixed at 400 nm. We use the geometry and boundary conditions illustrated in figure F.1(b) (presented in Appendix F), and we use a value of the elastic modulus of 2.24 GPa for the unmodified polystyrene film. Figures 3.6 and 3.7 show example results for a trial value of the damaged layer elastic modulus equal to 400 GPa, within the range determined indirectly<sup>3.3</sup>, and a density of 2.36 g/cm<sup>3</sup><sup>3.3</sup>.

The calculated local vertical displacement of volume elements within the probe and the film are shown in figure 3.6 for a load of 38 nN and a series of damaged layer thickness. We see that a thicker damaged layer results in smaller vertical deflection beneath the probe apex, as expected from simple considerations. Figure 3.7 summarizes the simulated load-vs.-penetration plotted as open circles for the same set of damaged layer thicknesses. We see that thicker damaged layers result

in curves with larger curvature corresponding to stiffer bilayer films, again as expected. Fits to a 3/2-power law dependence are shown by the solid curves. The goodness of fit is increasingly poor as the damaged layer thickness increases from 1nm to 10 nm, but seems to saturate beyond this, as evidenced by the residual curves for each fit, presented in figure 3.8. To quantify the effect of the damaged layer thickness, we calculated the apparent effective bilayer elastic modulus ( $E_{BL}$ ) based upon these fits. This is plotted as a function of damaged layer thickness in figure 3.9. We see that  $E_{BL}$  increases monotonically with increasing thickness of the damaged layer, as expected.

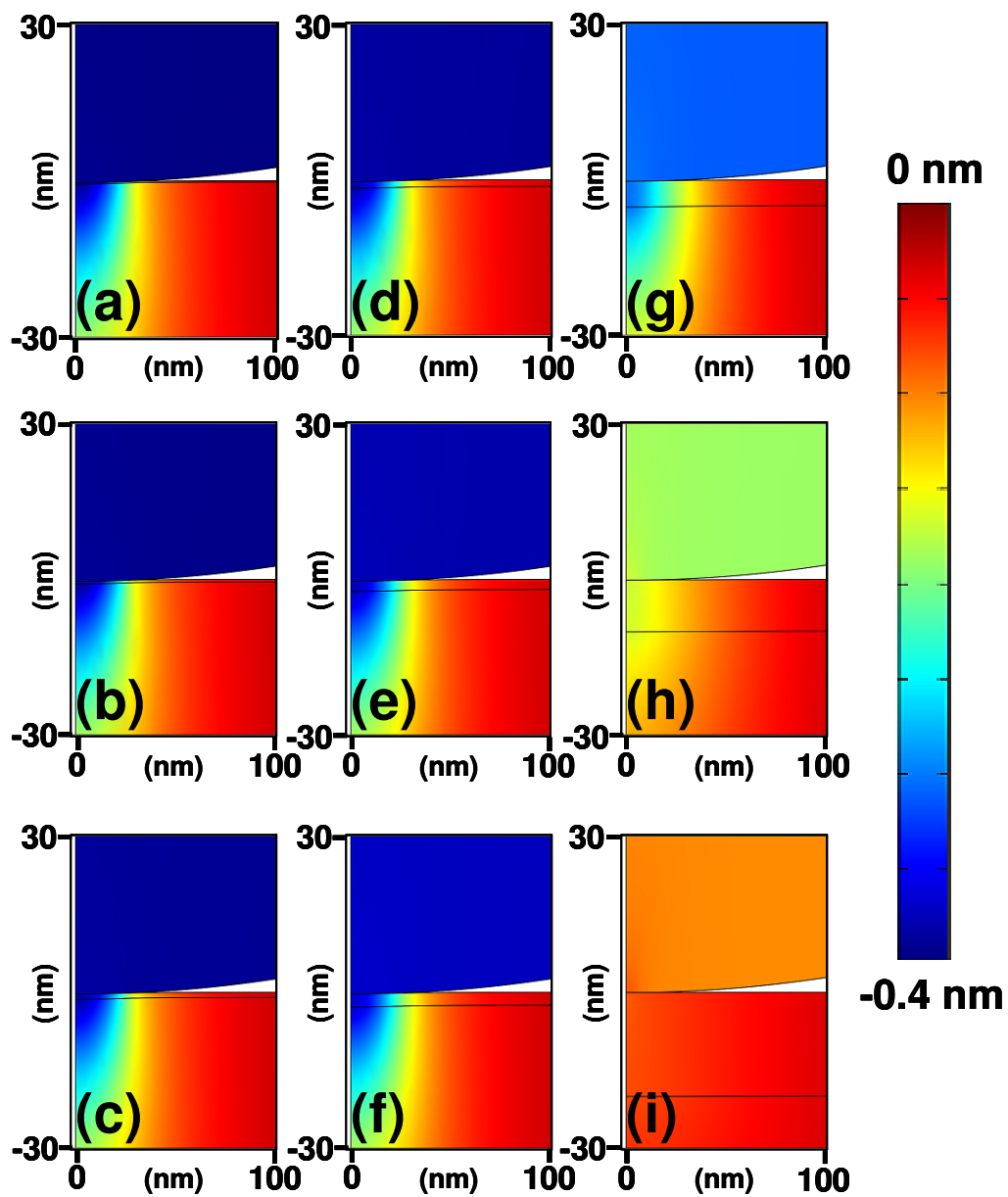


**Figure 3.6** Simulated vertical displacement maps of penetration on a damaged layer (DL)/polystyrene film with different DL thickness: (a) 0.25 nm; (b) 0.5 nm; (c) 1 nm; (d) 1.29 nm; (e) 1.98 nm; (f) 2.5 nm; (g) 5 nm; (h) 10 nm; (i) 20 nm. For all cases, the underlying polystyrene layer is 400 nm, and the applied load is 38 nN.

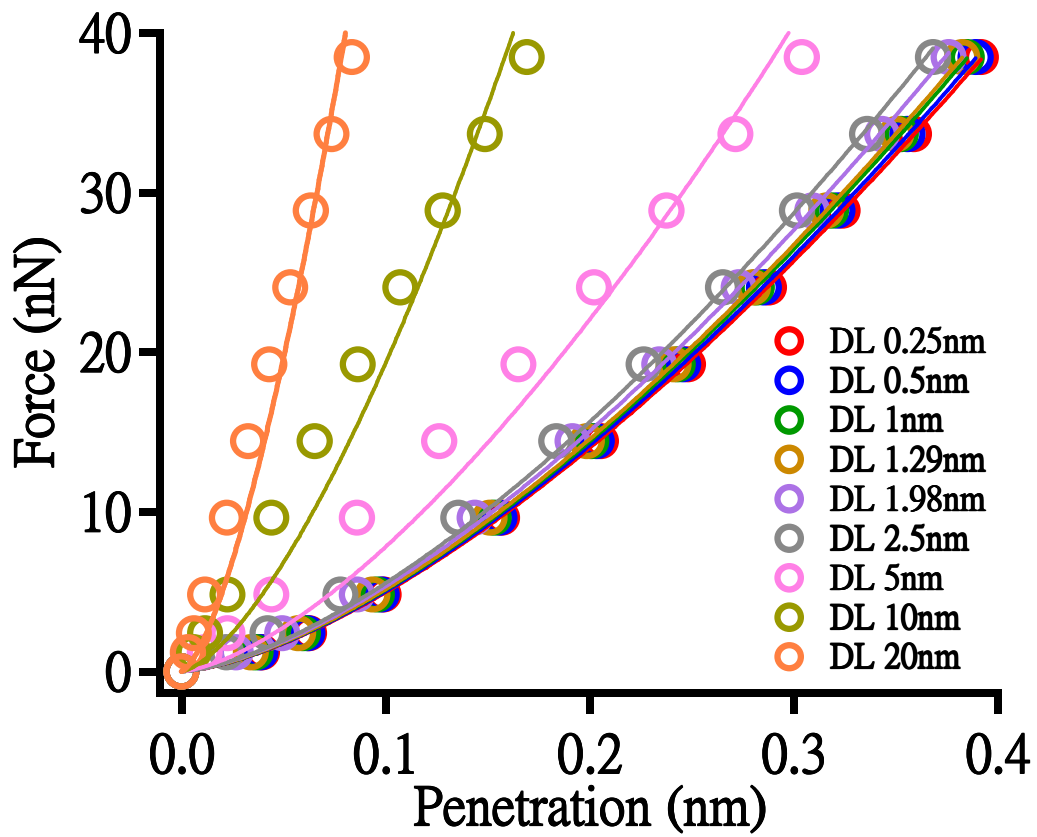


**Figure 3.7** The simulated load-penetration relations (open circle) and the 3/2-power law fits (solid line) for different thick damaged layers on top of a fixed thickness (400 nm) polystyrene film.

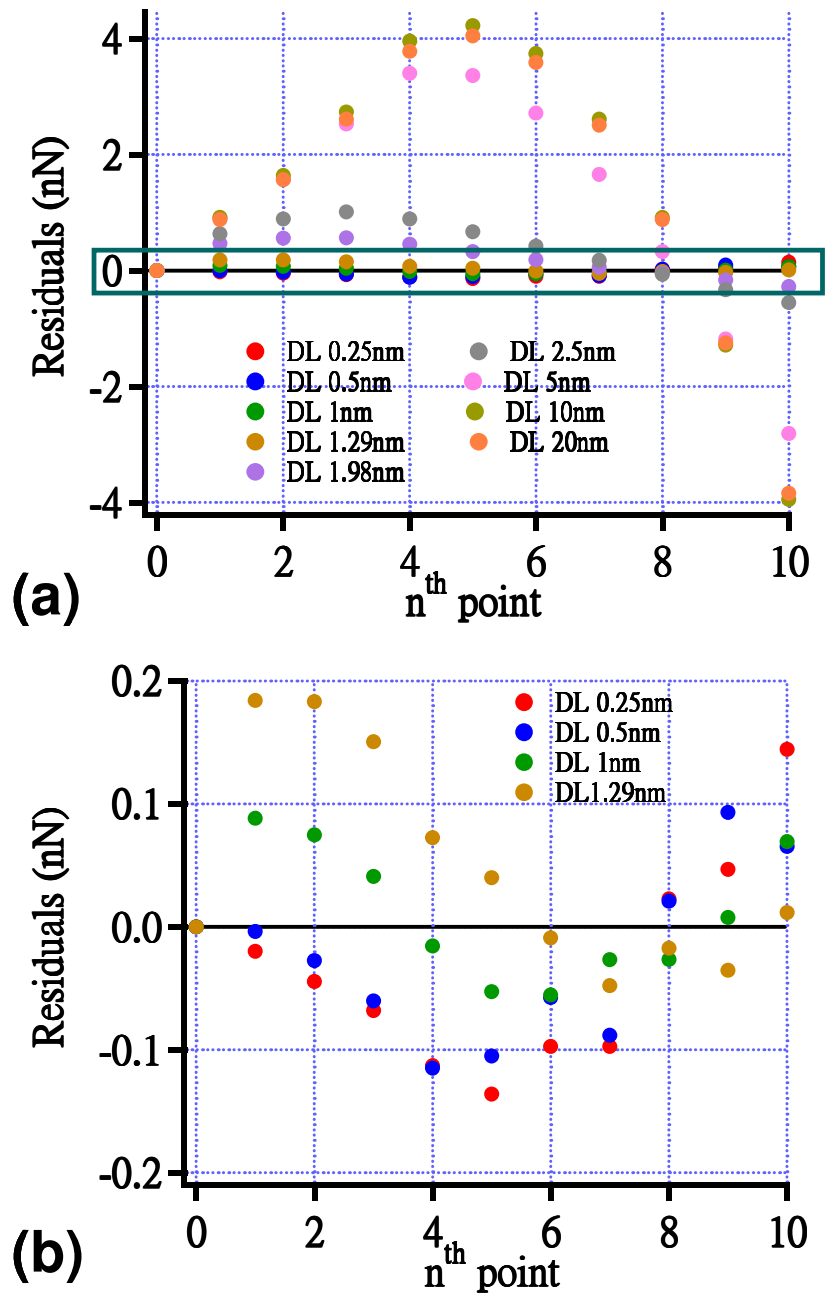


**Figure 3.8** (a) Residual curves for 3/2-power law fits of the simulated load-penetration data in figure 3.7; (b) zoomed-in residuals of the highlight in (a).

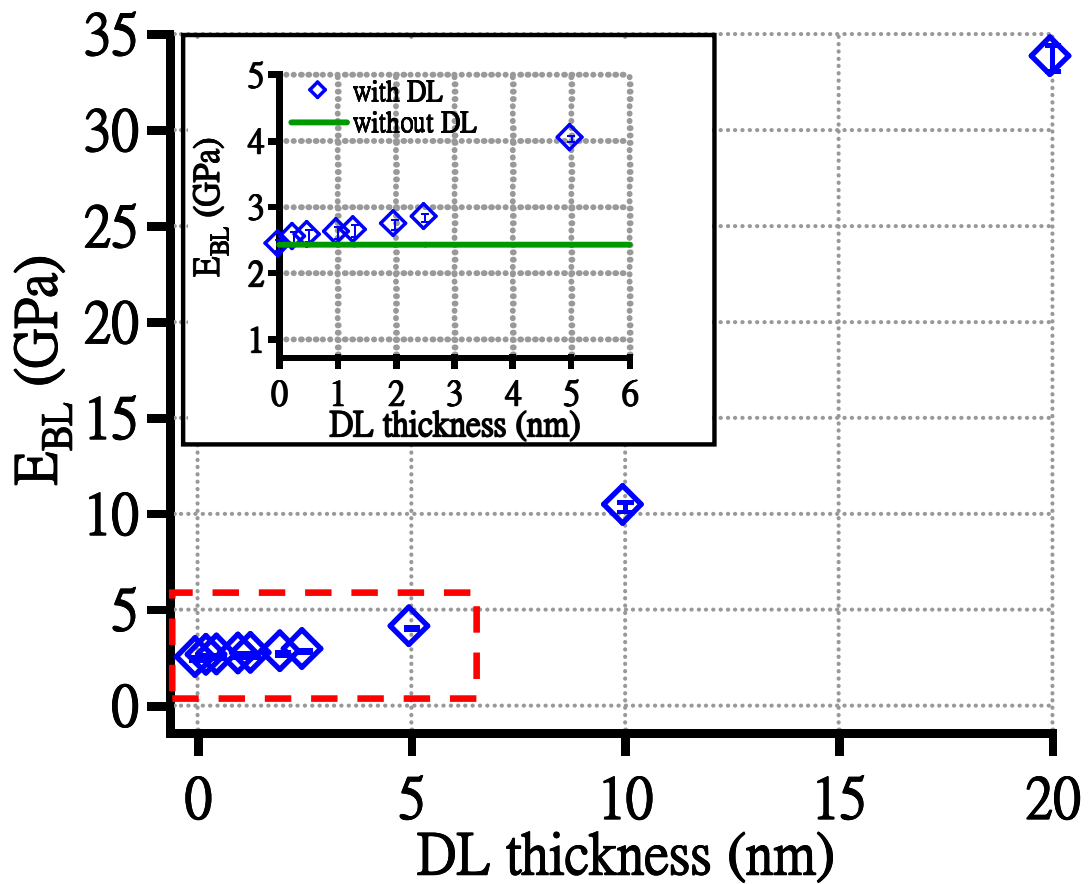


**Figure 3.9** Apparent effective elastic modulus ( $E_{BL}$ ) for a damaged layer/polystyrene bilayer structure as a function of damaged layer thickness. The values within the area highlighted by red dashed rectangle are replotted with a different vertical scale in the inset, with the green solid line indicating the simulated elastic modulus for a 400 nm thick unetched polystyrene film.

We next carried out simulations for bilayer films of the etched polystyrene terminated by damaged layers whose thicknesses were determined based on previous x-ray photoelectron spectroscopy (XPS) analysis subsequent to etching of polystyrene by Ar-plasma at different ion-energies. These thicknesses (energies) are 1.08 nm (50 eV), 1.29 nm (75 eV), 1.61 nm (100 eV), and 1.98 nm (150 eV).<sup>3.3</sup>

Figure 3.10 shows examples of the calculated local vertical displacement of volume elements for model damaged layers of these thicknesses, again under a load of 38 nN, and for a trial damaged layer elastic modulus ( $E_{DL}$ ) of 400 GPa. Summary plots of the simulated load-vs.-penetration plots are shown in figure 3.11. Once again the open circles are the simulated values, and the least mean-square-error fits of these simulated data points to a 3/2-power law are presented as solid curves. The apparent effective elastic modulus ( $E_{BL}$ ) extracted from the pre-factor of best fits for the four cases are 2.61, 2.64, 2.68, and 2.73 GPa in the sequence of the thickness of the damaged layers. We note that in spite of the very large trial damaged-layer modulus, that the simulated effective bilayer moduli are very close to that of the unetched polystyrene (2.43 GPa). Thus the effect of the damaged layer resulting from our etching conditions is rather subtle compared to the huge difference between the damaged layer elastic modulus ( $E_{DL}$ ) and the elastic modulus of the underlying unmodified polystyrene ( $E_{PS}$ ).

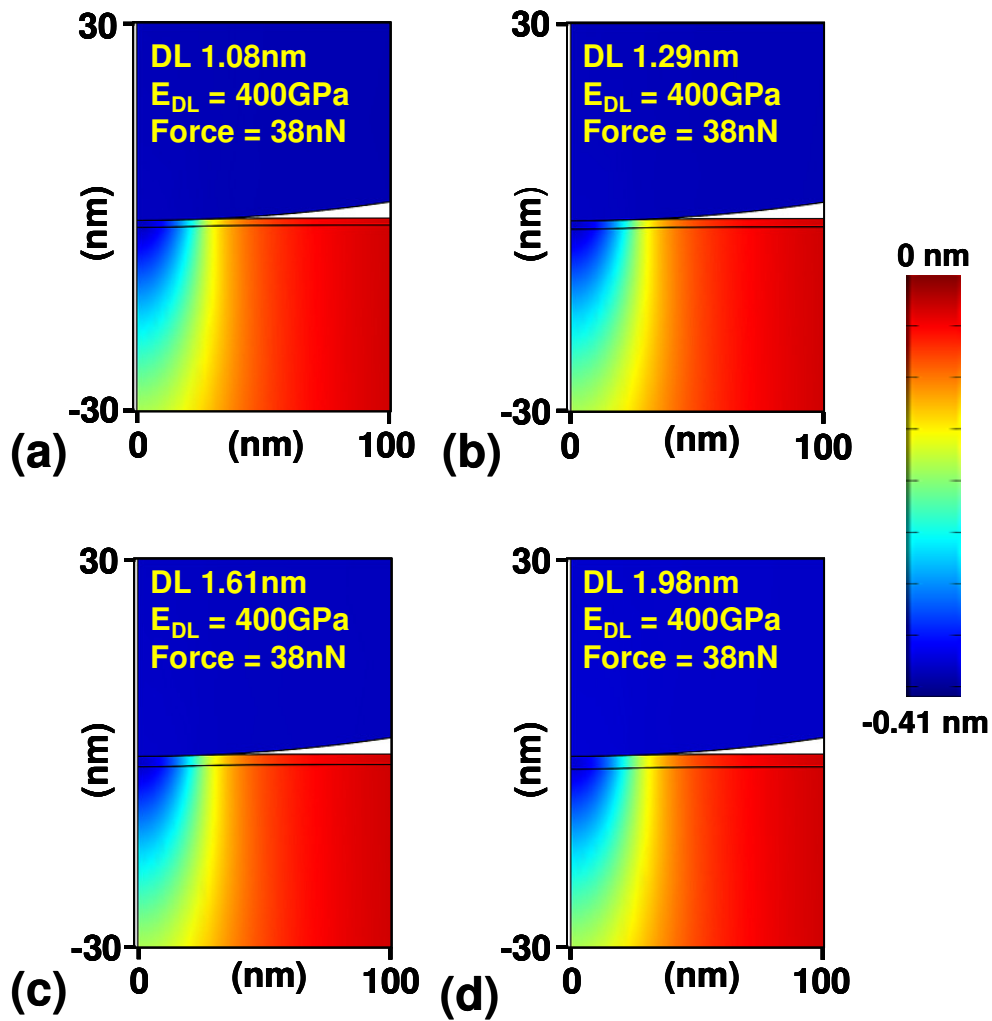


**Figure 3.10** Simulated vertical displacement maps for a load of 38 nN between a spherical silica probe and a bilayer film structure with damaged layer thicknesses of: (a) 1.08 nm, (b) 1.29 nm, (c) 1.61 nm, and (d) 1.98 nm.  $E_{DL}$  is 400 GPa and the underlying polystyrene thickness is 400 nm for all cases.

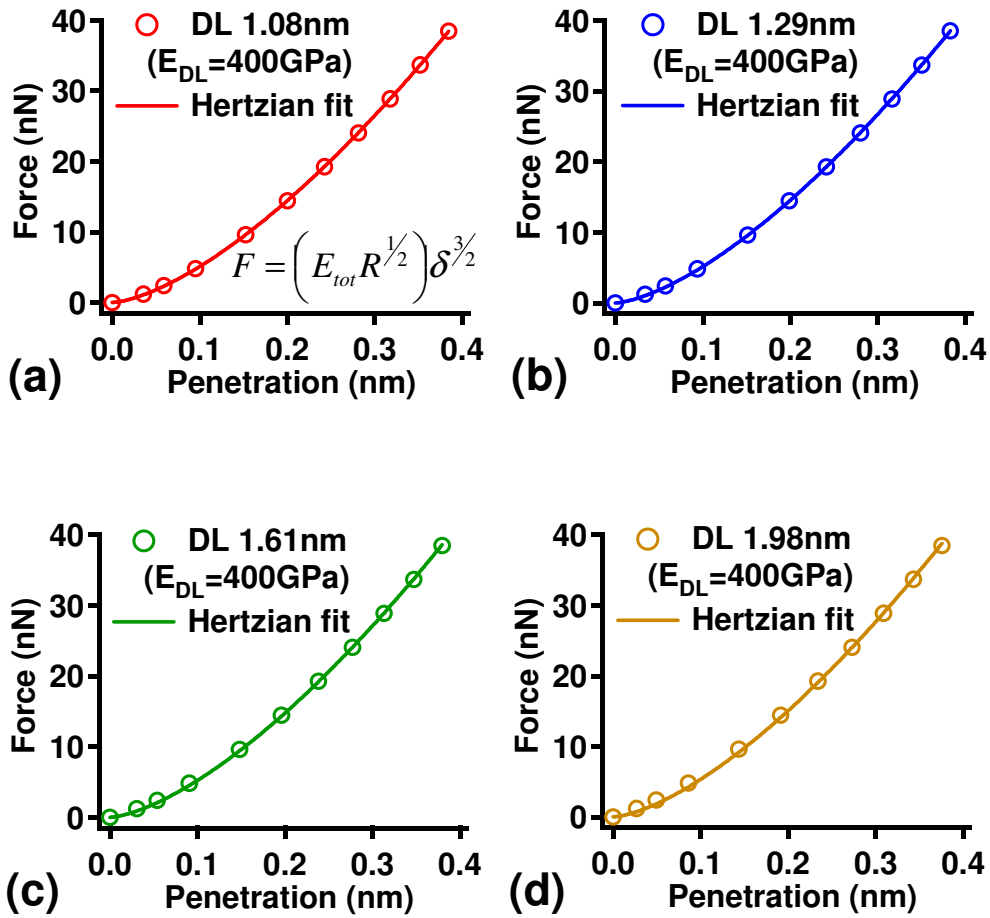


**Figure 3.11** Simulated Force-versus-Penetration curves for a bilayer film structure with damaged layer thicknesses of: (a) 1.08 nm, (b) 1.29 nm, (c) 1.61 nm, and (d) 1.98 nm. The open circles represent the simulated values, and the fits to a 3/2-power law are shown as the solid lines.  $E_{DL}$  is 400 GPa and the underlying polystyrene thickness is 400 nm for all cases.

We carried out additional simulations for model flat bilayer film structures for each of the top layer thicknesses given above, varying the damaged layer modulus over a range spanning 2 orders of magnitude. Plots of the resulting apparent effective bilayer film modulus ( $E_{BL}$ ), normalized to the elastic modulus of the polystyrene film (2.43 GPa) from the same simulation, versus damaged layer modulus ( $E_{DL}$ ) for each top layer thickness are plotted as solid curves in figure 3.12. The difference between the vertical and horizontal scales is notable.  $E_{DL}$  varies by over two orders of magnitude while the  $E_{BL}$  varies in only about 15%. This again reflects that only a small change in the effective bilayer elastic modulus results from a very large change in the damaged layer elastic modulus. A corollary of this is that relatively small errors in the effective bilayer modulus would generate large uncertainties in the derived damaged layer modulus. We conclude that good statistics, and careful systematic determination of the bilayer moduli, as described above, are required to achieve high precision in the determination of the damage layer moduli.

We next used interpolation within the calculated curves shown in figure 3.12 to determine the damaged layer modulus corresponding to each effective bilayer film values determined from our force curve analysis; these are shown by the open circles in each case. The so-determined effective bilayer elastic moduli ( $E_{BL}$ ) were normalized to that for the unetched polystyrene film (2.24 GPa). This normalization allows us to eliminate the difference in the resulting  $E_{BL}$  due to the finite thickness effect. In figure 3.13, we summarize the extracted damaged layer elastic moduli ( $E_{DL}$ ) as a function of ion energy. We find that indeed  $E_{DL}$  increases monotonically with the ion energy, as reported earlier, based upon our indirect determination<sup>3.3</sup>.

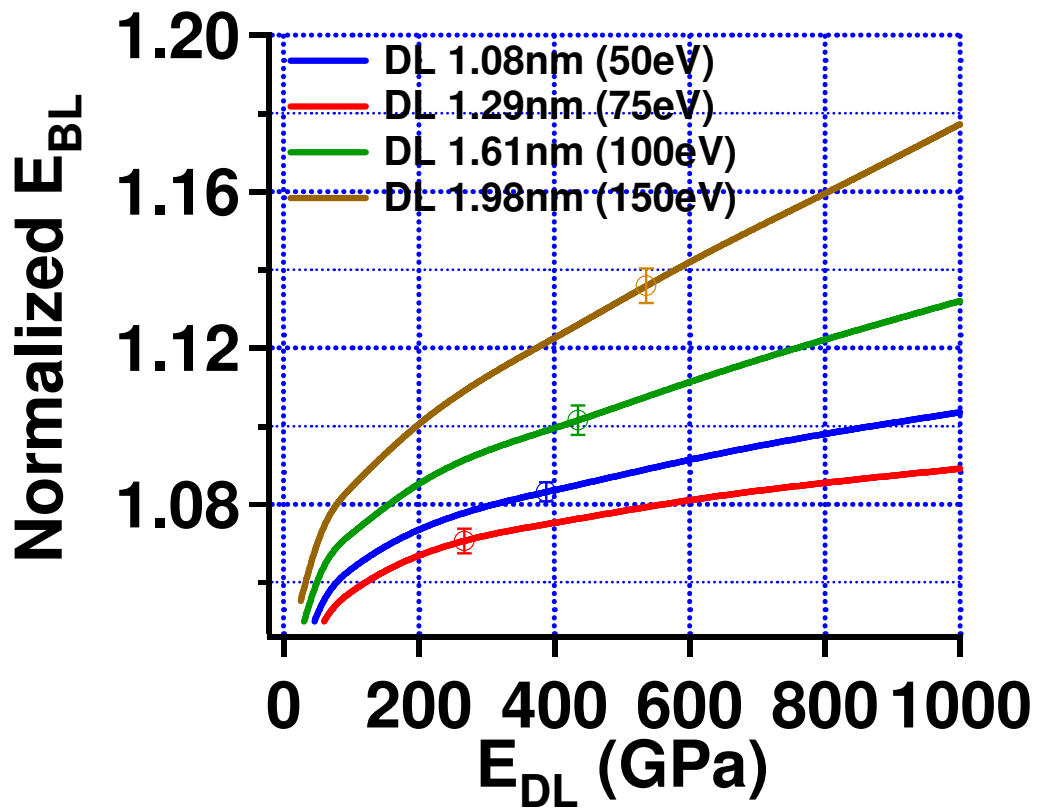


**Figure 3.12** Simulated effective bilayer elastic modulus ( $E_{BL}$ ) vs. damaged layer elastic modulus ( $E_{DL}$ ) for a 400 nm thick polystyrene layer, covered with thin model damaged layers. Each solid curve corresponds to a measured damaged layer thickness, as indicated. The open circles are interpolated from the AFM-measured effective bilayer moduli. All values of  $E_{BL}$  are normalized to the elastic modulus of unetched polystyrene film. The normalization factor was obtained by force curve measurement (2.24 GPa) and finite element simulation (2.43 GPa), for the measured, and calculated cases, respectively.

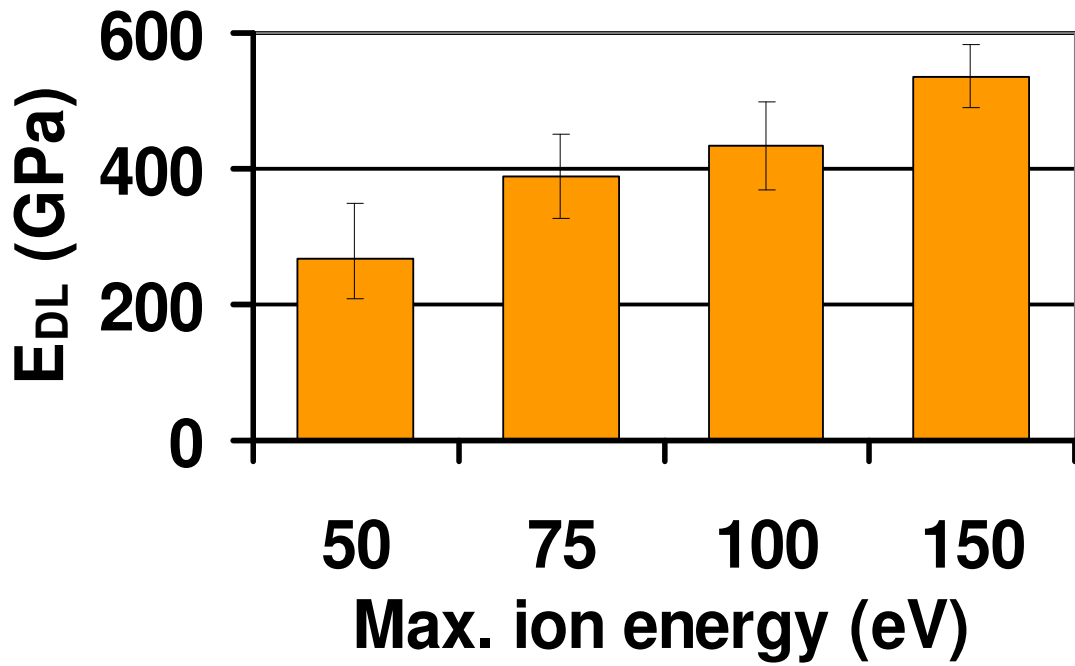


**Figure 3.13** Value of the elastic modulus of the damaged layer ( $E_{DL}$ ) determined by interpolation in figure 3.12 as a function of Ar-ion energy. The uncertainty for each value corresponds to the uncertainties of the measured effective bilayer elastic moduli ( $E_{BL}$ ) on each curve in figure 3.12.

We now use our experimental and numerical results to test the accuracy of the buckling instability model we proposed earlier<sup>3.3</sup> as a mechanism for roughening of our polystyrene film surfaces during exposure to an Ar-ion plasma. We use the elastic modulus of the damaged layers ( $E_{DL}$ ), derived above, to calculate the corresponding value of the ratio of the dominant wrinkle wavelength to the thickness of the damaged layer ( $\lambda/t$ ) using equation 1.1. For this calculation we used literature values for the remaining elastic constants, i.e.  $E_{PS}=2.24$  GPa,  $\nu_{PS}=0.33$ <sup>3.3</sup>, and  $\nu_{DL}=0.30$ <sup>3.3</sup>. We compare the resulting calculated ratios to the values determined by the dominant wrinkle wavelength ( $\lambda$ ) measured by AFM and the damaged layer thickness ( $t$ ) measured by XPS (see table 2.1). A comparison of the values of  $\lambda/t$  determined by the two different approaches is summarized in figure 3.14. We see that the form of the dependence on ion energy for these two is similar. However, there is an obvious systematic deviation between them. The values of  $\lambda/t$  determined by force curve measurement are consistently higher by ~30% than those determined using the buckling model; the difference is outside the uncertainties in the determinations.

We now consider what might cause this deviation. One possibility is our neglect of the effect of the surface corrugations in our numerical simulations. This might be expected to result in a more contact within the contact of a flat surface than a rough one. Qualitatively this might explain an over-estimation of the simulated effective bilayer elastic modulus ( $E_{BL}$ ), and thus a larger apparent damaged layer elastic modulus ( $E_{DL}$ ). In the next section, I will test this possibility, carrying out finite element method simulations for corrugated films.

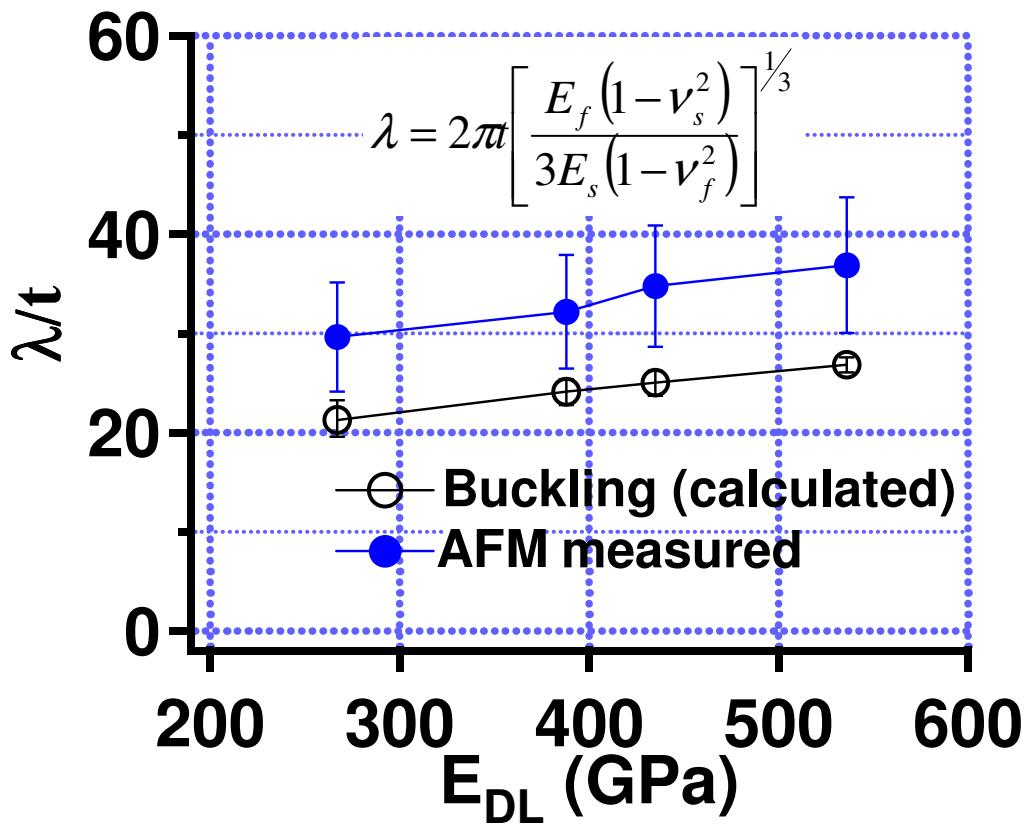


**Figure 3.14** The ratio of the dominant wrinkle wavelength ( $\lambda$ ) to the damaged layer's thickness ( $t$ ), plotted as a function of damaged layer's elastic modulus ( $E_{DL}$ ) determined by two methods. The results from calculation based on the buckling instability theory, with  $E_{DL}$  determined from force curve analysis are shown as open circles; the ratios of the measured dominant wavelength to the thickness determined from XPS are shown by open circles (see table 2.1).

### 3.4.2 Corrugated surface approximation

In last section, we demonstrated that with the flat surface assumption, the apparent damaged layer elastic modulus derived from the simulations results in good qualitative but not quantitative agreement in the values of  $\lambda/t$  predicted by buckling theory and those measured directly. To test whether the quantitative discrepancy might be due to film corrugation, we carried out simulations in which corrugation is included in an approximate manner. In this section, I discuss the results of these simulations.

In this investigation we approximate the corrugation as radially symmetric about the axis of the sphere perpendicular to the average surface plane, with a sinusoidal corrugation radially, i.e. at right angles to this axis. We use the dominant wrinkle wavelength ( $\lambda$ ) and amplitude determined from our AFM measurements and height-height correlation analysis in chapter 2. The use of 2D cylindrical coordinates (schematically shown in figure 3.15) reduces the memory required, and makes the calculations practical. In these simulations, the radial position of the apex of the tip with respect to the corrugated surface is important. This is because the initial contact area depends on this lateral position. A larger contact area results in stiffer contact in the initial stage than a small one. In our simulations we consider two extreme cases, with the apex of the spherical tip either centered above a crest or above a trough. These are illustrated schematically, including the meshes used in the FEM simulations, in figure 3.16.

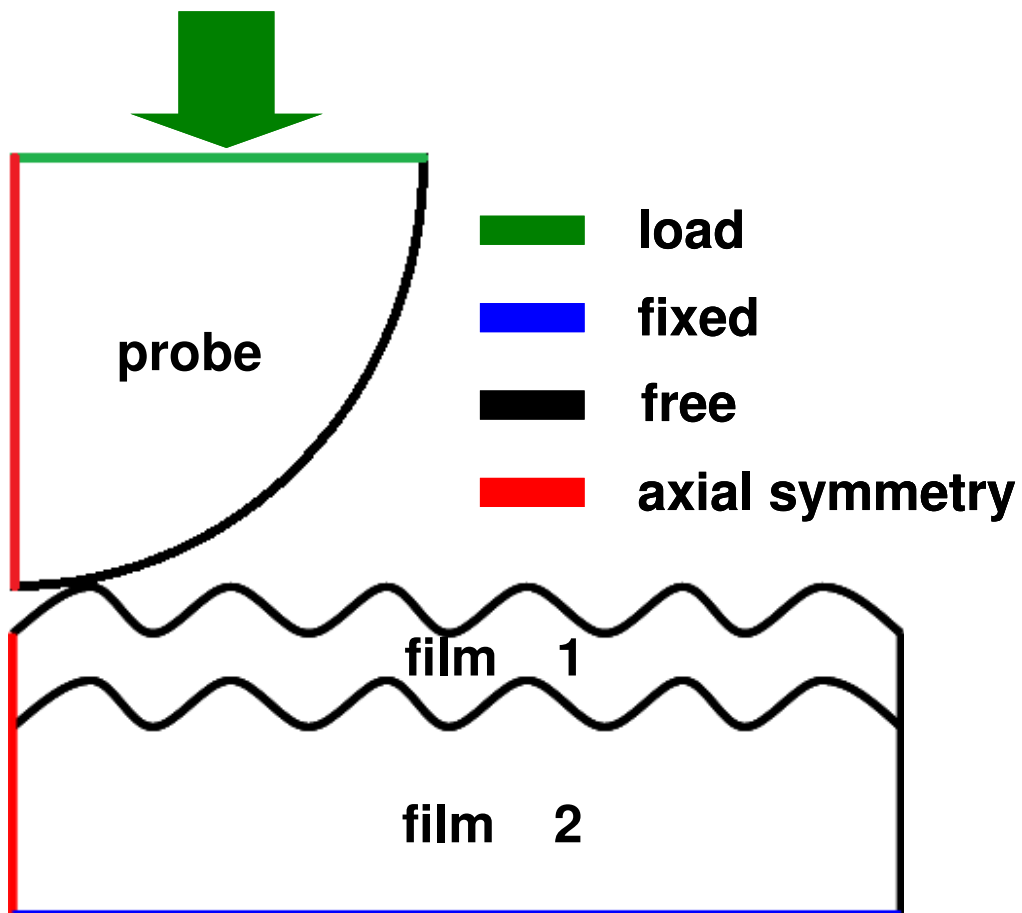


**Figure 3.15** Schematic geometry and the boundary conditions for simulation of local vertical strain for a spherical probe loaded against a corrugated surface. The corrugation is assumed axially symmetric (axis shown in red) and radially sinusoidal, with the wavelength and amplitude determined experimentally by AFM and height-height correlation analysis.

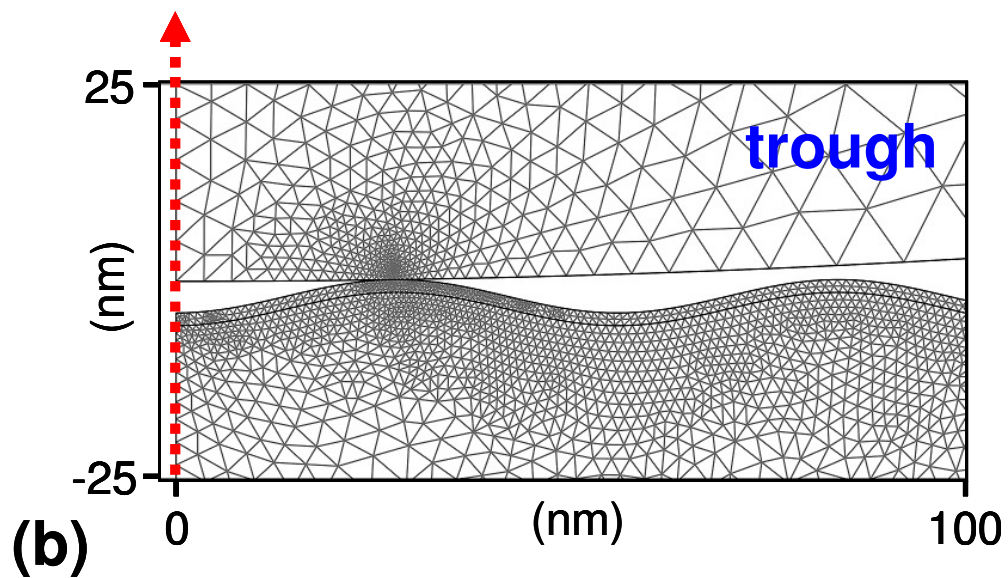
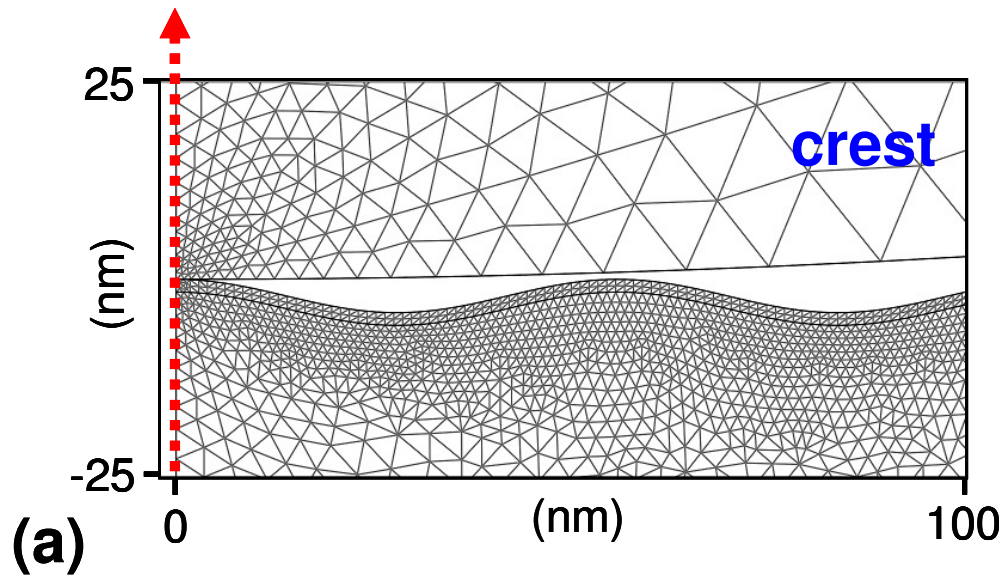
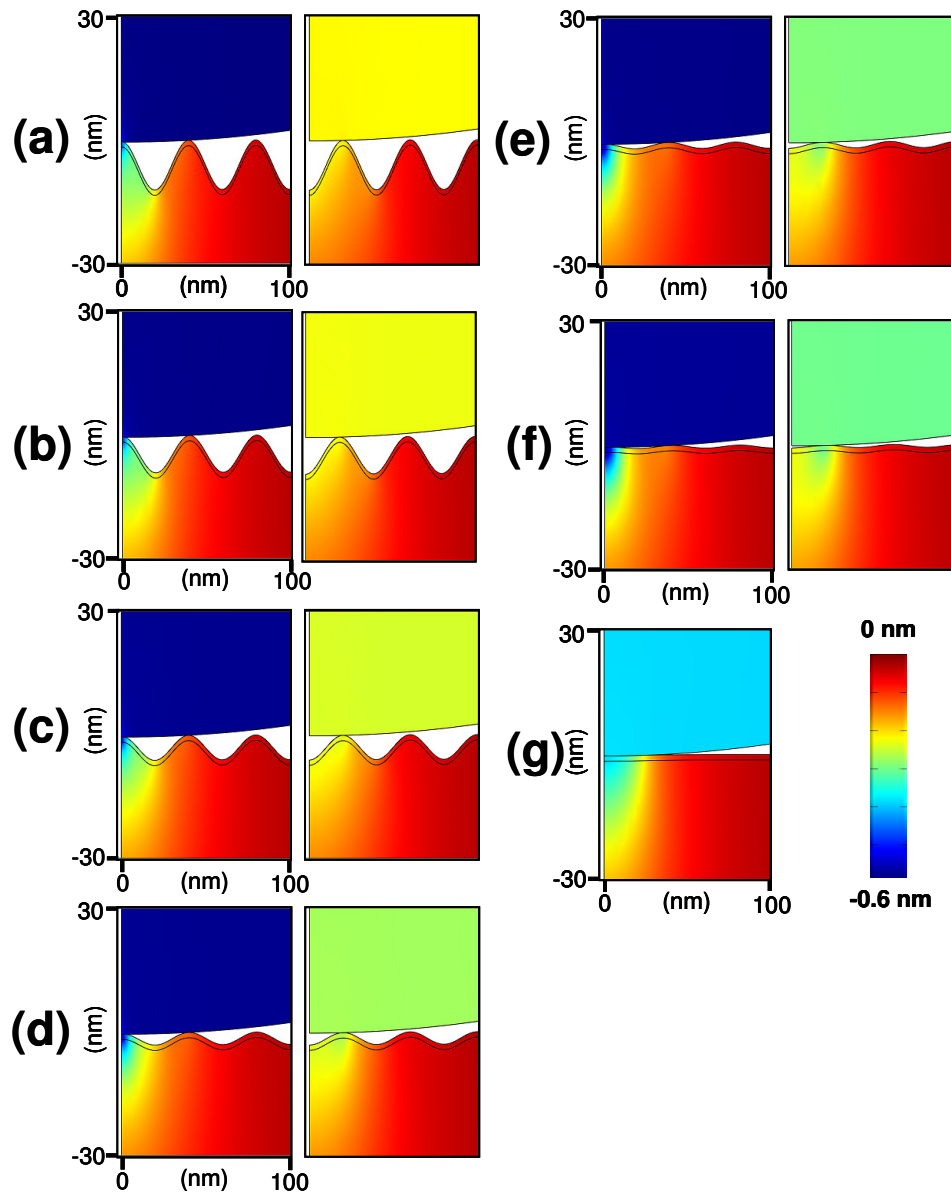


**Figure 3.16** Meshed geometries for FEM simulations of the contact systems for two extreme cases, with the apex of the probe centered above: (a) a crest, and (b) a trough. The red dashed arrows denote the 2D symmetry axis.

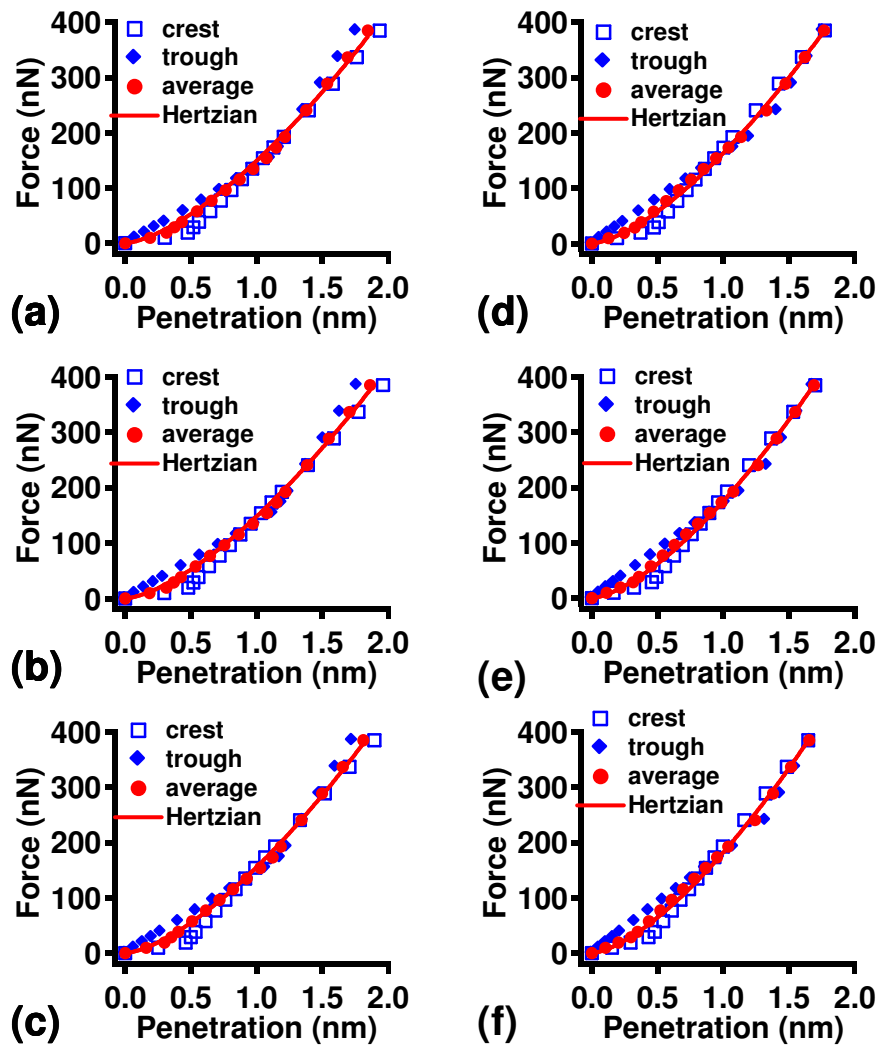
In this section we investigate how the apparent effective elastic modulus of the bilayer film ( $E_{BL}$ ) is affected by two parameters describing the corrugations: the amplitude and the wavelength. On the former case, we vary the amplitude of the sine corrugation keeping the other geometrical parameters and materials properties constant. For the example illustrated in figure 3.17: the damaged layer thickness is fixed at 1.29 nm, the damaged layer elastic modulus ( $E_{DL}$ ) at 400 GPa, the damaged layer density at  $2.36 \text{ g/cm}^3$ , the polystyrene thickness at 400 nm, the polystyrene elastic modulus ( $E_{PS}$ ) at 2.24 GPa, and the corrugation wavelength at 40 nm. For these parameters we simulated two extreme cases of contact with the apex of the probe centered above a crest or a trough of the corrugated surface. We analyze the simulated load-vs.-penetration curves for these two extremes.

Figure 3.17 shows examples of the calculated local vertical displacement of volume elements within the tip and the film for the two extreme cases, and for different corrugation amplitudes at a fixed wavelength of 40 nm under an applied load of 38 nN. The results show that the apex-above-trough cases show stiffer behavior than the apex-above-crest ones for all amplitudes. These results also show that the larger the amplitude the stiffer the film behaves. Experimentally, we used force curves determined from several positions across the surface in our determination of the effective bilayer modulus, taking an average. To compare with this we take a simple average of the simulated load vs. penetration curves for the two cases illustrated schematically in figure 3.16. The average load-penetration curves for the two extremes are found to be well fitted by a  $3/2$ -power law relation, shown in figure 3.18 and 3.19. Again the effective bilayer moduli ( $E_{BLS}$ ) were calculated from

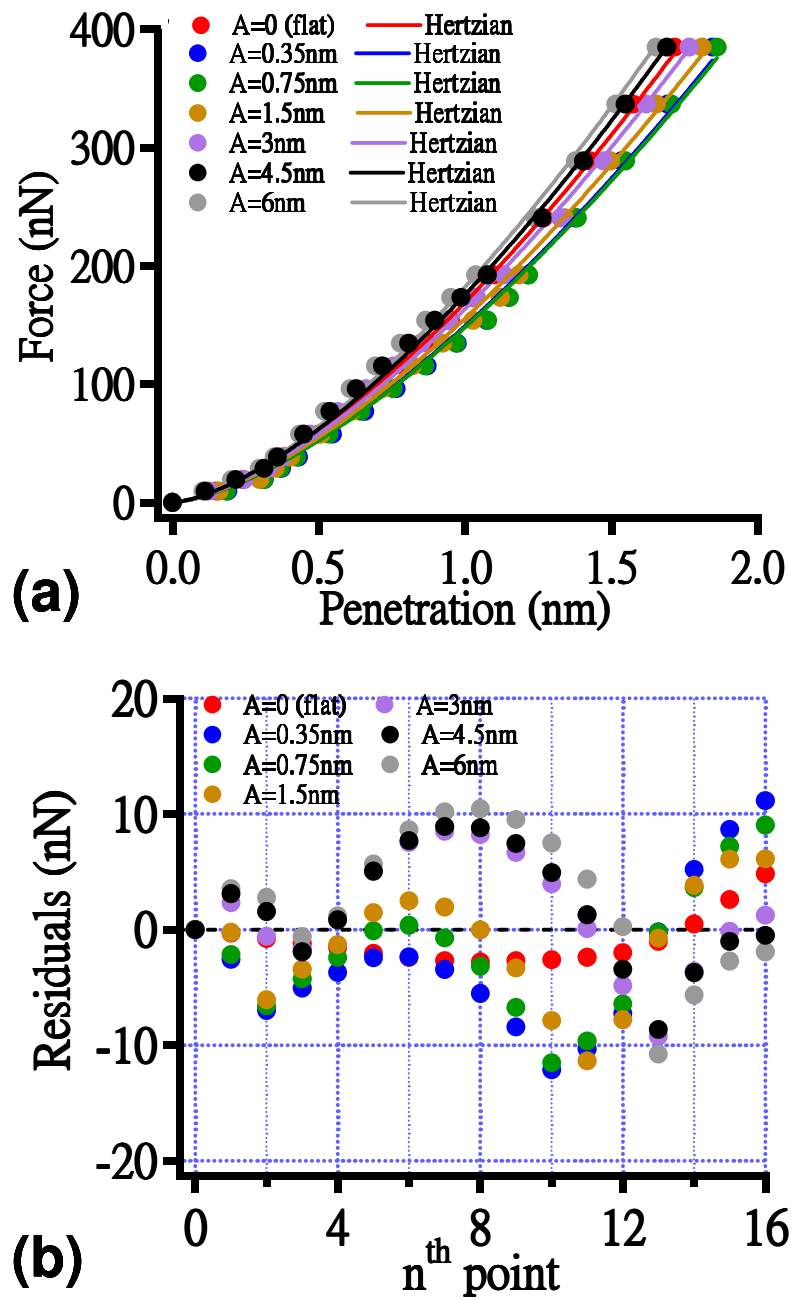
these fits. They are summarized versus amplitude in figure 3.20. We find an increasing trend of  $E_{BL}$  with increasing amplitude crossing through the flat film value at a certain point, ~4 nm. We interpret the initial drop from the zero-amplitude due to a sudden decrease of contact area between the probe and the surface, while the eventual increase is due to the increase in the effective damaged layer thickness projected along the vertical axis averaged over a sinusoidal period.



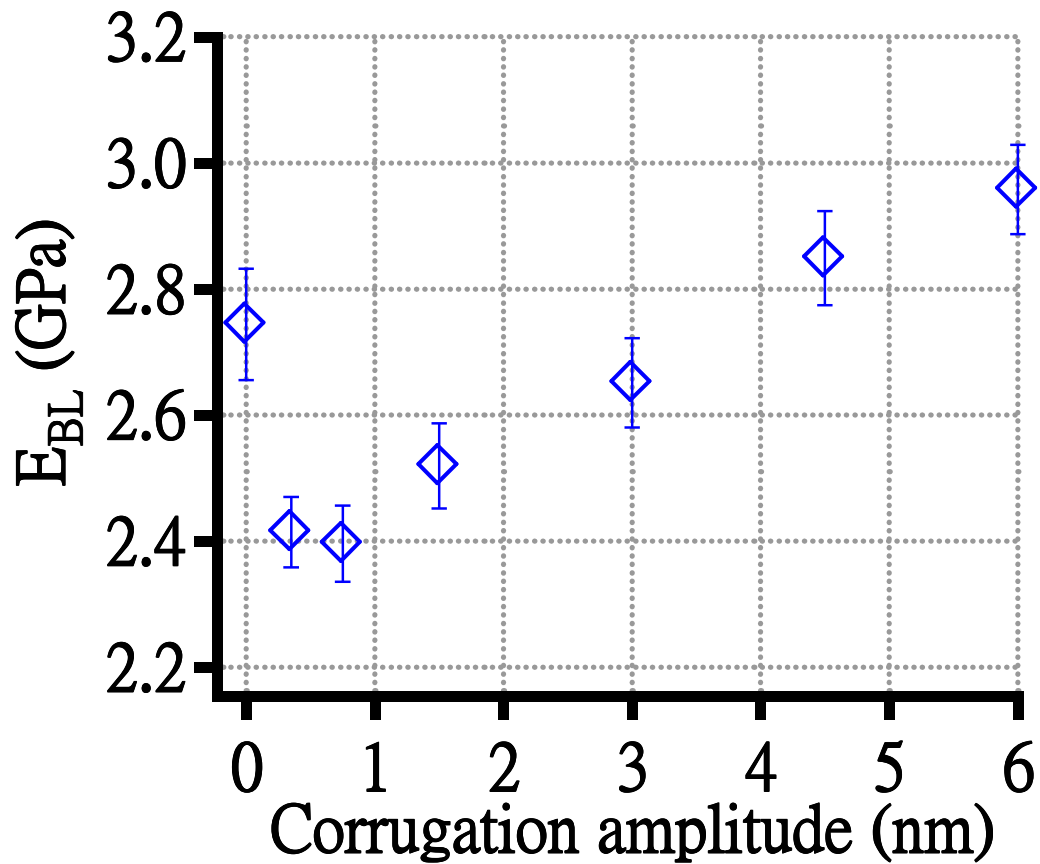
**Figure 3.17** FEM-simulated vertical displacement for the probe apex centered above a crest (left) or a trough (right) of a corrugated bilayer film, for corrugation amplitudes of: (a) 6 nm; (b) 4.5 nm; (c) 3 nm; (d) 1.5 nm; (e) 0.75 nm; (f) 0.35 nm; (g) 0 nm. The thickness of the damaged layer and the underlying polystyrene layer are 1.29 nm and 400 nm respectively, and the applied load is 38 nN.



**Figure 3.18** Summary of simulated load-penetration relations for a spherical probe loaded against cylindrically corrugated surfaces. In each case the variation for the sphere apex centered above a crest is shown by open squares, apex above a trough is shown by closed diamonds, and the average by close circles. The solid curves show best fits of the average to a  $3/2$ -power law. The individual panels are for different corrugation amplitudes: (a) 0.35 nm; (b) 0.75 nm; (c) 1.5 nm; (d) 3 nm; (e) 4.5 nm; (f) 6 nm.



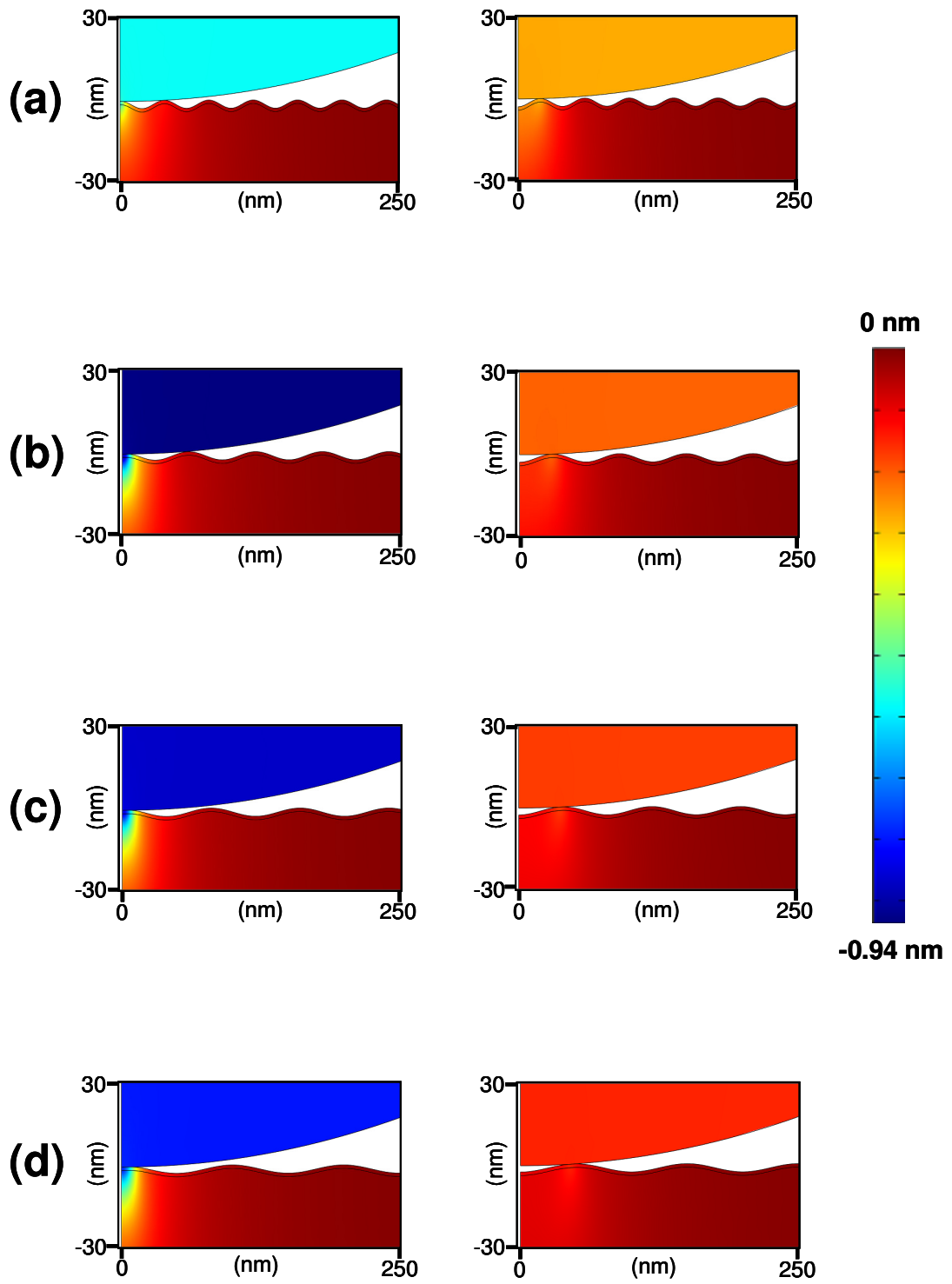
**Figure 3.19** (a) FEM-simulated average load-penetration curves and 3/2-power law fits for the example shown in figure 3.18; (b) residual curves for corresponding fits in (a).

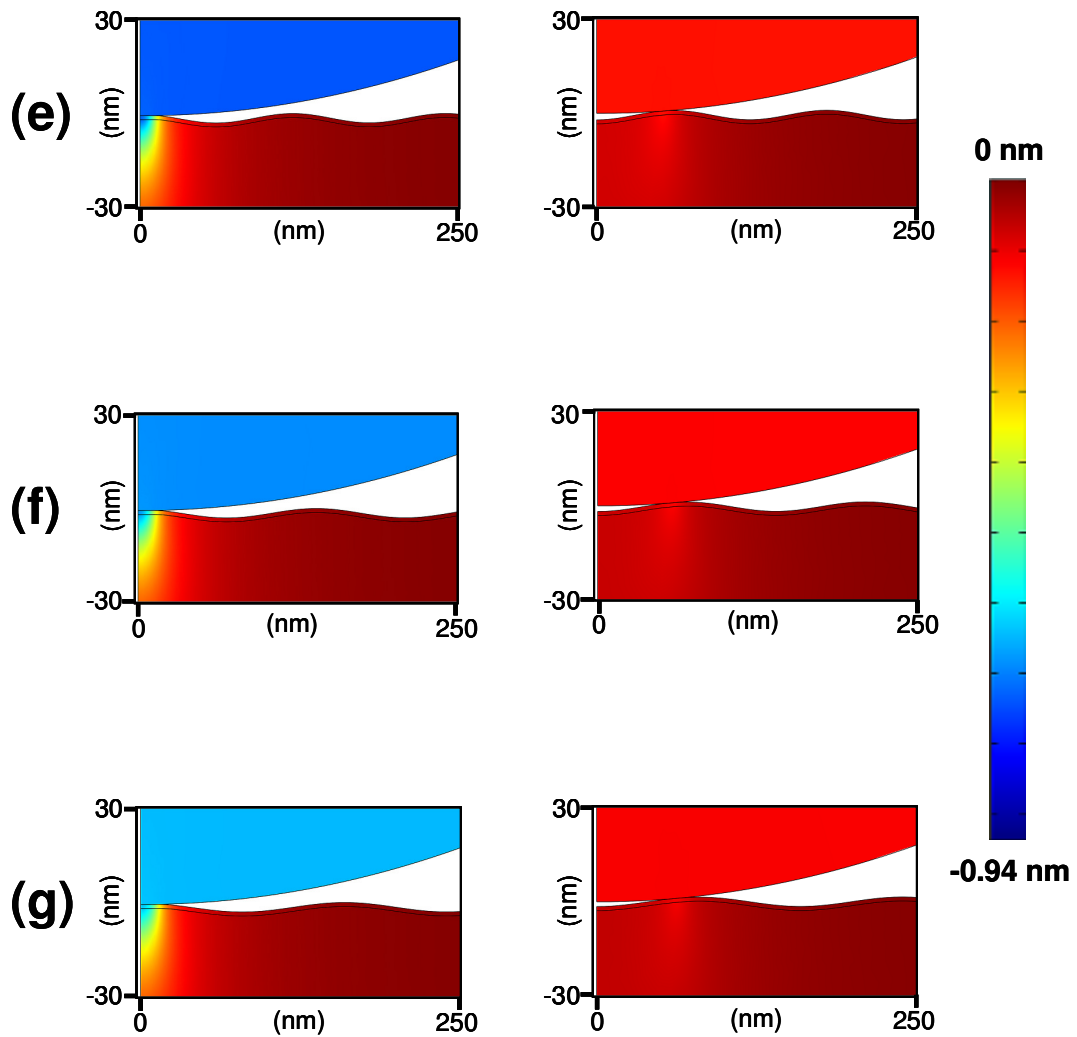


**Figure 3.20** Simulated average effective bilayer elastic modulus ( $E_{BL}$ ) for a corrugated bilayer film structure as a function of corrugation amplitude. The elastic modulus and thickness of the damaged layer used in the series of simulation are 400 GPa and 1.29 nm respectively, while the underlying polystyrene layer was fixed at 400nm thick. The wavelength is fixed at 40 nm for all cases.

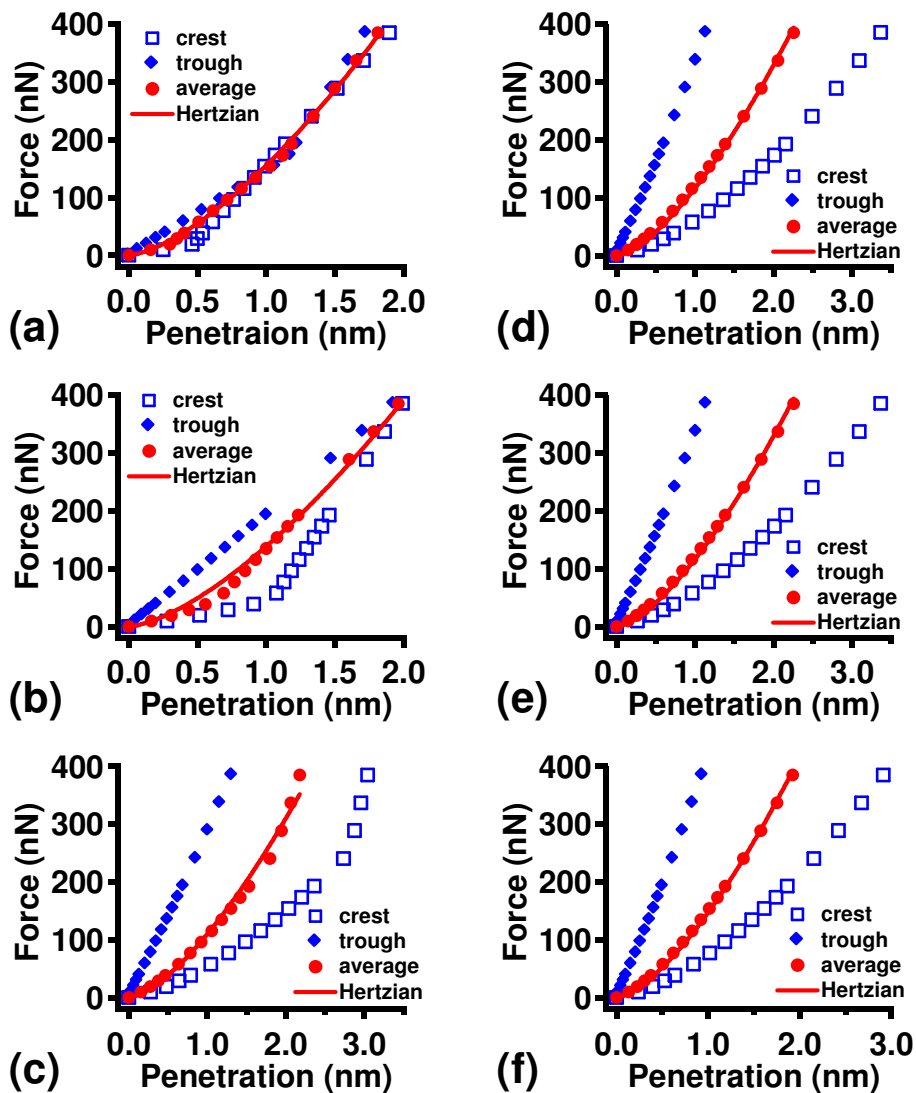
Next we investigated the dependence of the effective bilayer modulus on the corrugation wavelength. We adopted the same geometry design, boundary conditions, the dimensions, and materials properties as those used for the study of amplitude dependence, except that we fixed the corrugation amplitude at 1.5 nm for all these simulations.

Figure 3.21 shows the calculated local vertical displacement of volume elements within the tip and the film, again for the two extreme cases of apex-above-crest and apex-above-trough for different corrugation wavelengths under the same applied load. Similar to the results of amplitude dependence, the apex-above-trough cases show stiffer behavior than the apex-above-crest in all cases. The simulated load-penetration curves for the crest and trough positions, and the average of these are plotted in figure 3.22 for a series of different wavelengths. Fits of the average of the two curves to a  $3/2$ -power law are shown for each as solid curves in each case. We find the fits are good except for some wavelength due to kinks on the plot. By checking corresponding displacement map for the simulated penetration, we find that these kinks show up as a result of subsequent contact between the probe and the adjacent crests on the corrugated surface. We summarize the calculated effective average bilayer moduli as a function of corrugation wavelength in figure 3.24. Once again we see evidence for competing effects, with an initial decrease with wavelength beneath  $\sim 100$  nm, and an increase above this. This is seemingly associated with the variation of the number of crests contacted with wavelength over the range of penetration explored.





**Figure 3.21** Simulated vertical displacement maps for a spherical probe centered above a crest (left) or a trough (right) on corrugated bilayer films with different wavelengths: (a) 40 nm; (b) 60 nm; (c) 80 nm; (d) 100 nm; (e) 120 nm; (f) 140 nm; (g) 160 nm. The thickness of the damaged layer and the underlying polystyrene film are 1.29 nm and 400 nm respectively, and the applied load is 38 nN.



**Figure 3.22** Summary of simulated load-penetration relations for a spherical probe loaded against a model cylindrically corrugated surface. The dependence for the apex above the crest is shown by open squares, above the trough by solid diamonds, the average by solid circles. The solid curves show a fit of the average to a  $3/2$ -power law. The corrugation wavelengths varying as follows: (a) 40 nm; (b) 60 nm; (c) 100 nm; (d) 120 nm; (e) 140 nm; (f) 160 nm.

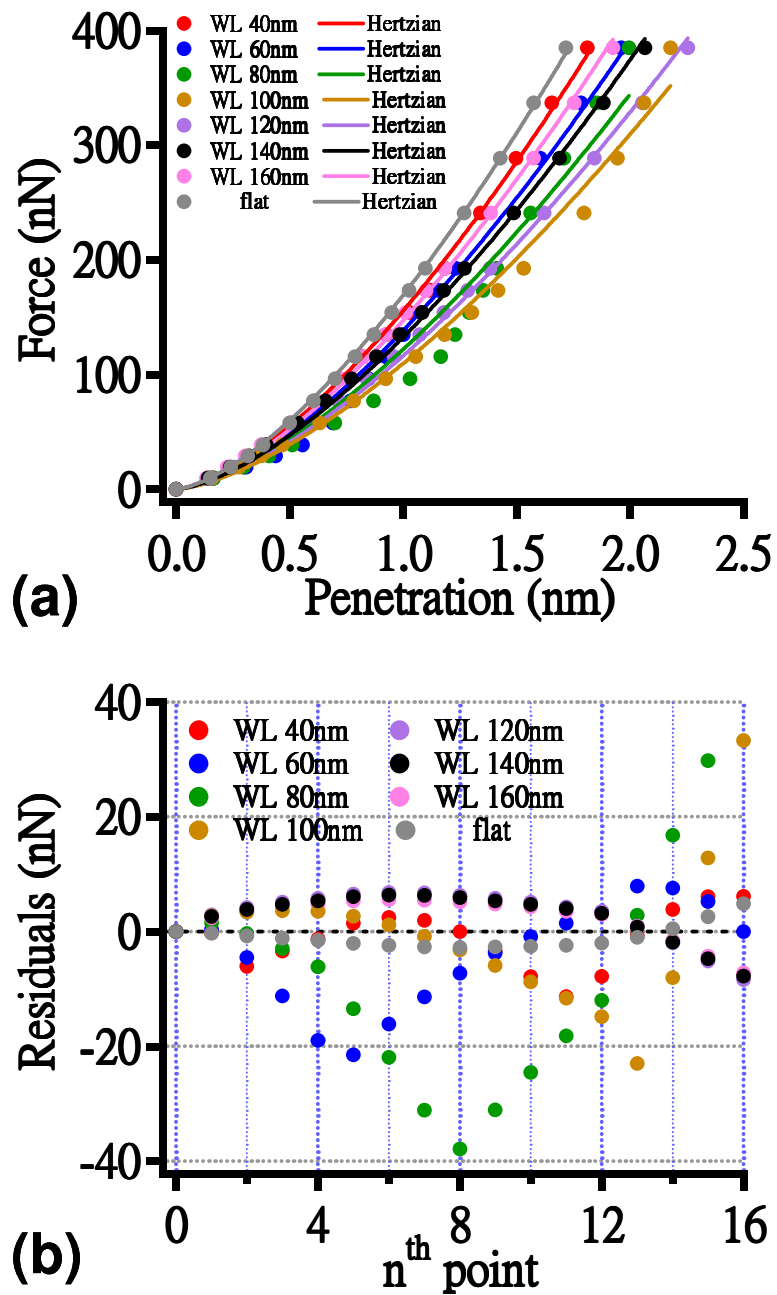


**Figure 3.23** (a) Summary of simulated average load-penetration curves and fits to a  $3/2$ -power law for the example for the wavelength dependence shown in figure 3.22; (b) the corresponding residual curves for the fits shown in (a).

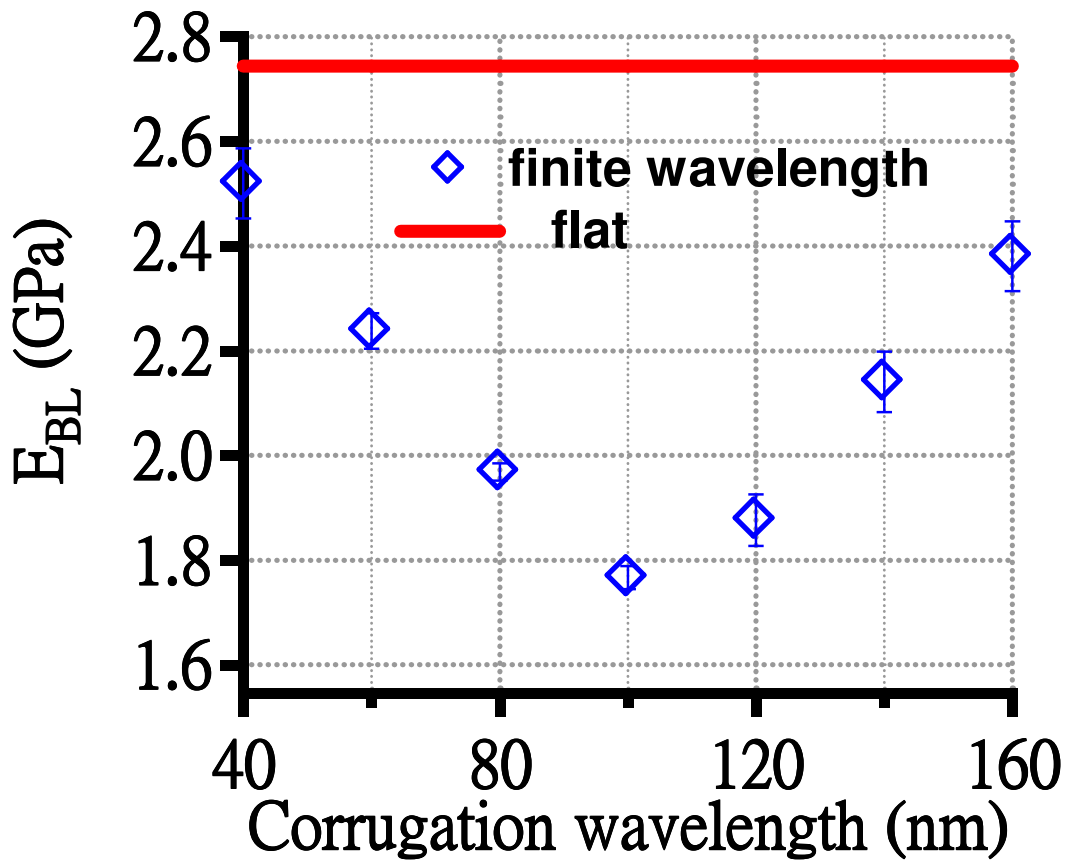


**Figure 3.24** Simulated average effective bilayer elastic modulus ( $E_{BL}$ ) of a corrugated bilayer film as a function of corrugation wavelength. The elastic modulus and thickness of the damaged layer used in the series of simulation are 400 GPa and 1.29 nm respectively, while the thickness of the underlying polystyrene film is fixed at 400 nm thick. The amplitude is fixed at 1.5 nm for all cases.

Next we use the dominant wavelength and RMS roughness measured by AFM (and summarized in table 2.1) to construct model corrugated surfaces corresponding to each of the plasma-etched polystyrene films modeled above in the flat surface approximation (figure 3.10-3.14). Example calculations of the local vertical displacements within the probe and etched polystyrene film with the damaged layers of different thicknesses, both for the apex-above-crest and apex-above-trough are shown in figure 3.25. Similar to the example result discussed above, we find that loading the probe apex above the trough results in shallower penetration depth at the film surface than above the crest, reflecting the fact that contact of the spherical probe at the position of a trough of the corrugated surface results in larger contact area than at the position of a crest.

Summary plots of the simulated load-vs.-penetration for the model corrugated bilayer films of etched polystyrene with different thickness damaged layers for the apex-above-crest and apex-above-trough cases and their average are shown in figure 3.26. In each case, we again find that the load required to cause a certain penetration depth is larger when the probe is centered at a trough position than at a crest. The average load-vs.-penetration curves for the different ion energies resulting polystyrene films are all well fitted by a 3/2-power law load-penetration relation (equation 3.10), as seen by the solid curves in each plot in figure 3.26.

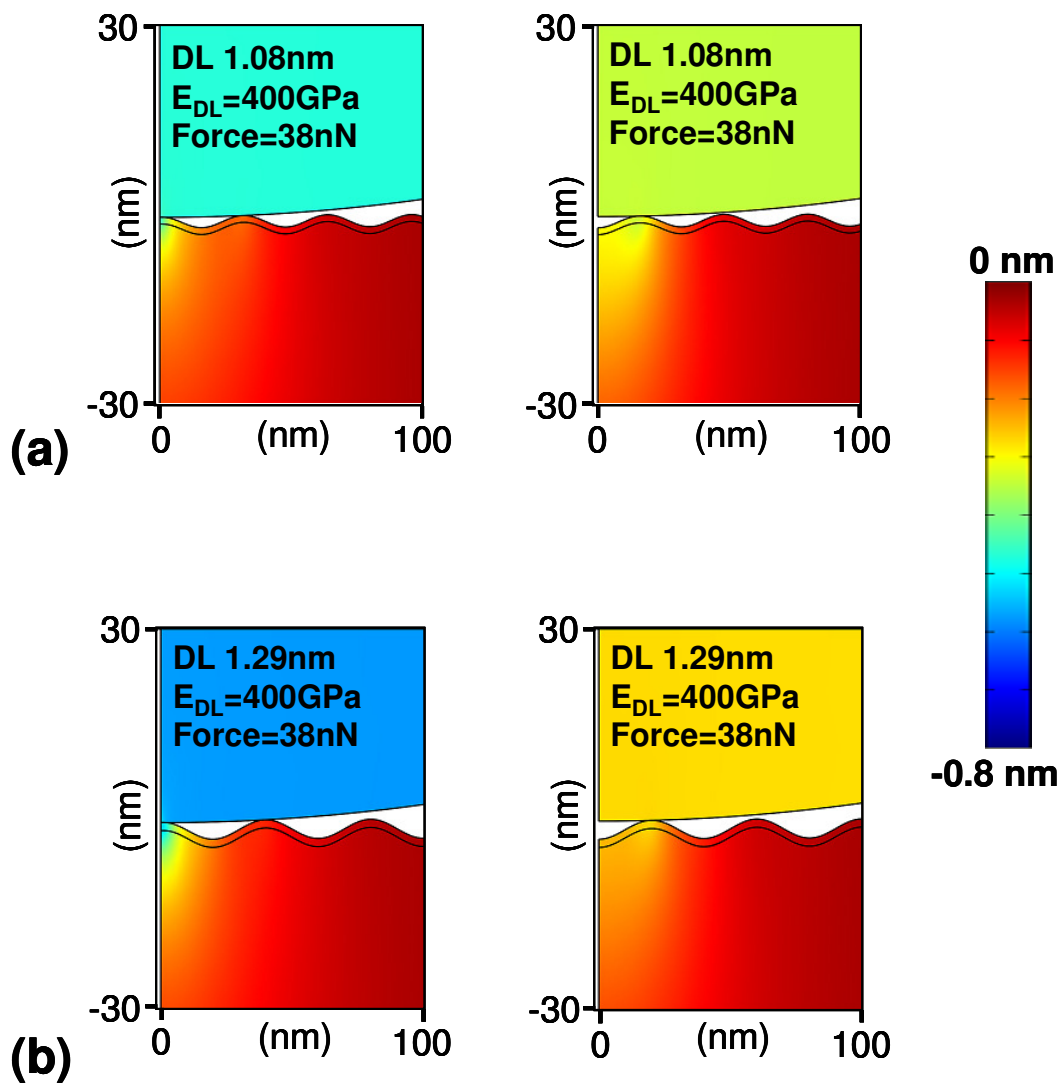


**Figure 3.25** Simulated vertical displacement maps for a spherical silica probe loaded against a cylindrically corrugated surface for the apex centered above a crest (left) and above a trough (right) for damaged layers of thickness: (a) 1.08 nm (b) 1.29 nm.  $E_{DL}$  is 400 GPa, and the load is 38 nN for all cases in the example.

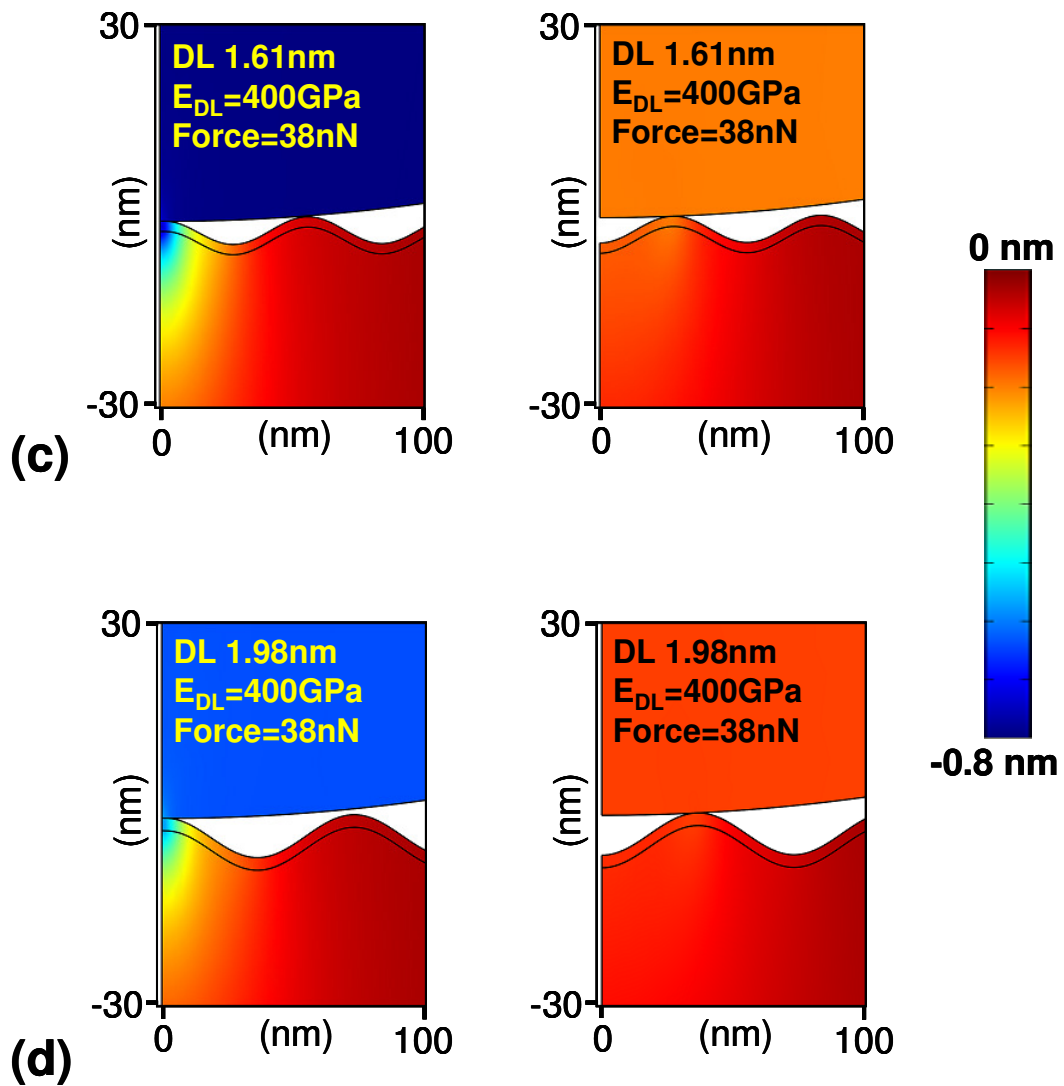


**Figure 3.25** Simulated vertical displacement maps for a spherical silica probe loaded against a cylindrically corrugated surface for the apex centered above a crest (left) and above a trough (right) for damaged layers of thickness: (c) 1.61 nm (d) 1.98 nm.  $E_{DL}$  is 400 GPa, and the load is 38 nN for all cases in the example.

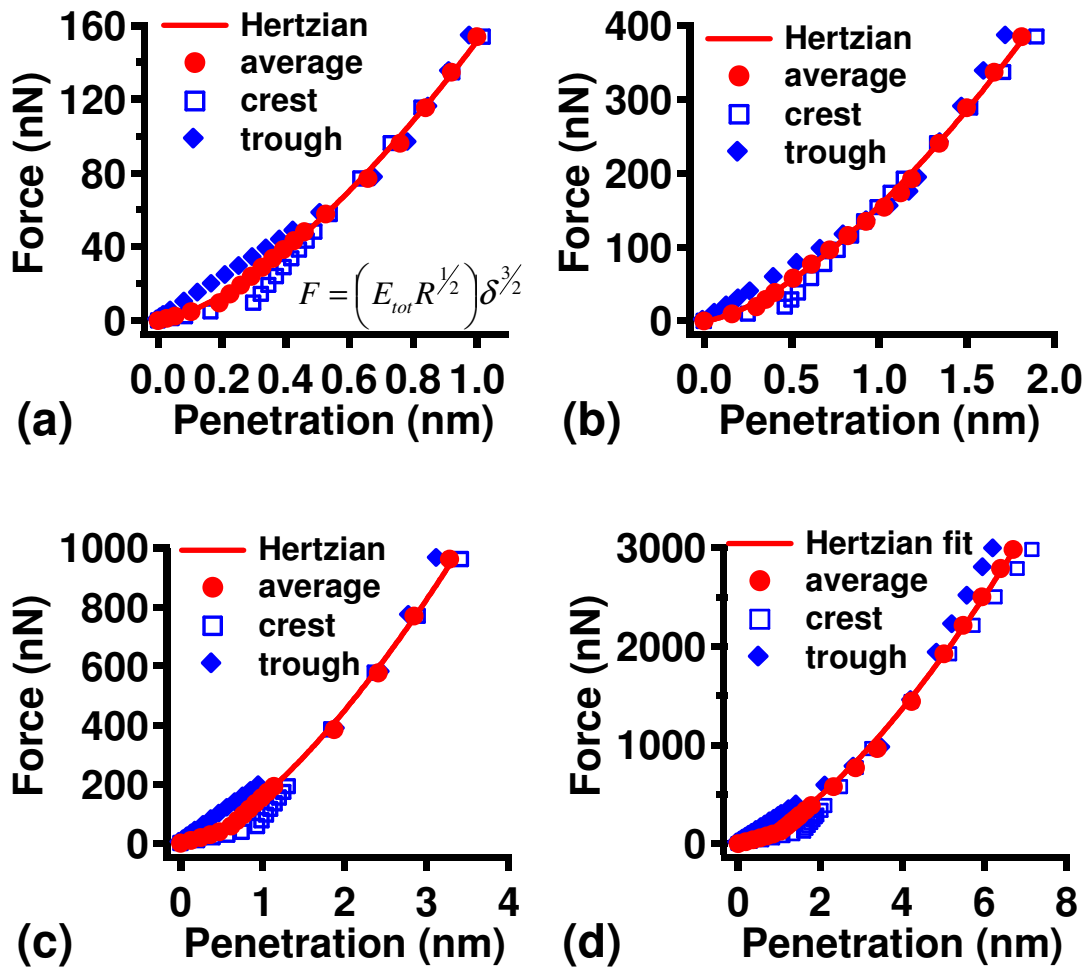


**Figure 3.26** Simulated load-vs.-Penetration curves for a spherical silica probe-bilayer film system. The case for the apex of the probe centered above the crest is plotted as open squares; the case for the apex centered above the trough is plotted as close diamonds. The average of these two cases is plotted as closed circles; the solid curves best fits to a 3/2-power law. The damaged layer thicknesses are (a) 1.08 nm, (b) 1.29 nm, (c) 1.61 nm, and (d) 1.98 nm.  $E_{DL}$  is 400 GPa for all cases.

We summarize the simulated effective average bilayer elastic modulus ( $E_{BL}$ ) as a function of damaged layer elastic modulus ( $E_{DL}$ ) for damaged layers of thicknesses determined by XPS <sup>3.3</sup> in figure 3.27. In a similar manner as our analysis for the flat surface approximation, we normalized the values of  $E_{BL}$  to the simulated elastic modulus of the unetched polystyrene film (2.43 GPa) obtained from our previous flat surface approximation, as described in section 3.3. In addition, the values for the open squares in figure 3.27 are also normalized, to the value of the measured elastic modulus for unetched polystyrene (2.24 GPa) by AFM force curve analysis, for polystyrene films treated by Ar plasma at the corresponding ion energies, as described and summarized in chapter 2. Finally, the damaged layer moduli corresponding to the effective bilayer moduli determined by force curve analysis were extracted by interpolation from the simulated  $E_{BL}$ -vs.- $E_{DL}$  relations shown in figure 3.27. These values are summarized as a function of Ar<sup>+</sup> ion energy in figure 3.28. As was the case for the flat surface approximation, we find that the corrugated surface approximation yields values of the damaged layer elastic modulus which increases monotonically with Ar<sup>+</sup> ion energy. with the values however, are a factor of between 2 to 3 larger than those which were simulated on a flat surface (compare to figure 3.13).

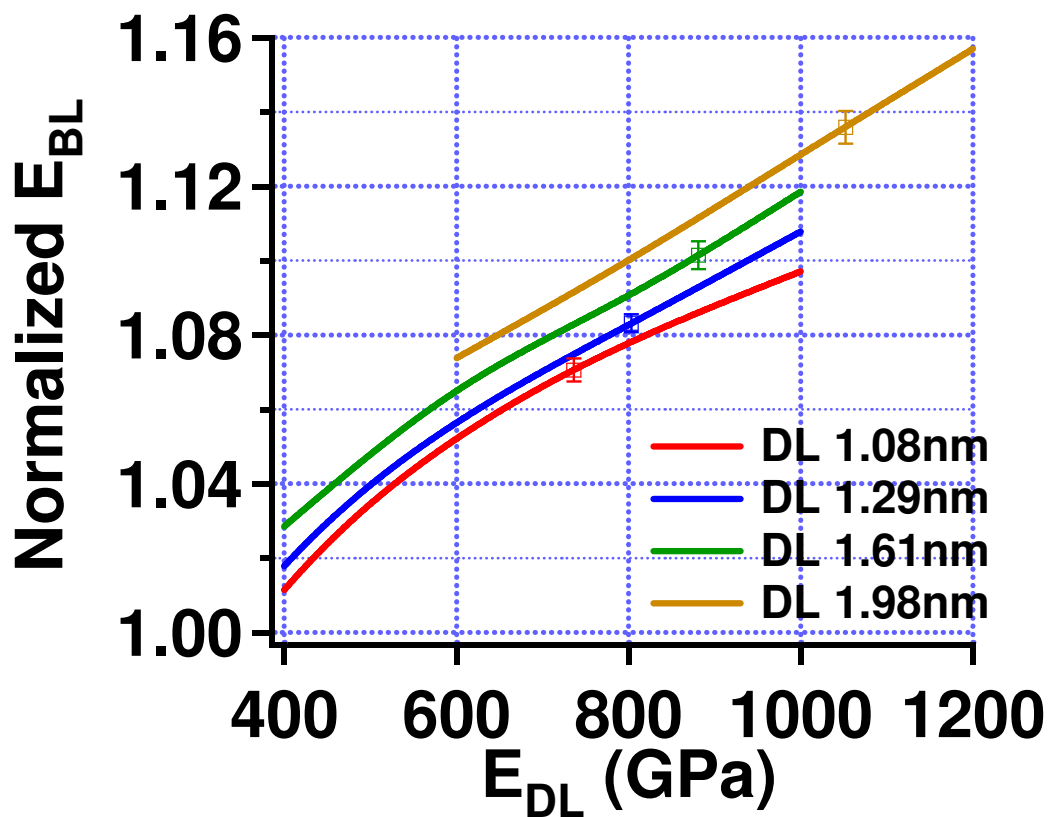


**Figure 3.27** Simulated effective bilayer elastic modulus ( $E_{BL}$ ) as a function of damaged layer elastic modulus ( $E_{DL}$ ) for a 400 nm thick polystyrene layer, covered with thin corrugated damaged layers, with thicknesses as indicated (solid lines). The open squares are the interpolated values using the effective bilayer moduli determined by force curve analysis. The interpolated and the simulated values are normalized to the elastic modulus of the unetched polystyrene film, obtained by force curve measurement (2.24 GPa), and finite element simulation (2.43 GPa) respectively.

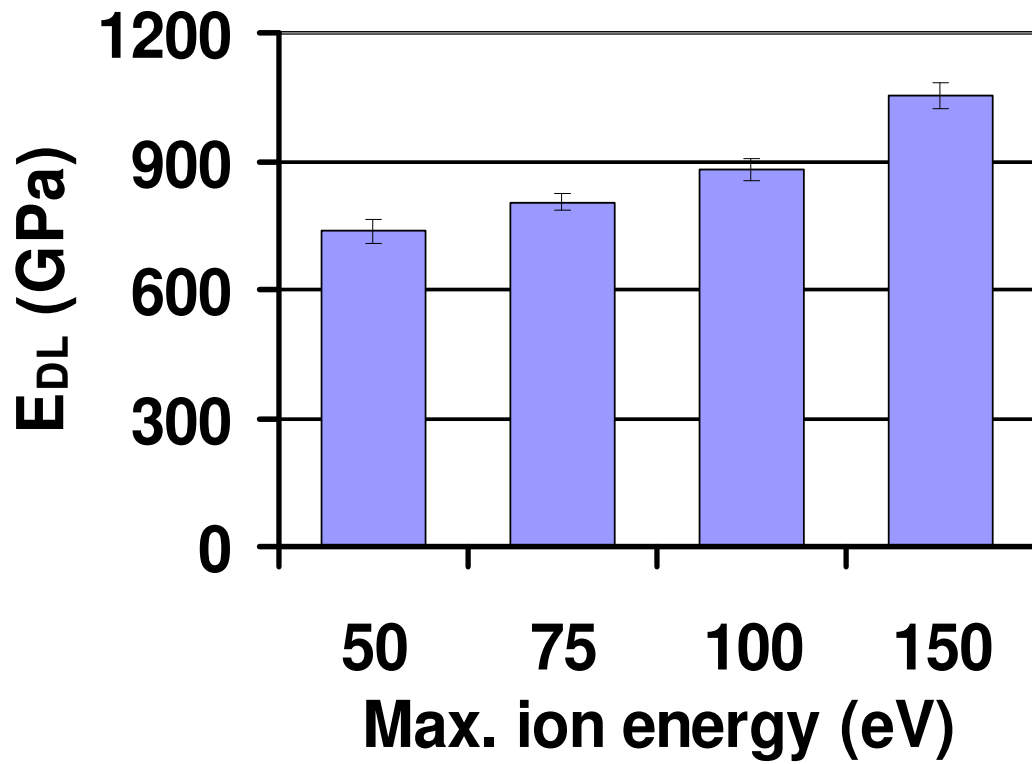


**Figure 3.28** The interpolated elastic modulus of the damaged layer ( $E_{DL}$ ) as a function of  $\text{Ar}^+$  ion energy. The uncertainty for each value comes from the uncertainties of the measured effective bilayer elastic moduli ( $E_{BL}$ ).

Finally, we used the values of the damaged layer modulus obtained based on the corrugated surface approximation to calculate the ratio of  $\lambda/t$  using equation 1.1. The values of remaining elastic constants were again taken from the literature:  $E_{PS}=2.24$  GPa,  $\nu_{PS}=0.33$ <sup>3.3</sup>, and  $\nu_{DL}=0.30$ <sup>3.3</sup>. These values are compared to those measured by AFM and XPS (see table 2.1), in the right panel of figure 3.29. Compared to the result from a rather simple flat surface approximation, shown in the left panel in figure 3.29, we see not only qualitative agreement between the theoretical prediction and experimental measurement, but good quantitative agreement for the corrugated surface, with all the values predicted by buckling theory within the uncertainties set by the experimental measurement.

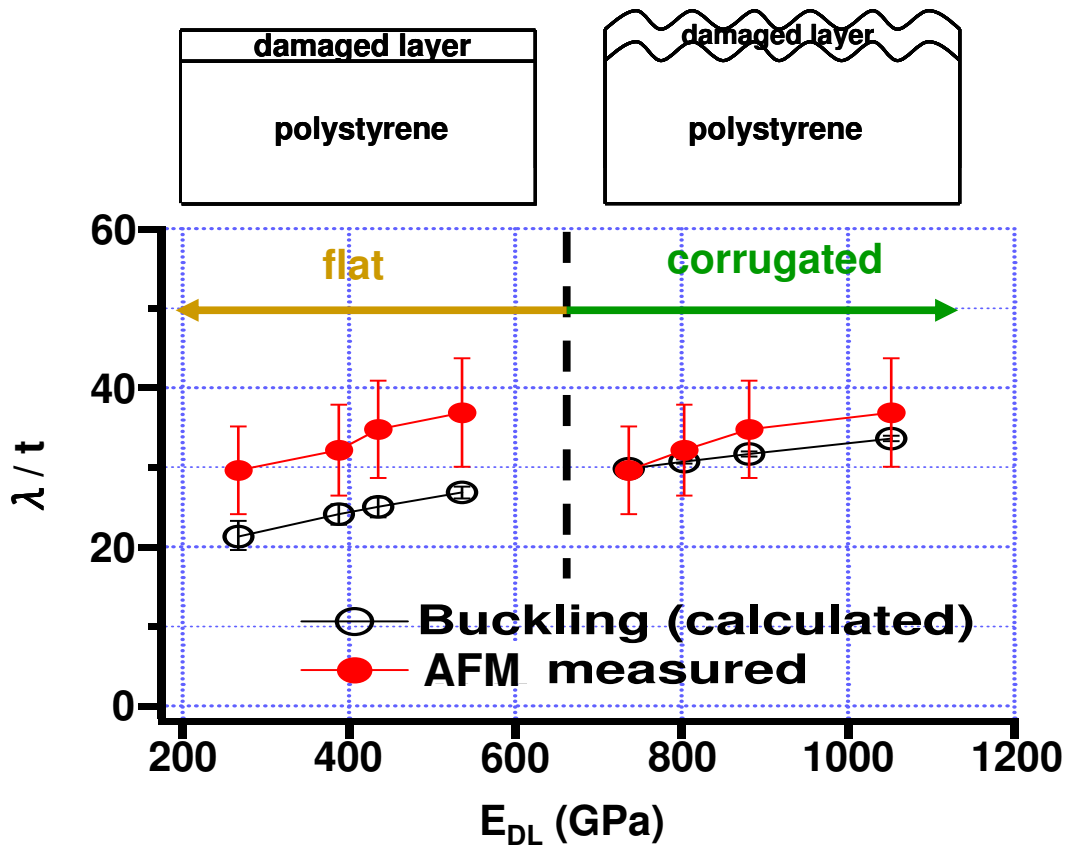


**Figure 3.29** The ratio of the dominant wrinkle wavelength ( $\lambda$ ) to the damaged layer thickness ( $t$ ), plotted as a function of damaged layer elastic modulus ( $E_{DL}$ ), based on buckling theory (open circles), and experimentally measured closed circles. Comparison based on the flat surface approximation is shown on the left; that based on the approximation with consideration of surface roughness is shown on the right.

### 3.5 Summary

In this chapter, we demonstrated how the effective elastic modulus of the etched polystyrene films changes with geometrical parameters including film thickness, corrugation amplitude, and wavelength. To do this we used finite element method simulations of the load-vs.-penetration relations for a model spherical AFM probe loaded against finite thickness films of various types.

First, we simulated the penetration versus load for an unetched initially flat polystyrene film. We found that the apparent elastic modulus of a 400 nm thick polystyrene film ( $E_{ps}$ ), based upon a simple 3/2-power law fit, is ~8% higher than the nominal value (input) extracted by AFM force curve measurement (2.43 GPa compared to 2.24 GPa). We carried out further simulations for the thickness dependence, demonstrating that the accepted value is approached in the limit of very thick films.

Second, we carried out finite element method simulations for a spherical probe loaded against initially flat bilayer structured etched polystyrene films. We found that: (1) the thickness of a stiff ( $E_{DL}=400$  GPa) damaged layer thickness affects the effective bilayer elastic modulus ( $E_{BL}$ ) at different levels.  $E_{BL}$  is dominated by the modulus of thick underlying unmodified polystyrene for a thin damaged layer, while it is dominated by that of the damaged layer as it becomes thick; (2) the damaged layer elastic modulus ( $E_{DL}$ ) extracted from the simulations in which the layer thicknesses are set at values measured after etching polystyrene films at different ion energies are all found to be two orders of magnitude larger than the elastic modulus of the underlying polystyrene ( $E_{PS}$ ), increasing monotonically with  $Ar^+$  ion energy. A

comparison with predictions of the buckling model revealed a ~30% systematic difference in the ratio of surface dominant wrinkle wavelength to the damaged layer thickness ( $\lambda/t$ ).

Third, we included surface corrugation in our simulations in an approximate way. We first determined how the apparent corrugated bilayer films response to changes as the corrugation amplitude and wavelength are varied. We find that these two parameters affect the effective elastic modulus ( $E_{BL}$ ) in different ways: (1)  $E_{BL}$  initially decreases with amplitude, then begins to increase, surpassing the flat film value. We attribute this to a competition between an initial decrease in contact area, followed by eventual contact with additional crests; (2) wavelength affects  $E_{BL}$  with an initial decrease in  $E_{BL}$  with increasing wavelength followed by an increase with wavelength. This is also attributed to competing effects of area of contact and number of contacts. The values of the damaged layer elastic moduli ( $E_{DLS}$ ) for the Ar plasma etched polystyrene films determined for thicknesses corresponding to different ion energies are found to be much greater (~2 $\times$ ) than those obtained by the simulations based on flat surface approximation. This is result of the decrease in the simulated effective elastic modulus ( $E_{BL}$ ) for the same damaged layer elastic modulus ( $E_{DL}$ ). It results in much improved agreement with  $\lambda/t$  ratios predicted by a buckling instability model. The good quantitative agreement supports our model of the buckling instability as the mechanism for the major contribution to roughening of a polystyrene film during exposure to an Ar plasma.

## ***Chapter 4:***

### ***Summary and Conclusions***

In this chapter, we summarize our conclusions from the major work presented in this thesis. We have performed investigations of the influence of ion kinetic energy on the surface morphology and nanomechanical properties of a fundamental resist material (polystyrene) during exposure to an Ar plasma. We used AFM topographical characterization along with height-height correlation analysis to determine the dominant wavelength and amplitude of the surface roughness. We in addition used AFM force curve measurement to determine the effective elastic modulus of the bilayer films consisting of a top ultrathin ( $< 2$  nm) ion-induced damaged layer and a thick, unmodified polystyrene underlayer. We next employed finite element method simulations to determine the effective bilayer elastic modulus for various model systems, varying the thickness and elastic modulus of individual layers, considering either a flat or a rough (corrugated) surfaces. From these simulations we determined the damaged layer elastic moduli corresponding to the values of the effective bilayer modulus determined by AFM force curves for each model geometry. This in turn allowed for a quantitative test of the predictions of the buckling model.

In chapter 2, we presented measurements of the surface roughness of unetched and Ar-plasma etched polystyrene samples using AFM, as well as the height-height

correlation function analysis to determine the dominant wavelength,  $\lambda$ . The  $\lambda$  and the measured RMS roughness were both found to increase with increasing Ar<sup>+</sup>-ion energy, which qualitatively agrees with what could be visually observed from the AMF topography images.

Upon the determination of the effective elastic modulus of the plasma etched sample, we demonstrated that reliability and reproducibility can be achieved by well-controlled measurement setup (e.g. utilization of spherical AFM probe, measurement performed in dry nitrogen ambient, etc.) and systematic data analyzing procedures in which an intermediate adhesive contact was considered. Our force curve measurement and analysis show directly that the effective bilayer elastic modulus ( $E_{BL}$ ) increases monotonically with increasing Ar<sup>+</sup>-ion energy imposed on the sample during plasma exposure.

A comparison between the measured elastic modulus of an unetched polystyrene film and those for plasma etched samples shows that the impact on the overall film stiffness with the introduction of the top ultrathin damaged layer is subtle, but consistent with damaged layer moduli orders of magnitude larger than that of the underlying unmodified layer.

In chapter 3, we present results of a numerical approach, based on the finite element method simulations of Hertzian mechanics to determine the elastic modulus of the ultrathin damaged layers. Here we present the main results of this thesis, i.e. an examination of the applicability of a buckling instability model in explaining the roughening of polystyrene during the plasma exposure. By simulating the penetration of a spherical probe into a single layer pristine polystyrene film or a damaged

layer/polystyrene bilayer structured film under varying load applied on the probe without taking into account the adhesive interaction, we were able to extract the effective elastic modulus of the film with given elastic modulus of individual layer fitting the results to a 3/2-power law Hertzian load-penetration relation. Using a series of models with different damaged layer thicknesses and moduli, we produced curves giving the relationship between the effective elastic modulus ( $E_{BL}$ ) and the damaged layer elastic modulus ( $E_{DL}$ ). Thus we extracted the  $E_{DL}$ s of the corresponding plasma etched samples by interpolating the AFM measured  $E_{BL}$  from the simulated  $E_{BL}$ - $E_{DL}$  relationship.

From simulations of the penetration of a model sphere into an unetched polystyrene film (single-layer film structure), we found that the apparent extracted elastic modulus of a 400 nm thick polystyrene film ( $E_{ps}$ ), based upon a fit to a 3/2-power law, is ~8% higher than the actual value (2.43 GPa compared to 2.24 GPa). We confirmed this to be a finite thickness effect. This difference must be taken into account, when the experimentally measured  $E_{BL}$  is compared to the simulated  $E_{BL}$ , by normalization respectively.

We next presented simulations for bilayer films based on a flat surface approximation. These supported our earlier, indirect determination<sup>4.1</sup> that the  $E_{DL}$  are about two orders of magnitude larger than the elastic modulus of the underlying polystyrene ( $E_{PS}$ ), and increase monotonically with Ar ion-energies. A quantitative comparison between the predictions of a buckling instability model for the surface roughening and the results of our measurements yielded good quantitative agreement,

but a ~30% quantitative difference in the ratio of surface dominant wrinkle wavelength to the damaged layer thickness ( $\lambda/t$ ).

We then used a simplified corrugated surface model to carry out additional simulations, obtaining ~2 times greater values for the apparent damaged moduli than those obtained from the flat surface approximation. These simulations improve the agreement between the  $\lambda/t$  ratios resulting from the buckling instability model and our experimental measurement. The resulting qualitative and quantitative agreement supports a buckling instability as the dominant mechanism for the roughening of a polystyrene film during exposure to an Ar plasma.

We note that the value of the modulus is comparable to that of graphene.<sup>4.2-4.4</sup> It is interesting to further note that the instability requires a stress greater than a critical value for the buckling to occur.<sup>4.5</sup> Although it had been claimed in our previous publications<sup>1.9, 1.10, 1.30</sup> that the stress comes from the large differences in either density or elastic modulus, we speculate that if indeed the damaged layer is graphene-like, this stress might result from a relatively small amount of heating during the etching, given the relatively large coefficient of thermal expansion of polymers, and the extremely small coefficient for graphene.<sup>4.6, 4.7</sup> If so, then avoiding roughening will only be possible etching under conditions of good thermal contact, and extremely low ion power density.

## ***Chapter 5:***

### ***Future Work***

In this chapter, I mention possible future work which would extend our current understanding of the scientific and technical issues dealt with in earlier chapters of this thesis.

In this thesis work we tested the applicability of a buckling instability model in describing resulting roughening of a rather simple resist-plasma system, i.e. polystyrene in Ar plasma, by using height-height correlation analysis for surface topography, AFM force curve measurement, and finite element method, and found quantitative agreement between the theoretical prediction and measured result. However, a remaining question concerns the generality of this phenomenon. A deeper understanding for the plasma induced roughening of resist surface would be achieved if the same investigation approach were extended to different combinations of the resist materials and plasmas.

For the resist-plasma system reported on in this thesis, we have shown that the buckling instability is applicable within the range set for Ar ion bombardment. However, to what extent that this theory would fail would be an interesting topic to understand the limit at which it can be applied. We could extend this investigation by increasing the Ar ion energy in causing more surface heating, and thus a more highly

stressed interface between the damaged layer and the underlying unmodified polystyrene film. An interesting possibility would be that local delamination might occur once exceeding a certain, higher level of stress.

As to the other model resist materials, it would be interesting to extend these studies to resists with lower coefficients of thermal expansion, and higher thermal conductivity to determine if the stress which drives the instability is due to local surface heating, followed by differential expansion on cooling.

Another issue which might be investigated in future work is that both an ion-damaged layer and a significant VUV-modified layer can be formed during exposure to plasmas. It would be useful to extend this investigation by using the same instrumental measurements, analysis, as well as the similar numerical simulations but with a trilayer film structure (i.e. unmodified resist\VUV-modified layer\ion-damaged layer). In other words, this would require an extra thorough work in characterizing the VUV modified layer.

It would also be of considerable interest to carry out similar investigations on rather complicated plasma (i.e.  $C_4F_8/Ar$  plasma) etching for these model resist materials, since a layer of fluorocarbon (F-C) film is deposited on the surface as well. Such investigation would be important to understand the role of buckling instability plays under the presence of more complex plasma chemistry.

Finally one might perform simulations of the nano-penetration on a randomly rough surface, i.e. 3D simulation. We expect that this might improve the agreement between the model and experiment. This would involve importing the measured

topography to the platform of simulation, and would for sure require sophisticated computing system.

# ***Appendix A: Nanolithography with AFM***

## **A.1 Introduction**

As we mentioned in section 1.1, the resist line-edge roughness (LER) which occurs during pattern transfer by plasma etching is one of the key issues limiting device performance. Present technology widely uses resists during the process of pattern transferring, motivating interests in understanding the response of resist materials to different ambient treatments, e.g. heat and plasma. Previously, Kwon *et al.*<sup>A.1</sup> observed evidence for spatial-period selection during plasma etching-induced roughening of poly(alpha-methylstyrene) (PαMS) which is one of the prototype resist materials. To extend our understanding of this spontaneous pattern formation from the studies of blank sample surfaces, we decided to perform a more controlled study in which we pre-pattern the resist surface with periodic grooves of nanometer scale. These we created using an AFM-based nano-scratching technique. We then studied the persistence of these nano-grooves during thermal annealing. As a starting point, we chose PαMS (the same as in Kwon's study) as our sample for patterning.

## **A.2 Experiment**

The PαMS we used in this experiment was synthesized by one of our collaborators, Professor C. G. Willson's group at University of Texas, with a number-average molar mass ( $M_n$ ) of 30000 g/mole, a polydispersity of 1.5, and a bulk glass transition temperature ( $T_g$ ) of  $\sim 160^\circ\text{C}$ . The synthesized PαMS solution was spin-coated onto Si wafers and baked at  $90^\circ\text{C}$  for 1 minute. The average starting thickness

of the polystyrene films was ~400 nm. The coated wafer was diced into similar sized (~ 1 inch × 1 inch) small pieces for further nanolithography and an annealing experiment.

### **A.2.1 Nano-scratching**

We initiated the patterning by using an AFM-based “nano-scratching” technique, rather than e-beam lithography, due to the limit set by the proximity effect of our e-beam facility when the feature size goes down to ~100 nm. Another motivation for AFM-based lithography in our consideration for patterning is that AFM is capable of performing both patterning and characterization on non-conducting materials, e.g. polymers, which simplifies the process of the experiment.

We performed nanolithography using a commercial AFM system (DI 5000 series) along with the NanoScript™ macro language <sup>A.2</sup>. Lithography was executed by manipulating the tip, scratching over the sample surface using a C++ language coded program including NanoScript™ macro Litho functions. For the patterning of our polymer samples, we used commercial “standard” AFM probes (tip radius of 10 nm, cantilever length of 125 μm, force constant of 40 N/m, and resonant frequency of 300 kHz), and conducted patterning at room temperature in air. For more effective and practical patterning, we used our previously developed C++ code along with a commercial standard compiler supplied by Veeco, so that we could make arrays of patterns continuously and quickly.

### **A.2.2 Annealing of nano grooves**

The patterned PαMS samples were used for the annealing experiment described below to investigate the relaxation of the nano-patterns. The annealing

experiment was performed on a custom-built setup including two aluminum-topped commercial, programmable hot plates as well as a homemade stage with a rotatable sample holder and a quench table, schematically shown in figure A.1. Before the annealing experiment, the programmable hot plates were calibrated at the freezing point and boiling point of water (DI water was used for this calibration). The sample holder and quench table were both made of aluminum for efficient heat transfer. The temperature at the surface of the aluminum sample stage was measured with an external thermometer when being placed on the hot plate with a nominal temperature, hence, we can determine the proper setting value of the hot plate to ensure the sample stage is at the desired temperature. To control the annealing time at temperature effectively, the sample heating was performed in two steps. We first pre-heated the sample on a hot plate at temperature approximately  $150^{\circ}\text{C}$ , which is 10 degrees below the glass transition temperature ( $T_g-10^{\circ}\text{C}$ ). Once the sample temperature equilibrated, it was immediately transferred to a second hot plate with temperature of  $170^{\circ}\text{C}$  ( $T_g+10^{\circ}\text{C}$ ). Since the relaxation below  $T_g$  is expected to be negligible, we further expect that the relaxation is dominated by the annealing time at temperature above  $T_g$ . This procedure significantly reduces the time (from minutes to seconds) required to reach thermal equilibrium between the sample and the hot plate surface with the expected annealing temperature. The topographic characterization of the as-patterned and the annealed nano-patterns was carried out using commercial carbon nanotube-terminated (CNT-terminated) probes (tip radius of 10-30 nm according to manufacturer) for reducing the tip shape effect on the scanned topographic images.

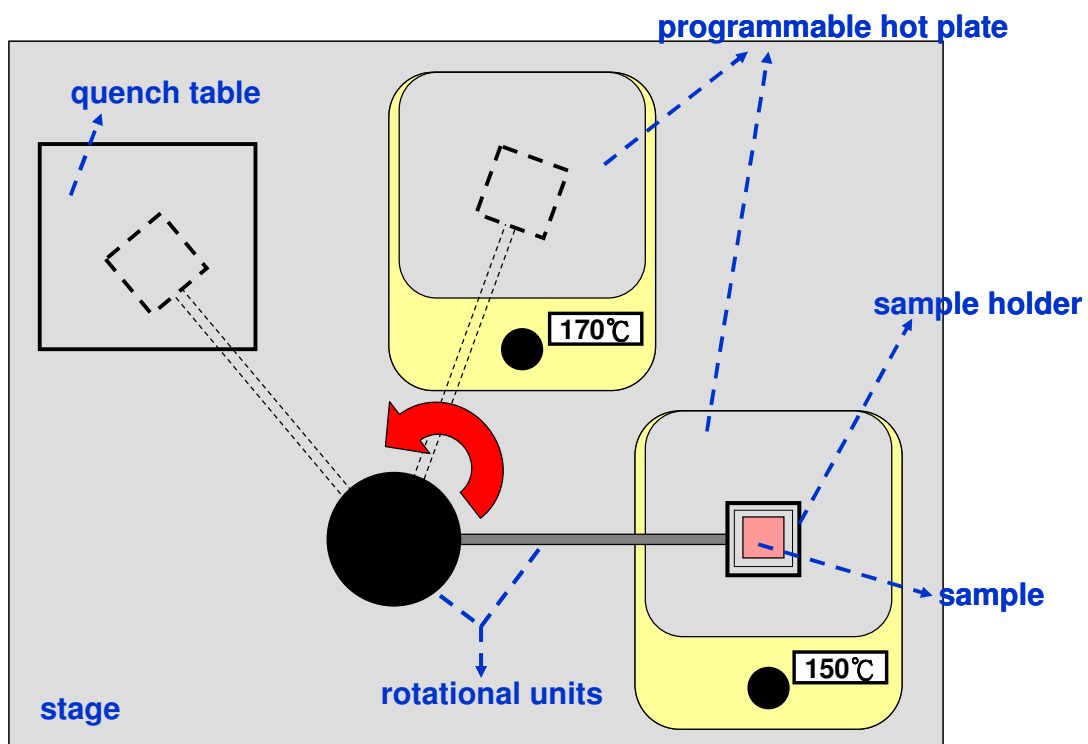


**Figure A.1** Schematic of the experimental setup for the annealing of the patterned PaMS sample.

### A.3 Results

We first established a procedure to make arrays of grooves. We began it by a trial of making a single groove. Controlled by the NanoScript™ code, the piezo scanner drives the AFM probe scribing the sample surface in a zigzag route which is schematically shown in figure A.2. The length and depth of the groove are defined by the values in the unit of length (e.g.  $\mu\text{m}$ ), while the width is defined by the number of passes for the scribing including a single scratch along the set length and a single scratch in between two adjacent equal-length scratches. Figure A.3 shows a single groove scribed with 100 passes of 2  $\mu\text{m}$  long, 0.003  $\mu\text{m}/\text{spacing}$ , and 0.07  $\mu\text{m}$  deep scratches. We see significant accumulation of the film material along the sides where the ends of the plowing of the probe are. The asymmetric shoulders are not desirable since it makes analysis of the relaxation in terms of Fourier components more complicated. An intuitive way to generate symmetric shoulders is to repeat the plowing at the doubling depth but in the opposite direction, which is expected to cause an equal amount of accumulations at the other shoulder, schematically shown in figure A.4. However, during several trials of this approach, we found that we need to triple the depth in the backward plowing to obtain a comparably equal size shoulder at the other side. This however resulted in a wilder groove, as shown in figure A.5. We followed this approach to make arrays of the same sort of grooves. Figure A.6 shows a 5 $\times$ 1 array of 2  $\mu\text{m}$  long grooves (scribed with 50 passes for each single groove and 1 $\mu\text{m}$  spacing between each groove). We found those grooves appearing with good fidelity to each other, except that we see small increasing in period due to creep in the lateral displacement of the piezotube scanner.

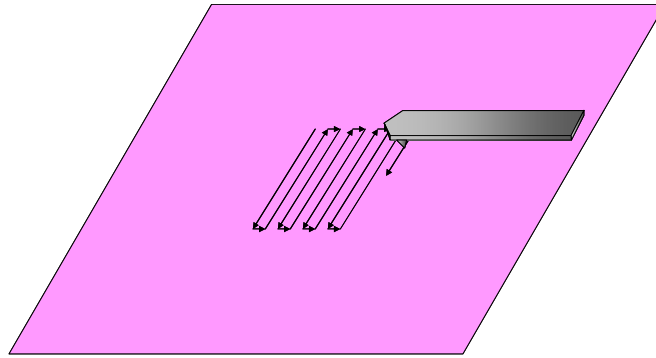


**Figure A.2** Schematic of a zigzag path scribing by an AFM probe. Individual segments are along the direction perpendicular to the long side of the groove.

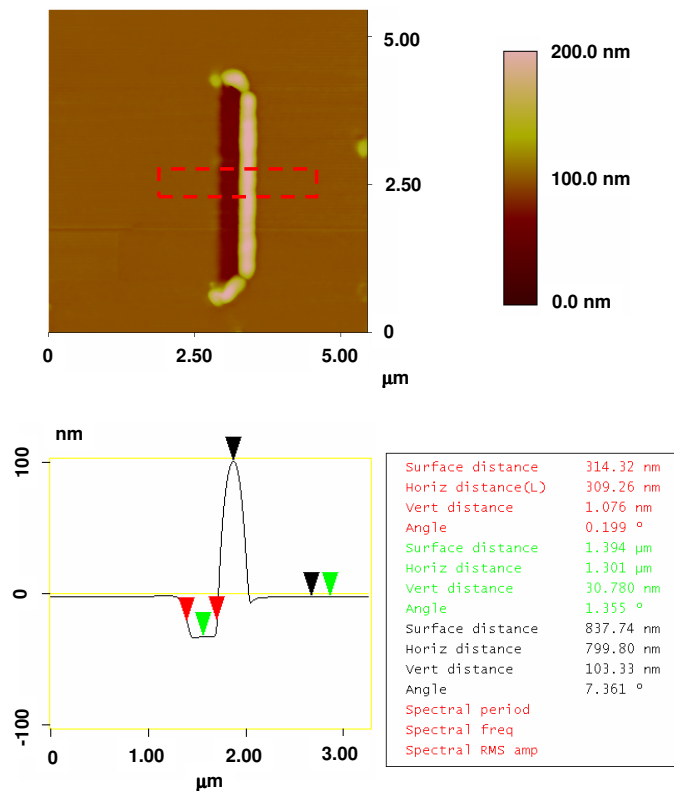


**Figure A.3** Topographic AFM image and the averaged cross-sectional profile of a section (marked red) for a groove scribed by 100 passes, as illustrated in figure A.2.

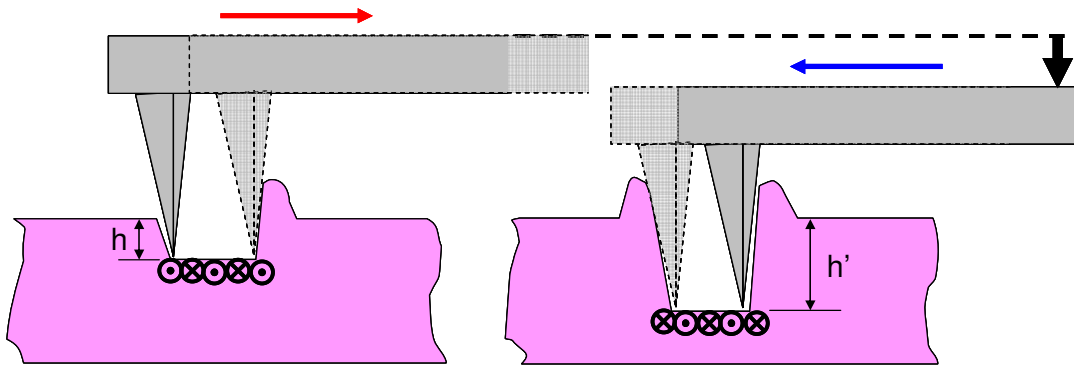


**Figure A.4** Schematics of a 2-step zigzag scribing of an AFM probe to make symmetric shoulders for a single groove.

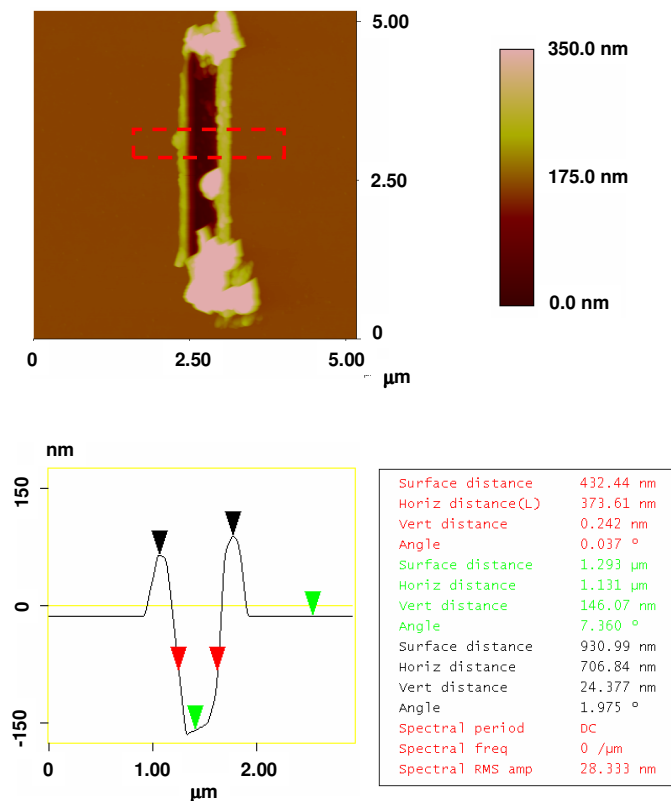


**Figure A.5** Topographic AFM image and the averaged cross-sectional profile of a section (marked in red) for a groove scribed by 100 passes as illustrated in figure A.4.

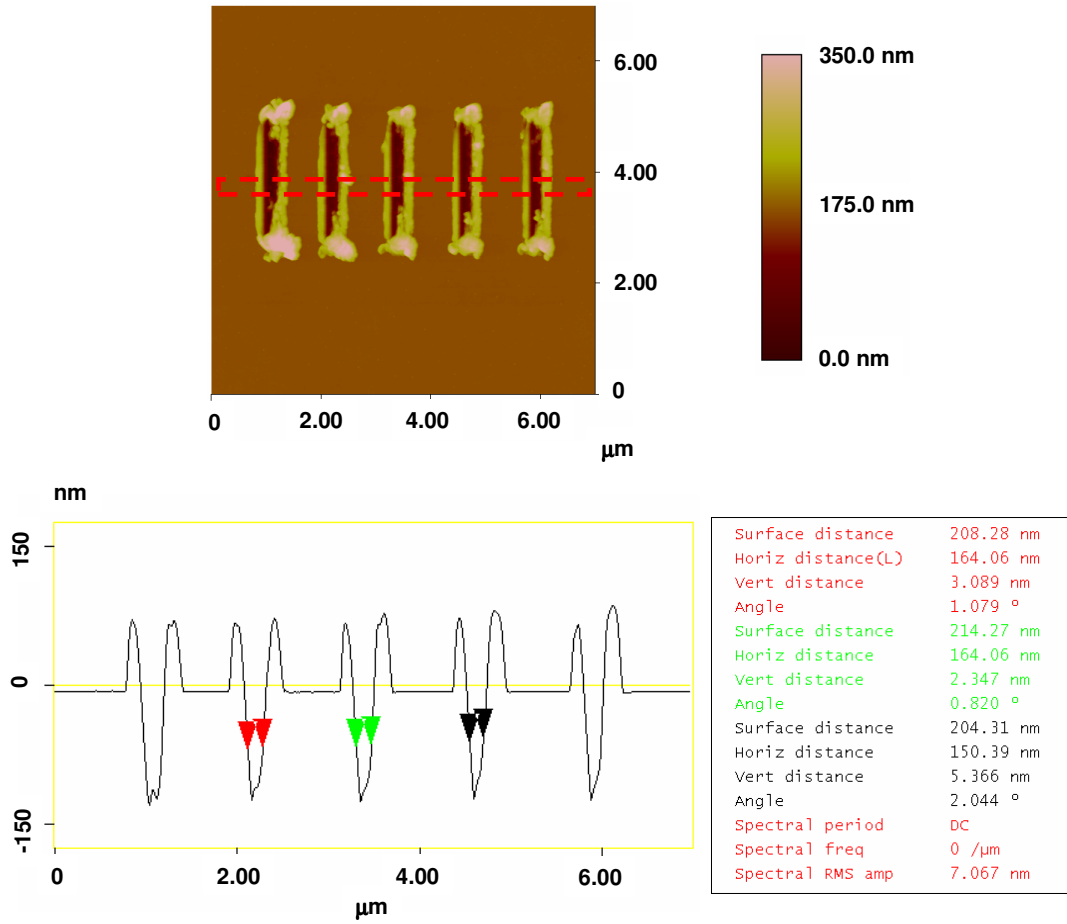


**Figure A.6** Topographic AFM image and the averaged cross-sectional profile of a section (marked in red) for a 5x1 array of 2  $\mu\text{m}$  long grooves scribed by 2-step zigzag scratching with 50 passes for each single groove.

Following this procedure, we made smaller sized arrays of grooves by defining fewer numbers in passes of scratch for each single groove. One thing to note is that the shoulders of the grooves would squeeze to each other if the spacing between them is small so that the overall structure of the array would be degraded. To avoid this, we set the center-to-center groove spacing to be multiple times of the groove width, and we found a minimum pitch/width ratio of  $\sim 6$  is required for a single groove scribed by just one pass. We kept this ratio of 6 for following patterning of varying sized arrays of grooves, and then we annealed the patterned P $\alpha$ MS sample at  $\sim 170^\circ\text{C}$ .

Figure A.7 shows results as a series of AFM images, for annealing of different sized arrays of grooves at different amounts of total annealing time. Note that the center-to-center spacing between each groove was set at 6 times of the product of the number of passes for a single groove and the spacing between each pass. We found, however, that the resulting pitch/width ratio does not follow the nominal value (i.e. 6). This might be attributed to creep of the piezo scanner. We observe different degrees of relaxation for these nano-grooves after annealing for times up to 43200 seconds. We can qualitatively distinguish from the image contrast that the smaller sized array of grooves relaxed faster than the larger one, with disappearance of ridges in all cases. This difference in relaxation behavior is evidence for a length scale dependence of relaxation for the nano-grooves. In the following sections, I will present our preliminary results from analysis of experimental data with theoretical modeling.

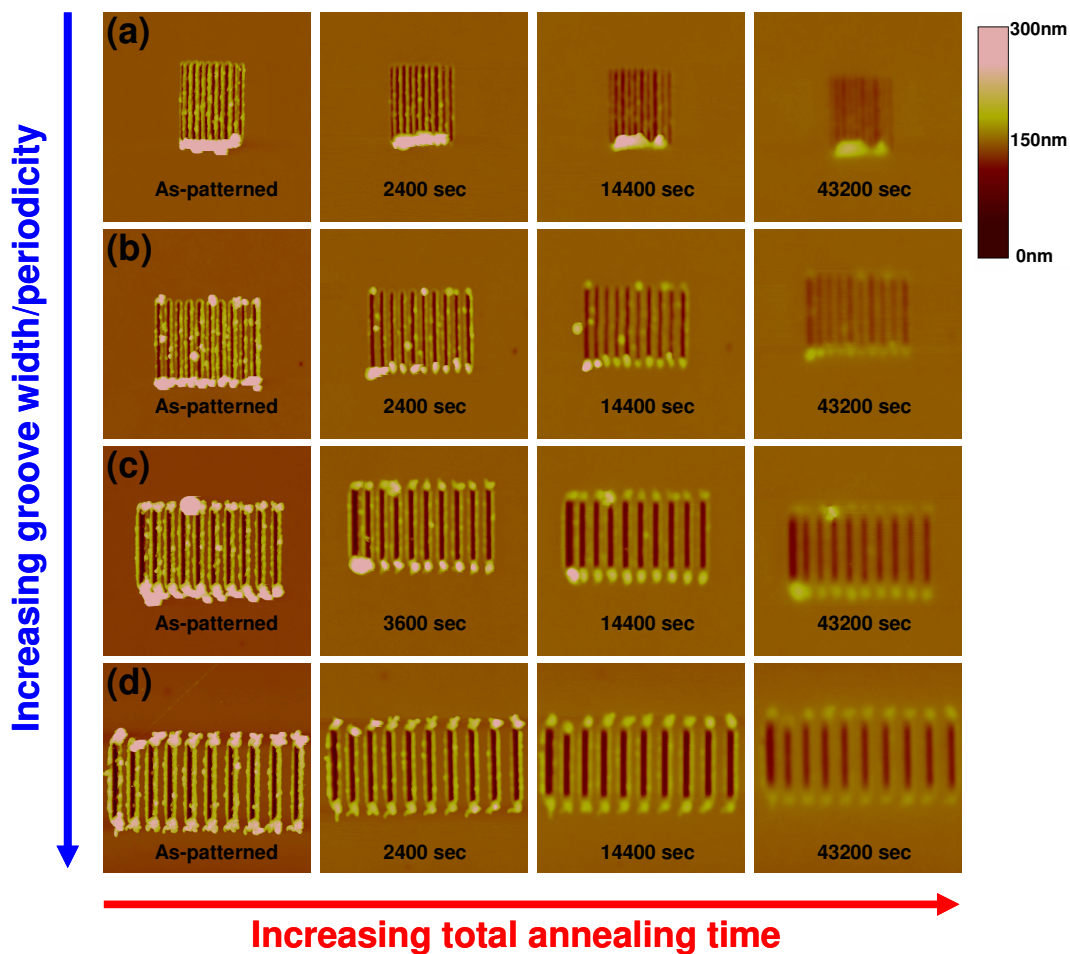


**Figure A.7** Topographic AFM images of the as-patterned and thermally-annealed (at  $\sim 170^{\circ}\text{C}$ ) nanogroove patterned PaMS. Grooves are  $2\mu\text{m}$  long. Panels left to right show effect of increasing amount of annealing time. Rows are for various average-groove widths/periodicities: row (a) 35.2 nm / 86.3 nm, row (b) 41.0 nm / 307.6 nm, row (c) 57.4 nm / 448.8 nm, row (d) 62.5 nm / 617.2 nm. Note that the image field of view for each case shown is  $6\mu\text{m} \times 6\mu\text{m}$ .

#### A.4 Theoretical model and simulation

To further understand the evolution of these nano-grooves, we analyze the average cross-sectional line profiles across the middle sections of each array of grooves for different amounts total annealing time, presented as solid lines in figure A.8. Generally, morphological evolution of solid surfaces is driven by one or more of the following mass transport mechanisms: viscous flow, evaporation/condensation, volume diffusion, and surface diffusion.<sup>A.3</sup> We first compared our result to a model for pattern reflow of polymers proposed by Leveder et al.<sup>A.4</sup>. In their model, the reflow of patterns on a polymer surface is a result of minimization of surface free energy slowed by viscous behavior of the polymer. The surface equation for a 2D pattern with its surface topography in small angle regime, based on the Navier-Stokes and continuity equations with considering both Laplace and disjoining pressure but slip length,<sup>A.4</sup> can be written as

$$\partial_t h = \frac{A}{6\pi\eta} \partial_x \left( \frac{\partial_x h}{h} \right) - \frac{\sigma}{3\eta} \partial_x (h^3 \partial_x^3 h), \quad (\text{A.1})$$

where  $h$  is the height of any point on the surface,  $\eta$  is the dynamic viscosity,  $\sigma$  is the surface tension, and  $A$  is the Hamaker constant. The dashed lines shown in figure A.8 are the calculated line profiles as functions of total annealing time by using the average line profiles measured from as-patterned AFM images. The Hamaker constant ( $A$ ) and surface tension ( $\sigma$ ) used in our calculations are  $10^{-19}$  J<sup>A.5</sup> and 39 mN/m<sup>A.6</sup> respectively. As we do not know the value of the dynamic viscosity ( $\eta$ ) for

our PαMS at temperatures near  $T_g$ , we calculate the time-dependent profile with varying  $\eta$  to seek the best fit to the measured line profiles corresponding to each annealing time. The calculated profiles shown in figure A.8 were determined by the  $\eta$  which results in the least difference between the maximum and minimum height within the surface, shown in figure A.9. We find it requires a value in an order of  $\sim 10^{12}$  Pa-s to match the calculated result to the measured one; we note however, that this value is much larger than the typical range ( $10^2$ - $10^5$  Pa-s or even less) for polymers at a temperature near  $T_g$ . This might indicate that the surface evolution of our patterned PαMS at a temperature slightly above  $T_g$  is not simply driven by just one mechanism only. Hence, we extend our investigation to see if other possible mechanisms are involved.

We start this extended investigation by determining if there is mass loss from our patterned samples during annealing. This would be an indication of concurrent sublimation occurring during thermal annealing at this temperature. The way we account for mass loss is to calculate the difference ( $\Delta h$ ) between the average height of the entire topography image and that of the unpatterned area in the same image, i.e. the mass loss is the variation in the product of  $\Delta h$  and the area of the whole image with respect to total annealing time, schematically illustrated in figure A.10. We plot the value of difference in average height for those images taken after each annealing step as a function of total annealing time, presented in figure A.11. We indeed find a decrease of this value with increasing annealing time, suggesting a mass loss due to sublimation during thermal annealing at a temperature slightly above  $T_g$ .

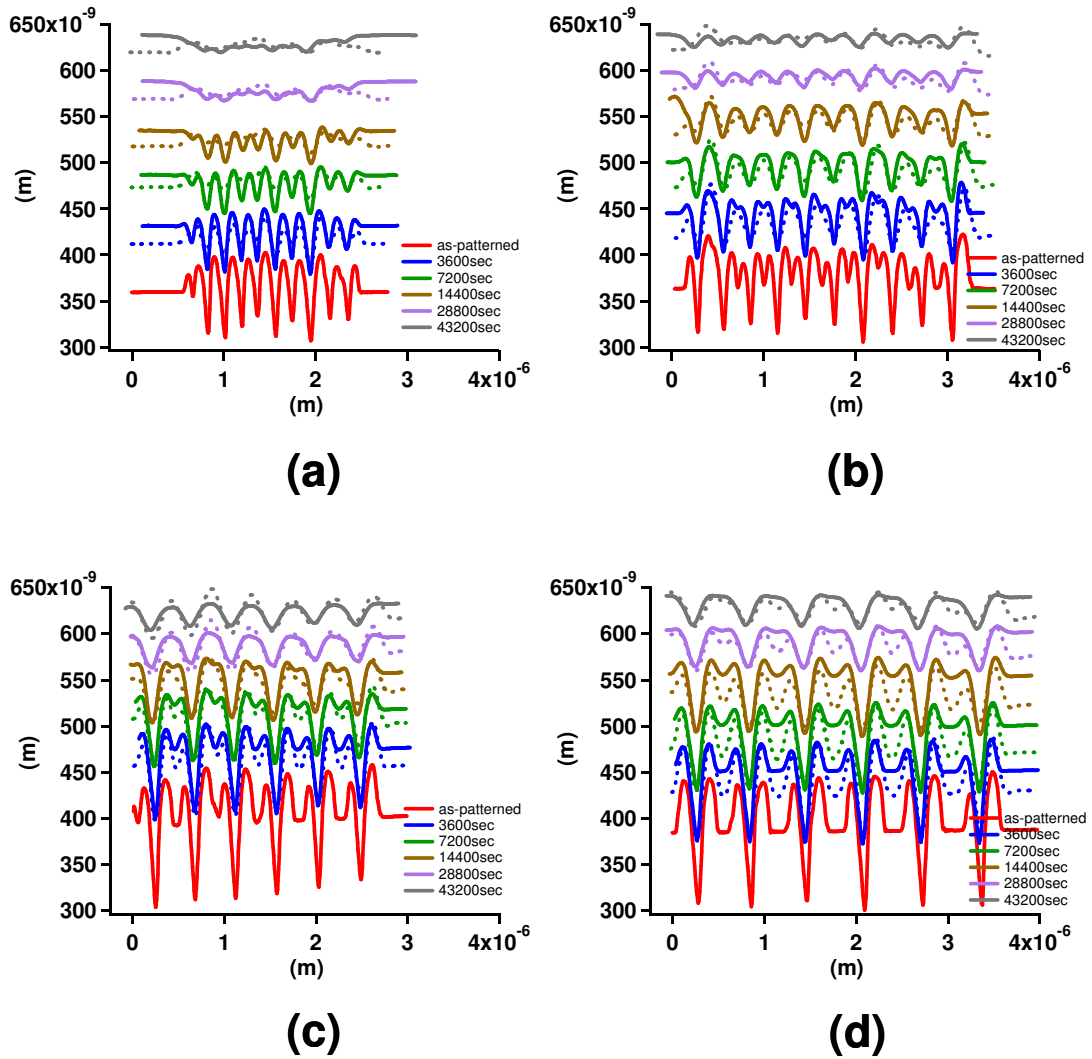


**Figure A.8** Average cross-sectional line profiles (solid lines) within a section around the middle of the array of grooves; results for groove width/periodicity: (a) 35.2 nm / 86.3 nm, (b) 41.0 nm / 307.6 nm, (c) 57.4 nm / 448.8 nm, (d) 62.5 nm / 617.2 nm, are presented for different total annealing time as indicated. The dashed curves are calculated line profiles based on equation A.1 with  $\mu=4 \times 10^{12}$  Pa-s for each total annealing time.

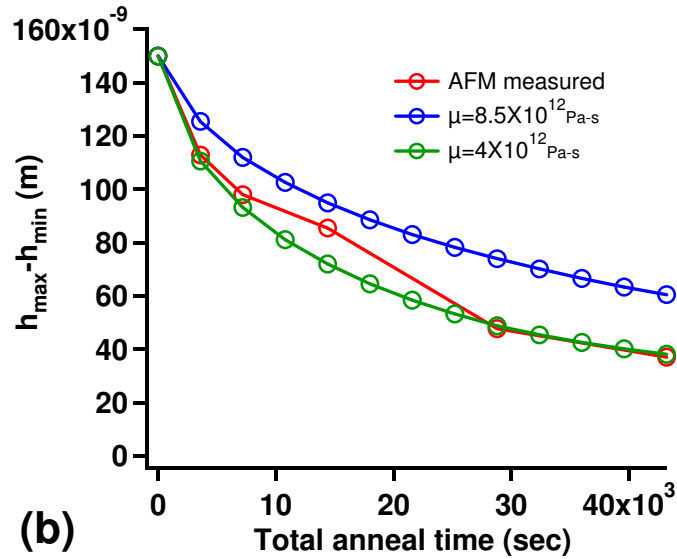
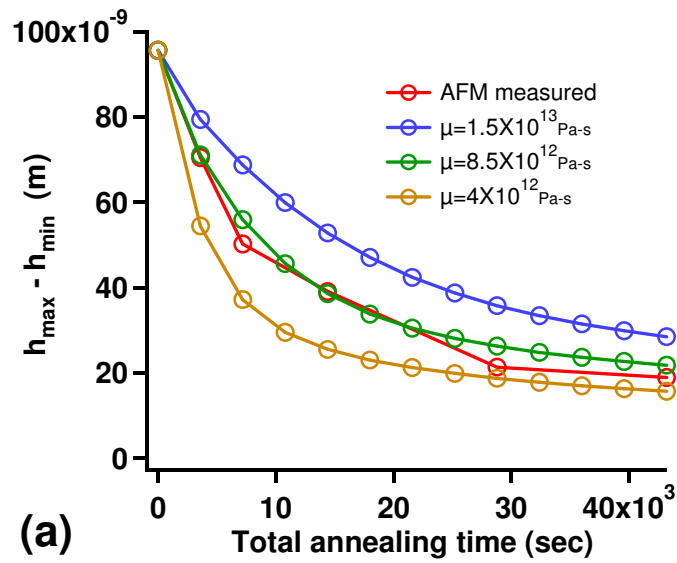


**Figure A.9** The difference in the height between the highest ( $h_{\max}$ ) and the lowest ( $h_{\min}$ ) points on the measured and calculated line profile for different  $\mu$  as a function of total annealing time, for two cases with groove width/periodicity: (a) 35.2 nm / 86.3 nm, (b) 62.5 nm / 617.2 nm.

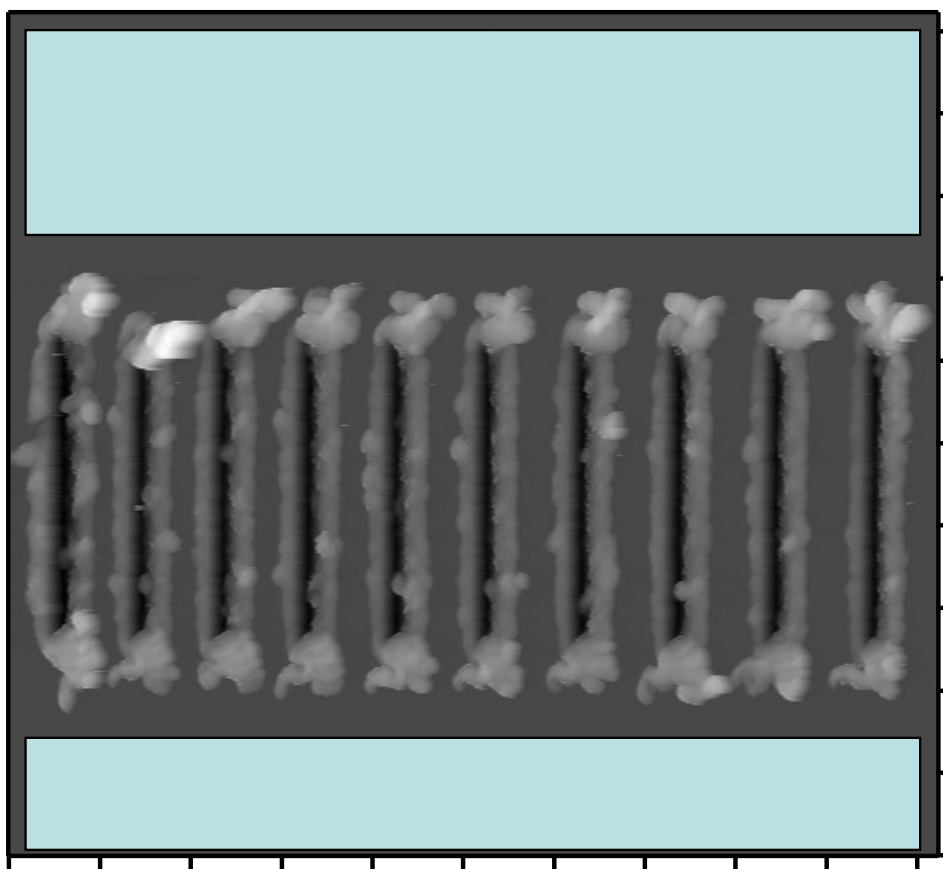


**Figure A.10** Graphical illustration for the calculation of mass loss from AFM measured topographic image. The mass loss is the variation in the product of the area of the scanned image and the value of the difference between the average height over the whole image and that over the unpatterned area ( □ ) in the same image with respect to total annealing time.

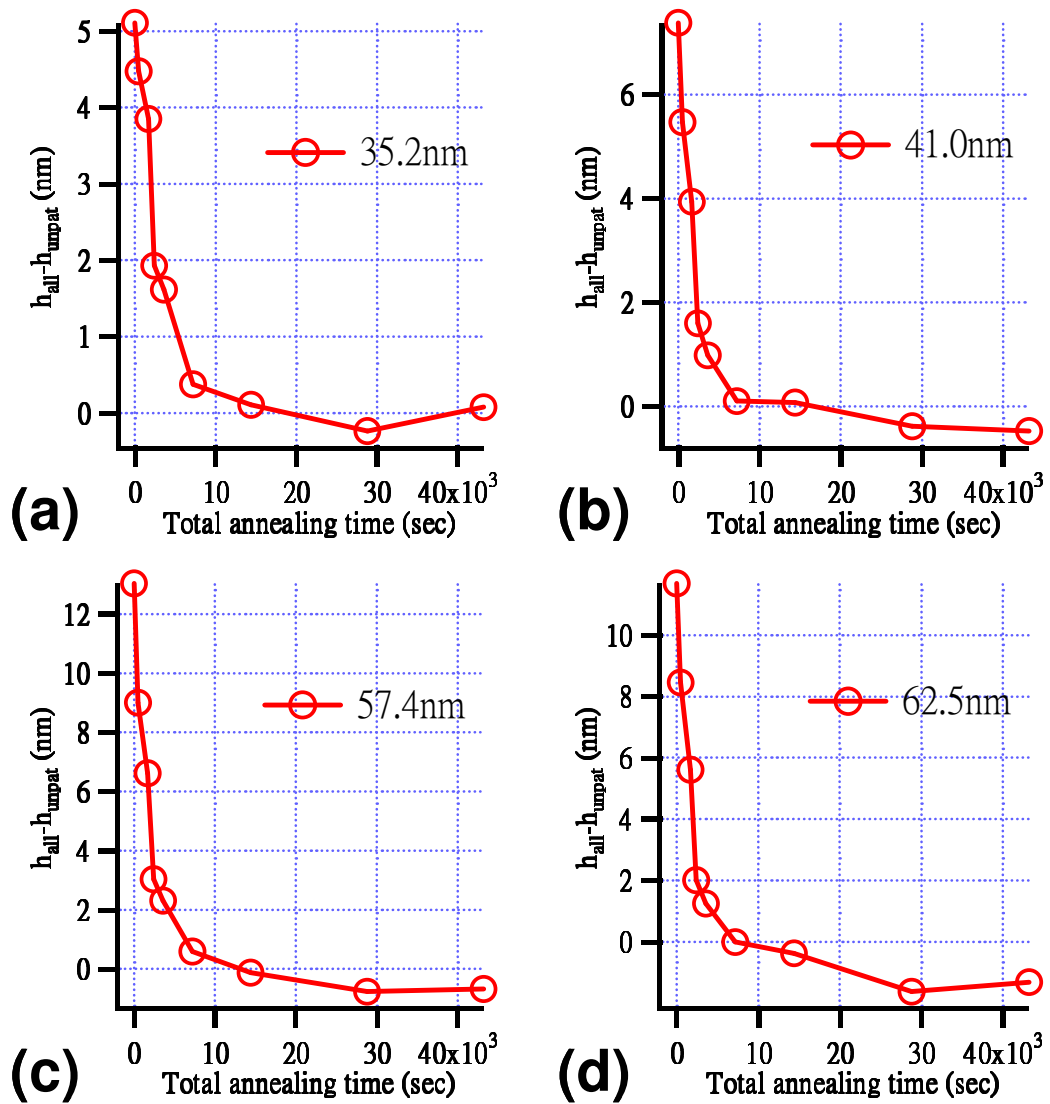


**Figure A.11** The difference between the average height over the whole AFM image ( $h_{\text{all}}$ ) and that of the unpatterned area ( $h_{\text{unpat}}$ ) plotted as functions of total annealing time for groove arrays with groove width/periodicity: (a) 35.2 nm / 86.3 nm, (b) 41.0 nm / 307.6 nm, (c) 57.4 nm / 448.8 nm, (d) 62.5 nm / 617.2 nm. Note that all cases were calculated from  $6 \mu\text{m} \times 6 \mu\text{m}$  AFM images.

## A.5 Discussion

To further understand the relaxation quantitatively, we analyzed these average cross-sectional line profiles (shown in figure A.8) using Fast Fourier Transform (FFT). The dashed lines shown in figure A.12 are composed of the fundamental and first few harmonic components obtained from the FFT of some of the corresponding AFM images measured average cross-sectional line profiles (solid lines shown in figure A.12). We see a good agreement between them.

Next we examine the relaxation of the coefficients of these Fourier components. These are plotted as a function of total annealing time in figure A.13, where the error bars come from the standard deviation from individual profiles. We calculated the relaxation times ( $\tau$ ) for the exponentially-like and monotonically decreased curves in figure A.13 by fitting them with simple exponential function. These fits are shown as solid curves in the same figure. For solids with surface morphology under the small slope assumption, the mechanisms responsible for exponential relaxation of surface features can be related to a power dependence of the relaxation time ( $\tau$ ) on corresponding surface wavelength ( $\lambda$ ), where the power of 1, 2, 3, and 4 correspond to a transport mechanism of viscous flow, sublimation/condensation, volume diffusion, and surface diffusion respectively.<sup>A.3</sup> Hence we check the relation between  $\tau$  and  $\lambda$ , as our first attempt to use that theory in correlating the responding mechanism for pattern relaxation in our soft material system. We plot  $\tau$  as a function of  $\lambda$  in a log-log fashion, which is shown in figure A.14, where the error bars come from the deviation from each simple exponential fitting. A straight line fitting for these points results in a best fit with a slope of  $\sim 1.3$ ,

suggesting a value between those for viscous flow (1) and for sublimation (2). This result does not indicate the dominant mechanism responsible for the pattern relaxation of our PaMS nano-grooves at the temperature slightly above  $T_g$ , but we can see a clue of a complex mechanism involving viscous flow and sublimation, at least agreeing with our observation of mass loss.

This result suggests that the model (equation A.1) to describe the evolution of height of our PaMS nano-grooves needs to be modified since sublimation takes part as well. We expect that a precise profile of the shape of each groove is important since the evolution rate of height is sensitive to the curvature of the surface. Unfortunately in our measured profiles from the nano-grooves, there is only one data point at the bottom of each groove, which is likely due to the finite size and the orientation of the carbon nanotube probe. We expect to obtain more reasonable results from such simulation if a faithful line profile could be extracted by deconvolution of the measured one with the function of the probe shape, as well as the addition of the sublimation term.

Further refinements would be to reduce the complexity of the features (ridges around each groove) and the non-consistent periodicity induced by the piezo creep. These might be reduced by an alternative patterning technique, such as imprint lithography.

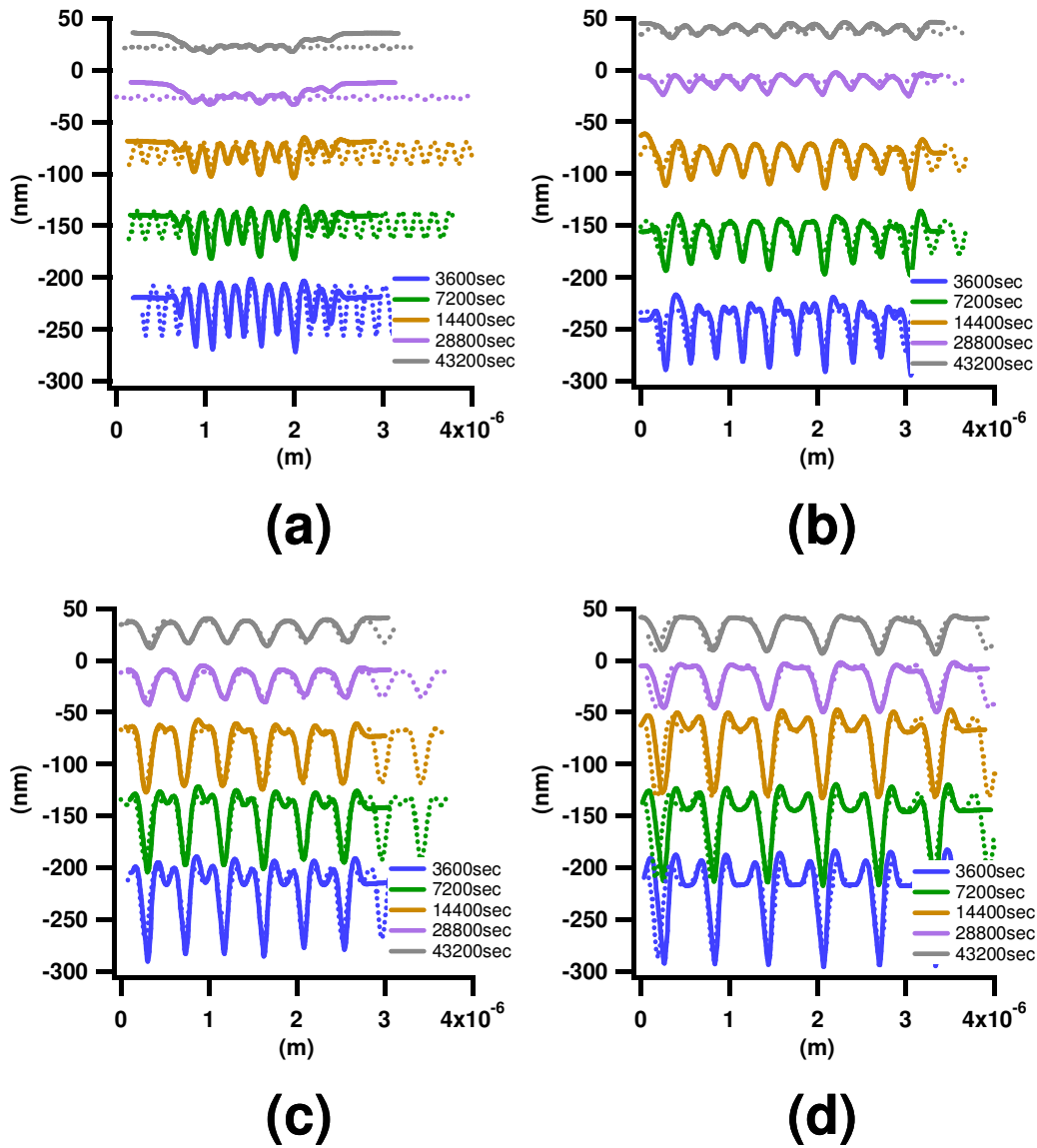


**Figure A.12** The functions of the Fourier series composed by the coefficients and wavelengths of the first few Fourier components obtained from the FFT of the corresponding AFM measured average cross-sectional line profiles for different arrays of grooves with groove width/periodicity of: (a) 35.2 nm / 86.3 nm, (b) 41.0 nm / 307.6 nm, (c) 57.4 nm / 448.8 nm, (d) 62.5 nm / 617.2 nm, presented for different total annealing time respectively.

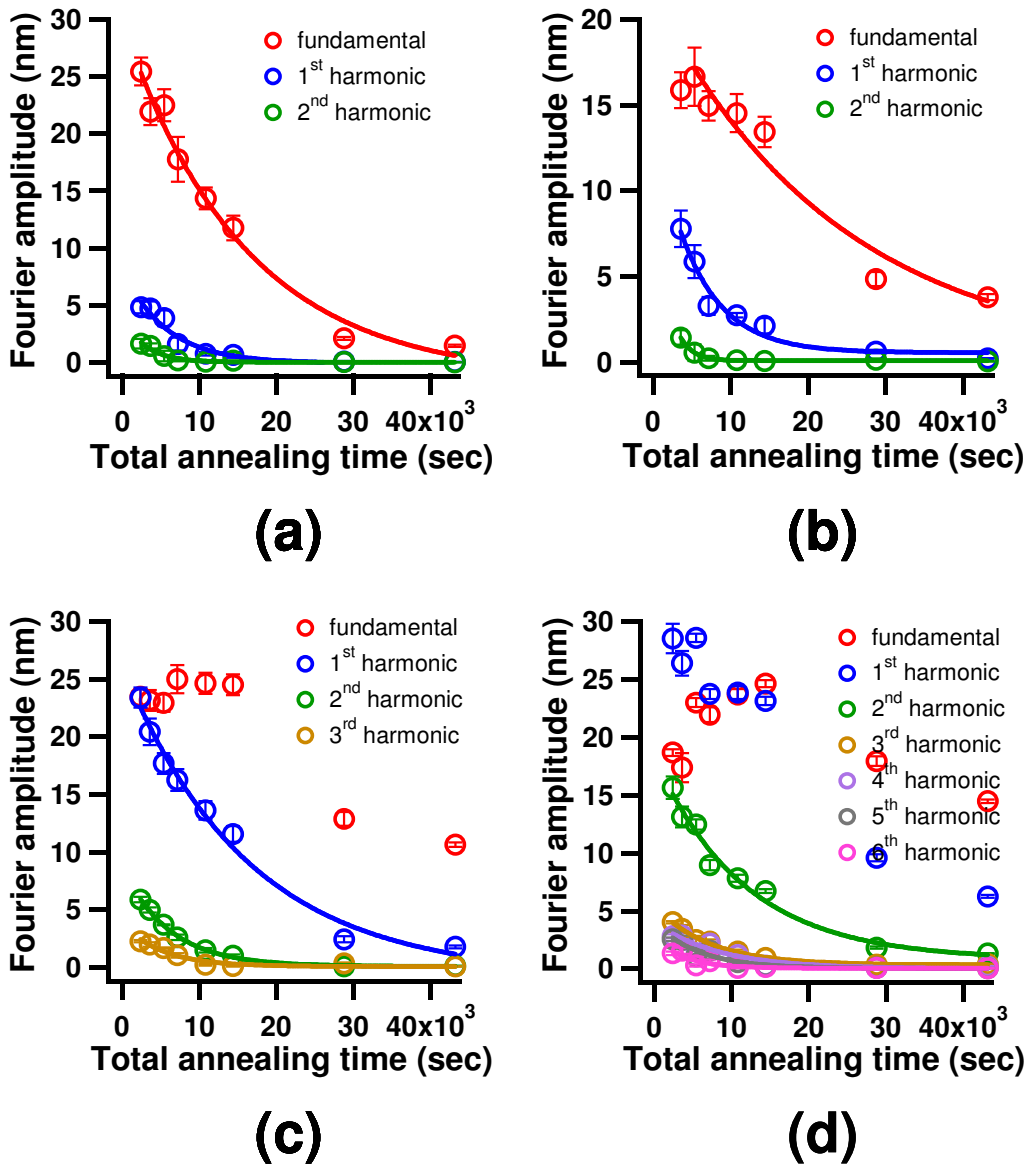


**Figure A.13** Relaxation of the amplitudes for corresponding Fourier components obtained by FFT from the average cross-sectional AFM line profiles, as functions of total annealing time, for different arrays of grooves with groove width/periodicity of: (a) 35.2 nm / 86.3 nm, (b) 41.0 nm / 307.6 nm, (c) 57.4 nm / 448.8 nm, (d) 62.5 nm / 617.2 nm.

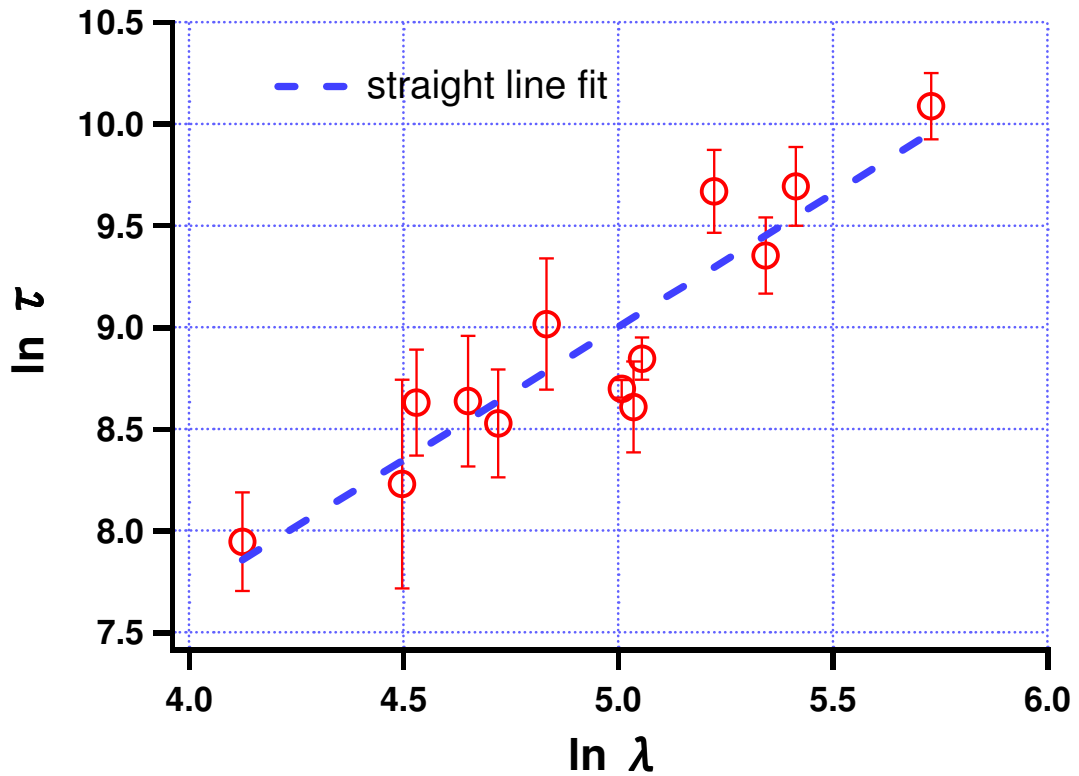


**Figure A.14** Plot of logarithm of the relaxation time ( $\tau$ ) obtained from the simple exponential fit of some of the relaxation curves shown in figure A.13 plotted versus logarithm of the wavelength ( $\lambda$ ) for corresponding Fourier components obtained by FFT from the AFM measured average cross-sectional line profiles. The overall data points shown in this plot were well fitted by a straight line with a slope of  $1.31 \pm 0.166$ .

## ***Appendix B: X-ray Photoelectron Spectroscopy (XPS)***

X-ray photoelectron spectroscopy (XPS, or known as “ESCA” standing for “Electron Spectroscopy for Chemical Analysis”) is a surface analysis technique which provides information such as elemental composition, empirical formula, chemical state, and electronic state of the elements that exist within a material. The spectra are obtained by irradiating a material with a beam of X-rays while simultaneously measuring kinetic energy and number of core-level electrons escaping from the near-surface (i.e. < 10 nm under the surface) of the spot being analyzed. XPS requires working under ultra-high vacuum (UHV) conditions in order to provide long enough mean-free-path for photoelectron to reach the detector.

The principle of XPS is based on the photoelectric effect where the concept of the photon was used to describe the ejection of electrons from the surface when photon impinging upon it, schematic shown in figure B.1. This process can be expressed as following equation,

$$E_B = h\nu - E_K - \phi$$

where  $E_B$  is the binding energy of the electron in the atom,  $h\nu$  is the photon energy (typically from 200 to 2000 eV) of the X-ray source,  $E_K$  is the kinetic energy of the ejected electron that is detected by the spectrometer, and  $\phi$  is the spectrometer work function.<sup>B.1</sup> Al K $\alpha$  source (1486.5 eV) or Mg K $\alpha$  source (1253.6 eV) is the common choice of photon energy.

The XPS technique is highly surface specific due to the short range of photoelectrons that are excited from the material. The energy of the photoelectrons leaving the sample is determined using an analyzer and this gives a spectrum with a series of photoelectron peaks. The binding energies of the peaks are characteristic of each element. With appropriate sensitivity factors, the peak areas can be used to determine the composition of the sample surface. The shape of each peak and the binding energy can be altered by the chemical state of the irradiated atom, which allows XPS to provide chemical bonding information as well. Normally, in the outmost 10 nm of the sample surface, XPS can detect all elements (present at concentration > 0.1 atom %) except hydrogen (H) and helium (He).<sup>B.1</sup>

One of the important applications of XPS in material analysis is compositional depth profiling which detects the variation of elemental composition with depth. The depth profiling analysis can be categorized by destructive and non-destructive.

For the non-destructive depth profiling, the escape depth of a photoelectron increases with its kinetic energy in the energy range higher than 50 eV. By observing the dependence of peak intensity on the photoelectron kinetic energy, one can deduce the escape depth via either varying photoelectron take-off angle<sup>B.2</sup> or varying energy of source photon at a given take-off angle<sup>B.3</sup>. Such analysis gives very precise measurement in thickness for ultra thin films (e.g. the precision is  $\pm 0.1$  nm for film thickness < 2 nm).

The destructive depth profiling is achieved by bombardment of the material surface with Ar<sup>+</sup> ions at controlled power and timing.<sup>B.4</sup> After certain amount of time of such “bombardment erosion”, the composition is analyzed before next

bombardment starts. Thus a composition depth profiling is obtained. This provides the benefit for measuring thin film thickness larger than 10 nm.

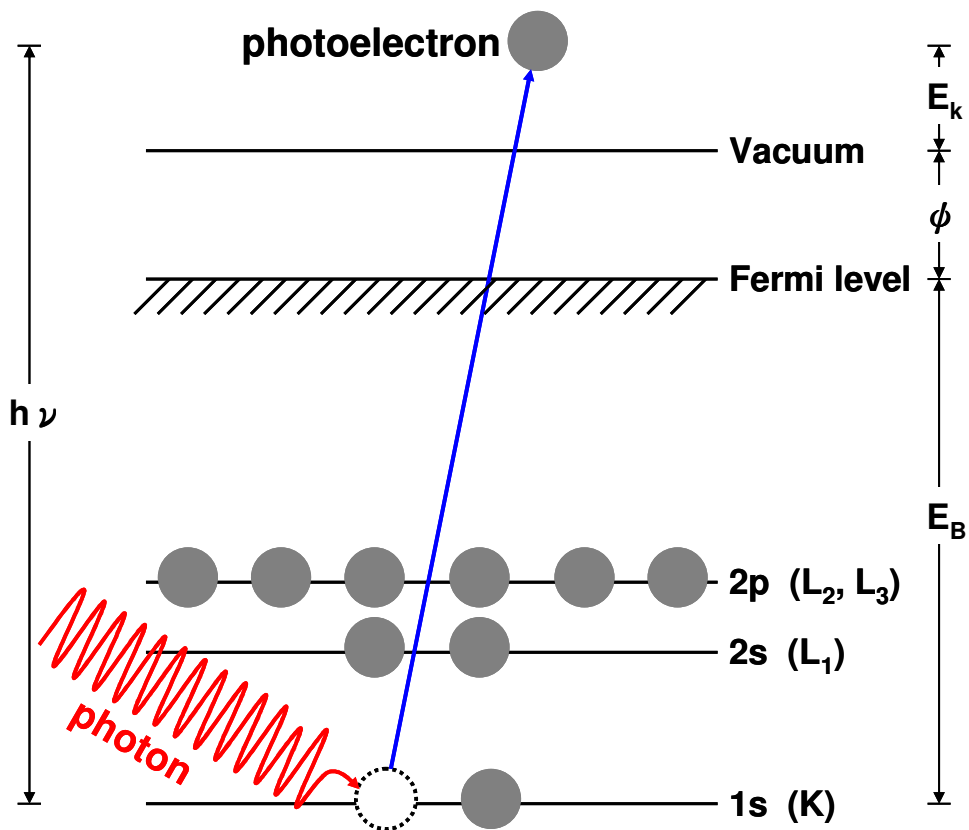


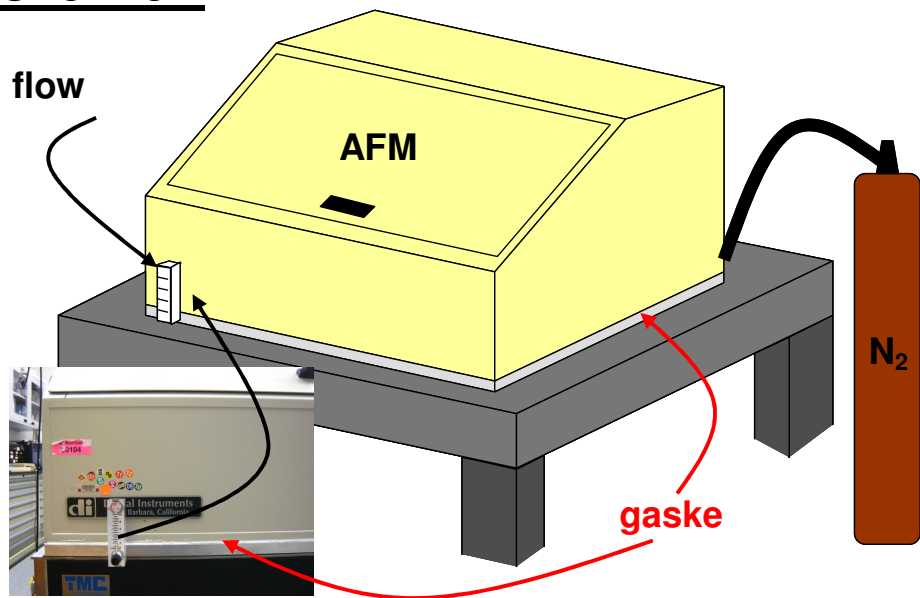
**Figure B.1** Schematic of the principle of X-ray photoelectron spectroscopy (XPS). A core level electron is ejected with kinetic energy ( $E_K$ ) by an incident photon with energy ( $h\nu$ ) higher than the sum of binding energy ( $E_B$ ) and instrumental work function ( $\phi$ ).

## ***Appendix C: Ambient-controlled AFM***

When an AFM is operated under ambient condition, water, which is present in the air and on the substrate, forms a meniscus between the apex of the probe and the substrate surface. The resulting attractive capillary force can both cause deformation, and move particles with comparable size on the substrate surface. Moreover, the change of the capillary force can lead to unstable and uncontrollable scanning conditions during the force curve measurement, which can trigger additional elastic or even plastic deformations on both the probe and sample surface.<sup>C.1, C.2</sup>

To reduce the effect caused by the water meniscus during our force curve measurement, we performed our experiments in an ambient-controlled AFM in which we purge the AFM chamber with dry nitrogen for certain amount of time. Figure C.1 shows a schematic drawing as well as photographs of this modified AFM setup. Between the housing bottom and the surface of the vibration-isolating table, we added a homemade half-inch thick aluminum gasket which allows us to introduce dry nitrogen into the chamber. An additional outlet on the gasket is set with connection to a flow meter in order to let us to monitor the nitrogen flow inside the chamber. For better sealing, we placed rubber strips between the housing bottom and the gasket top, between the gasket bottom and the isolation table surface, and at the edges of the front lid. In addition, the opening on the back of the housing for the AFM electronic system wiring is sealed using room-temperature-curing silicone rubber putty (Alley Goop).

## Overview



## Back-side view

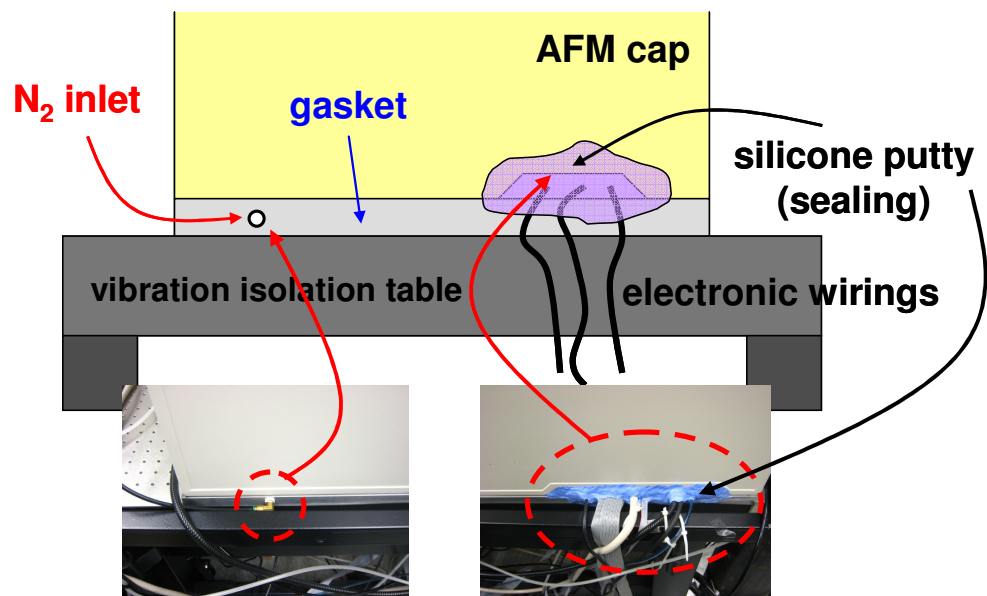


**Figure C.1** Schematic drawing and corresponding pictures of the modified AFM with the function of ambient controlling.

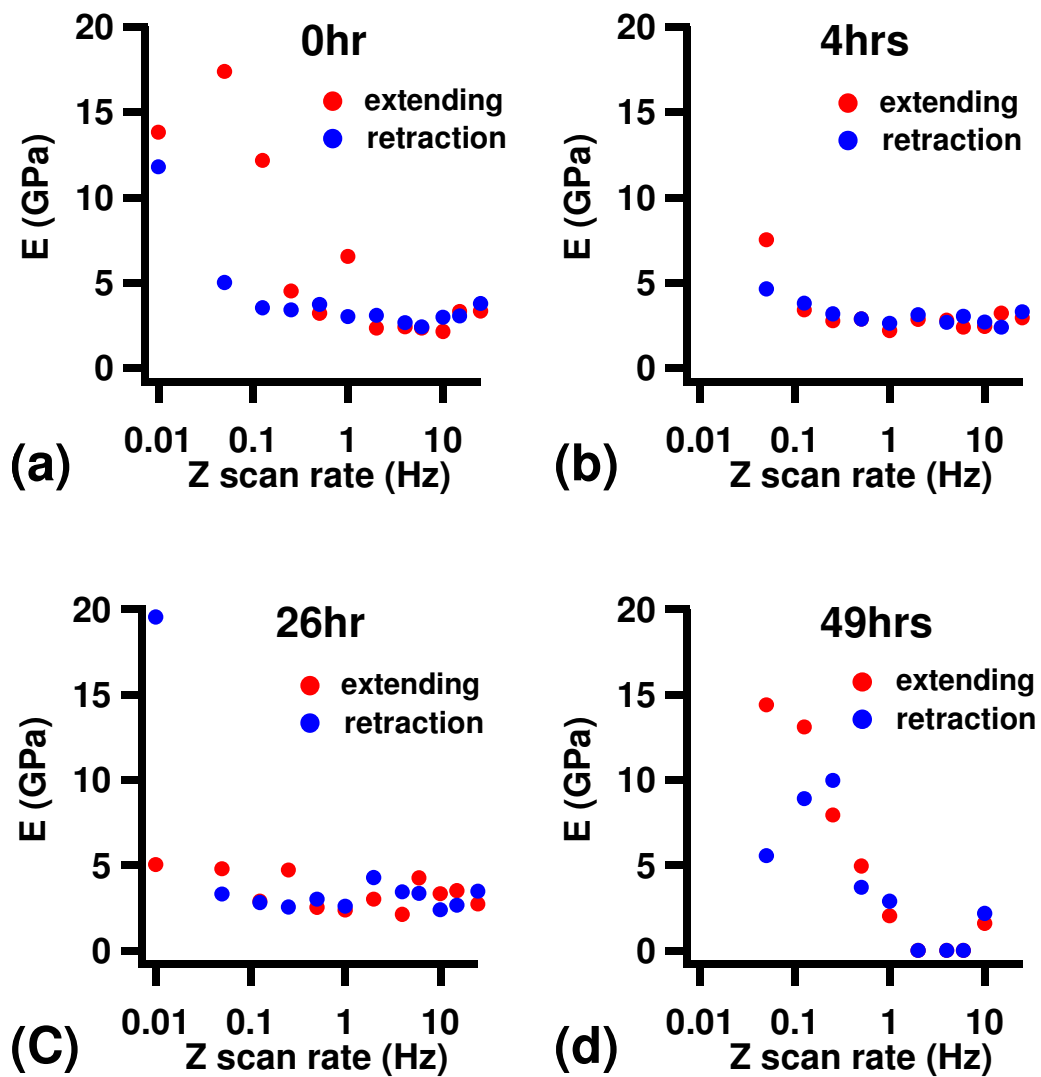
Before carrying out force curve measurements on plasma-etched polystyrene films by using our modified ambient-controlled AFM, we determined the proper conditions. We investigated how force curves are affected by varying following parameters during measurement: the purging time of dry nitrogen, the scan rate of cantilever during force curve acquisition, and the z-directional offset of initial position of cantilever where the cycles of measurements begin. In these investigations we used poly(methyl methacrylate) (PMMA) films whose elastic properties are well known. We fixed the range of the cantilever motion during force curve measurements at 70 nm. We checked the variation in the elastic modulus ( $E$ ) extracted from the measured force curves, utilizing the procedure proposed by Lin et al.<sup>C.3, C.4</sup>, and described in section 2.3.3.2.

Figure C.2(a)-(d) shows the measured elastic modulus as a function of Z-directional scan rate with different dry nitrogen purging time. Note that the Z-directional scan offset which is determined with respect to the zero-deflection point, in the part of repulsive regime of the force curve, was maintained at 4.5 nm. We see that the values of extracted elastic modulus from the approach and retraction curves are more consistent, and close to the literature value<sup>C.5</sup> with a wider range of Z-directional scan rate, when measurements were done after 4-hour dry nitrogen purging, while we see more scattered results when done in the air or after longer purging time.

In figure C.3(a)-(c), the effects of dry nitrogen purging time and Z-directional scan offset on the values of extracted elastic modulus from approach and retraction curves respectively are presented. Note that during this series of tests we kept the Z-

directional scan rate at 1 Hz. We found that keeping the offset below 5 nm results in consistent and close-to-literature-values of the elastic modulus, both for approach and retraction curves under a wide range of dry nitrogen purging time.

Based on these investigations, we conclude force curve measurement under dry nitrogen ambient is essential. In the study case of PMMA, we found that the best conditions for measuring the force curve which resulting in consistent elastic modulus compared to literature values in our modified AFM system is summarized as following: first, purge with dry nitrogen before measurement for at least 4 hours; second, keep the Z-directional scan rate at or below 1 Hz; and third, move the cantilever toward the sample surface for 4.5 nm beyond the zero-deflection point in the repulsive part of the force curve.



**Figure C.2** Extracted elastic modulus ( $E$ ) of PMMA from approach and retraction force curves as a function of Z-directional scan rate, under various amount of dry nitrogen purging time: (a) in air; (b) 4 hours; (c) 26 hours; (d) 49 hours.

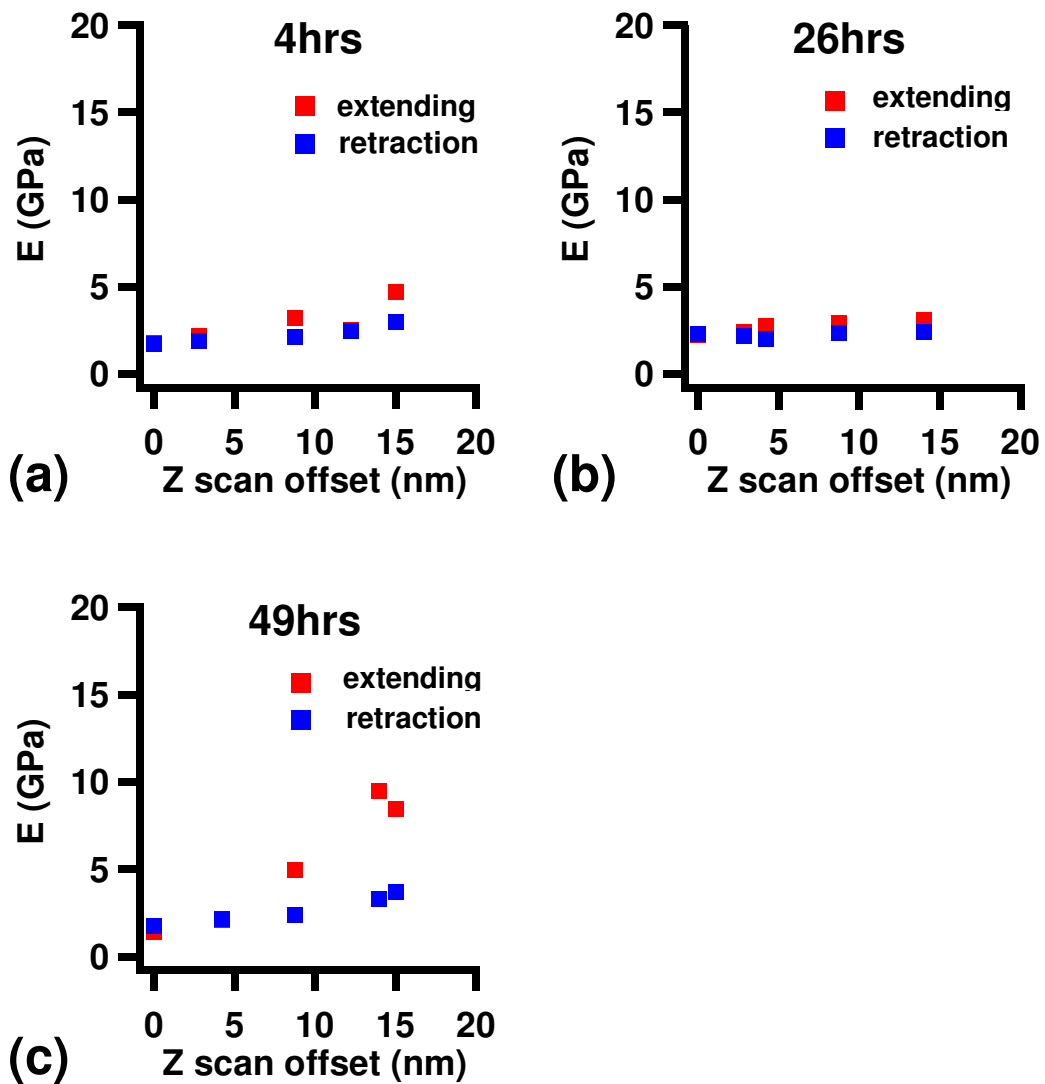


**Figure C.3** Extracted elastic modulus ( $E$ ) of PMMA from approach and retraction force curves as a function of Z-directional scan offset, under various amount of dry nitrogen purging time: (a) 4 hours; (b) 26 hours; (c) 49 hours.

## ***Appendix D: FORTRAN program code for analyzing measured force curves***

AFM-measured force curves were analyzed with the approach suggested by Lin et al., and we used the program coded by FORTRAN to perform the overall algorithm. Figure D.1 shows a schematic process flow of using this program. Before using this program, the measured force curve data are saved in ASCII format. In the example in figure D.1, we rename the saved ASCII raw data file as “pri\_polystyrene”, and placed this file and the FORTRAN program related files in the same file folder before executing the program, see the top left part in figure D.1. Next we execute the program by clicking the .exe file (marked blue dashed line). Input the ASCII raw data file name, then follow the instruction to input the materials constants (e.g. tip radius, elastic modulus of tip material, etc.). In addition, the range and the number of data points can be defined by input the initial (N1) and destination (N2) point for range and an integer value (idata) for the number of data points to be treated.

$$\text{Number of data pts to be treated} = \frac{\text{Total number of data pts}}{\text{idata}}$$

After inputting all the values required, the program begins to run the algorithm, and generates a set of DAT files named beginning with the input ASCII file name for the analyzed results, see the example files shown in the bottom left part of figure D.1.

The generated DAT files, except for the one named XXX\_RECORD, are all able to be loaded and plotted by Igor data analysis package. The numbers 1 and 2 in some file names stand for “approach” and “retract” respectively. The meanings of some of the generated DAT files in the example shown in figure D.1 are summarized as following:

- “XXX\_D-P” – the raw  $D_{pd}$ -versus- $\delta$  data (both approach and retract curves)
- “XXX\_D-Z” – the raw  $D_{pd}$ -versus- $Z_{piezo}$  data (both approach and retract curves)
- “XXX\_D-P-Z1” – the selected  $D_{pd}$ -versus- $\delta$ -versus-  $Z_{piezo}$  data points in the approach force curve by determining N1, N2, and idata
- “XXX\_LJfit\_Cur1” – the data of the L-J fit for the selected approach  $D_{pd}$ -versus- $\delta$  data points
- “XXX\_LJfit\_SUM1” – the least MSE of “XXX\_LJfit\_Cur1”
- “XXX\_PWfit\_Cur1” – the data of the “power + linear” function fit for the selected approach  $D_{pd}$ -versus- $\delta$  data points
- “XXX\_PWfit\_SUM1” – the least MSE of “XXX\_PWfit\_Cur1”
- “XXX\_PTfit\_Cur1” – the data of the P-T fit for the selected approach  $D_{pd}$ -versus- $Z_{piezo}$  data points
- “XXX\_PTfit\_SUM1” – the  $\alpha$  values used in the P-T fitting for “XXX\_PTfit\_Cur1”, and the corresponding  $Z_0$ ,  $D_0$ , and  $a$  which result in the least MSE
- “XXX\_RECORD” – a summary of the fitting result of the least MSE, including ( $D^*$ ,  $\delta^*$ ), ( $D_1$ ,  $\delta_1$ ), ( $D_0$ ,  $Z_0$ ),  $\alpha$ ,  $\gamma$ ,  $F_{ad}$ , and elastic modulus of sample ( $E$ ), etc..

Figure D.2 shows the FORTRAN code of the whole algorithm.

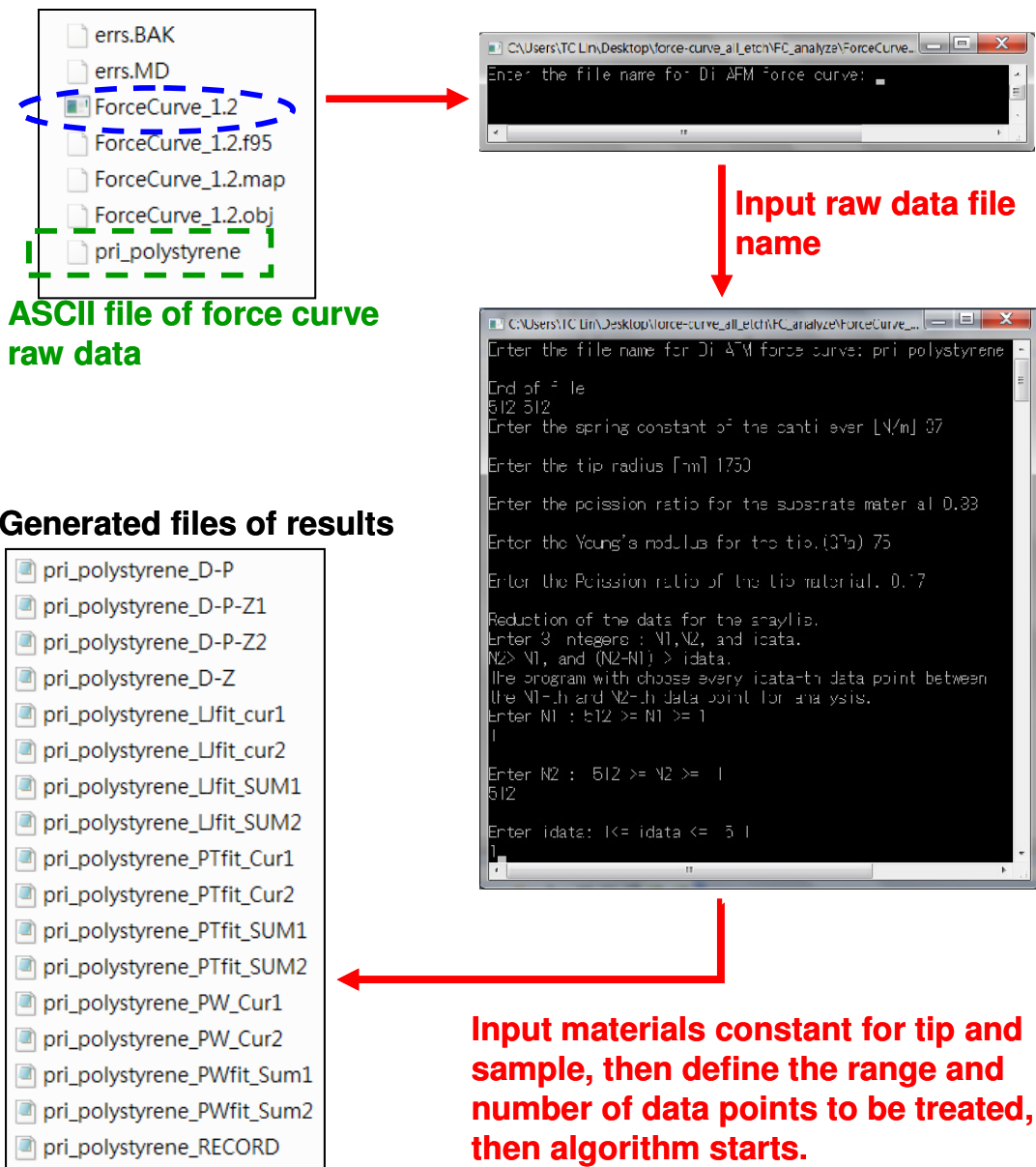


**Figure D.1** Schematic illustration of the execution and resulting files generated by the FORTRAN program code for the algorithm of the analysis of the raw data of the AFM measured force curve.

```

C   Last change: MD 16 Feb 2012 12:20 pm
!   Last change: HCK 7 Dec 2010 10:54 am
program ForceCurve
!Input
CHARACTER :: fn*80,line*80
DOUBLE PRECISION, ALLOCATABLE, DIMENSION (:): Zin,Din,Zout,Dout,Fin,PENin,Fout,PENout
DOUBLE PRECISION :: Kc, R, nu, Etip, Ytip, nutip
!general
INTEGER :: istat,i1,i2,i,j,k1,k2,j1,j2 ,IP,idot,idata
INTEGER :: Nt,Nt0
INTEGER,DIMENSION(1)::Dum1
DOUBLE PRECISION, ALLOCATABLE, DIMENSION (:): Qz1,Qz2,Qd1,Qd2,Qp1,Qp2
DOUBLE PRECISION, ALLOCATABLE, DIMENSION (:): Z,D,F,P
DOUBLE PRECISION, ALLOCATABLE, DIMENSION (:): m,B
DOUBLE PRECISION, ALLOCATABLE, DIMENSION (:): MSE1,MSE2,c
DOUBLE PRECISION, DIMENSION (100):: MSE3, Qz0,Qa0
DOUBLE PRECISION, ALLOCATABLE, DIMENSION (:): df
DOUBLE PRECISION :: pi
DOUBLE PRECISION :: Bpw,mpw
DOUBLE PRECISION :: D1,P1,Dp,Pp
DOUBLE PRECISION :: a0,Z0,D0,Fad
DOUBLE PRECISION :: Q0,Q1,Q2,Q3,QX,QY,QXX,QXY,QA,QB
DOUBLE PRECISION :: a,bt,S,Fn0
double precision :: a0bar,Fadbar, Gamma
INTEGER :: kpw,kLJ,kad,keq,kmin
INTEGER :: N1,N2
! Force curve key parameter
!DOUBLE PRECISION, ALLOCATABLE, DIMENSION (:): m1,m2,B1,B2
!DOUBLE PRECISION :: Bin,Bout,m_in,m_out
!DOUBLE PRECISION :: D1in,P1in,D1out,P1out,Dpin,Dpout,Ppin,Ppout
!DOUBLE PRECISION :: a0in,a0out,Z0in,Z0out,D0in,D0out,Fadin,Fadout
INTEGER :: Isin,Isout

pi = ATAN(1.0)*4.0

PRINT *, 'Enter the file name for Di AFM force curve: '
read *,fn
OPEN(101,FILE=fn)
i1=0 ; i2=0 ; j = 0
do
  READ(101,FMT='(A80)',IOSTAT=istat) line
  !PRINT *,line
  if (istat <0) exit
  if (TRIM(line)=='Extend Data') j=1
  if (TRIM(line)=='Retract Data')j=2
  if (TRIM(line)=='')j=0
  !read (line),
  if (j==1) i1=i1+1
  if (j==2) i2=i2+1
end do
CLOSE(101)
PRINT *, 'End of file'
i1=i1-1;i2=i2-1
PRINT *,i1,i2
ALLOCATE (Zin(i1),Din(i1),Zout(i2),Dout(i2),Fin(i1),PENin(i1),Fout(i2),PENout(i2))
OPEN(101,FILE=fn)
do
  READ(101,FMT='(A80)',IOSTAT=istat) line
  !PRINT *,line
  if (istat <0) exit
  if (TRIM(line)=='Extend Data') then
    do i=1,i1

```

```

        READ(101,*) Zin(i),Din(i)
        !PRINT *,i, Zin(i),Din(i)
    end do
    else if (TRIM(line)=='Retract Data') then
        do i=i1,1,-1
            READ(101,*) Zout(i),Dout(i)
            !print *,i, Zout(i),Dout(i)
        end do
    end if
    !read (line),
end do
CLOSE(101)

!Zin=Zin/1d9
!Din=Din/1d9
!Zout=Zout/1d9
!Dout=Dout/1d9

PRINT *,'Enter the spring constant of the cantilever [N/m] '
read *, Kc

PRINT *,'Enter the tip radius [nm] '
read *, R !; R = R/1d9

PRINT *,'Enter the poission ratio for the substrate material '
read *,nu

PRINT *,'Enter the Young',''', 's modulus for the tip.(GPa) '
read *,Etip ; Etip = Etip*1d9

PRINT *,'Enter the Poission ratio of the tip material. '
read *,nutip
!*****!
!
! Convert Delfection vs Tip translation into Delfection vs Penetration.
!
!*****!
Zout = Zout(1)-Zout
PENin=Zin-Din!*COS(15.0/180.0*pi)
PENout=Zout-Dout!*COS(15.0/180.0*pi)

idot=INDEX(fn,')-1
if (idot<=0) idot = LEN(TRIM(fn))

OPEN(110,FILE=fn(1:idot)['_RECORD.dat])
WRITE(110,*)'DATA FIEL : ',fn
WRITE(110,*)'Spring constant = ',Kc,' N/M'
WRITE(110,*)'Tip Radius = ', R, ' nm'
WRITE(110,*)'Tip Young''''s modulus = ',Etip/1d9, ' GPa'
WRITE(110,*)'Tip Poission ration = ',nutip
WRITE(110,*)'Poisson Ratio of the substance under test = ',nu

Nt0 = i1

OPEN(102,FILE=fn(1:idot)['_D-P.dat])
WRITE(102,(4(2x,A22)))'PENin',Din',PENout',Dout'
do i = 1,Nt0
    WRITE(102,(5(2x,E22.10))) PENin(i),Din(i),PENout(i),Dout(i)
end do
CLOSE(102)

```

```

OPEN(102,FILE=fn(1:idot)//'_D-Z.dat')
WRITE(102,'(5(2x,A22))')Zin',Din',Zout',Dout'
do i = 1,Nt0
  WRITE(102,'(4(2x,E22.10))') Zin(i),Din(i),Zout(i),Dout(i)
end do
CLOSE(102)

!*****!
!                                     !
! Select a portion of the data for analysis.           !
!                                     !
!*****!
PRINT *,'Reduction of the data for the anaylis.'
PRINT *,'Enter 3 integers : N1,N2, and idata.'
PRINT *,'N2> N1, and (N2-N1) > idata.'
print *,'The program with choose every idata-th data point between '
PRINT *,'the N1-th and N2-th data point for analysis. '
PRINT *,'Enter N1 :',Nt0,'>= N1 >= 1'
PRINT *,'
read *, N1
PRINT *,'Enter N2 : ',Nt0,'>= N2 >= ',N1
PRINT *,'
read *, N2
PRINT *,'Enter idata: 1<= idata <= ',N2-N1
PRINT *,'
read *,idata

  Nt = (N2-N1)/idata+1
PRINT *,'Nt = ',Nt
ALLOCATE (Z(Nt), D(Nt),F(Nt), P(Nt))
!ALLOCATE (m1(i1),m2(i2),b1(i1),b2(i2))
!ALLOCATE (MSE1(i1),MSE2(i2),df1(i1),df2(i2),c1(i1),c2(i2))
ALLOCATE (m(Nt),b(Nt))
ALLOCATE (MSE1(Nt),MSE2(Nt),df(Nt),c(Nt))

do IP=1,2
  Q0=REAL(idata,8)
  if (IP == 1) then
    do i=N1,N2
      if (MOD(i-N1,idata)==0) then
        Z((i-N1)/idata+1)=Zin(i)
        P((i-N1)/idata+1)=PENin(i)
        D((i-N1)/idata+1)=Din(i)

      end if
    end do

    WRITE(110,*) '***** Approach ***** '
  else
    do i=N1,N2
      if (MOD(i-N1,idata)==0) then
        Z((i-N1)/idata+1)=Zout(i)
        P((i-N1)/idata+1)=PENout(i)
        D((i-N1)/idata+1)=Dout(i)
      end if
    end do
    WRITE(110,*) '***** Retract ***** '
  end if

OPEN(102,FILE=fn(1:idot)//'_D-P-Z'//CHAR(48+IP)//'.dat')

```

```

WRITE(102,'(3(2x,A22))')Z_R//CHAR(48+IP),P_R//CHAR(48+IP),D_R//CHAR(48+IP)
do i = 1,Nt
  WRITE(102,'(3(2x,E22.10))')Z(i), P(i),D(i)
end do
CLOSE(102)

! *****!
!
! Overall Fit: for i = 2 to i2-20, divide the data into two parts.
! for j = 1 to i fit the data to a linear function y=a*x+c
! for j = i, i1 fit the data to a power law y = d(i)+(x-PENin(i))**1.5
!
! *****!

MSE1=-1.0; MSE2=-1.0
OPEN(103,file = fn(1:idot)['_PWfit_Sum']//CHAR(48+IP)['_dat'])
WRITE(103,'(7(A22,2x))')
'PW_PEN'//CHAR(48+IP),'PW_MSE_Total'//CHAR(48+IP),'PW_MSE_linear'//CHAR(48+IP) &
'PW_MSE_Power'//CHAR(48+IP),'Pw_m'//CHAR(48+IP),'PW_c'//CHAR(48+IP),'PW_b'//CHAR(48+IP)

PRINT *, 'Linear + 2/3 Power Law fit of the D-P curve.....'

Do i=2,Nt-2
  QX = SUM(P(1:i))
  QY = SUM(D(1:i))
  QXX = SUM(P(1:i)**2d0)
  QXY = SUM(P(1:i)*D(1:i))

  m(i)= (REAL(i,8)*QXY-QX*QY)/(REAL(i,8)*QXX-QX**2d0)
  c(i)= (QY-m(i)*QX)/REAL(i,8)
  MSE1(i)=SUM((m(i)*P(1:i)+c(i)-D(1:i))**2)/REAL(i,8)

  call PowerLaw(Nt,i,D,P,B(i),MSE2(i))

  write (103,'(7(E22.10,2x))')P(i),MSE1(i)+MSE2(i),MSE1(i),MSE2(i),m(i),c(i),B(i)
!PRINT *, P(i),MSE1(i)+MSE2(i),MSE1(i),MSE2(i),m(i),c(i),B(i)
  if (MOD(i,100)==0) PRINT *, ' data point ',i
END DO
CLOSE(103)
MSE1 = MSE1+MSE2
dum1 = MINLOC(MSE1,mask=MSE1>0);kpw=dum1(1)
mpw = m(kpw)
Bpw = b(kpw)
Q0 = C(kpw)

PRINT *, 'kpw = ',kpw
PRINT *, 'P*,D* = ',P(kpw),D(kpw)
WRITE(110,*)'P*,D* = ',P(kpw),D(kpw)

! *****!
!
! Export the optimum fit curve to file 'PowerLawfit_Cur.dat'
!
! *****!

OPEN(103,FILE=fn(1:idot)['_PW_Cur']//CHAR(48+IP)['_dat'])
WRITE(103,'(2(A22,2x))') 'Pwx'//CHAR(48+IP),'Pwy'//CHAR(48+IP)
DO i=1,kpw

```

```

WRITE(103,'(2(E22.10,2x))' P(i),mpw*P(i)+Q0
END DO

do i=kpw+1,Nt
  Q1 = (MAX(P(i)-P(kpw),0))**(1.5)
  WRITE(103,'(2(E22.10,2x))' P(i),D(kpw)+Bpw*Q1
end do
CLOSE(103)

PRINT *, 'Linear + 2/3 Power Law fit of the D-P curve finished.'

!*****!
!                                     !
! Find Minimum D for approach curve   !
!                                     !
!*****!

Dum1=MINLOC(D);kmin=Dum1(1) !; PRINT *,kmin,D(kmin)

!*****!
!                                     !
! Routine to fit data between (PENin(1),Din(1)) and (PENin(i),Din(i)) with y = Din(i), and !
! Data between (PENin(i),Din(i)) and (PENin(k1),Din(k1)) with Lennard-Jones potential like !
! curve : y = A*((B/r)**12+(B/r)**6)+Dref. !
!                                     !
!*****!
PRINT *, 'Linear + Lennard-Jones fit of the D-P curve.....'

df=-1
c=-1
Q0= MAXVAL(D(1:kmin))
MSE1=-1; MSE2=-1
OPEN(103,FILE=fn(1:idot)['_LJfit_SUM']//CHAR(48+IP)['_dat'])

WRITE(103,'(6(A22,2x))'['_LJ_PEN']//CHAR(48+IP),'['_LJ_MSE_total']//CHAR(48+IP),'['_LJ_MSE_Linear']//CHAR(48
+IP) &
      ,['_LJ_MSE_LJ']//CHAR(48+IP),'['_LJ_Dref']//CHAR(48+IP),'['_LC_c']//CHAR(48+IP)
do i=2,kmin-2
  ! Linera fit data point from 1 to i , to d = df(i), a constant but vary with the choice of i
  df(i)=D(i)
  MSE1(i)=SUM((D(1:i)-df(i))**2)/REAL(i,8)
  call LJfit(Nt,i,kmin,Q0,D,P,C(i),MSE2(i))
  !MSE1(i)=MSE1(i)+Q1*10
  !print *, i,PENin(i),MSE1(i),MSE2(i),df(i),c(i)
  ! Fit the data points from i to k1 with a Lennard-Johes like relation
  WRITE(103,'(6(E22.10,2x))' P(i),MSE1(i)+10000.0*MSE2(i),MSE1(i),MSE2(i),df(i),c(i)
  IF(MOD(i,50)==0)PRINT *,'data point ',i
end do
CLOSE(103)
MSE1=MSE1+2.0*MSE2
Dum1=MINLOC(MSE1,mask = MSE1>0); kLJ = Dum1(1)

!*****!
!                                     !
! Export optimum fit to file 'LJfit_cur.dat' !
!                                     !
!*****!

open (103,FILE=fn(1:idot)['_LJfit_cur']//CHAR(48+IP)['_dat'])
WRITE(103,'(2(A22,2x))'['_LJx']//CHAR(48+IP),'['_LJy']//CHAR(48+IP)
do j= 1,kLJ

```

```

WRITE(103,*) P(j),df(kLJ)
end do

QA = -4*(D(kmin)-Q0)
QB = (1d0/2d0)**(1d0/6d0)
do j=kLJ+1,kmin
  Q1 = 1.0-P(j)/P(kmin) ; !PRINT *,Q1
  Q1 = QB/(1.0+C(kLJ)*Q1) ; !PRINT *,Q1 /QB , 'a',Q1**12-Q1**6
  Q1 = QA*(Q1**12 - Q1**6) + Q0
  WRITE(103,*) P(j), Q1
end do
CLOSE(103)

PRINT *, 'Linear + Lennard-Jones fit of the D-P curve finished.'

!PRINT *,QB,Q1,Q0,Din(k1)

!*****!
!
! Search for (D1,W1) the zero deflection point
!
!*****!

D1=Df(kLJ)
do i=kmin,Nt-1
  if ((D(i)-D1)*(D(i+1)-D1) <0) then
    P1 = (D1-D(i)) / ( (D(i+1)-D(i))/(P(i+1)-P(i)) ) + P(i)
    keq=i
    !PRINT *,P(i),D(i)
    !PRINT *,P1,D1
    !PRINT *,P(i+1),D(i+1)
  else
    if (D(i)==D1) P1 = P(i)
  end if
end do

PRINT *,P1, D1 = ',P1, D1
write (110,*) 'P1, D1 = ',P1, D1
!*****!
!
! Search for (Dprime,Wprime) where the maximum adhesive force Fad occur
!
!*****!

dum1 = MINLOC(D(kpw:keq)); kad = dum1(1)-1+kpw
Dp = D(kad)
Pp = P(kad)
Fad= -Kc*(D1-DP)
!PRINT *,kpw,kad,keq
!PRINT *, MINVAL(D(kpw:keq)),D(kad)
PRINT *,Pp, Dp = ', Pp, Dp
PRINT *,Fad =',Fad
write (110,*) 'Pp, Dp = ', Pp, Dp
write (110,*) 'Fad =',Fad
!*****!
!
! Fit the data between kpw and i1 to PT (Pietrement - Troyon) model
!
!*****!
i=1
open (104,FILE=fn(1:idot)['_PTfit_SUM//CHAR(48+IP)'].dat')
WRITE (104,(5(A22,2x))'PT_Alpha//CHAR(48+IP), 'PT_Z0//CHAR(48+IP), 'PT_D0//CHAR(48+IP) &

```

```

, 'PT_a0//CHAR(48+IP) , 'PT_MSE//CHAR(48+IP)
do a = 0.01, 1.0, 0.01
  S = (-2.16d0)*a**(1.9d-2) + (2.7531d0)*a**(6.4d-2) + (7.3d-2)*a**(1.919d0)
  bt = (0.516d0)*a**(4d0) - (0.683d0)*a**(3d0) + (0.235d0)*a**(2d0) + (0.429d0)*a
  Fn0 = (( (1d0 + a)*S**(3.0/(4d0-2d0*Bt)) - a )**2d0 - 1d0 )*(-Fad)
  d0 = Fn0/Kc + D1
  CALL PTfit(Nt,kpw,Nt,Z,D,R,Kc,-Fad,a,Bt,S,d0,D1,Qz0(i),Qa0(i),MSE3(i))
  !PRINT *, 'P0,D0 ',(Qz0(i)-D0) ,D0
  write (104,'(5(E22.10,2x))') a, Qz0(i),d0,Qa0(i),MSE3(i)
  i=i+1
end do
CLOSE(104)

dum1=MINLOC(MSE3); j1 = dum1(1)

a = REAL(j1,8)*0.01
S = (-2.16d0)*a**(1.9d-2) + (2.7531d0)*a**(6.4d-2) + (7.3d-2)*a**(1.919d0)
bt = (0.516d0)*a**(4d0) - (0.683d0)*a**(3d0) + (0.235d0)*a**(2d0) + (0.429d0)*a
Fn0 = (( (1d0 + a)*S**(3.0/(4d0-2d0*Bt)) - a )**2d0 - 1d0 )*(-Fad)
d0 = Fn0/Kc + D1
z0 = Qz0(j1)
a0 = Qa0(j1)
OPEN(105,FILE=fn(1:idot)//'_PTfit_Cur//CHAR(48+IP)//'.dat')
WRITE(105,'(2(A22,2x))') 'PTx//CHAR(48+IP), 'PTy//CHAR(48+IP)
do i = kpw, Nt
  Q0 = ( a + sqrt(1d0 + Kc*(D(i)-d1)/(-Fad) ) )/(1 + a)
  Q1 = z0 + d(i) - d0 + a0**2.0/R*( Q0**(4.0/3.0) - S* Q0**(2.0/3.0*Bt) )
  WRITE(105,'(2(E22.10,2x))') Q1, D(i)
end do

a0bar = -0.451*a**4.0 + 1.417*a**3.0 - 1.365*a**2.0 + 0.950*a + 1.264
Fadbar = 0.267*a**2.0 - 0.767*a + 2.0
Gamma = -Fad/(R*Fadbar*pi)
Y = pi*Gamma*R*R*(a0bar/a0)**3.0
Ytip = 4.0*Etip/(1.0-nutip**2.0)/3.0
Y = 1.0/(1.0/Y-1.0/Ytip)
E = 3.0*(1-nu**2.0)*Y/4.0

PRINT *, 'alpha = ', a
PRINT *, 'p0, D0= ', (z0-d0), d0
PRINT *, 'a0bar = ', a0bar
PRINT *, 'a0 = ', a0, 'nm'
PRINT *, 'Gamma = ', Gamma, 'nN/nm'
PRINT *, 'E = ', E, 'nN/nm**2'
PRINT *, 'Y = ', Y, 'GPa'

write (110,*) 'alpha = ', a
write (110,*) 'p0, D0= ', (z0-d0), d0
write (110,*) 'a0bar = ', a0bar
write (110,*) 'a0 = ', a0, 'nm'
write (110,*) 'Gamma = ', Gamma, 'nN/nm'
write (110,*) 'Substrate Spring Constant K = ', Y, 'nN/nm**2'
write (110,*) 'Substrate Young', ''', ' Modulus E = ', E, 'GPa'
end do
CLOSE(110)

contains

```

```

!*****!
!
!  subroutine PowerLaw(N,K,D,P,B,MSE)
!
!*****!

subroutine PowerLaw(N,K,D,P,B,MSE)
DOUBLE PRECISION,INTENT(IN),DIMENSION(N)::D,P
INTEGER, INTENT(IN) :: N,K
DOUBLE PRECISION, INTENT(OUT) :: B,MSE

DOUBLE PRECISION, DIMENSION(N-K+1) :: Z,F
DOUBLE PRECISION :: di,zi
double precision :: f1,f2,f3,b1,b2,b3
di = D(k); zi = P(k)

b1 = 0d0; b2=1d0
!Z=(P(K:N)-zi)
Z=(MAX(P(K:N)-zi,0.0))**(1.5)
!PRINT *,k,z(1)
do
  F=2*(di+b1*Z-D(K:N))*Z
  f1=SUM(F)

  F=2*(di+b2*Z-D(K:N))*Z
  f2=SUM(F)
  if (K>490) then
    !PRINT *,k
    !PRINT *,b1,b2
    !PRINT *,f1,f2
  end if

  if (f1*f2<0) exit
  b1=b1-0.1
  b2=b2+0.1

end do

do
  b3=(b1+b2)/2
  F=2*(di+b3*Z-D(K:N))*Z
  f3=SUM(F)
  if (f3*f1<0) then
    b2=b3
    f2=f3
  else if (f3*f2<0) then
    b1=b3
    f1=f3
  end if
  if (ABS(f3)<1e-8) exit
  if (K>490) then
    !PRINT *,k
    !PRINT *,b1,b3,b2
    !PRINT *,f1,f3,f2
  end if
end do
!PRINT *,k
!PRINT *,b1,b3,b2
!PRINT *,f1,f3,f2
B=b3
F=di+b3*Z

```

```

MSE = SUM((F-D(K:N))**2)/REAL(N-K+1,8)
end subroutine

!*****!
!
! Subroutine LJfit(N,L,K,Dref,D,PEN,C,MSE)
!
!*****!

subroutine LJfit(N,L,K,Dref,D,PEN,C,MSE)
INTEGER, INTENT (IN):: N,L,K
DOUBLE PRECISION , INTENT(IN)::Dref
DOUBLE PRECISION , intent (IN), DIMENSION(i1):: D(N),PEN(N)
DOUBLE PRECISION,INTENT (OUT) :: MSE,C

DOUBLE PRECISION,DIMENSION(K-L+1)::x,x1,DD,DD1,DD0
DOUBLE PRECISION :: A,B, F0,Wk,F1,F2,F3
DOUBLE PRECISION :: C1,C2,C3
INTEGER :: i,j
Wk= PEN(K)
A =-4*(D(K)-Dref)
B=(1d0/2d0)**(1d0/6d0)
DD0=D(L:K)
F0=2*SUM(D(L:K))
c=-1
C1=1;C2=10
X1 = 1.0-PEN(L:K)/Wk
do
  X=B/(1.0+C1*X1)
  DD = A*(X**12d0 - X**6d0 ) + Dref
  DD1 = 6*A/B*(-2*X**13d0 + X**7d0)*X1
  F1= 2d0*SUM(DD1*(DD-DD0))
  X=B/(1d0+C2*X1)
  DD = A*(X**12d0 - X**6d0 ) + Dref
  DD1 = 6*A/B*(-2d0*X**13d0 + X**7d0)*X1
  F2= 2*SUM(DD1*(DD-DD0))
  !PRINT*,C1,C2
  !PRINT*,F1,F2
  if (F2*F1<0) exit
  C2=C2+0.1
  C1=C1-0.01
end do

do
  C3 = (C1+C2)/2d0
  X = B/(1d0+C3*X1)
  DD = A*(X**12d0 - X**6d0 ) + Dref
  DD1 = 6*A/B*(-2d0*X**13d0 + X**7d0)*X1
  F3= 2d0*SUM(DD1*(DD-DD0))
  if (F1*F3<0) then
    C2=C3
    F2=F3
  else IF(F2*F3<0) then
    C1=C3
    F1=F3
  else if (F3==0) then
    C=C3
    exit
  else
    end if
  !print *,C1,C2,C3

```

```

!print *,F1,F2,F3

if ((ABS(F3) <1e-8)) exit

!PRINT *,L
end do
C=C3
X = B/(1d0+C3*X1)
DD = A*(X**12d0 - X**6d0 ) + Dref
MSE=SUM((DD-DD0)**2d0)/REAL(K-L+1)
end subroutine

!*****!
!                                     !
! Subroutine PTfit                    !
!                                     !
!*****!

SUBROUTINE PTfit(N,k1,k2,Z,D,R,kc,Fad,a,Bt,S,d0,d1,z0,a0,MSE)
INTEGER, INTENT (IN) :: N, k1,k2
DOUBLE PRECISION , INTENT (IN), DIMENSION (N):: Z , D
DOUBLE PRECISION , INTENT (IN) :: R, Kc,Fad, a,Bt, S, d0, d1
DOUBLE PRECISION , INTENT (OUT) :: z0, a0, MSE

DOUBLE PRECISION, DIMENSION (K2-K1+1) :: X, Y, W
DOUBLE PRECISION :: a02, dk, Q11,Q12,Q13,Q21,Q22,Q23

!PRINT *,a,S,Bt!,d0,z0,a02

X = ( a + sqrt(1d0 + Kc*(D(k1:k2)-d1)/Fad ) )/(1 + a)
!do i=1,k2-k1+1
!PRINT *,X(i)
!end do
Y = ( X**(4d0/3d0) - S*X**(2d0/3.0*Bt) )/R
W = D(k1:k2) - d0 - Z(k1:k2)
dk =REAL( k2-k1+1,8)
Q11 = dk
Q12 = SUM(Y)
Q13 = -SUM(W)
Q21 = Q12
Q22 = SUM(Y**2.0)
Q23 = -SUM(Y*W)
z0 = (Q13*Q22-Q23*Q12)/(Q22*Q11-Q12*Q21)
a02 = (Q13-Q11*z0)/Q12

MSE = SUM((z0+a02*Y+W)**2.0)
a0=SQRT(a02)
END SUBROUTINE

END program

```

**Figure D.2** FORTRAN program code for the algorithm of analysis of the AFM measured force curve.

## ***Appendix E: Finite element method with COMSOL***

Finite element method (FEM) is one of several numerical methods that can be used to solve complex problems, and has become a dominant tool in solving scientific and engineering problems nowadays. As its name states, it takes a complex problem and breaks it down into a finite number of simple problems. For example, a continuous structure theoretically has an infinite number of simple problems, but FEM approximates the behavior of the continuous structure by analyzing a finite number of simple problems. Each element in the finite element method is one of these simple problems. Each element (usually called “mesh”) in a finite element model has a fixed number of nodes that define the element boundaries to which loads and boundary conditions can be applied. In general, the smaller the element, the closer we can approximate the geometry of the structure, the applied load, as well as the stress and the strain gradients. However, it’s not always true. In fact, there is a tradeoff that the smaller the element, the more computational power, e.g. computer memories and speed, is required to solve the problem. Thus, a good strategy of optimizing the element size can greatly reduce the time needed for computation without compromising of the quality of analyzed result.

In general, a finite element method consists of three principle steps:<sup>E.1</sup>

### **1. *Preprocessing:***

One constructs a model of the structure to be analyzed in which the geometry of the structure is divided into a number of elements connected at discrete points called “nodes”. Certain of these nodes will have fixed

displacements, while others will have prescribed loads. Generally, the model includes the physics to be applied, material properties (e.g., density and elastic modulus), coordinate system, and boundary conditions, etc.

### ***2. Analysis:***

The structure geometry and corresponding parameters preset by the preprocessing step are used as input to the FEM program (or code) itself, which constructs and solves a system of linear or nonlinear algebraic equations. During the analyzing process, the governing equations are assembled into matrix form and solved numerically. This step is normally a batch process, and is the most consuming part of the computation resource.

### ***3. Postprocessing:***

The postprocessing process generally begins with a checking process of numerical error, or this checking step is sometime occurring during the analysis step depending on how the procedure is defined. Once the solution is verified to be within the acceptable numerical error, the quantities of interest can be further examined. Numbers of options are available for displaying the quantities, the choice of which depends on the mathematical form of the quantity as well as its physical meaning.

In the three principle steps for a finite element method analysis, the preprocessing and the post processing are usually time-consuming, while the process of analysis is highly demanding on computation resource. Which FEM package to use is the subject of choices involving personal preferences as well as package functionality. Where to run the FEM package depends on the type of analysis being

performed. Typically, a finite element solution requires a fast, modern computation system for acceptable performance. Memory requirements are normally dependent on the code, but in the interest of performance of computation, undoubtedly the more the better, with a typical range measured in gigabytes per user. Several key factors for processing power, e.g., clock speed, cache memory, pipelining and multi-processing, all contribute to the bottom line for the acceptable performance. These analyses can run for hours even on the fastest systems, thus computing power is of great importance to conduct a efficient finite element method analysis.

We use COMSOL Multiphysics FEM package for our numerical simulation of the nano-indentation system, with interactive graphical user interfacial (GUI) environment and built-in fundamental physics models which facilitate the massive works needed for pre- and post-processing in the FEM analysis (see the example in figure E.1 for the operating environment of COMSOL for pre- and post-processing). The FEM analysis is operated on a Dell Studio XPS 8100 machine with an Intel Core™ i7 CPU of maximum clock speed of 2.80 GHz and a RAM of 8.00 GB, which is operated on a Windows 7 Home Premium 64-bit operating platform.

We use the structural mechanics module of COMSOL to simulate the penetration depth of a spherical probe at the apex position with respect to varying load applied on the sphere, see the example geometry in figure E.1.

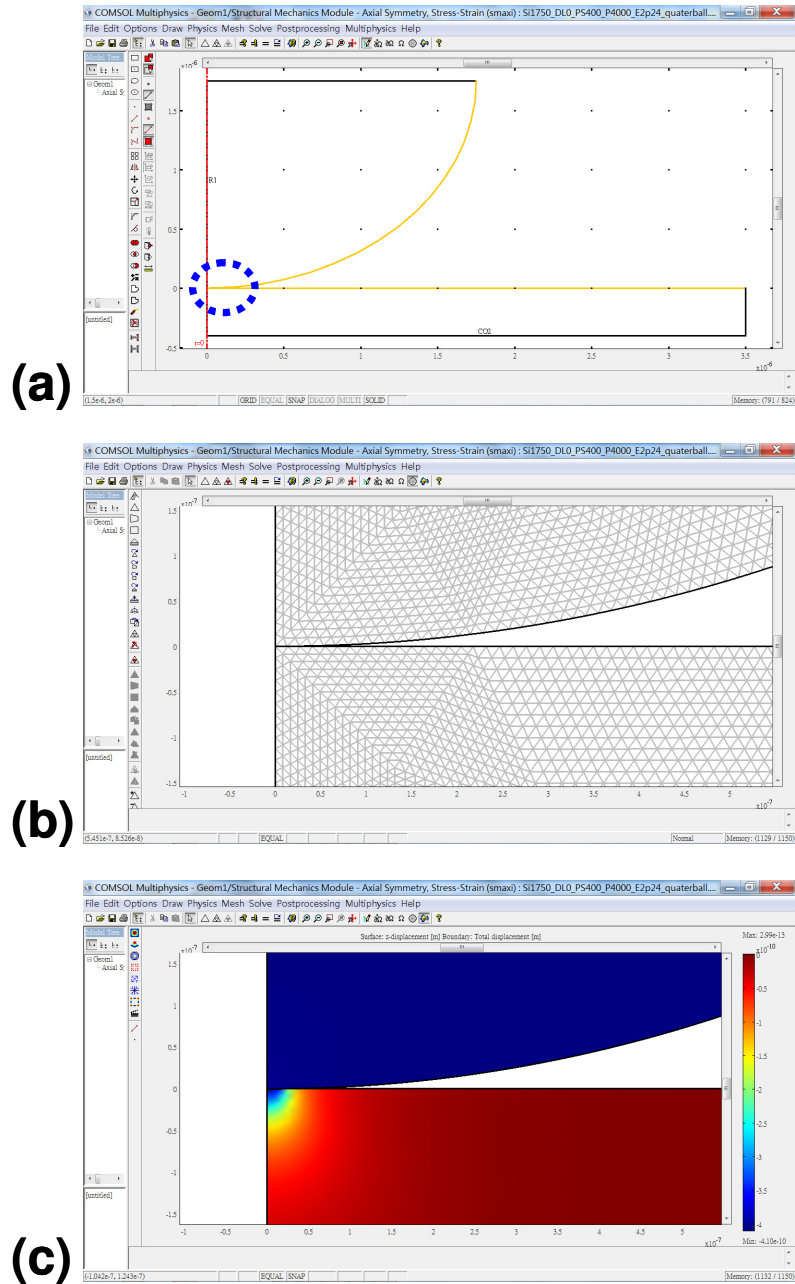


**Figure E.1** Examples of the operating environment of COMSOL Multiphysics FEM package in a 2D axial-symmetric coordinate system: (a) CAD drawing mode, (b) Mesh mode (zoomed-in), and (c) Post-processing mode (zoomed-in Z-direction displacement map).

## E.1 Theory background of stress-strain relationship in COMSOL

We use the 2D Axial Symmetry Stress-Strain Application mode of the COMSOL Structure Mechanics Module for our simulation. In this section, I will give a brief introduction to the theory that COMSOL's calculation is based on.

Consider a point of an object which deforms following the small-displacement assumption in a 3D Cartesian coordinate space, the strain components at that point are given as following,<sup>E.2</sup>

$$\begin{aligned}\varepsilon_x &= \frac{\partial u}{\partial x} & \gamma_{xy} &= \frac{\partial u}{\partial y} + \frac{\partial v}{\partial x} \\ \varepsilon_y &= \frac{\partial v}{\partial y} & \gamma_{yz} &= \frac{\partial v}{\partial z} + \frac{\partial w}{\partial y} \\ \varepsilon_z &= \frac{\partial w}{\partial z} & \gamma_{xz} &= \frac{\partial u}{\partial z} + \frac{\partial w}{\partial x}\end{aligned}, \quad (\text{E.1})$$

where  $\varepsilon$  and  $\gamma$  denote normal and shear strains, while  $u$ ,  $v$ ,  $w$  are the displacement components in  $x$ ,  $y$ ,  $z$  directions respectively. In general, these strain components can be represented in a form of symmetric strain tensor,

$$\boldsymbol{\varepsilon} = \begin{bmatrix} \varepsilon_x & \gamma_{xy} & \gamma_{xz} \\ \gamma_{xy} & \varepsilon_y & \gamma_{yz} \\ \gamma_{xz} & \gamma_{yz} & \varepsilon_z \end{bmatrix}. \quad (\text{E.2})$$

The same as the strain, the corresponding stress components can be described by the symmetric stress tensor,

$$\boldsymbol{\sigma} = \begin{bmatrix} \sigma_x & \tau_{xy} & \tau_{xz} \\ \tau_{yx} & \sigma_y & \tau_{yz} \\ \tau_{zx} & \tau_{zy} & \sigma_z \end{bmatrix} \quad \begin{matrix} \tau_{xy} = \tau_{yx} \\ \tau_{xz} = \tau_{zx} \\ \tau_{yz} = \tau_{zy} \end{matrix}, \quad (\text{E.3})$$

where  $\sigma$  and  $\tau$  are normal and shear stress respectively. In the linear elastic limit, the stress and the strain follow the relationship,

$$\boldsymbol{\sigma} = D\boldsymbol{\varepsilon}, \quad (\text{E.4})$$

where  $D$  is a 6×6 elasticity matrix, and the stress and strain components are represented in vector form with the six stress and strain components in column vectors defined as,

$$\boldsymbol{\sigma} = \begin{bmatrix} \sigma_x \\ \sigma_y \\ \sigma_z \\ \tau_{xy} \\ \tau_{yz} \\ \tau_{xz} \end{bmatrix} \quad \boldsymbol{\varepsilon} = \begin{bmatrix} \varepsilon_x \\ \varepsilon_y \\ \varepsilon_z \\ \gamma_{xy} \\ \gamma_{yz} \\ \gamma_{xz} \end{bmatrix}. \quad (\text{E.5})$$

For an isotropic material, the elasticity matrix  $D$  is defined as,

$$D = \frac{E}{(1+\nu)(1-2\nu)} \begin{bmatrix} 1-\nu & \nu & \nu & 0 & 0 & 0 \\ \nu & 1-\nu & \nu & 0 & 0 & 0 \\ \nu & \nu & 1-\nu & 0 & 0 & 0 \\ 0 & 0 & 0 & \frac{1-2\nu}{2} & 0 & 0 \\ 0 & 0 & 0 & 0 & \frac{1-2\nu}{2} & 0 \\ 0 & 0 & 0 & 0 & 0 & \frac{1-2\nu}{2} \end{bmatrix}, \quad (\text{E.6})$$

where  $E$  is the elastic modulus (known as “Young’s modulus”), and  $\nu$  is Poisson’s ratio of the material. The equilibrium equations expressed in the stresses for 3D are,

$$\begin{aligned} -\frac{\partial \sigma_x}{\partial x} - \frac{\partial \tau_{xy}}{\partial y} - \frac{\partial \tau_{xz}}{\partial z} &= F_x \\ -\frac{\partial \tau_{xy}}{\partial x} - \frac{\partial \sigma_y}{\partial y} - \frac{\partial \tau_{yz}}{\partial z} &= F_y, \\ -\frac{\partial \tau_{xz}}{\partial x} - \frac{\partial \tau_{yz}}{\partial y} - \frac{\partial \sigma_z}{\partial z} &= F_z \end{aligned} \quad (\text{E.7})$$

where  $F$  denotes the volume force (body force). The stress-force relation can be expressed using a compact notation,

$$-\nabla \cdot \boldsymbol{\sigma} = \boldsymbol{F}, \quad (\text{E.8})$$

where  $\boldsymbol{\sigma}$  is the stress tensor. By substituting the stress-strain and strain-displacement relationships using the above equations results in the equation for force-displacement relationship.

As mentioned in the beginning of this section, we set up the model in a 2D axial symmetry mode which uses the cylindrical coordinates,  $r$ ,  $\varphi$ , and  $z$ . This application solves the equations for the global (3D) displacement ( $u$ ,  $w$ ) in the  $r$  and  $z$  directions. The displacement  $v$  in the  $\varphi$  direction together with the  $\tau_{r\varphi}$ ,  $\tau_{\varphi z}$ ,  $\gamma_{r\varphi}$ , and  $\gamma_{\varphi z}$  components of stresses and strains are assumed to be zero. In this mode, loads are independent of  $\varphi$ , and it allows them only in the  $r$  and  $z$  directions. Therefore the strain-displacement relationships are,<sup>E.2</sup>

$$\varepsilon_r = \frac{\partial u}{\partial r} \quad \varepsilon_\varphi = \frac{u}{r} \quad \varepsilon_z = \frac{\partial w}{\partial z} \quad \gamma_{rz} = \frac{\partial u}{\partial z} + \frac{\partial w}{\partial r} \quad . \quad (\text{E.9})$$

The equilibrium equations are described by,

$$\begin{aligned} \frac{\partial \sigma_r}{\partial r} + \frac{\partial \tau_{rz}}{\partial z} + \frac{\sigma_r - \sigma_\varphi}{r} + F_r &= 0 \\ \frac{\partial \tau_{rz}}{\partial r} + \frac{\partial \sigma_z}{\partial z} + \frac{\tau_{rz}}{r} + F_z &= 0 \end{aligned} \quad . \quad (\text{E.10})$$

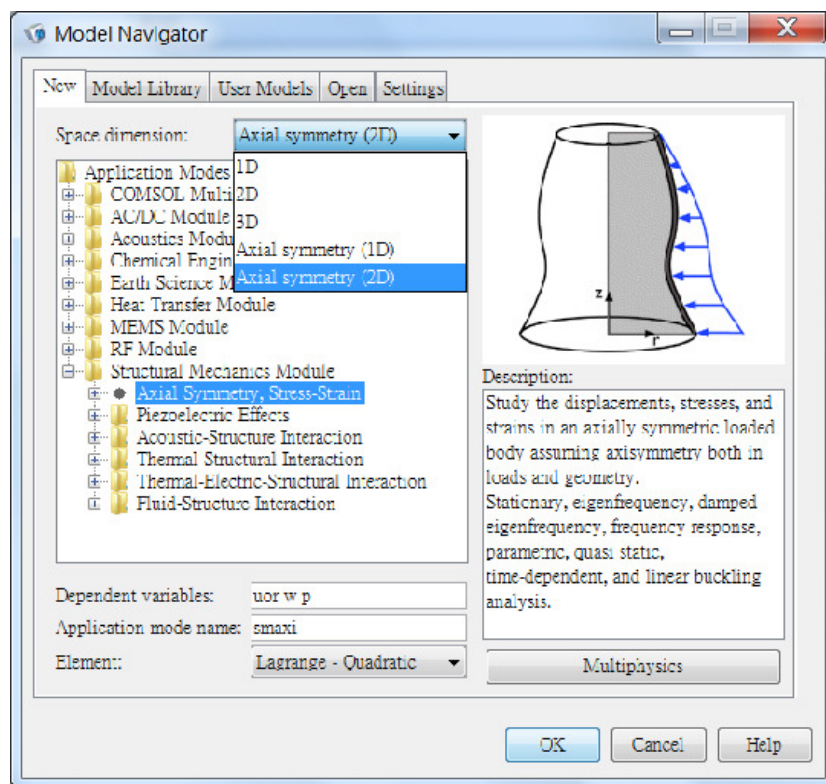
To avoid infinite occurring at  $r=0$  (symmetry axis), this application mode transforms the equations by multiplies the first equation by  $r^2$  and the second by  $r$ , which is common in the principle of virtual work.

## E.2 Step by step procedure for COMSOL simulation

1. Start COMSOL by double-clicking the COMSOL Multiphysics 3.5a icon.

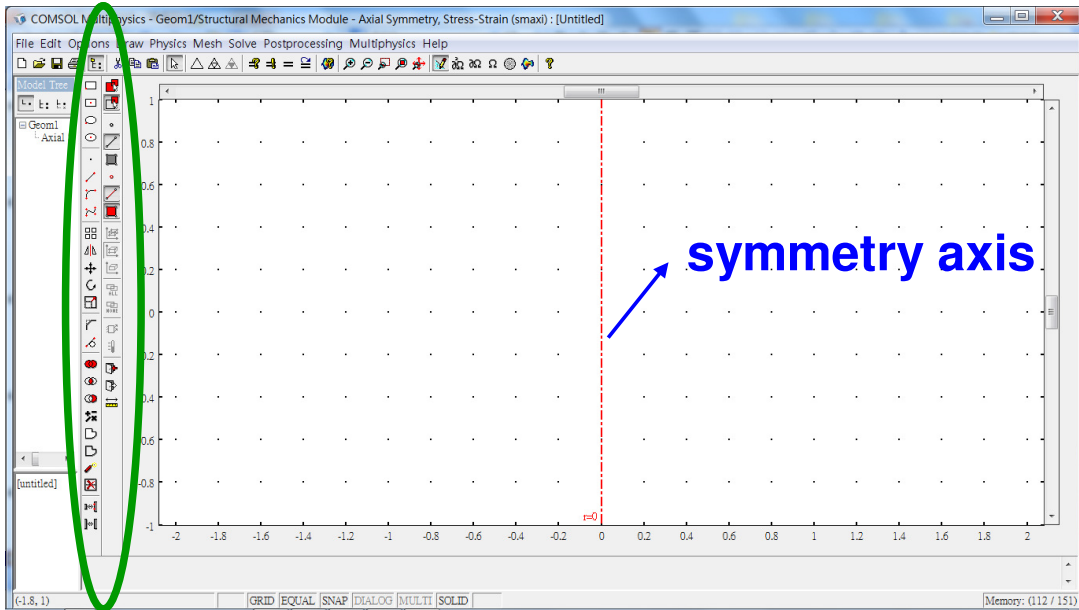


2. When COMSOL Multiphysics starts, the Model Navigator window appears:

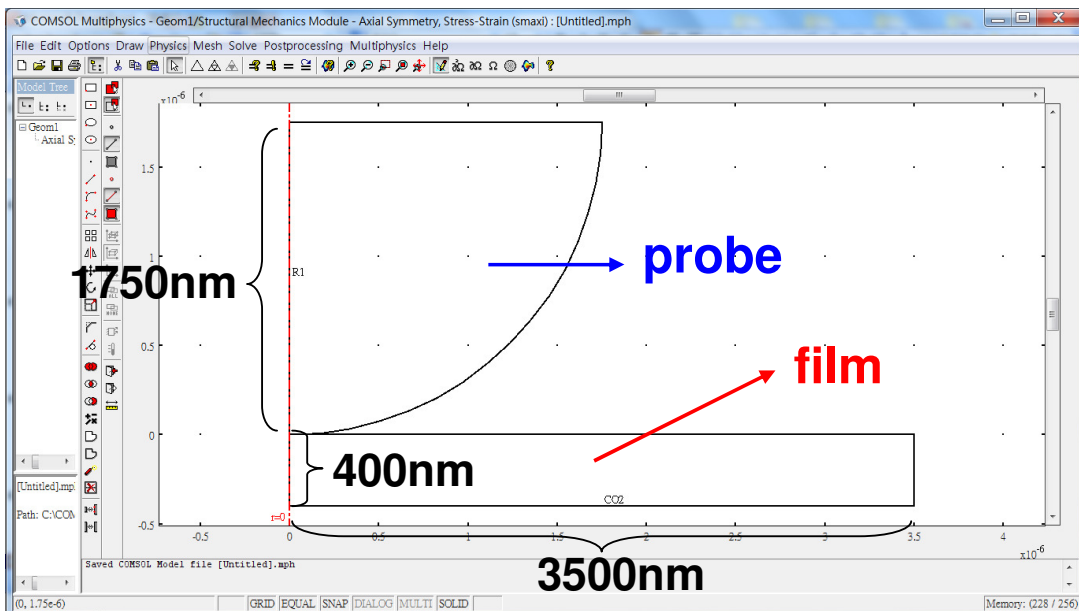


Choose “Axial Symmetry (2D)” as the space dimension, then pick the “Axial Symmetry, Stress-Strain” under the “Structural Mechanics Module”. Then click “OK”.

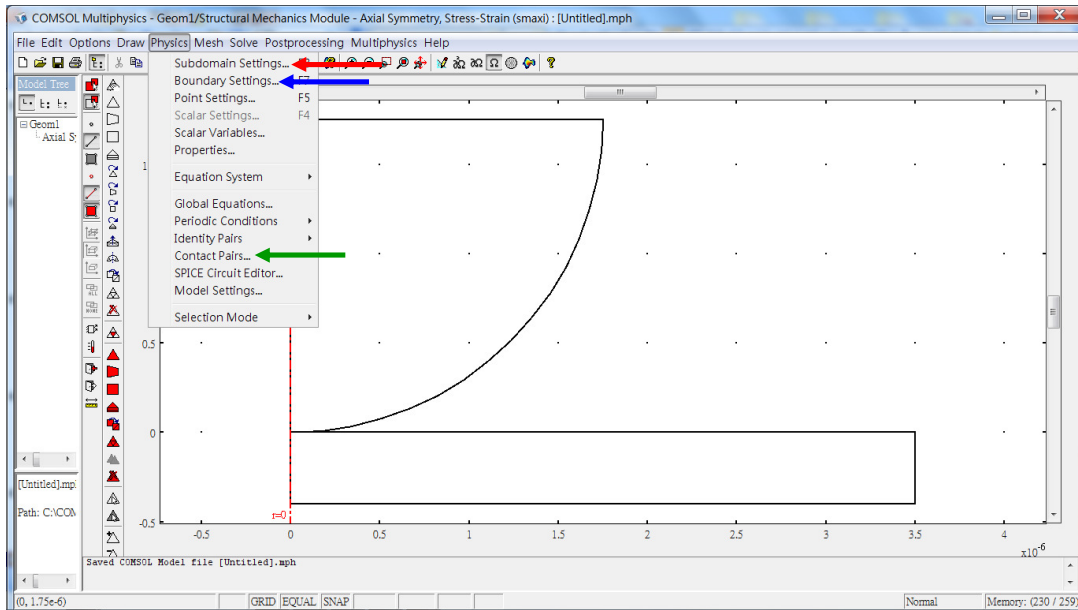
3. After the Model Navigator setting, COMSOL jumps to the “Drawing Mode” for creating geometry of the object of interest.



Use the highlighted tool bar to draw the objects. Due to cylindrical symmetry, we just draw a semi-circle for the probe and a rectangle for the film, with these two coinciding at the origin, show below.



4. This step is to set up for the physics modeling which basically includes three types of setting in our case: “Subdomain Settings”, “Boundary Settings”, and “Contact Pairs”.



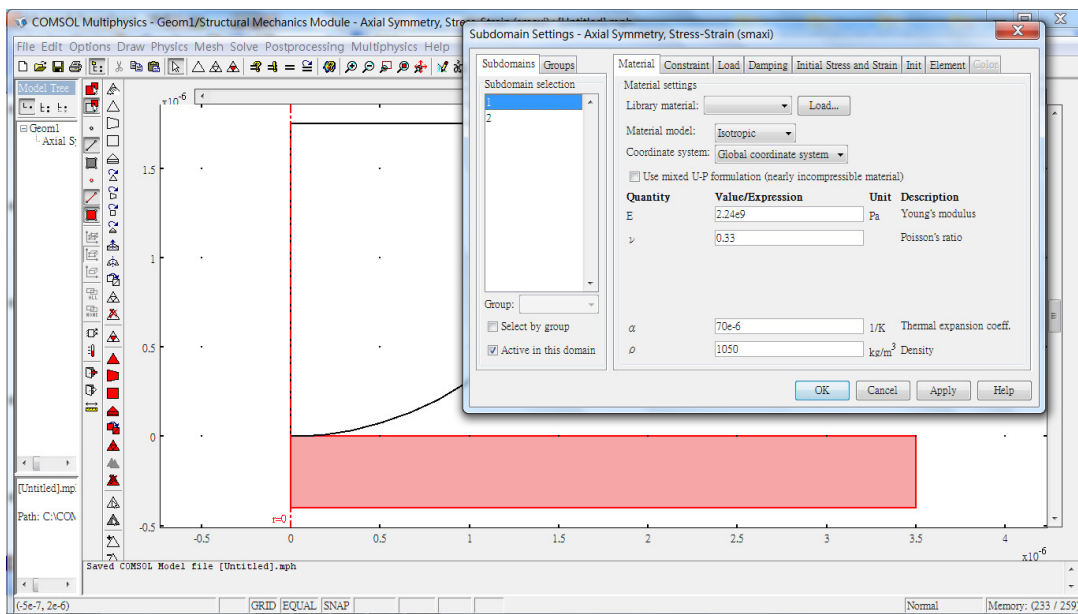
**“Subdomain Settings”** – We mainly specify the materials properties here. In addition, one can implement some specific constraints, e.g. initial stress/strain, body force, etc., by using the setting dialog box.

**“Boundary Settings”** – Here we specify the load and constraints on the edges of the specified object.

**“Contact Pairs”** – For efficiently solving contact problem, this setting allows us to define a “master” and a “slave” for the stiffer and softer boundaries respectively when they actually contact each other during the calculation.

## Subdomain Settings

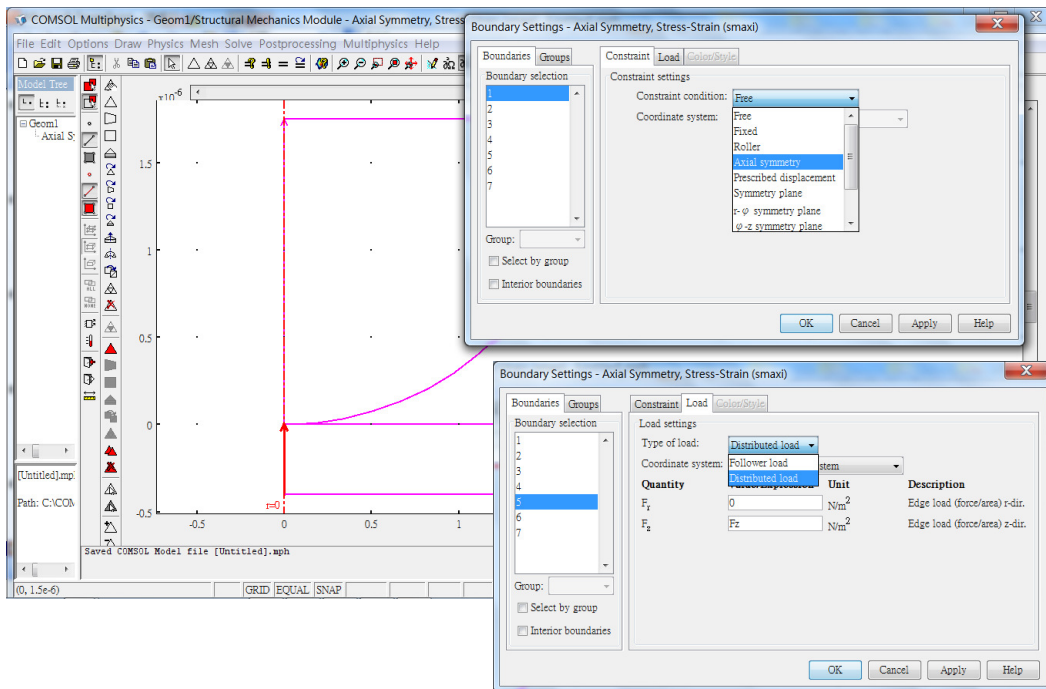
Choose **Physics>”Subdomain Settings”** to enter the setting windows. In the **“Subdomain Settings”>Subdomains>Material** dialog box, choose **“Isotropic”** and **“Global coordinate system”** for the Material model and Coordinate system respectively. Then input the value of the elastic modulus (E), Poisson’s ratio ( $\nu$ ), and density ( $\rho$ ) for each specified geometric object. In this example, we input  $E=2.24e9$  Pa,  $\nu=0.33$ , and  $\rho=1050 \text{ kg/m}^3$  for the polystyrene film material (subdomain 1, pink-highlighted object). Repeat the same procedure to input these values for the probe material (subdomain 2, the hemi-circle object).



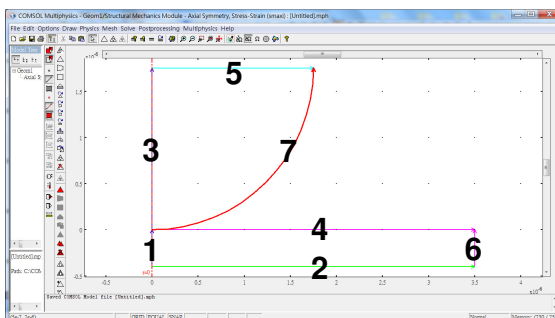
Then click **“OK”** to complete the **“Subdomain Settings”**.

## Boundary Settings

Choose **Physics>”Boundary Settings”** to enter the setting window. In the **“Boundary Settings”>Boundaries>Constraints** dialog window, specify the constraint type for each boundary of the geometry based the box shown below. Note that each boundary is numbered by COMSOL when the geometry is drawn, specified in the bottom figure. We applied load on the boundary 5, so choose **“Boundary Settings”>Boundaries>5>load**. Choose “distributed load”, and input “Fz” for Fz. “Fz” will be specified in the “Solving Parameter” later.



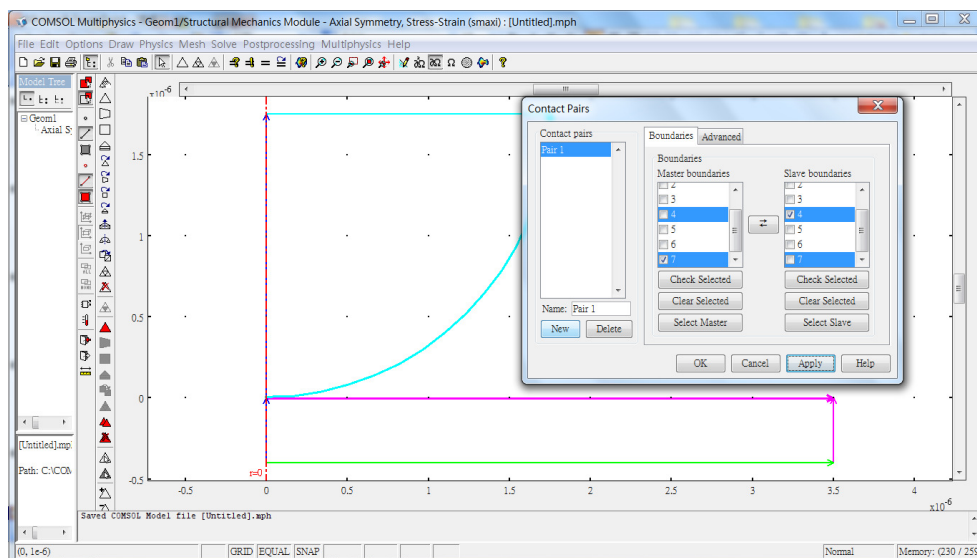
Then click “OK” to complete the “Boundary Settings”.



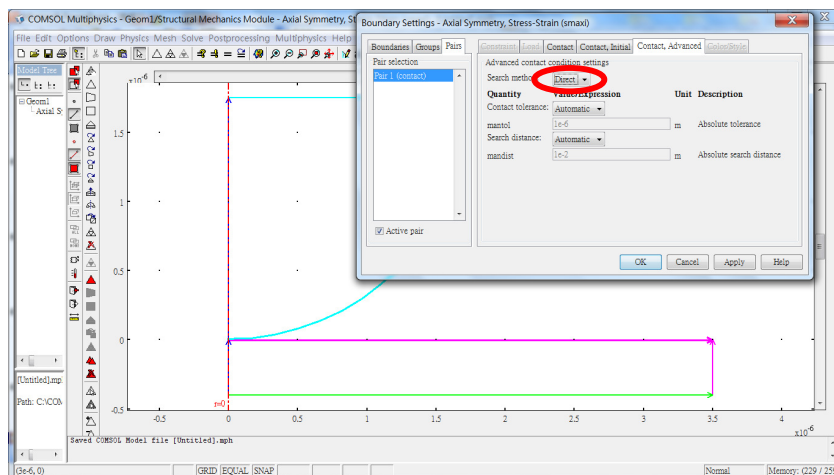
<u>Constraint type</u>	<u>Boundary</u>
axial symmetry	1, 3
fixed	2
free	4, 5, 6, 7

## Contact Pair

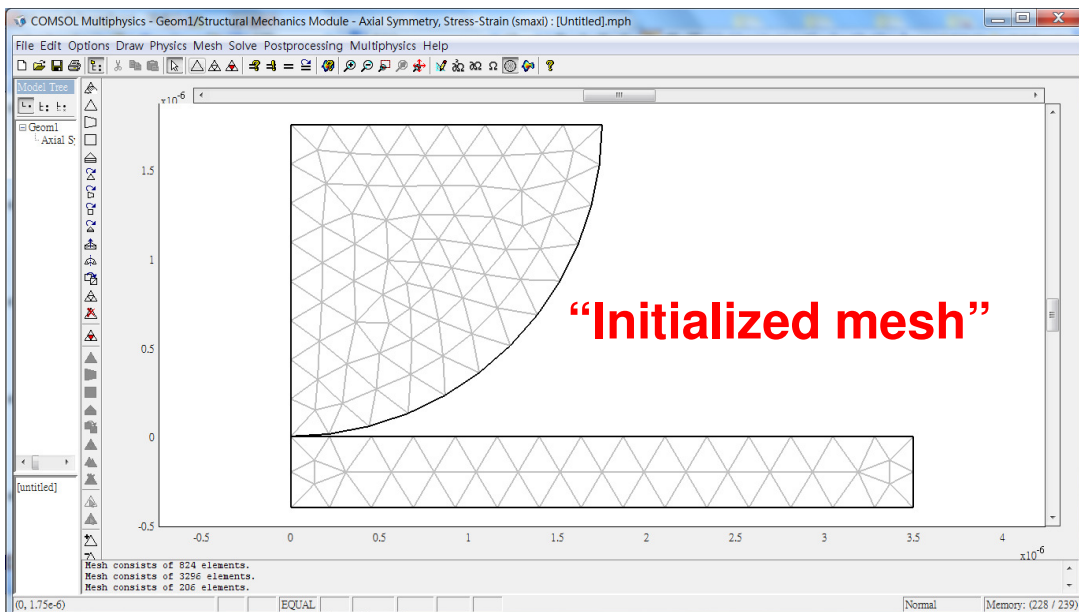
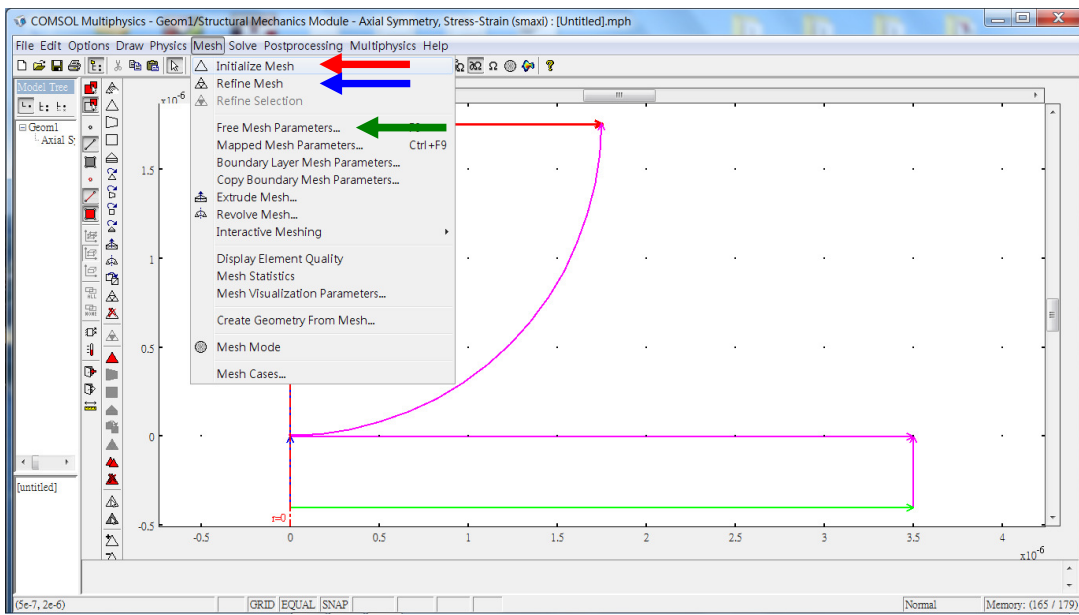
Choose **Physics>”Contact Pairs”** to enter the setting window. In the **“Contact Pairs”>Boundaries** dialog box, create a contact pair by clicking **“New”**, then select the boundaries that contact each other. Choose the boundaries of the stiffer object for the **“Master boundaries”** and those of the softer material for the **“Slave boundaries”**.



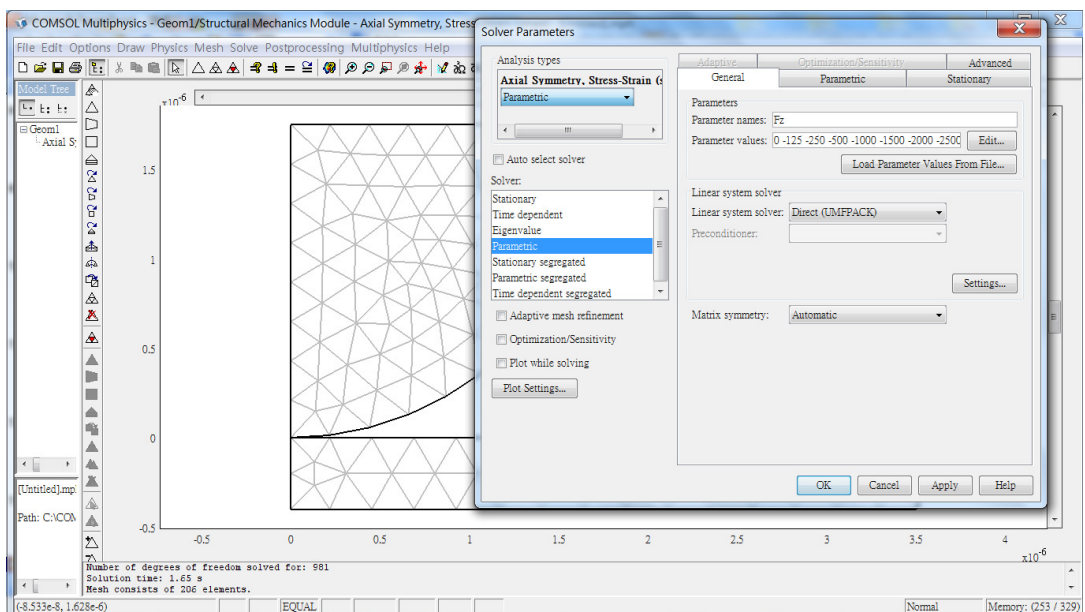
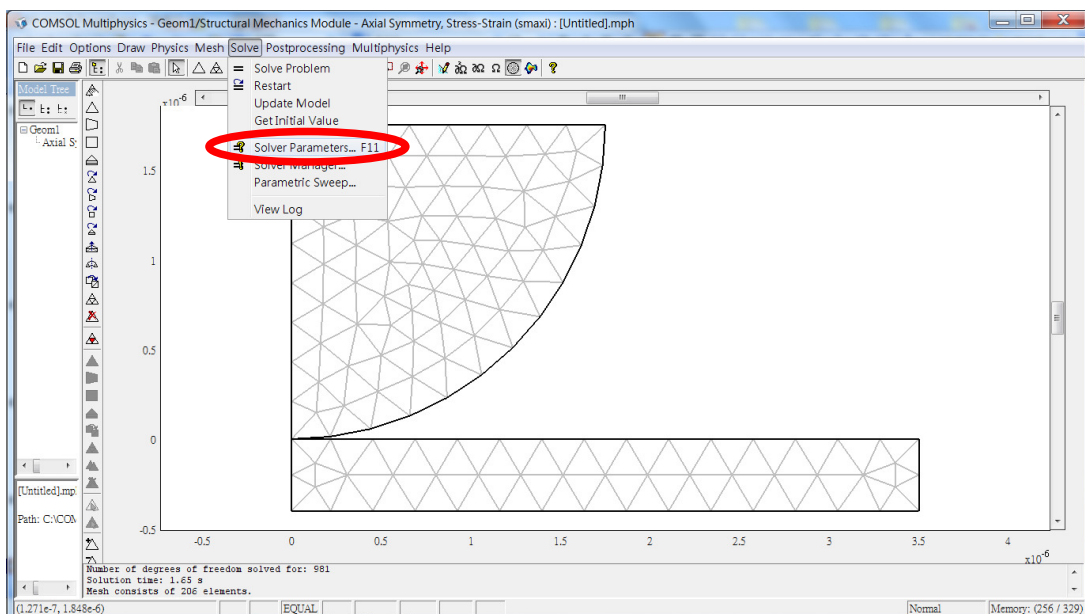
Then click **“OK”** to complete the **“Contact Pairs”** setting. Back to **“Boundary Settings”>Pairs>Contact Advanced**, choose **“Direct”** as the Search Method. Click **“OK”** to complete the physics modeling settings.



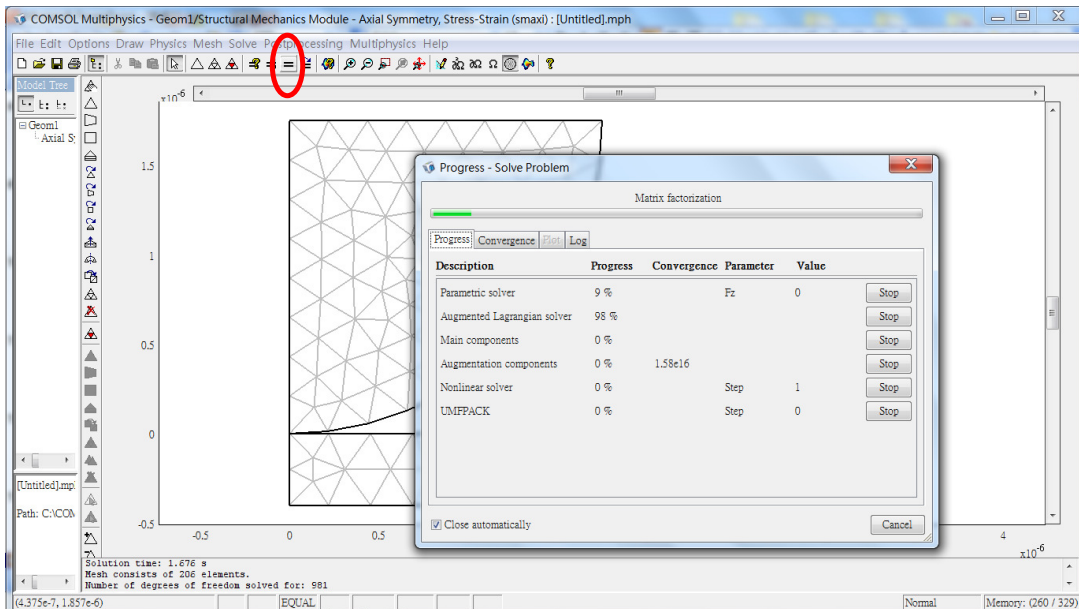
5. After the physics modeling setting, next step is to generate meshes. Choose **Mesh>”Initialize Mesh”** (or **Mesh>”Free Mesh Parameters”** for detailed setting) to generate meshes by default setting. If finer meshes are needed, one can choose **Mesh>”Refine Mesh”** several times after “Initialize Mesh” being chosen.



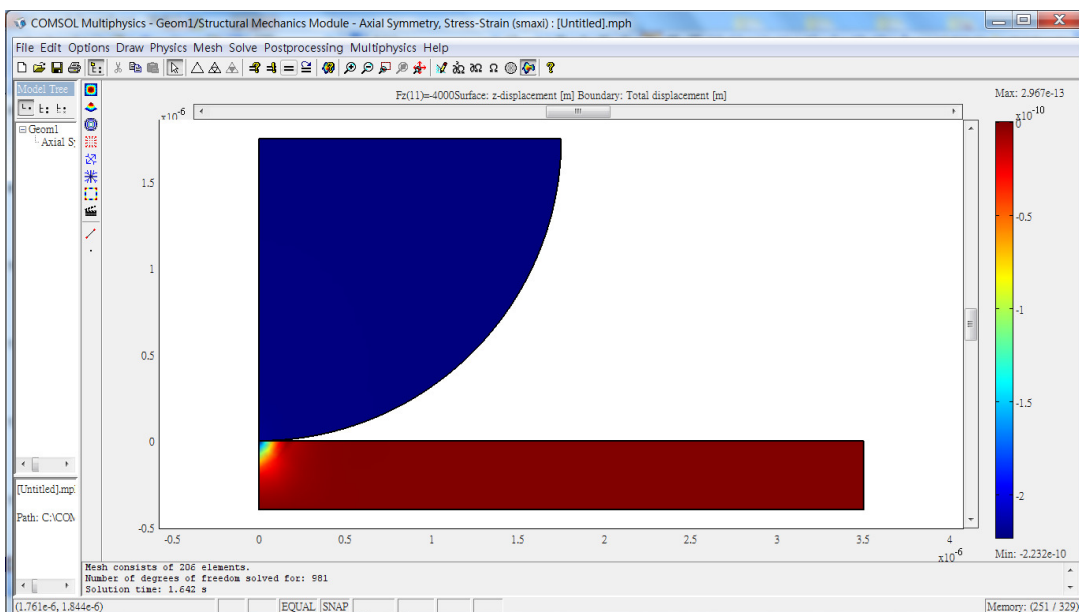
- Before solving, choose **Solve>”Solver Parameters”** to select solver. In the “Solver Parameters” dialog box, select “Parametric” for both “Analysis types” and “Solver”. In the “Solver Parameters”>**General**, input “Fz” for the “Parameter name” and a set of values of load in the unit (N/m<sup>2</sup>) the same as that in the “Boundary Settings”>**Boundaries**>**Load**. Click “OK” to complete setting.



- Click “=” on the tool bar to start solving the problem. During solving, one can monitor the progress by the prompted progress window on the screen.

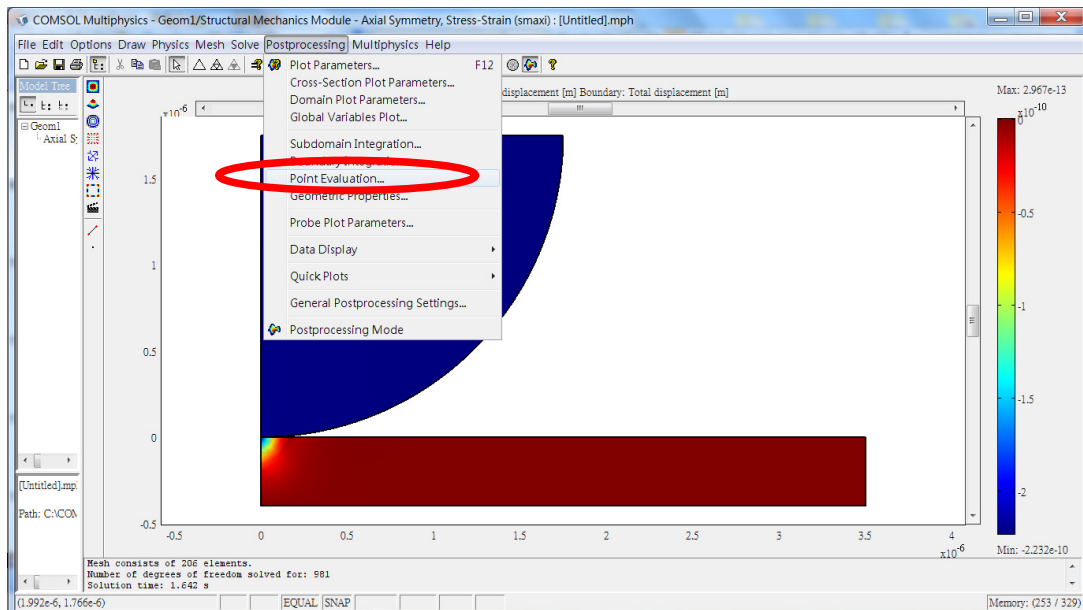


When COMSOL completes the calculation, a resulted plot presented based on user's setting of postprocessing plot replaces the meshed geometric object. In the example shown below is the calculated local vertical displacement of volume elements within the probe and the film under certain value of load ( $F_z=4000$ ).

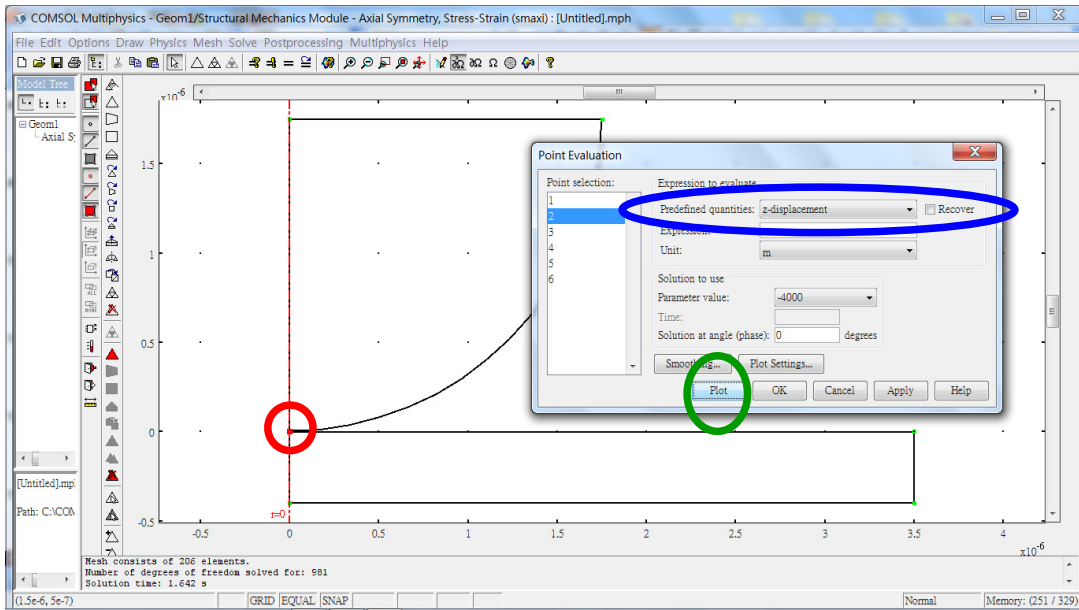


8. After the problem being solved, we can extract the data that we are interested.

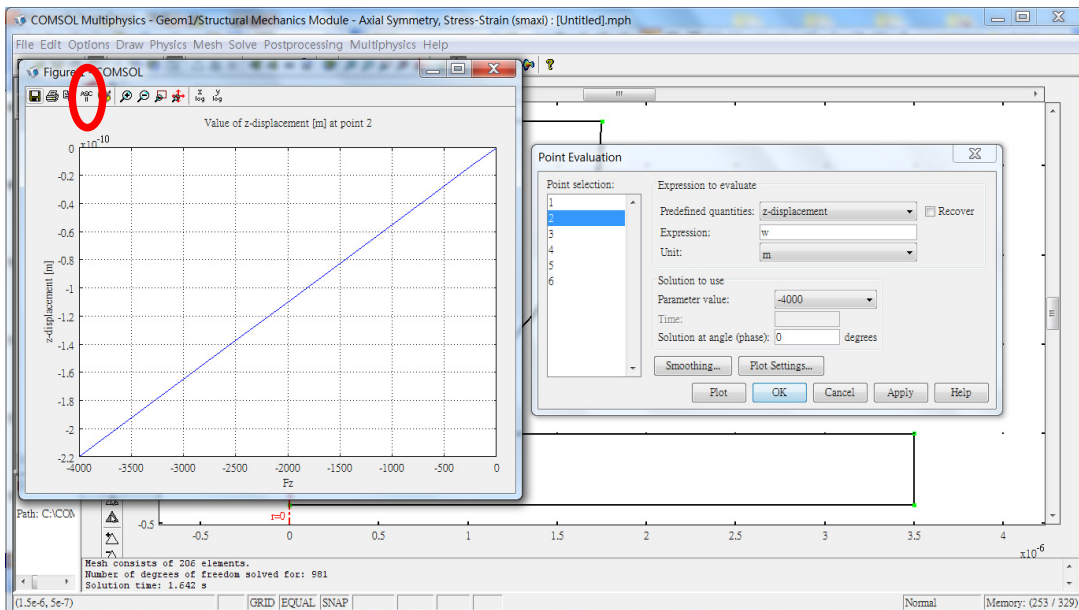
In this example, we are interested in the indentation depth at the position of the probe apex, then we can choose **Postprocessing>”Point Evaluation”** to obtain the displacement of that point (apex).



In the “Point Evaluation” dialog box. We select “2” which is the point of the probe apex (red dot on the geometry) under the “Point selection”, then we choose “z-displacement” for the “Preferred quantities”. If one clicks “OK”, the value of the z-displacement of point 2, corresponding to a certain load parameter ( $-4000\text{N/m}^2$  in this case), will display in the message window at the bottom of the COMSOL parent window. If one clicks “Plot”, one will obtain a window of a plot of z-displacement as a function of applied load ( $Fz$ ) used in this simulation. In the newly generated plot, click the “ASCII” bottom on the toolbar, and COMSOL will generate a DAT file which can be used for further analysis.



By clicking “Plot”, a window of the plot of “z-displacement vs. Fz” is generated.



This example of step-by-step guide of using COMSOL is presented for the purpose of helping first-time user to have a general understanding of how to perform a simulation with COMSOL. One should check the user’s guide [E.2](#), [E.3](#) for more functions for specific needs in the simulation.

## ***Appendix F: Model geometry design and boundary conditions***

Instead of a rather complicated 3D geometry which involves the deflection of cantilever with a spherical tip when being pressed upon a film underlying it, we simplified it by using a much simpler geometry set in which a sphere is pressed against the film with varying prescribed loads. To efficiently use the processing power in our calculation, we use a cylindrically (2D) symmetric configuration in which a hemi-spherical probe is pressed onto a disc-shaped single-layer or bilayer films. The radius of the hemi-sphere is set the same as that of the probe used in the AFM force curve measurement, which is 1750 nm, and the thickness of the films (single polystyrene film, representing a pristine polystyrene film, and a polystyrene film with a damaged layer on top, representing a Ar-plasma exposed polystyrene film) are set according to the measurement result by ellipsometry and XPS<sup>3.2</sup>, which had been detailed in chapter 2. The schematic geometry design of the simulation for the case penetration on an unetched polystyrene film and that on a damaged layer plus underlying unmodified polystyrene film are shown in figure F.1 (a) and (b) respectively. Note that the scales of the films and the probe in figure F.1 are represented in an exaggerated way in order to clearly show the whole scene. In real geometry design, the thickness of the single polystyrene film (film and film 1 in figure F.1) is 400 nm (approximately 1/4 of the probe radius), the thickness of the damaged layer (film 2 in figure F.1) is under 2 nm (almost three orders of magnitudes smaller than the probe radius), and the length of the films are set to be double of the radius of the probe, which is 3500 nm. In addition, we made an approximation which

is that we neglect the surface roughness of the film. This approximation is more proper for the unetched polystyrene film than the Ar-plasma exposed ones, since no significant dominant wavelength ( $\lambda$ ) is observed in the former one.

To decide the elastic constants corresponding to each part of the geometry shown in figure F.1 for the simulation, we use values from both our experimental measurement and literatures. The elastic moduli are 2.24 GPa (from force curve measurement in Chapter 2) for the unetched polystyrene ( $E_{ps}$ ), 75 GPa<sup>F.1</sup> for silica probe ( $E_{tip}$ ), while we vary that ( $E_{DL}$ ) for the damaged layer. The Poisson's ratios are 0.33<sup>3.2</sup> for polystyrene ( $\nu_{ps}$ ), 0.17<sup>F.2</sup> for silica probe ( $\nu_{tip}$ ), and 0.3<sup>3.2</sup> for all damaged layers ( $\nu_{DL}$ ). The densities are 1.05 g/cm<sup>3</sup> <sup>F.3</sup> for polystyrene ( $\rho_{ps}$ ), 2.2 g/cm<sup>3</sup> <sup>F.4</sup> for silica probe ( $\rho_{tip}$ ), and 2.36 g/cm<sup>3</sup>, 2.61 g/cm<sup>3</sup>, 2.68 g/cm<sup>3</sup>, as well as 2.84 g/cm<sup>3</sup> for damaged layers ( $\rho_{DL}$ ) produced by Ar-plasma with ion energies of 50 eV, 75 eV, 100 eV, 150 eV, respectively<sup>3.2</sup>.

The boundary conditions are shown schematically in figure F.1. The boundary with green color is where a uniformly-distributed load is prescribed, and the range of applied load was determined by varying the load so that the load-penetration data can be fit by a 3/2-power law relation (equation 3.10) with the minimum error of fitting, i.e. deformed within elastic range.

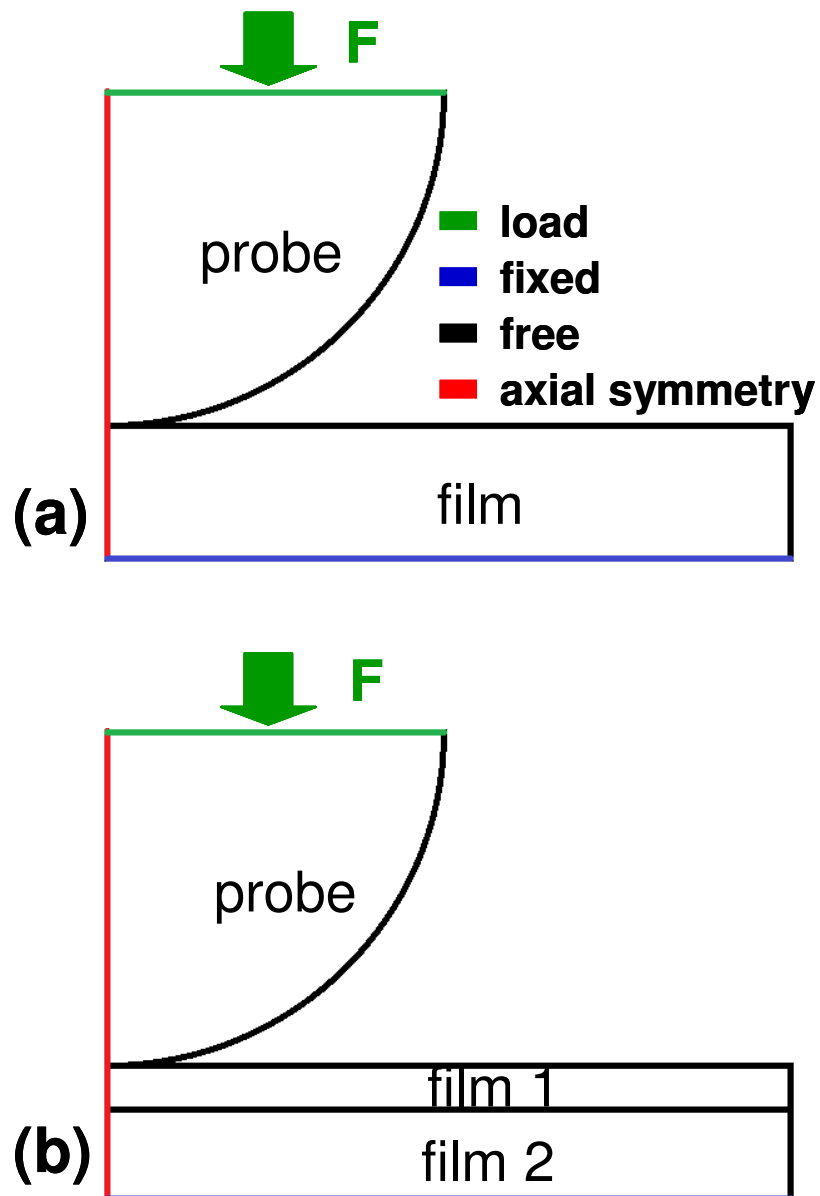


**Figure F.1** Schematic geometry and the boundary conditions for finite element analysis simulation of the penetration for two cases, (a) penetration on a single-layer film (PS only); (b) penetration on a bilayer film structure (polystyrene film plus damaged layer).

# Bibliography

## *Chapter 1*

- 1.1 A. A. Tseng, K. Chen, C. D. Chen, and K. J. Ma, *IEEE Transactions on Electronics Packaging Manufacturing* **26**, 141 (2003).
- 1.2 A. M. Hawryluk and L. G. Seppala, *Journal of Vacuum Science and Technology B* **6**, 2162 (1988).
- 1.3 B. Wu and A. Kumar, *Journal of Vacuum Science and Technology B* **25**, 1743 (2007).
- 1.4 S. Y. Chou, P. R. Krauss, and P. J. Renstrom, *Applied Physics Letters* **67**, 3114 (1995).
- 1.5 D. J. Resnick, W. J. Dauksher, D. Mancini, K. J. Nordquist, T. C. Bailey, S. Johnson, N. Stacey, J. G. Ekerdt, C. G. Willson, S. V. Sreenivasan, and N. Shumaker, *Journal of Vacuum Science and Technology B* **21**, 2624 (2003).
- 1.6 W. Hu, K. Sarveswaran, M. Lieberman, and G. H. Bernstein, *Journal of Vacuum Science and Technology B* **22**, 1711 (2004).
- 1.7 B. Päivänranta, A. Langner, E. Kirk, C. David, and Y. Ekinici, *Nanotechnology* **22**, 375302 (2011).
- 1.8 S. Y. Chou and P. R. Krauss, *Microelectronic Engineering* **35**, 237 (1997).

- 1.9 R. L. Bruce, F. Weirnboeck, T. Lin, R. J. Phaneuf, G. S. Oehrlein, B. K. Long, C. G. Willson, J. J. Vegh, D. Nest, and D. B. Graves, *Journal of Applied Physics* **107**, 084310 (2010).
- 1.10 G. S. Oehrlein, R. J. Phaneuf and D. B. Graves, *Journal of Vacuum Science and Technology B* **29**, 010801 (2011).
- 1.11 H. Jiang, D.-Y. Khang, J. Song, Y. Sun, Y. Huang, and J. A. Rogers, *Proceedings of the National Academy of Sciences U.S.A.* **104**, 15607 (2007).
- 1.12 C. M. Stafford, C. Harrison, K. L. Beers, A. Karim, E. J. Amis, M. R. Vanlandingham, H.-C. Kim, W. Volksen, R. D. Miller, and E. E. Simonyi, *Nature Materials* **3**, 545 (2004).
- 1.13 P. J. Yoo and H. H. Lee, *Macromolecules* **38**, 2820 (2005).
- 1.14 H. Jansen, H. Gardeniers, M. de Boer, M. Elwenspoek, and J. Fluitman, *Journal of Micromechanics and Microengineering* **6**, 14 (1996).
- 1.15 Y. Hsu, T. E. F. M. Standaert, G. S. Oehrlein, T. S. Kuan, E. Sayre, K. Rose, K. Y. Lee, and S. M. Rossnagel, *Journal of Vacuum Science and Technology B* **16**, 3344 (1998).
- 1.16 J. J. Végh, D. Nest, D. B. Graves, R. Bruce, S. Engelmann, T. Kwon, R. J. Phaneuf, G. S. Oehrlein, B. K. Long, and C. G. Willson, *Applied Physics Letters* **91**, 233113 (2007).
- 1.17 Y. Koval, *Journal of Vacuum Science and Technology B* **22**, 843 (2004).
- 1.18 K. J. Orvek and C. Huffman, *Nuclear Instruments and Methods in Physics Research B* **7-8**, 501 (1985).

- 1.19 T. Hori, M. D. Bowden, K. Uchino, K. Muraoka, and M. Maeda, *Journal of Vacuum Science and Technology A* **14**, 144 (1996).
- 1.20 X. Li, G. S. Oehrlein, M. Schaepkens, R. E. Ellefson, and L. C. Frees, *Journal of Vacuum Science and Technology A* **21**, 1971 (2003).
- 1.21 C. M. Chan, T. M. Ko, and H. Hiraoka, *Surface Science Reports* **24**, 1 (1996).
- 1.22 H. Kawahira *et al.*, *Proc. SPIE* **6153**, 615319 (2006).
- 1.23 F. Weilmboeck, R. L. Bruce, S. Engelmann, G. S. Oehrlein, D. Nest, T.-Y. Chung, D. B. Graves, M. Li, D. Wang, C. Andes, and E. A. Hudson, *Journal of Vacuum Science and Technology B* **28**, 993 (2010).
- 1.24 L. A. Wall, *Journal of Polymer Science Part B* **17**, 141 (1955).
- 1.25 K. Dawes and L. C. Glover, *Physical Properties of Polymers Handbook*, edited by J. E. Mark (AIP Press, NY, 1996), p. 557.
- 1.26 J. Zekonyte, V. Zaporojtchenko, and F. Faupel, *Nuclear Instruments and Methods in Physics Research B* **236**, 241 (2005).
- 1.27 J. R. Woodworth, M. E. Riley, V. A. Arnatucci, T. W. Hamilton, and B. P. Aragon, *Journal of Vacuum Science and Technology A* **19**, 45 (2001).
- 1.28 J. F. Rabek, *Mechanisms of Photophysical Processes and Photochemical Reactions in Polymers: Theory and Applications* (Wiley, Chichester, NY, 1987), p. 5.
- 1.29 J. F. Rabek, *Photodegradation of Polymers: Physical Characteristics and Applications* (Springer, New York, 1996), p. 4.

- 1.30 R. L. Bruce, F. Weirnboeck, T. Lin, R. J. Phaneuf, G.S. Oehrlein, B. K. Long, C. G. Willson, and A. Alizadeh, *Journal of Vacuum Science and Technology B* **29**, 0416041 (2011).
- 1.31 A.-L. Barabási and H. E. Stanley, *Fractal Concepts in Surface Growth* (Cambridge University Press, New York, 1995).
- 1.32 Y.-P. Zhao, J. T. Drotar, G.-C. Wang, and T.-M. Lu, *Physical Review Letters* **87**, 136102 (2001).
- 1.33 J. T. Drotar, Y.-P. Zhao, T.-M. Lu, and G.-C. Wang, *Physical Review B* **61**, 3012 (2000).
- 1.34 S. Park, B. Kahng, H. Jeong, and A.-L. Barabási, *Physical Review Letters* **83**, 3486 (1999).
- 1.35 E. Chason and M. J. Aziz, *Scripta Materialia* **49**, 953 (2003).
- 1.36 D. G. Cahill, *Journal of Vacuum Science and Technology A* **21**, S110 (2003).
- 1.37 Z. X. Jiang and P. F. A. Alkemade, *Applied Physics Letters* **73**, 315 (1998).
- 1.38 E. Pargon, D. Nest, and D. B. Graves, *Journal of Vacuum Science and Technology B* **25**, 1236 (2007).
- 1.39 V. K. Singh, E. S. G. Shaqfeh, and J. P. McVittie, *Journal of Vacuum Science and Technology B* **10**, 1091 (1992).
- 1.40 V. K. Singh, E. S. G. Shaqfeh, and J. P. McVittie, *Journal of Vacuum Science and Technology B* **12**, 2952 (1994).

- 1.41 T. Kwon, PhD Thesis, Department of Materials Science and Engineering, University of Maryland, College Park, MD (2007).
- 1.42 M. Sumiya, R. L. Bruce, S. Engelmann, F. Weirnboeck, and G. S. Oehrlein, *Journal of Vacuum Science and Technology B* **26**, 1637 (2008).
- 1.43 M. Sumiya, R. L. Bruce, S. Engelmann, F. Weirnboeck, and G. S. Oehrlein, *Journal of Vacuum Science and Technology B* **26**, 1647 (2008).
- 1.44 M. Sumiya, R. L. Bruce, S. Engelmann, F. Weirnboeck, and G. S. Oehrlein, *Journal of Vacuum Science and Technology B* **26**, 1978 (2008).
- 1.45 T.-Y. Chung, D. Nest, D. B. Graves, F. Weirnboeck, R. L. Bruce, G. S. Oehrlein, D. Wang, M. Li, E. A. Hudson, *Journal of Physics D* **43**, 272001 (2010).
- 1.46 D. Nest, T.-Y. Chung, J. J. Végh, D. B. Graves, R. L. Bruce, T. Lin, R. J. Phaneuf, G. S. Oehrlein, B. K. Long, and C. G. Willson, *Journal of Physics D* **43**, 085204 (2010).
- 1.47 R. L. Bruce, S. Engelmann, T. Lin, T. Kwon, R. J. Phaneuf, G.S. Oehrlein, B. K. Long, C. G. Willson, J. J. Végh, D. Nest, D. B. Graves, and A. Alizadeh, *Journal of Vacuum Science and Technology B* **27**, 1142 (2009).
- 1.48 J. J. Végh, D. Nest, D. B. Graves, R. L. Bruce, S. Engelmann, T. Kwon, R. J. Phaneuf, G. S. Oehrlein, B. K. Long, and C. G. Willson, *Journal of Applied Physics* **104**, 034308 (2008).
- 1.49 D. Nest, PhD thesis, University of California, Berkeley, CA (2009).
- 1.50 J. Genzer and J. Groenewold, *Soft Matter* **2**, 310 (2006).

- 1.51 S. Singamaneni and V. V. Tsukruk, *Soft Matter* **6**, 5681 (2010).
- 1.52 R. Huang and S. H. Im, *Physical Review E* **74**, 026214 (2006).
- 1.53 N. Bowden, S. Brittain, A. G. Evans, J. W. Hutchinson, and G. M. Whitesides, *Nature* **393**, 146 (1998).
- 1.54 Y. Q. Fu, S. Sanjabi, Z. H. Barber, T. W. Clyne, W. M. Huang, M. Cai, J. K. Luo, A. J. Flewitt, and W. I. Milne, *Applied Physics Letters* **89**, 171922 (2006).
- 1.55 D.-Y. Khang, H. Jiang, Y. Huang, and J. A. Rogers, *Science* **311**, 208 (2006).
- 1.56 C. Harrison, C. M. Stafford, W. H. Zhang, and A. Karim, *Applied Physics Letters* **85**, 4016 (2004).
- 1.57 H. Jiang, D.-Y. Khang, J. Song, Y. Sun, Y. Huang, and J. A. Rogers, *Proceedings of the National Academy of Sciences U.S.A.* **104**, 15607 (2007).
- 1.58 K. J. Lee, M. J. Motala, M. A. Meitl, W. R. Childs, E. Menard, A. K. Shim, J. A. Rogers, and R. G. Nuzzo, *Advanced Materials* **17**, 2332 (2005).
- 1.59 H.-H. Yu and J. W. Hutchinson, *International Journal of Fracture* **113**, 39 (2002).
- 1.60 B. Cotterell and Z. Chen, *International Journal of Fracture* **104**, 169 (2000).
- 1.61 B. Bhushan and X. Li, *International Materials Reviews* **48**, 125 (2003).
- 1.62 C. Ortiz and G. Hadziioannou, *Macromolecules* **32**, 780 (1999).
- 1.63 B. Bhushan, *Philosophical Transactions of the Royal Society A* **366**, 1351 (2008).

- 1.64 H.-J. Butt, B. Cappella, and M. Kappl, *Surface Science Report* **59**, 1 (2005).
- 1.65 J. N. Israelachvili, *Intermolecular and Surface Forces 3<sup>rd</sup> edition* (Academic Press, Burlington MA, 2011).
- 1.66 H. Hertz, *Journal für die Reine und Angewandte Mathematik* **92**, 156 (1882).
- 1.67 K. L. Johnson, K. Kendall, and A. D. Roberts, *Proceedings of the Royal Society of London A* **324**, 301 (1971).
- 1.68 B. V. Derjaguin, V. M. Muller, and Y. P. Toporov, *Journal of Colloid Interface Science* **53**, 314 (1975).
- 1.69 D. S. Grierson, E. E. Flater, and R. W. Carpick, *Atomic Force Microscopy in Adhesion Studies*, edited by J. Drelich and K. L. Mittal (VSP, Leiden-Boston, 2005), p. 75.
- 1.70 D. Maugis, *Journal of Colloid Interface Science* **150**, 243 (1992).
- 1.71 R. W. Carpick, D. F. Ogletree, and M. Salmeron, *Journal of Colloid Interface Science* **211**, 395 (1999).
- 1.72 O. Piétremont and M. Troyon, *Journal of Colloid Interface Science* **226**, 166 (2000).
- 1.73 I. N. Sneddon, *International Journal of Engineering Science* **3**, 47 (1965).

## ***Chapter 2***

- 2.1 R. L. Bruce, PhD Thesis, Department of Materials Science and Engineering, University of Maryland, College Park, MD (2010).

- 2.2 R. L. Bruce, F. Weirboeck, T. Lin, R. J. Phaneuf, G.S. Oehrlein, B. K. Long, C. G. Willson, J. J. Végh, D. Nest, and D. B. Graves, *Journal of Applied Physics* **107**, 084310 (2010).
- 2.3 J. J. Végh, D. Nest, D. B. Graves, R. Bruce, S. Engelmann, T. Kwon, R. J. Phaneuf, G. S. Oehrlein, B. K. Long, and C. G. Willson, *Applied Physics Letters* **91**, 233113 (2007).
- 2.4 J. P. Aimé, Z. Elkaakour, C. Odin, T. Bouhacina, D. Michel, J. Curély, and A. Dautant, *Journal of Applied Physics* **76**, 754 (1994).
- 2.5 V. N. Blisnyuk, H. E. Assender, and G. A. D. Briggs, *Macromolecules* **35**, 6613 (2002).
- 2.6 D. Tranchida, Z. Kiflie, S. Acierno, and S. Piccarolo, *Measurement Science and Technology* **20**, 095702 (2009).
- 2.7 J. K. Gimzewski, *Science* **283**, 1683 (1999).
- 2.8 F. Mugele, T. Becker, R. Nikopoulos, M. Kohonen, and S. Herminghaus, *Journal of Adhesion Science and Technology* **16**, 951 (2002).
- 2.9 I. T. S. Li and G. C. Walker, *Journal of American Chemical Society* **132**, 6530 (2010).
- 2.10 M. Rief, F. Oesterhelt, B. Heymann, and H. E. Gaub, *Science* **275**, 1295 (1997).
- 2.11 H. Li, B. Liu, X. Zhang, C. Gao, J. Shen, and G. Zou, *Langmuir* **15**, 2120 (1999).

- 2.12 I. T. S. Li and G. C. Walker, *PNAS* **108**, 16527 (2011).
- 2.13 N. A. Burnham, D. D. Dominguez, R. L. Mowery, and R. J. Colton, *Physical Review Letters* **64**, 1931 (1990).
- 2.14 N. A. Burnham and R. J. Colton, *Journal of Vacuum Science and Technology* **A7**, 2906 (1989).
- 2.15 D. H. Gracias and G. A. Somorja, *Macromolecules* **31**, 1269 (1998).
- 2.16 H.-J. Butt, B. Cappella, and M. Kappl, *Surface Science Reports* **59**, 1 (2005).
- 2.17 F. L. Leite and P. S. P. Herrmann, *Atomic Force Microscopy in Adhesion Studies*, edited by J. Drelich and K. L. Mittal (VSP, Leiden-Boston, 2005), p3.
- 2.18 Veeco Metrology Group, Force Measurement (Support Note No. 228).
- 2.19 K. L. Johnson, K. Kendall, and A. D. Roberts, *Proceedings of the Royal Society of London A* **324**, 301 (1971).
- 2.20 B. V. Derjaguin, V. M. Muller, and Y. P. Toporov, *Journal of Colloid Interface Science* **53**, 314 (1975).
- 2.21 D. Maugis, *Journal of Colloid Interface Science* **150**, 243 (1992).
- 2.22 R. W. Carpick, D. F. Ogletree, and M. Salmeron, *Journal of Colloid Interface Science* **211**, 395 (1999).
- 2.23 O. Piétrement and M. Troyon, *Journal of Colloid Interface Science* **226**, 166 (2000).
- 2.24 D. C. Lin, E. K. Dimitriadis, and F. Horkay, *Transactions of the ASME* **129**, 430 (2007).

- 2.25 D. C. Lin, E. K. Dimitriadis, and F. Horkay, *Transactions of the ASME* **129**, 904 (2007).
- 2.26 Y. Sun, B. Akhremitchev, and G. C. Walker, *Langmuir* **20**, 5837 (2004).
- 2.27 I. W. Gilmour, A. Trainor, and R. N. Haward, *Journal of Applied Polymer Science* **23**, 3123 (1979).

### ***Chapter 3***

- 3.1 P. L. Gould, *Introduction to Linear Elasticity* (Springer-Verlag, New York, 1983).
- 3.2 H. Hertz, *Journal für die Reine und Angewandte Mathematik* **92**, 156 (1882).
- 3.3 R. L. Bruce, F. Weirnboeck, T. Lin, R. J. Phaneuf, G.S. Oehrlein, B. K. Long, C. G. Willson, J. J. Végh, D. Nest, and D. B. Graves, *Journal of Applied Physics* **107**, 084310 (2010).
- 3.4 R. Sburlati, *International Journal of Solids and Structures* **46**, 975 (2009).

### ***Chapter 4***

- 4.1 R. L. Bruce, F. Weirnboeck, T. Lin, R. J. Phaneuf, G.S. Oehrlein, B. K. Long, C. G. Willson, J. J. Végh, D. Nest, and D. B. Graves, *Journal of Applied Physics* **107**, 084310 (2010).
- 4.2 C. Lee, X. Wei, J. W. Kysar, and J. Hone, *Science* **321**, 385 (2008).

- 4.3 J. S. Bunch, S. S. Verbridge, J. S. Alden, A. M. van der Zande, J. M. Parpia, H. G. Craighead, and P. L. McEuen, *Nano Letters* **8**, 2458 (2008).
- 4.4 J.-W. Jiang, J.-S. Wang, and B. Li, *Physical Review B* **80**, 113405 (2009).
- 4.5 H. Jiang, D.-Y. Khang, J. Song, Y. Sun, Y. Huang, and J. A. Rogers, *Proceedings of the National Academy of Sciences U.S.A.* **104**, 15607 (2007).
- 4.6 W. Bao, F. Miao, Z. Chen, H. Zhang, W. Jang, C. Dames, and C. N. Lau, *Nature Nanotechnology* **4**, 562 (2009).
- 4.7 J.-W. Jiang, J.-S. Wang, and B. Li, *Physical Review B* **80**, 205429 (2009).

## ***Appendix A***

- A.1 T. Kwon, PhD Thesis, Department of Materials Science and Engineering, University of Maryland, College Park, MD (2007).
- A.2 Veeco, *Digital Instruments User Manual: Nanolithography Software Version 5.12*.
- A.3 W. W. Mullins, *Journal of Applied Physics* **30**, 77 (1959).
- A.4 T. Leveder, S. Landis, and L. Davoust, *Applied Physics Letters* **92**, 013107 (2008).
- A.5 D. C. Blackley, *Polymer Lattices: Science and Technology: Volume 1 – Fundamental Principles 2<sup>nd</sup> edition* (Springer, 1997), p.90.
- A.6 T. Hata, *Kobunshi* **17**, 594 (1968).

## ***Appendix B***

- B.1 J. C. Vickerman, *Surface Analysis – The Principle Techniques* (John Wiley & Sons, 1997).
- B.2 M. F. Hochella Jr. and A. H. Carim, *Surface Science* **197**, L260 (1988).
- B.3 H. Yamamoto, Y. Baba, and T. A. Sasaki, *Surface Science* **349**, L133 (1996).
- B.4 H. Maiwa and N. Ichinose, *Journal of the European Ceramic Society* **21**, 1573 (2001).

## ***Appendix C***

- C.1 J. Grobelny, N. Pradeep, D.-I. Kim, and Z. C. Ying, *Applied Physics Letters* **88**, 091906 (2006).
- C.2 E.-S. Yoon, S. H. Yang, H.-G. Han, and H. Kong, *Wear* **254**, 974 (2003).
- C.3 D. C. Lin, E. K. Dimitriadis, and F. Horkay, *Transactions of the ASME* **129**, 430 (2007).
- C.4 D. C. Lin, E. K. Dimitriadis, and F. Horkay, *Transactions of the ASME* **129**, 904 (2007).
- C.5 S. L. Hsu, *Polymer Data Handbook* (Oxford University Press, 1999), p656.

## ***Appendix E***

- E.1 W. B. Bickford, *A First Course in the Finite Element Method*/2<sup>nd</sup> edition (McGraw-Hill Higher Education, 1994).

E.2 COMSOL AB, *Structural Mechanics Module User's Guide*/Version 3.5a (2008).

E.3 COMSOL AB, *COMSOL Multiphysics User's Guide*/Version 3.5a (2008).

## ***Appendix F***

F.1 B. Hälg, *Micro Electro Mechanical Systems, 1990 Proceedings – An Investigation of Micro Structures, Sensors, Actuators, Machines and Robots. IEEE* , 172 (1990).

F.2 M. T. Kim, *Thin Solid Films* **283**, 12 (1996).

F.3 Z. Pu, *Polymer Data Handbook* (Oxford University Press, 1999), p830.

F.4 T. Leveder, S. Landis, and L. Davoust, *Applied Physics Letters* **92**, 013107 (2008).